Imperial College London

Numerical Simulation and Characterisation of the Packing of Granular Materials

Romain Guises

July 2008

Department of Earth Sciences and Engineering
Imperial College London

A dissertation submitted to the Department of Earth Science and Engineering of Imperial College London in partial fulfilment of the requirements for the degree of Doctor of Philosophy

The material in this thesis is entirely the result of my own independent research under the supervision of Dr. J.-P. Latham, Prof. A. Munjiza, and is not the outcome of any collaborative work. The research was carried out in the Department of Earth Science and Engineering at Imperial College London. All published or unpublished material used in this thesis has been given full acknowledgment.
No part of this work has been previously submitted to this or any other academic institution for a degree or diploma, or any other qualification.

Romain GUISES

PhD Student
Earth Science and Engineering Department
Imperial College London

Abstract

The scientific problems related to granular matter are ubiquitous. It is currently an active area of research for physicists and earth scientists, with a wide range of applications within the industrial community. Simple analogue experiments exhibit behaviour that is neither predicted nor described by any current theory. The work presented here consists of modelling granular media using a two-dimensional combined Finite-Discrete Element Method (FEM-DEM). While computationally expensive, as well as modelling accurately the dynamic interactions between independent and arbitrarily shaped grains, this method allows for a complete description of the stress state within individual grains during their transient motion.

After a detailed description of FEM-DEM principles, this computational approach is used to investigate the packing of elliptical particles. The work is aimed at understanding the influence of the particle shape (the ellipse aspect ratio) on the emergent properties of the granular matrix such as the particle coordination number and the packing density. The differences in microstructure of the resultant packing are analysed using pair correlation functions, particle orientations and pore size distributions. A comparison between frictional and frictionless systems is carried out. It shows great differences not only in the calculated porosity and coordination number, but also in terms of structural arrangement and stress distribution. The results suggest that the particle's shape affects the structural order of the particle assemblage, which itself controls the stress distribution between the pseudo-static grains.

The study then focuses on describing the stress patterns or "force chains" naturally generated in a frictional system. An algorithm based on the analysis of the contact force network is proposed and applied to various packs in order to identify the force chains. A statistical analysis of the force chains looking at their orientation, length and proportion of the particles that support the loads is then performed. It is observed that force chains propagate less efficiently and more heterogeneously through granular systems made of elliptical particles than through systems of discs and it is proposed that structural differences due to the particle shape lead to a significant reduction in the

length of the stress path that propagates across connected particles. Finally, the effect of compression on the granular packing, the emergent properties and the contact force distribution is examined. Results show that the force network evolves towards a more randomly distributed system (from an exponential to a Gaussian distribution), and it confirms the observations made from simulations using discs.

To conclude, the combined finite-discrete element method applied to the study of granular systems provides an attractive modelling strategy to improve the knowledge of granular matter. This is due to the wide range of static and dynamic problems that can be treated with a rigorous physical basis. The applicability of the method was demonstrated through to a variety of problems that involve different physical processes modelled with the FEM-DEM (internal deformations, fracture, and complex geometry). With the rapid extension of the practical limits of computational models, this work emphasizes the opportunity to move towards a modern generation of computer software to understand the complexity of the phenomena associated with discontinua.

Acknowledgements

I would like to express my most sincere gratitude to Dr John-Paul Latham for giving me the opportunity to complete my PhD thesis, for trusting me despite my initially broken English and for his constant support. I would also like to take this opportunity to specially acknowledge Prof. Ante Munjiza for providing excellent technical assistance, for hosting me at QMUL for several months and for sharing his views on the many aspects of sciences and life.

I had the chance during my PhD to collaborate with and to benefit from many fruitful discussions at Imperial College. In particular, the present research has gained from generous comments and suggestions from Prof. Peter King during the weekly group meetings. Among this small team, I am greatly indebted to Dr Gady Frenkel not only for his technical recommendations but also for sharing a passion for the Tour de France. I am very grateful to Dr Rafi Blumenfeld for his impressively clear physical approach of the granular matter. This work has deeply benefited from his wise and experienced advice.

It is very sincerely that I would like to thanks both of my examiners, Prof. Kim Christensen and Dr. Paul Langston for the constructive corrections and comments that they provided during my oral examination.

I am grateful to the VGW research group members, in particular Julian, Xavier and Jason, for promptly answering my numerous questions and for their enthusiasm that makes days more enjoyable. I was lucky to meet many friends at Imperial College. I would like to thanks them for all the good times spent in strange places all around London. In alphabetic disorder, thank you to: Karl, Matthew (for giving a Caribbean touch with your English revision of the manuscript), Bobby, Claudia, Martin, Ran, Peter D., Peter H., Irina, Ioannis, Reini...

By providing constant support, my family has been an essential ingredient of this work and I would like to thank them for their patience throughout so many years.

To finish, the last but for sure not the least, I wish to acknowledge my wife Jingyi for her patience, her constant support and advices. I would have never achieve it without you.

Contents

1 General introduction **25**

1.1 Introduction to the Virtual Geoscience Workbench (VGW) 25

1.2 Granular matter 26

1.3 Packing 26

1.4 Outline of the thesis 27

2 Review on particle packing of arbitrary shapes **29**

2.1 Introduction 29

2.2 Particle shape: importance and difficulties 30

2.2.1 Introduction to the shape descriptors 31

2.3 Experimental work on packing 33

2.3.1 Two-dimensional packing 34

2.3.2 Random packing of spherical particles 35

2.3.3 Monodisperse packing of spheres 35

2.3.4 Bidisperse and polydisperse packing of spheres 36

2.3.5 Random packing of non-spherical particles 37

2.4 Numerical simulations of granular systems 40

2.4.1 The Finite-Element Method (FEM) 40

2.4.2 The material-point method (MPM) 41

2.4.3 Monte-Carlo (MC) simulations 42

2.4.4 The discrete Element Method (DEM) 42

2.4.5 The Discontinuous Deformation Analysis (DDA) 47

2.5 Review of methods to produce granular packs 47
2.5.1 Geometric approaches 48
2.5.2 The micro-mechanical approaches 53
2.6 Summary of the influence of shape on 2D packing densities 54
2.6.1 Packing of discs 54
2.6.2 Packing of arbitrary shapes 56
2.7 Conclusions 56

3 Using the Combined Finite-Discrete Element method for the study of granular materials 59

3.1 Introduction and historical developments 59
3.2 Contact Interaction 62
3.2.1 Normal Forces $\mathbf{f}_n$ 63
3.2.2 Tangential Forces $\mathbf{f}_t$ 67
3.3 Contact Detection 71
3.4 Deformability of DE (Finite Element Formulation) 72
3.4.1 Introduction to the different coordinate systems 72
3.4.2 Constitutive laws and calculation of the Cauchy stress and the strain in the FE 74
3.5 Temporal Discretisation 76
3.5.1 Choice of the integration scheme 76
3.5.2 The Central Difference Time Integration Scheme (CD) 77
3.5.3 Critical time step 78
3.5.4 Dissipation of energy of the combined finite-discrete element simulation 79
3.6 Finite Element mesh creation 79
3.6.1 Mesh criteria and creation of particles with arbitrary shapes . . . 82
3.7 Computational cost 82
3.8 Friction validation: The sliding block model 83
3.9 Conclusion 84

4 Numerical deposition and geometrical characterization of the packing of elliptical particles 87

4.1 Introduction 87

4.2 Description of the numerical experiment 89

4.2.1 Numerical Experiment 89

4.2.2 Parameters of the numerical experiment 92

4.3 Structural dependence of the packing with the particle aspect ratio . . . 93

4.3.1 Evolution of the emergent properties during the deposition stage . 95

4.3.2 Coordination number and packing density 97

4.4 Structure characterisation with particle correlation functions 107

4.4.1 Radial distribution function 107

4.4.2 Characterization of the particle orientation 112

4.4.3 Statistical analysis of the pore space 118

4.5 Conclusion 122

5 Analysis of the heterogeneities of stresses and forces of a granular packing 125

5.1 Introduction 125

5.2 Effect of inter-particle friction and particle shapes on the stress distribution (Qualitative description) 127

5.2.1 Frictionless case 131

5.2.2 Frictional Case 131

5.2.3 Distribution of the forces 131

5.3 Distribution of the differential stress 134

5.3.1 Elemental approach 134

5.3.2 Particle averaging approach 138

5.3.3 Results and discussion 140

5.4 Stress correlations in granular packs 142

5.4.1 Motivations 142

5.4.2 Correlation map $C(x, y)$ 142
5.4.3 Results & discussions 144
5.5 Conclusions 147

6 Force Chain detection: strategy, algorithm and calibration 149
6.1 Introduction and motivations 149
6.2 Description of the FCD algorithm 150
6.2.1 Definition and principles of the algorithm 150
6.2.2 Influence of the filter threshold criteria on force chain detection and calibration 158
6.3 Comparison of the method and validation 161
6.3.1 Numerical experiment 161
6.3.2 Algorithm validation 162
6.3.3 Results and discussion 163
6.3.4 Additional comments - drawback of the algorithm 169
6.4 Conclusion 169

7 Some applications related to FEM-DEM 171
7.1 Introduction 171
7.1.1 Compaction of granular materials 171
7.1.2 Silo discharge 173
7.2 Powder compaction 173
7.2.1 Objectives 173
7.2.2 Numerical set up 174
7.2.3 Results and discussion 175
7.2.4 Summary 181
7.3 Silo discharge 181
7.3.1 Aim 181
7.3.2 Experimental set up 182

7.3.3 Results and discussions 183
7.4 Conclusion 188

8 Conclusions and future work **191**
8.1 Conclusions 191
8.2 Recommendations for future work 194

A Shape descriptors **197**
A.1 Form factors 198
A.2 Sphericity 199
A.3 Roundness 200

B Implementation details of the Discrete Element Method **201**

References **205**

List of Figures

2.1 Power's roundness for the description of the particle shape. From [162] . 30

2.2 Representation of the three distinct levels of shape characterisation. a) perfect sphere. Scale of influence on the particle shape of b) the form, c) the roundness and d) the surface texture 31

2.3 Example of complex giant particles, Correloc, used for the coastal defences. Courtesy of Sogreah. 31

2.4 This figure shows that a mixture of beads can increase the packing density compared to mono-disperse assemblies. The packing density of a mixture depends both on the relative amount of large and small particles, and the ratio of size of the particles (from Cumberland [38]). 37

2.5 Example of packing with non-spherical particle shapes. a) colloidal materials with aspect ratios $\alpha = 1.7$ and $\alpha = 2.9$ (from [186]). b) Examples of packing with macroscopic non-spherical particles with different shapes and aspect ratios. The figure suggests the importance of geometrical effects on the granular system. 38

2.6 Sphericity-Porosity relationship for different granular materials (from [232]) 39

2.7 Six three-dimensional example of shapes defined using superquadrics mathematical function (from *http://aig.cs.man.ac.uk/research/reveal/squids/index.html*) 44

2.8 Two-dimensional approximation of a particle shape using an equivalent disc (b)), or a assemblage of discs such as the multi-sphere model(c) . . . 45

2.9 Acquisition of a 3D particle shape. a) original rock sample. b) 3D mesh of the discretise particles 46

2.10 Packing algorithm of Cui et al. [37]. a) Division of the computational domain in a triangular mesh b) insertion of the inscribed discs inside each triangular element. c) Optimisation of the solid area by addition of the maximum diameter discs at each vertex. 51

2.11 Different method of packing construction using mechanical approaches. a) Individual deposition. b) Collective localised deposition. c) Collective deposition. 53

3.1 Flow chart of the routines used in the combined finite-discrete element method. 61

3.2 Definition of the variables used for the contact forces. 64

3.3 Contact force interactions. 66

3.4 Origin of friction between two surfaces. During the tangential motion between two surfaces, the asperities of the material deforms plastically which generates some resistance to the lateral motion and energy losses. . 69

3.5 Distribution of the tangential force among the finite element nodes. . . . 70

3.6 Contact detections between 3 triangular particles E_1, E_2 and E_3. 71

3.7 Definition of the frame of reference for the computation of the material deformations. 73

3.8 Initial mesh of a combined finite-discrete system. Notice that the boundary possesses a structured mesh while each discrete elements contained within the domain are divided into an unstructured meshed that was created by using the meshing tool of the GID software. This structure is made of 30244 nodes and 39244 finite elements. The inset shows a magnified particle mesh (an ellipse of aspect ratio $\alpha = 1.2$). 80

3.9 Verification of the run out distance traveled by a sliding cube for varying time steps. The scale of the inset picture is 1:2.5. 83

4.1 Deposition sequence of granular particles, ellipses of aspect ratio $\alpha = 1.5$ with friction. The colour scheme indicates the magnitude of the differential stress calculated inside each element of each particle. The stress state of the final deposit is characterised by force chain patterns that are carrying high load through several grains. The frames are taken at $t = 0; 0.5; 1; 1.5; 2; 2.5; 3; \infty s$. 91

4.2 Coefficient of restitution for an impact between two discs of 10 cm diameter. The curves in inset shows the exponential relationship between coefficient of restitution and impact velocity. 93

4.3 Evolution of the kinetic energy curve during the dynamic deposition of the grains. The different zoom in illustrates the different stages of the deposition sequence, starting from the initial mixing and ending with the micro adjustment of the structure as a consequence of the material relaxation. 94

4.4 Temporal evolution of the emergent properties for a packing simulation performed with particles of aspect ratio 1.2 interaction with friction (red diamonds) or without friction (green discs). The final values are taken once both porosity and coordination number reach a stable value over a long time. 95

4.5 Packing of two systems with N=900 particles, with a) $\alpha = 1.2$ and $\mu = 0.0$, b)$\alpha = 1.2$ and $\mu = 0.5$, c) $\alpha = 5.0$ and $\mu = 0.0$, d) $\alpha = 5.0$ and $\mu = 0.5$. The initial condition are identical for the frictional and the frictionless systems to allow comparison. 97

4.6 Definition of a representative volume element (RVE) within which the packing density is measured. The RVE exclude from the calculation a layer of 2 equivalent diameters near the wall, in order to reduce the uncertainties generated by the walls. 98

4.7 Influence of the wall effect on the final packing fraction with the number of particles comprised inside the container. Above 1000 particles near the container walls, the finite size effects becomes negligible (error $< 0.3\%$). . 99

4.8 Evolution of the packing density as a function of the particle aspect ratio. Note dotted lines intersecting the horizontal axis at $\alpha = 1.6$ highlight a maximum for the frictional case and a transition for the frictional case. Error bar = $\pm 1\%$ 100

4.9 Distribution of the number of contact per particles for a packing of ellipses of aspect ratio 2.5 for a)frictionless systems, and b) frictional ones. 103

4.10 Distribution of the number of contacts per particle, Z_n, for a packing of ellipses for frictionless systems (Cold colors) and frictional ones (Warm colors). The coordination number of ellipses of aspect ratio of $\alpha = 1.5$ has the same coordination number as frictionless disc. These two systems are compared in terms of stress distribution in the Chapter 5. 104

4.11 Left) Evolution of the coordination number with the aspect ratio of the ellipses for both frictionless (red squares) and frictional systems (blue diamonds). Right) The evolution of the coordination number towards its limiting value is shown by plotting $z_\infty - \overline{z}(t)$ vs. α. 105

4.12 Radial distribution function of a packing composed of rounded particles (aspect ratio of $\alpha = 1.0$ (Top) and $\alpha = 1.2$ (Bottom)). Blue colors ($\bullet$ and $\blacktriangle$) are indicating $g(r)$ for particles without friction and red colors ($*$ and .) correspond to particles interacting with a coefficient of friction $\mu = 0.5$. The inset plots show the geometry of idealised dense packed systems and the color key used to identify the peaks. Vertical lines indicate the distances between points separated in an hexagonal lattice. 109

4.13 Random close packing of ellipses. There exists several configurations of close packing for ellipses. The pack in a) is called CP1 and in b) CP2. Both packs are in a close configuration but as indicated by the colour scheme, the nearest neighbour configuration differs, which has consequences for the radial distribution function. 110

4.14 Radial distribution function of frictionless system of particles with varying aspect ratios ($\alpha = 1.0$ (top left), $\alpha = 1.2$ (top right), $\alpha = 2.5$ (bottom left), $\alpha = 5.0$ (bottom right)). It is important to point out the dispersion of the correlation peaks with ellipses when $\alpha = 1.2$. For larger aspect ratios, the correlation peaks become attenuated and diffused that RDF is no longer useful to detect the presence of ordered structure. 111

4.15 Radial distribution function of frictional ($\mu = 0.5$) system of particles with varying aspect ratios ($\alpha = 1.0$ (top left), $\alpha = 1.2$ (top right), $\alpha = 2.5$ (bottom left), $\alpha = 5.0$ (bottom right)). 112

4.16 Orientational distribution of particles within a packing made of ellipses with increasing aspect ratios ($1 < \alpha < 5$). 113

4.17 a) Temporal evolution of the orientational order parameter during the deposition process for four different aspect ratios ($\alpha = 1.1, 1.3, 2.5, 5.0$). It is worth mentioning that in the early stage of the deposition, the OOP goes to 0, confirming the efficiency of the particle mixing phase. It then tends towards a steady value while the ellipses stabilize in their final position. We call Q_∞ the value of the OOP when the time tends to infinity. b) Evolution of the final orientational order parameter Q_∞ as a function of the particle aspect ratio. One can see rapid rise of $Q_\infty(\alpha)$ at low aspect ratios and the stagnation of Q_∞ when $\alpha > 2$ which suggest that above $\alpha = 2$, the system reach of maximal amount of orientational correlation. The vertical thick black line is the estimated error and the fitting red line is only a guide. . 115

4.18 Angular correlation between ellipses with different aspect ratios, $\alpha = 1.3$, $\alpha = 1.5$ and $\alpha = 2.0$ ($\mu = 0.5$). 116

4.19 Scheme of the typical clusters form with elongated particles of large aspect ratios. 117

4.20 Extraction of the particle outline using an image analysis software. a) Original binary picture of the particles and associated pores b) Extraction of the particle outlines. c) Determination of the pore characteristics by analysis of the size distribution of the black areas (pores). 119

4.21 Dependance of the pores size cumulative distribution function with the particle aspect ratio. a) for frictionless systems and b) for frictional ones ($\mu = 0.5$), as generated in the simulations described in this chapter. . . . 120

4.22 Distribution of the pores sizes for the simulated frictional and frictionless systems. Best-fit gamma distribution have been superimposed. 121

5.1 Experimental comparison of the stress response of a granular media to an external punctual pressure point. Photo-elastic beads are used to visualize the stress path. The stress response is shown to depend on the particle shape. a) case of bricks packing (adapted from [41]). b) case of packing of pentagonal shaped particles (adapted from [63]). 126

5.2 Aspect ratio $\alpha = 1.0$. a) $\mu = 0$. b) $\mu = 0.5$. Colour ranges from blue (low stress) to red (high stress) 128

5.3 Aspect ratio $\alpha = 1.4$. a) $\mu = 0$. b) $\mu = 0.5$. Colour ranges from blue (low stress) to red (high stress) 129

5.4 Aspect ratio $\alpha = 5.0$. a) $\mu = 0$. b) $\mu = 0.5$. Colour ranges from blue (low stress) to red (high stress) 130

5.5 Identification of the nodes contributing to the total contact force (local contact forces are represented by a red vector) 132

5.6 a) Force distribution for packing with constant shape and varying friction. b) Force distribution for frictionless packing with varying aspect ratio . . 133

5.7 Stress distribution of the differential stress of the granular packs plotted on linear and log scales. The stress is calculated inside each finite element of each particle. a) and b) influence of the particle friction, c) and d) influence of the particle shape, e) and f) Stress distribution of two systems with different particle shape and inter-particle friction at constant $\overline{z}$. 135

5.8 a) Force distribution for the 4 large systems of ellipses. 139

5.9 Distribution of each of the component of the particulate stress tensor inside the large packing of ellipses a) Distribution curve of T^p_{xx}. b) Distribution curve of T^p_{yy}. c) Distribution of the non-diagonal component T^p_{xy} d) Distribution of the differential stress average over the particle area. 141

5.10 PDSM image used for the computation of the correlations a) Stress map for $\alpha = 1.0$. b) $\alpha = 2.0$. The friction coefficient between the grains is set to $\mu = 0.5$. For the ease of comparison, the greyscale is identical in both packing. The particles stress is depth-normalised. We can see from this figures that the particulate differential stress possesses a spatial distribution which is a function of the shape of the particles employed. 143

5.11 Correlation map of the differential stress average over the particle area with a) $\alpha = 1.0$, b) $\alpha = 1.1$, c) $\alpha = 2.0$. The darker regions correspond to low correlation values, and brighter ones to high correlation values. The horizontal and vertical red lines indicates the direction of correlation represented in Fig.5.12 145

5.12 a) Correlation in the horizontal direction for pack with $\alpha = 1.0; 1.1; 2.0$ b)Correlation in the vertical direction for pack with $\alpha = 1.0; 1.1; 2.0$. The correlation along the vertical axis propagates over a larger range which confirm the influence of the particle shape on anisotropy of the stress distribution. 146

6.1 Three types of force chain configurations handled by the FCD algorithm. a) Chain splitting, a old chain continue while a new connected chain is created. b) Chain joint, two chains joints in a single particle and the weakest stops automatically. c) chain crossing, two chains cross in a single particles, but both of the chains continue their way throughout the system with no (or negligible) attenuation of their strength. 151

6.2 a) Figure of a grain packing of discs. The color scheme represents the magnitude of the differential stress (blue is low differential stress and red is large differential stress). b) Network defined by the depth-normalised contact forces larger than a cutoff value ($f_{cut} > 1$). c) One can see that the force network superimposes upon the highly stressed paths hence justifying the use of the contact forces alone to identify the chains. Similar conclusions can be drawn for systems with non-spherical particles. 152

6.3 a) Decomposition of the domain into iso-layers. b) σ_{zz} vs. depth z and the fit function $\sigma_{zz}(z) = \phi\rho_g gz$ 154

6.4 Description of the neighbour list and sublist established in order to analyse the force chains. 155

6.5 a) Links between the contact forces and comparison with the path described by the connection between particle centres. This picture also illustrates that the angle between consecutive particle centres, i.e. the path ABCD, would be erroneous and non physical. b) Case where several contacts fulfill the condition imposed by the force orientation filter. An additional filter considering the angles between the branch vectors (black) and the force vectors (red) is applied in order to discard chains considered unrealistic for force chain propagation. The dashed line represents a potential chain direction that does not fulfill the requirement imposed by the second filter while the continuous lines do. 156

6.6 Chart of the FCD algorithm 157

6.7 Variation of the fraction of the total number of selected contact forces as a function of the cutoff value for different contact forces illustrated for ellipses with aspect ratios α from 1 to 2. 159

6.8 Influence of the cutoff length on the proportion of particles composing the forces chains. a) $\alpha = 1.0$, b) $\alpha = 1.3$, c) $\alpha = 1.5$, d) $\alpha = 2.0$ 160

6.9 Variation of the cutoff curve as a function of θ. a) $\alpha = 1.0$, b) $\alpha = 2.0$ . . . 161

6.10 Chain path recognition verification. In this figure, the differential stress received by the particles is used to evaluate the magnitude of the stress supported. The blue color correspond to the less stressed area while the red color represents the most constrained domains. A good agreement between the red patterns (i.e. the force chains) and the superimposed black lines which are the paths identified by the FCD algorithm is observed. 163

6.11 Chain path recognition verification. The caption the Fig. 6.10 is identical with $\alpha = 2.0$. The figure in zoom in a small area of the system in order to insure the applicability of the algorithm to non-spherical particles. 164

6.12 Influence of the particle aspect ration on the shape of the curve. 165

6.13 Orientation of the chain links for a systems of discs and a system of ellipses both interacting with friction for $f_{cut} = 1.5\overline{f}$. A pronounced directionality of the chain in the case of discs with an orientation more likely in the direction $30° - 90° - 150°$ given by the direction of hexagonal packing. In contrast, the ellipses show a preferred 90° alignement with a broad dispersion of angles. 166

6.14 Distribution of the force chain length (in terms of number of contacts) for a system of discs (blues circles) with $z = 4.37$ (z is the coordination number) and 2 systems of ellipses (green squares for $\alpha = 1.5$ and red triangles for $\alpha = 2.0$). All three curves exhibit a negative exponential distribution, $P(\ell) = \gamma e^{-\frac{\ell}{\zeta}}$, the shorter chains being the most frequent. The dashed blue line is the best fit distribution for the system of discs ($\gamma = 0.08$ and $\zeta = 4.0$), green is for ellipses of $\alpha = 1.5$ ($\gamma = 0.12$ and $\zeta = 3.3$) and red is for ellipses of $\alpha = 2$ ($\gamma = 0.3$ and $\zeta = 2.3$). All lengths are based on a f_{cut} threshold of $f_{cut} = 1.5\overline{f}$. Note that exponential distributions have the special properties that ζ is also the mean chain length. 167

6.15 Variation of the coordination number of the particles detected in the force chains, z_{chain} normalised by z_{max}, the average coordination number of the whole system. A clear transition is observed, which suggests that the particles constituting the force chains possess less contacts than the remaining ones. The value of f_{cut} at this transition can be used as cutoff value for the given set of L and θ. 168

7.1 Geometry of the system simulated for the powder compaction experiment. 174

7.2 Evolution of the packing density, Φ, and the average coordination number, Z, of the system with the indentation of the piston. a) $\alpha = 1.5$ b) $\alpha = 2.0$. 175

7.3 Variation of the vertical force applied by the piston as a function of its vertical displacement for packs consisting of two different ellipse shapes ($\alpha = 1.5$; $\alpha = 2.0$). 177

7.4 Percentage of particles detected in the force chains for $f_{cut} = 1$, $\theta = 60°$ and $L = 3$ by the FCD algorithm developed in Chapter 6. Because the load supported by each particle becomes more similar with the increasing compaction, the percentage of particles carrying load in the force chains increases with the punch displacement. 178

7.5 Evolution of the contact force distribution with the punch indentation. a) $\alpha = 1.0$, b) $\alpha = 1.5$, c) $\alpha = 2.0$ 179

7.6 Evolution of the stress patterns during the compaction of frictional particles ($\mu = 0.5$). a) $\alpha = 1.0, \delta = 0.00r_g$, b) $\alpha = 1.5, \delta = 0.00r_g$, c) $\alpha = 2.0, \delta = 0.00r_g$, d) $\alpha = 1.0, \delta = 4.00r_g$, e) $\alpha = 1.5, \delta = 0.70r_g$, f) $\alpha = 2.0, \delta = 0.70r_g$, g) $\alpha = 1.0, \delta = 6.00r_g$, h) $\alpha = 1.5, \delta = 1.40r_g$, i) $\alpha = 2.0, \delta = 1.40r_g$, j) $\alpha = 1.0, \delta = 6.00r_g$, k) $\alpha = 1.5, \delta = 1.98r_g$, l) $\alpha = 2.0, \delta = 1.98r_g$. The force chains identified by the FCD algorithm (cf. Chapter 6) are superimposed by black segments. The color scheme represent the differential stress calculated inside each particle. 180

7.7 Geometry of the system simulated for the silo discharge. 183

7.8 a) Total mass discharged from the silo aperture for frictional particles. b) frictionless particles. In the inset of each figure is plotted the value of the discharge rate. 184

7.9 Snapshots of the velocity field during the flux of grains through the aperture of the silo at different time for 3 types of frictional ($\mu = 0.5$) particles. The silo width is $D = 5.656r_g$. a) $\alpha = 1.0, t = 0s$, b) $\alpha = 1.2, t = 0s$, c) $\alpha = 2.5, t = 0s$, d) $\alpha = 1.0, t = 1s$, e) $\alpha = 1.2, t = 1s$, f) $\alpha = 2.5, t = 1s$, g) $\alpha = 1.0, t = 2s$, h) $\alpha = 1.2, t = 2s$, i) $\alpha = 2.5, t = 2s$, j) $\alpha = 1.0, t = 4s$, k) $\alpha = 1.2, t = 4s$, l) $\alpha = 2.5, t = 4s$ 186

7.10 Snapshots of the stress field during the flux of grains. It is observed that each system influence jams which consequently reduces the flux of grains. a) $\alpha = 1.0, t = 0s$, b) $\alpha = 1.2, t = 0s$, c) $\alpha = 2.5, t = 0s$, d) $\alpha = 1.0, t = 1s$, e) $\alpha = 1.2, t = 1s$, f) $\alpha = 2.5, t = 1s$, g) $\alpha = 1.0, t = 2s$, h) $\alpha = 1.2, t = 2s$, i) $\alpha = 2.5, t = 2s$, j) $\alpha = 1.0, t = 4s$, k) $\alpha = 1.2, t = 4s$, l) $\alpha = 2.5, t = 4s$. 187

B.1 Model of force-displacement relationship that can be implemented with the DEM 202

List of Tables

2.1 Value of random close packing for monodisperse systems of discs. 55

2.2 Value of random close packing for monosized arbitrary 2D shapes 56

3.1 Reference table of the number of mesh and nodes per particle. α is the aspect ratio of the particle. 81

4.1 simulation parameters 92

4.2 Reproducibility errors. $< \phi >$ is the average packing density calculated from n realisations of the experiment with particle of aspect ratio α and friction μ. S_ϕ is the standard deviation of the packing density. 99

4.3 Reproducibility errors for the coordination numbers. $< z >$ is the average coordination number calculated from n realisations of the experiment with particle of aspect ratio α and friction μ. S_z is the standard deviation of the average coordination number. 102

4.4 Summary of the theoretical [184, 45] and experimental results for $\overline{z}$ in 2D. Note that values are only reported for discs and ellipses with large aspect ratios. 106

4.5 Distance between first neighbour for ordered (hexagonal packing) for 2 monodisperse systems with varying aspect ratios. The indices $< ij >_\alpha$ designates the location of the i neighbour in direction j for a monodisperse system of ellipses with aspect ratio α. To keep simple notations, each distinct direction is given by an integer value. The distance are expressed as a function of b, the ellipses short axis 108

6.1 simulation parameters 153

6.2 Average chain length versus aspect ratio for $f_{cut=1.5}$. 167

A.1 Commonly used circularity (taken from [20]) 198

A.2 Commonly used circularity (taken from [20]) 199

A.3 Commonly used roundness indices (taken from [20]) 200

Chapter 1

General introduction

1.1 Introduction to the Virtual Geoscience Workbench (VGW)

The Virtual Geoscience Workbench is a long term and large scale project aimed to study discontinuous systems involved in earth science and earth engineering. The ultimate goal of this project will be to link VGW with a multi-phase and multi-physics modelling environment within the college department. The VGW capabilities aims to simulate realistically the behaviour of particles with arbitrary shapes interacting with others, with material deformations and eventually fracturing. The solid phase will be dynamically coupled together with an interstitial fluid phase with momentum exchange. In the first stage of the VGW development, the core of this workbench will be tested on problems such as granular dynamics, sedimentation, packing or heap stability. In the second stage, the modelling of the two-phase interactions will be encompassed by coupling a CFD (Computational Fluid Dynamic) solver with a combined finite discrete (FEM-DEM) one. This aspect of the project has many applications, notably in coastal engineering, an area in which the interaction between waves and coastal defence structures has critical human importance (e.g. protection of harbour breakwaters and of the coast from catastrophic waves). Within this framework, this thesis addresses the complex task of simulating and analyzing the structure and the properties of randomly generated two-dimensional dry granular packing constructed with non-circular particles.

1.2 Granular matter

Granular matter is ubiquitous on the earth surface, and nowadays, the explanation of some apparently trivial behaviours observed in granular systems is not clear and still remains a source of headache for physicist and engineers. About 90 % of the solid surface of the planet is covered by grains, with sizes varying from micrometers (clay) to reach up to 100 meters large particles (rock blocks). The type of interactions between the grains is wide. Factors such as chemical reactions, presence of interstitial fluid or rock breakage also impose a need to distinguish accurately in which parameter space the study is to take place.

In addition to the diversity of the materials involved, the granular world also covers a wide range of physical processes. For instance, a granular medium can either behave as a gas, a solid or a fluid depending on the degree of agitation (related to the granular temperature) of the grains.

When the influence of the interstitial fluid and cohesive forces between the grains can be neglected, the granular system can be classified as "dry granular material", a domain that has gained widespread attention due to the abundance of the phenomenology associated to it. The work performed in the scope of this PhD is to classify among this category of "dry deformable granular media".

Because it is complex to analyse physical characteristics of experimental granular media with non-destructive methods, numerical approaches are usually preferred. This has the major advantage to characterise the microscopic behaviour in different regions of the media, hardly accessible experimentally.

1.3 Packing

The packing of particles has been an extensive field of research with interest covering a wide category of fundamental or applied topics. It includes for instance models for the structure of fluids and glasses [16, 146, 119], characterisation of the rheology of granular flow [28, 69, 57], description of the transport properties of rocks, understanding the electric properties of discontinuous media, the description of force transmission through a grain assembly [41, 132, 118]. However, in many cases the fundamental role of particle shape is neglected. In this work, a method is proposed to investigate the effect of the particle shape on the packing properties and the stress transmission among the particles.

1.4 Outline of the thesis

Chapter 2 will review the literature addressed to the study of granular packing. The review will be essentially focused on the description of experimental studies of packing followed by a summary of the numerical methods usually adopted to simulate particle packing. An additional discussion on the different possibilities offered to produce packing of granular materials will conclude this section.

Chapter 3, the theoretical details of the combined discrete-finite element method are given. The chapter depicts the main algorithmic section encountered in the method. It is concluded by a validation of the coulomb friction implemented within this framework.

Chapter 4 consists of the description of the numerical experiment followed by an analysis of the influence of the particle shape on the emergent properties of a granular pack. Radial and orientational correlation functions are used to distinguish the structural characteristics of the system. The chapter ends with a statistical analysis of the pore space, showing the role played by the surface friction and the particle elongation.

Chapter 5 presents some quantitative results characterising the force chain networks in each packing sample. The analysis of the force and stress is used to demonstrate the importance of stress distribution in the stress transmission. Image analysis of the stress patterns further shows that the force chains follows different patterns when different particle elongations are considered.

Chapter 6 describes an algorithm (FCD algorithm) used to identify and to localize the force chains transmitted within the granular system. Well calibrated, the FCD algorithm permits the extraction of precise statistics concerning the length and orientation of the chains, as well as the coordination numbers of the particles constituting this network.

Chapter 7 describes two examples of application of the FEM-DEM technology in industrial applications. The first part of this chapter describes an uniaxial compression experiment performed for three different particle shapes. Afterwards, the influence of the particle elongation and friction coefficient on the discharge flux through a silo aperture is examined.

The concluding chapter will summarise the principal findings discussed in the thesis and future directions of the current research are then proposed.

Chapter 2

Review on particle packing of arbitrary shapes

2.1 Introduction

The packing of particles has long be considered in history, initiated as early as the antiquity. Around 200 BC, Appolonios describes a classic problem, named after him as "Appolonios packing", consisting of covering an area completely by arranging discs in a structure manner. Four centuries ago, Kepler conjectured that the maximum solid fraction of monosized spheres corresponds to a face-centered cubic (FCC) where each particles is surrounded by twelve neighbours and was equal to $\phi_{FCC} = \frac{\pi}{3\sqrt{2}} \approx 0.74$. It took almost 400 years, very complex mathematical investigation and extensive computational resources to prove Kepler's statement [73]. In two dimensional systems, monodisperse discs attain a maximal solid fraction $\phi_{2D} = \frac{\pi}{2\sqrt{3}} \approx 0.9069$.

Apart this ordered configurations, particulate systems in nature and industry are likely to be found in a disordered state. Random packings consists of a collection of disordered particles in contact. The particles forming those systems can be of any sizes and any shapes, ranging from the nanoscopic to the decametric scales. In a more general case, the system can be polydisperse, i.e. the particles have a specific distribution of sizes and shapes. Packing of particles are important in many contexts. Random packing can be used as a model for the structure of liquids or ideal mono-atomic glasses. Random packing also forms the basis for a constitutive theory of stress propagation in heterogeneous media [86, 63]. Models for assessing the stiffness or the speed of wave propagations in soils have been constructed. In an industrial context, they are relevant for a wide range of problems where the flow or storage of grains is encountered. This is the case for the motion of grains in a conveyor belt [227], the discharge of silos [104, 181, 125] or for the characterisation of

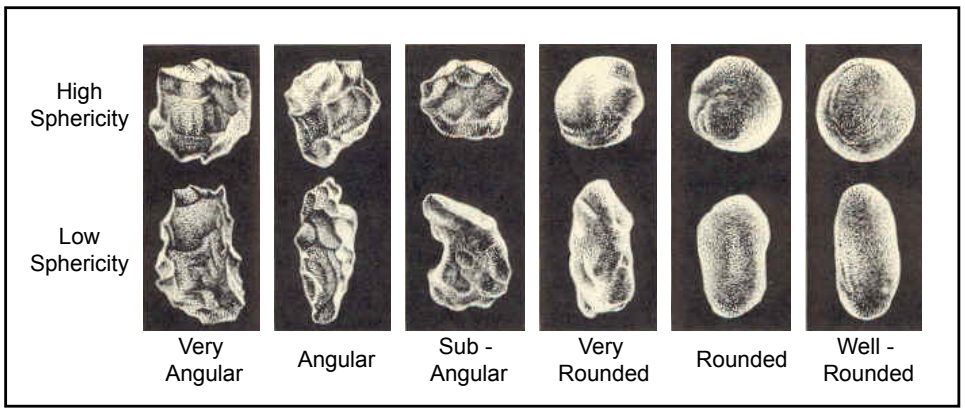


Figure 2.1: *Power's roundness for the description of the particle shape. From [162]*

the mechanical properties of concrete or composite materials.

Summaries of the extensive work done on granular matter in general, and packing in particular, are regrouped into a vast amount of literature. For complete reviews, the reader is referred to [64] for engineering related problems. An updated view of the large set of physical models can be found in [127], while recent computational developments applicable for the modelling of granular media are compiled in [158] or [135].

The aim of this literature study is to review some key aspects of the random packing of particles. The review is organised as follow. Because particle shape is one of the most important parameters controlling the structure of a granular media, a discussion presenting the various possibilities to characterise the shape of a particle is introduced. This section is followed by a review of the principal characteristics observed in experimental random packing. The emergence of the computational methods to simulate granular systems has gained importance, and it seems particularly appropriate in overcoming experimental difficulties. A summary of these methods is introduced and the different strategies to model particle shape are presented. Afterwards, different types of packing algorithms are depicted and compared. Finally, the literature study ends with a summary of the range of packing fraction covered by different types of 2D packing algorithms composed of discs and non-circular particles.

2.2 Particle shape: importance and difficulties

Powders and grains are ubiquitous in nature and can be encountered with a very large range of geometrical characteristics. The typical size of particles ranges from nanometric length scales with atoms to kilometric ones for the planets and asteroids. Unlike size, the shape of those particles is conceptually far more difficult to quantify. To distinguish not only different types of particles but also the physical process associated with a given

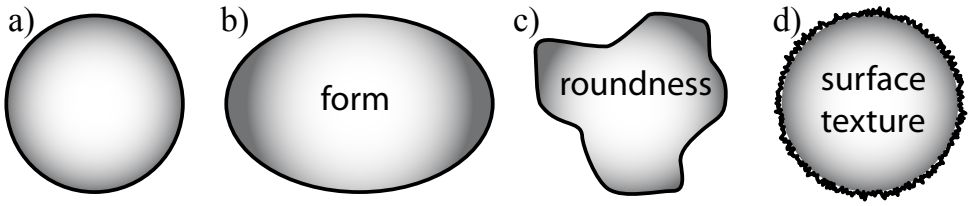


Figure 2.2: *Representation of the three distinct levels of shape characterisation. a) perfect sphere. Scale of influence on the particle shape of b) the form, c) the roundness and d) the surface texture*



Figure 2.3: *Example of complex giant particles, Correloc, used for the coastal defences. Courtesy of Sogreah.*

shape [48], a proper geometrical characterisation of particles appears to be a key aspect. Nevertheless, the description of particle shape remains a difficult task to address and is usually based on empirical descriptors (Fig. 2.1). The physical influence of the particle shape on the structure of granular media can be perceived in many ways. Porosity, connectivity of the inter-grain contacts, friction, liquid bridging to name but a few are strongly related to the geometrical nature of the grains. In this section, a description of some basic shape descriptors is proposed.

2.2.1 Introduction to the shape descriptors

Difference of shapes between particles can be classified and quantified in relation to specific geomorphical considerations. In his critical review Barett [13] proposed to divide the shape descriptors into three "independent" categories (form, roundness and surface texture) in order to identify the most appropriate descriptors (see Fig. 2.2). An updated review of most of the available shape descriptors can be found in [20]. As explained in [13] the main

problem of the shape descriptors introduced in the above references, is that their domain of influence can overlap. The geometry of a body can be described at several scales, all closely related. For instance the surface texture consists of the description of the very small scale patterns at the surface of a particle and it is expected to cause inter-particle friction. The friction hampers the tangential motion of two surfaces in contact. This is the consequence of the micro-scale deformation of the micrometric rugosity of the surface. The physical phenomena of friction is then linked to the category of surface texture type of descriptors. At larger scale concavities can infer some interlocking between particles which influence their domain of influence. Just as surface texture affects contact friction, interlocking influences the relative motion between particles and can lead to unpredictably high concentration of stress. For instance in coastal engineering the interlocking is used in order to stabilize granular layered systems of concrete units against wave attack (see Fig. 2.3). The physical origin of interlocking is related to the larger scale of geometrical variability related to their overall shapes. Between these two extreme spatial scales, the intermediate scales of the morphological characteristics also plays a crucial role as it affects the geometric configuration of inter-grain contacts which controls the magnitude and the orientation of the contact forces and thus the stress distribution within individual particles [179, 5].

To illustrate the complexity of shape characterisation, some of the principal shape descriptors are presented in this section. A more extensive list of the shape descriptors encountered is given in Appendix A. For a complete description of the characterisation of the particle shape the reader is referred to reviews [13, 20]. Nonetheless, relatively simple shape descriptors used for the assessment of the engineering materials like concrete aggregates or road dressing [107, 89] are often more practical to employ.

- Form (Fig. 2.2b)) : the form is used to characterise the overall morphology of a particle. The most important aspect of the form are well represented by using the elongation $\alpha = L/I$ or the flatness $f = S/I$ ratios, where L, I and S are perpendicular axes in the long, intermediate and short dimensions of the particle [96]. In two dimensions, $S = I$, and a unique descriptor the aspect ratio, $\alpha = L/I$ is enough to characterise the form. Other descriptors for the form are given in Appendix A.

- Sphericity & roundness (Fig. 2.2c)) : at the intermediate scale between form and surface roughness, the particle morphology is described by specific descriptors such as sphericity or roundness. In order to quantify the relative surface area of a particle compared to a spherical particle of equal volume, a shape descriptor called the sphericity was introduced. We used the sphericity as defined by [217]:

$$S_{3D} = \frac{S_s}{S}, \tag{2.1}$$

where S_s is the surface area of a sphere with the same volume as the test particle, and S is the actual surface of the particle. The sphericity can be equally expressed in two dimensions:

$$S_{2D} = \frac{P_d}{P}, \tag{2.2}$$

where P_d is the perimeter of a disc with the same area as the test particle, and P is the actual perimeter of the particle. A complementary qualitative index, the roundness, is also commonly used in geology to characterise grain angularity. However, unlike sphericity, the assessment of the particle roundness is somewhat subjective as it is based on the comparison of the particle outline with calibrated charts [162] (Fig. 2.1). For physical analysis of the particle shape the sphericity is generally preferred to the the roundness [231, 232]. Note also that the sphericity is also dependent on both form and roundness. Being related to the surface area, the sphericity is often the shape descriptor which is used for characterisation of powder technology.

- Surface texture (Fig. 2.2d)) : the *texture*, or roughness, defines the local irregularity and the asperities of the grains surface. Physically, the plastic deformation of the surface asperities is the source of contact friction forces. The surface texture of an aggregate is considered to have an impact on the engineering response of the material. To describe the texture, a fractal analysis of the projected particle outline has been proposed [211] and shown to be useful in distinguishing particles with distinct surface roughness [87]. Another quantitative approach consists of a statistical analysis of the height variation of the digitise grain surface by the mean of digital microscopy [3].

From the above discussion, it is apparent that particle shape can be best characterised by distinguishing three scales of observation. A complete discussion of shape descriptors is a complicated topic that falls outside the scope of this thesis. In this work, the focus is directed towards the analysis of elliptical bodies and the word *shape* relates in fact to the *form* of the particle. The shape descriptor considered in the thesis is the aspect ratio, α, which is the ratio of the long and the short axis of the grains. The contact friction is also treated and is considered to be a particle property with a value taken from empirical material property tables.

2.3 Experimental work on packing

It is experimentally difficult to constrain rigorously the geometry of a large system of grains. Moreover, information concerning the transient state of the system (velocity field

etc), or the quantification of the granular fabric, the force vectors, the particle deformation requires specific experimental set up adapted to the measurement of each quantity. The detailed analysis of both static and dynamic analogue granular systems remains therefore a very challenging task.

The richness of granular systems has been largely demonstrated experimentally. It includes discoveries of phenomena such as particle segregation [177, 25], spontaneous stratification [120] and also the heterogeneity of the stress distribution [86, 118, 61]. Most of those discoveries have been studied with well calibrated experimental set-ups such as sand box experiments or rotating drums. This section first introduces experimental studies of sphere packing followed by a summary of the principal experiments performed with non-spherical particles.

2.3.1 Two-dimensional packing

Two dimensional experiments of grain packing are rare because of the three dimensional nature of the materials. To overcome this problem, Hele-Shaw cells are used because it restricts the motion of the particles in a plan. Although the two parallel glass sheets is an efficient approach to constrain the particle motion, these type of experiments are usually small scale and they face experimental errors caused by friction between the grains and the glass sheets.

The experimental results of Bideau et al. [18] were performed for binary mixture of discs with large difference of diameters - $r_l/r_s > 6.46$, where r_l and r_s are the diameters of the large and small beads respectively - in order to avoid the small beads to fit into the interstitial space formed by three large ones. They performed several experimental runs using a binary mixture $r_l/r_s = 2$ with varying concentration. After tapping the system in order to reach a maximum random state, a packing fraction of $\phi = 0.84$ with a coordination number $z \approx 3.75$ was obtained consistently independently of the proportion of the small particles in the mixture. However, for larger mixture heterogeneities, the percentage of the small particles is expected to affect the packing fraction. Careful experiments, necessary to avoid crystalline structures, with monodisperse discs were also performed by Lemaitre et al. [108] who found a packing density of $\phi = 0.82$ in agreement with the theoretical value proposed in Berryman [16].

More recently, Rankenburg et al. [173] provide an original analogical investigation of the effect of particle shape on 2D packing by welding ball bearings together. The evolution of the packing fraction under regular tapping was characterised for 8 different particle shapes. It was notably observed that some particle shapes demonstrate more ability to resist crystallisation. The authors attributed the aptitude of a particle to pack

with ordering to the number of rotational axes of symmetry of its shape.

2.3.2 Random packing of spherical particles

It appears that historically, random packing of spheres has been used extensively to understand the more general problem of particle packing given the vast the amount of literature dealing about this topic [38, 64]. Despite the simplistic geometry and the extensive amount of research performed on this subject, some problems related to sphere packing still remain unanswered [209]. Nevertheless experiments on packing suggests the existence of geometrical mechanisms that control the system characteristics.

2.3.3 Monodisperse packing of spheres

2.3.3.1 Random Close Packing (RCP)

The notion of Random Close Packing (RCP) signifies that the maximum density of a random collection of grains (spherical) is bounded by an upper limit, and that this limit is universal [191, 209]. The solid fraction associated with the RCP limit is know to reach $\phi_{RCP} = 0.64$, a value significantly lower than hexagonal arrangements which pack as dense as $\phi_{FCC} \approx 0.74$. The value of ϕ_{RCP} appears to be independent of the sphere sizes, but is however a function of the size distribution of the grains and their deviation from spherical shapes.

The first experiments mentioning the possibility of a RCP state were performed by Bernal [15, 14] with the aim of describing the molecular structure of fluids. Bernal found that the maximal packing fraction of randomly packed spheres situated around $\phi \approx 0.64$. Shortly after, the classic experiment of Scott and Kilgour [191] consisting of pouring some lubricated monosized particles of steel in a cylindrical container, followed by further mechanical vibrations in order to maximize the solid fraction, attains the maximum packing fraction close to the upper limit expected by Bernal [15], $\phi = 0.6366 \pm 0.0005$.

Experiments on colloids shows that the packing fractions of the dense random packing are found up to $\phi \approx 0.64$, which is in accordance with ϕ_{RCP} [212]. These experiments suggest that the structure of dense spheres is indeed invariant with the scale of the particles. Consequently, micro or nano-structures which contain densely packed bodies can be studied experimentally by using larger particles which are easier to manipulate. Nevertheless, additional forces between very fine particles, such as Van der Walls interactions, electrostatic and capillary forces [168], predominate over gravitational forces and affects the dense packing structure [229, 230] for particle sizes lower than $100\mu m$.

Nevertheless, recent experiments [160] and numerical simulations have suggested the possibility that the notion of RCP is ill-defined as densities larger than ϕ_{RCP}, where partial crystallisation of the grains occurs, could be achieved. In the experiment of [160], packing densities of $\phi \approx 0.67$ were obtained by pouring metallic beads at low rates in a container horizontally shaken. To overcome the bias inherent to the definition of the RCP, [209] proposed to replace the RCP notion by the so-called concept of Maximally Random Jammed (MRJ) state, valid for d-dimensional systems ($d > 1$). This approach consists of identifying the MRJ state as the one that minimizes an appropriate order parameter of the structure geometry, which were in this case proposed to be related either to the bond orientational order or to the translational order parameters.

2.3.3.2 Random Loose Packing (RLP)

The lowest possible packing fraction in mechanical equilibrium is generally known as the random loose packing (RLP). Unlike the RCP state, the concept of the RLP proved to be ambiguous, resulting in vague agreement on its definition. The investigation of the RLP limit found mechanically stable state for uniform packing of sphere at a density $\phi_{RLP} \approx 0.55$ [148]. At the limit, the mechanical stability is affected by the magnitude of the gravitational forces. To counterbalance this effect, Onoda et al. [148] were able to generate loose packing configurations at the limit of zero gravitational forces by using an intserstitial fluid with the same density as the poured grains.

Equivalent limits were also identified in 2D systems although lower packing densities can be obtained by using ordered arrangements of particles [147].

2.3.4 Bidisperse and polydisperse packing of spheres

For systems with a distribution of sizes, the voids created by the large spheres can be filled in by smaller ones. As a consequence, there exist mixtures that optimise the packing density of the grains. For example, the case for binary mixtures (mixture of grain sizes), represented in the Fig. 2.4, shows that for each sample (differentiated by the ratio of the particle diameters), the packing fraction can be maximised by mixing the right proportion of grains. For ternary, quaternary or random particle size distributions, similar evolution of the packing density with ratio of particle sizes can be observed. In particular, increasing the order of polydispersity (ternary, quaternary ...) progressively improves the filling of the void space such that very high packing densities can be reached.

In term of structure, polydisperse packing are commonly used to avoid the crystallin ordering between sphere. The study of stress transmission in a granular medium has been

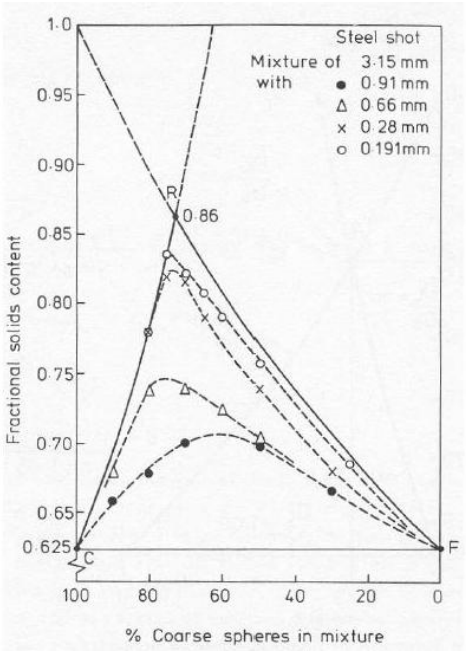


Figure 2.4: *This figure shows that a mixture of beads can increase the packing density compared to mono-disperse assemblies. The packing density of a mixture depends both on the relative amount of large and small particles, and the ratio of size of the particles (from Cumberland [38]).*

addressed using Narrow distribution of particles sizes in order as it naturally generates disordered structure [169]

2.3.5 Random packing of non-spherical particles

In granular matter, however, most of the particles are never perfectly spherical or uniform in sizes. Non spherical particles are ubiquitous and represent important economic interests. For example, the geometrical properties of sandstones possess a great variability relative to the size and shape of the quartz grains forming the rock. Because sandstones are also important reservoirs for oil and gas, the understanding of the effect of particle shape on the pore network is critical [60]. As shown in Fig. 2.5, examples in which the grain shape has a major influence are numerous.

Despite the great importance of the particle shape on a granular system, far fewer experiments have been assigned to non spherical particles than spherical ones. Unlike spherical ones, the orientation of arbitrary shaped grains is also relevant. For this reason, the analysis of the structure of the non-spherical granular systems is more difficult to perform than for the spherical particles. The first experimental study dedicated to the influence the particle shape on the packing of grains goes back several decades ago [222]. Interestingly, this seminal work identified that grain shapes, mixtures and ordering are the important factors governing the porosity of a granular media.

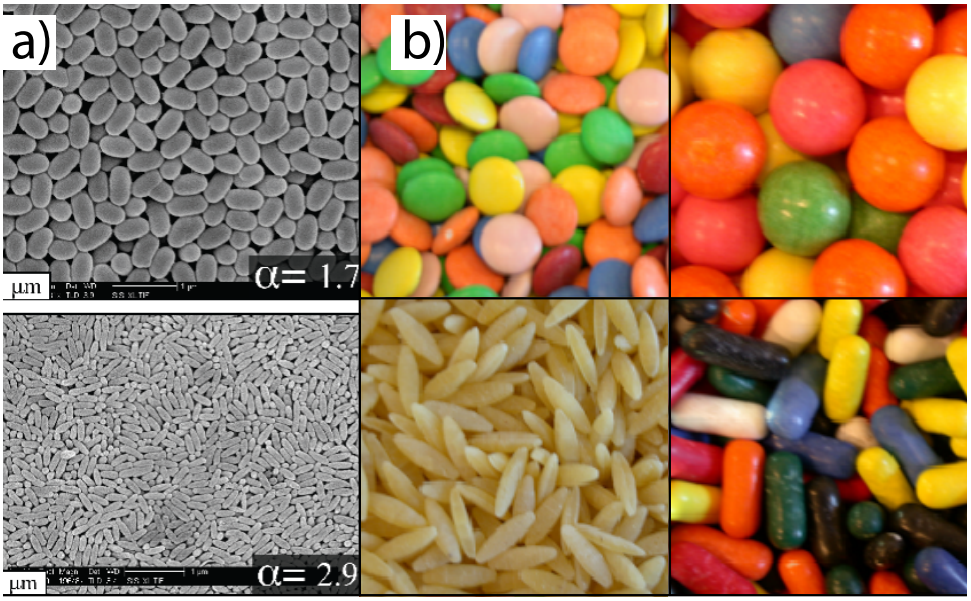


Figure 2.5: *Example of packing with non-spherical particle shapes. a) colloidal materials with aspect ratios $\alpha = 1.7$ and $\alpha = 2.9$ (from [186]). b) Examples of packing with macroscopic non-spherical particles with different shapes and aspect ratios. The figure suggests the importance of geometrical effects on the granular system.*

Experiments of packing relaxation using anisotropic cylindrical granular materials were performed by Villarruel et al. [214]. In their experimental protocol, the authors start with an initially disordered (with a low packing fraction $\phi \approx 0.5$) configuration of elongated grains. By stimulating the system with vertical vibrations, the packing evolves towards an ordered state (or nematic state) where particles align with the walls of the container at a dense packing fraction of up to $\phi \approx 0.72$, according to the frequency of the vertical oscillations. With the vibrations, the millimetric rods becomes first vertically oriented along the walls and then the ordering propagates in from the walls. This marginal behaviour obtained for rods packing, that leads to very high packing density, contrasts greatly from relaxation of spheres [94, 144].

Yu and co-workers investigated the influence of the particle shape on the packing arrangement with the aim of assimilating non-spherical particles into a packing theory on equivalent spherical ones. Their work is based on the assumption that the relationship between the sphericity of the particle (used to describe the particle shape in this work) follows a monotonic relationship with the porosity of the granular media. An empirical law predicting the sphericity-porosity relationship is derived from experimental results. A distinction is made between random loose packing and random dense packing for which the porosity decrease to a minimum as sphericity decreases (See Fig. 2.6). Among the observations of Zou et al. [232], it was noticed that the relationship between porosity and particle shape is complex and that, in particular, the porosity does not necessarily rise when the sphericity is close to 1.

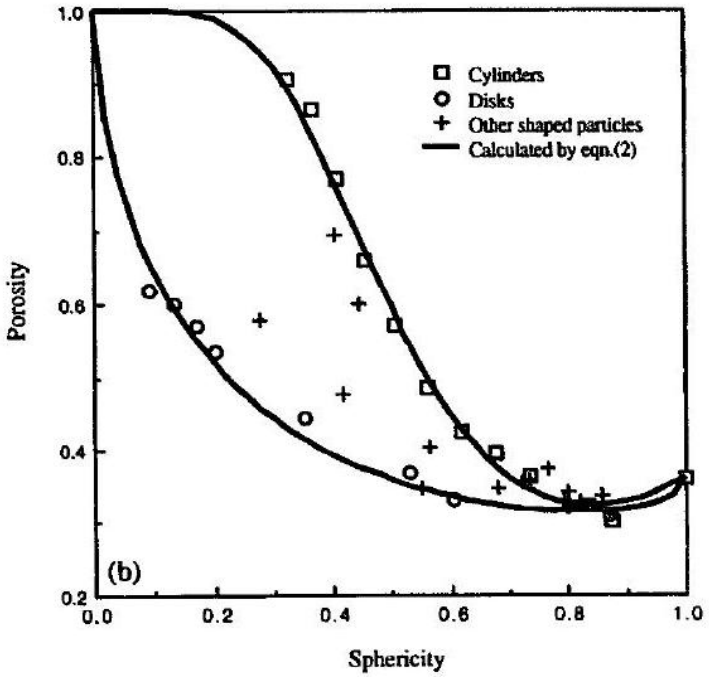


Figure 2.6: *Sphericity-Porosity relationship for different granular materials (from [232])*

For particles with axial or spherical symmetry axis, Nardin et al. [140] found that the inverse of the packing fraction varies linearly with the particle aspect ratio, when this aspect ratio is large. For aspect ratios close to 1, the packing density is shown to be constant and unrelated to the shape of the particle. Rahli et al. [172] performed similar work and found good agreement with previous experiments for various materials. In this work, where the range of aspect ratios is varies between $\alpha = 4$ and $\alpha = 70$, the relationship between porosity and aspect ratios was depicted in term of excluded area per particle. This lead to the relationship $\phi = 11/(\pi/2\alpha + 6 + 2\alpha)$, where 11 is a parameter adjusted to match the data set.

More recently, Man et al. [122, 45] investigated the packing of ellipsoids within a spherical flask in order to minimize the surface to volume ratio of the system, and thus to reduce the wall influence. With a precise experimental set up, they manage to generate packing exempt from any orientational ordering with a packing density that tends to a maximal value of $\phi = 0.74$, for a specific ellipsoid aspect ratio $\alpha = 1.3$, in the limit case of infinite container size where no finite size effects takes place. The volume fraction was calculated by injecting a measurable quantity of fluid inside the jammed system of particles, a procedure that minimise the measurement errors. Note that the packing fraction obtain with ellipsoids ($\phi_{RCP} = 0.64$) is significantly larger than the random packing density for sphere $\phi_{RCP} = 0.64$ and it emphasises the critical importance held by the particle shape.

Smaller particles, such as colloids, also permit the investigation of packing structure

for different particle shapes. Evidence was also pointed out showing the influence of the shape of various colloidal silica ellipsoids on the packing fraction [186]. A maximum packing fraction is found at aspect ratio $\alpha \approx 1.6$ in agreement with the recent packing simulation performed in Donev et al. [45] with ellipsoids.

2.4 Numerical simulations of granular systems

Numerical methods for modelling the behaviour of particulate systems have received increasing attention since 1970. The principal motivation was given by the opportunity to overcome the extreme complexity of the experimental approach, in terms of the control of the boundary condition, reproducibility and property analysis. In contrast to physical experiments, numerical modelling has the ability to explore the influence of parameters independently, which potentially provides some strong clues concerning the nature of the key physical parameters controlling the granular system. During these last three decades, many approaches have been proposed to address problems related to the packing of particles. The methods have lead to increasingly more complex modelling of the behaviour of granular materials in many different situations. In particular, the modelling capabilities have been greatly improved by the rapid expansion of the computational limits.

2.4.1 The Finite-Element Method (FEM)

At (very) large scales a discontinuous material can be assumed to behave as a continuum, i.e. the local fluctuations that occur at the discontinuous scale are negligible with regard to the size of the fluctuations occurring at the scale of the system. The continuous media is behaving in accordance with rheological constitutive laws characterising the response of a material to an external constraint at the scale of interest. The temporal evolution of the deformation of a material subject to external efforts can be handled using the Finite Element Method, which is perfectly adapted for the modelling of solid or fluid systems [152]. Adaptive meshes are an efficient way to track large material deformations, particularly for fluids, but is considered rather unsuited to describing the inhomogeneities, such as local variations of packing density, encountered in granular media. In certain case, the large deformations of the medium modify excessively the shape of the calculation mesh which lead to consequent numerical errors. Although continuum by nature, the FEM has been used to understand some problems related with granular matter. In this case some approximations concerning the local behaviour of grains, for instance due to the presence of inter-grain friction, are needed in order to reproduce specific systems such as rock avalanche run-out [187, 123]. The FEM was also extensively used to predict the

pressure distribution on the walls of silos filled up with granular materials [181, 83, 125]. To predict properly the system behaviour of the FEM method requires the calibration of mechanical parameters such as Lamé parameters, cohesion, friction angle, dilatancy angle characteristic of the granular material. Nevertheless, continuum approaches are widely disregarded for realistically reproducing the behaviour of granular materials. This is because the small scale fluctuations are neglected although they have a critical influence when the system size is relatively small, i.e. typically comprising a few thousand particles.

However, computational progress continues to provide new methods to simulate these complex materials. Before introducing discrete numerical approaches, we first introduce the material-point method as an interesting technique to improve our knowledge of discontinuous systems.

2.4.2 The material-point method (MPM)

Among the wide range of computational methods aimed at reproducing the physical behaviour of interacting bodies, the material-point method merits discussion as it can be seen as a particle-based FEM and, thus, an alternative to discrete methods to model systems enduring large deformations. In essence, the numerical principles involved in the MPM are closely related to the FEM and it was first developed by Sulsky [199, 200, 11] to solve solid mechanics problems of a dynamic nature. In the MPM, the solid or fluid particles are discretised through a set of material points that are followed during the deformation history. The Lagrangian grid (the material points) superimposes a computational grid (Eulerian) which receives the material points information in order to solve momentum equations and update the particle positions. The Eulerian grid is translated with the particle following the temporal integration of the particle displacement and is then replace at its original position. This method overcomes problems of numerical dispersion around the particle boundaries. This numerical scheme is in particular adapted for the modelling of granular systems due to the ease of detecting contacts. Individual grain deformations is made possible by using a continuum constitutive model applied for each grain interacting with frictional interactions. The MPM was used to study the influence of the mechanical properties of grains on the stress distribution in slowly sheared granular materials [12], and it was seen that for relatively small systems (about 100 particles), the internal stress calculated within particles is in good agreement with experiments [70]. However, the method shows a strong sensitivity regarding to the type of integration scheme employed and the mesh size use to describe the computational domain. At this stage, the MPM has been limited to the study of circular particles in two dimensional systems.

Because of the superposition of two different computational grids, an Eulerian and a Lagrangian one, the coupling between the present numerical scheme with computational

fluid dynamic formulation is made relatively straightforward. It is however worth noticing that the numerical time step for the temporal integration of the motion equations, which controls the CPU expense, is usually dissociated for the fluid and the solid phase. As a consequence, prohibitive CPU time can become a major drawback, notably for the simulation of granular behaviour. The calculation results of the MPM are also link to the mesh size and the mesh orientation, as they are for the FEM. The simulation of granular media at the meso-scale (typically $10^3 - 10^6$ grains) or the micro-scale (grain scale), that are of great importance in natural sciences and engineering applications, is made more efficient thanks to a class of methods known as discrete element methods to be presented in the next section.

2.4.3 Monte-Carlo (MC) simulations

The behaviour of granular ensembles can be statistically represented by considering that the displacement of individual grains is governed by statistical laws rather than by mechanical considering individually the mechanical constraints. In MC algorithms each particle is described using the location of its centroid (x, y) and its orientation θ [189]. In this technique one of the N particles forming the media is picked up randomly and its coordinates are changed either translationally, rotationally, or both, assuming a pre-selected probability law. The trial move is validated if the particle is not detected in contact with any other and refused if so. The MC algorithm pursues its iteration until the desired number of trials have been attempted (or succeeded). Although the MC is of interest for the understanding of granular phenomena of random nature, the statistical aspect of the MC simulations is unadapted to represent the micro-mechanical interactions occurring between contacting grains and limits the understanding to purely geometrically constructed media.

2.4.4 The discrete Element Method (DEM)

Approximatively thirty years ago, the Discrete/Distinct Element Method was developed by Cundall and Strack [40] as a numerical tool to investigate the micro mechanical behaviour of granular material. The Discrete Element Method can thus be used as an alternative method to continuum methods. The Discrete Element Method is a general term that designates the computer simulation technique for granular materials to be one based on the particle description at a discrete level. There are different formulations of the DEM with various degree of complexity that have been aimed to study a large range of industrial engineering or theoretical problems.

In the Discrete Element Method each particle of an assembly is considered individually

and its motion is controlled by the interactions with its neighboring particles. During a simulation, by systematically saving the position of the particles and their contact points, their velocities and the magnitude of the forces acting at each contact, detailed analysis of the micro-mechanical variables can be performed. These microscopic quantities can then be used to characterise the macroscopic behaviour of the assembly.

Although the DEM was originally intended to describe the behaviour of discs or spheres in dense heterogeneous media such as soils [40, 206], two decades later various improvements enabling the calculation of the interaction between polygons both in two and three dimensions have now been introduced [39, 75, 53]. However, passing from spheres to polygons imposes clear limitations in terms of 1) computational resources (up to 10 times more CPU requirements), 2) algorithmic complexity of the contact interaction. This second point becomes a limiting factor to the improvement of the contact interaction calculations as many complications arise from 3D interactions of arbitrary shaped bodies, essentially caused by the difficulty in determining the orientation of the normal and the tangential component of the contact force vector. The geometry of the overlap area (volume in 3D), that has to be determined with precision, can become extremely complex because of the variety of contact geometry that is usually encountered (edge to edge, node to edge, node to node). By convention, from an algorithmic point of view, a common feature of every DEM code is that it has to incorporate:

(*i*) A contact detection algorithm,

(*ii*) A contact force implementation,

(*iii*) A time integration scheme.

The details of the implementation of DEM for soft spheres is given in appendix B. In the next section, a summary of the different strategies employed to incorporate complex particle shape within the framework of DEM is presented.

Two categories of DEM can be distinguished: time-driven algorithms and event driven ones. For soft particles, time driven algorithms are usually selected [40, 43]. For the simulation of perfectly hard grains with DEM where contact becomes punctual, event-driven (EV) algorithms are preferred [47] as it permits an exact description of the particle motion. The EV algorithms schedule the sequence of events predicted to happen in the future. The simulation is advanced to the time predicted to process the event scheduled by the algorithm. At this stage, the list of event is updated and the process is repeated a desired number of times. Time-driven algorithm are conceived and well suited for simulation of soft particles interacting through a continuous inter-particle potential (e.g. the Hertz-Mindlin theory). Because of their simplicity, time-driven algorithm have also been adapted for hard particles [1].

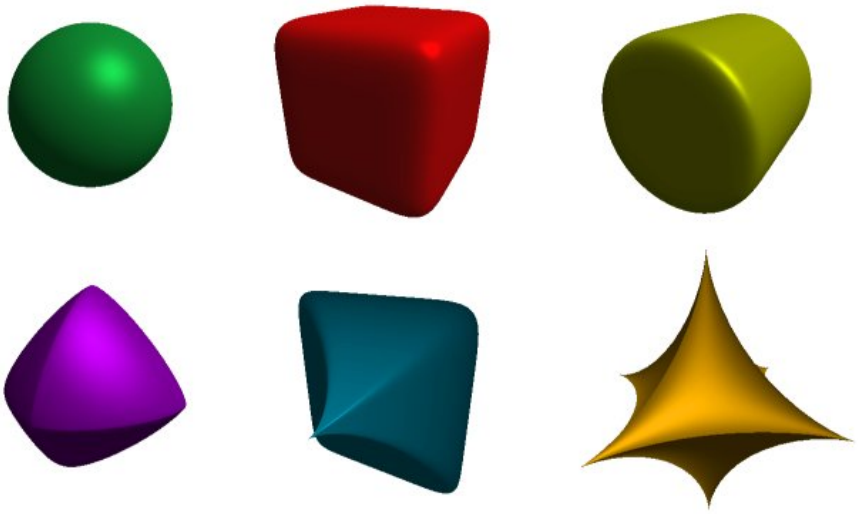


Figure 2.7: *Six three-dimensional example of shapes defined using superquadrics mathematical function (from http://aig.cs.man.ac.uk/research/reveal/squids/index.html)*

Our interest is focused on the packing of large particles [229] and the mass of each grain is large ($d > 10$ cm and $\rho_g = 2,650$ kg/m^3 for the particle diameter and the material density). Consequently the influence of the Van Der Waals interactions can reasonably be neglected. Assuming that the macroscopic behaviour of a granular material depends on the micro-mechanical properties governing the interaction between neighboring grains, micro-scale descriptions in which the granular system is described at the particle level have been adopted.

2.4.4.1 DEM and particle shape

As mentioned in the previous section, complex particle shapes can be represented and simulated with the Discrete Element Method. Different methods have been proposed to handle this task of critical importance. These include spheres, ellipsoids, clumped spheres, polyhedrons and superquadrics in 3D, and discs, ellipses, clumped discs, polygons, superquadrics and polar forms in 2D. The major problem with arbitrary shapes is often associated with the contact detection procedure. Additionally, the method to calculate the overlap area, intersections, contact points and normal and tangential directions is strategically important as it requires precision and CPU efficiency.

Ellipses and ellipsoids are commonly used shapes in granular simulations and according to [178], the compaction behaviour of ellipses differs substantially from discs, suggesting that elliptical rather than spherical shape represents granular materials more realistically. Details of implementations are proposed in [178] or [112]. The location of the intersection

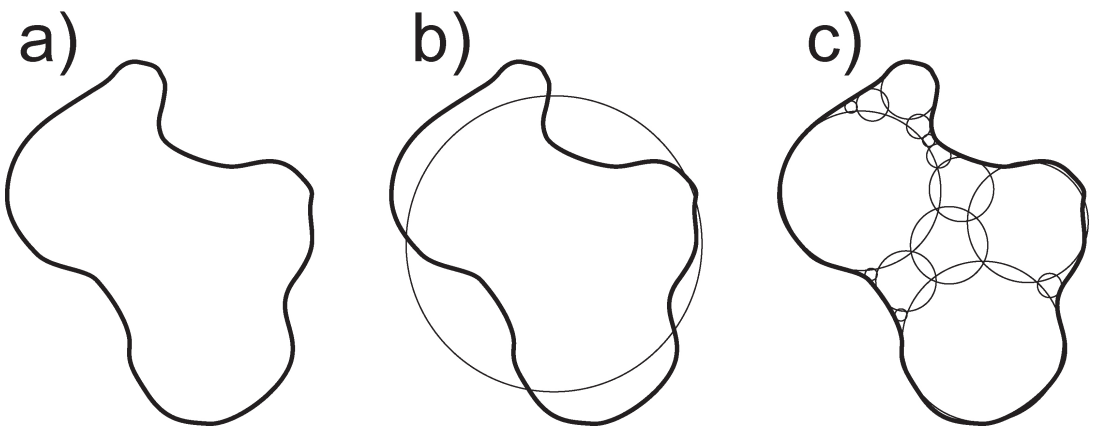


Figure 2.8: *Two-dimensional approximation of a particle shape using an equivalent disc (b)), or a assemblage of discs such as the multi-sphere model(c)*

points between a pair of ellipses can be determined analytically by solving a 4^{th} order polynomial. However, difficulties arise when the overlap area tends towards zero and the computational accuracy is degraded [178]. Alternative options for the determination of the contact normal have been proposed to overcome this issues by Ting et al. [208, 112] and applied successfully in simulations [111]. Although of physical interest, processing contact interactions between ellipsoids increase the CPU requirement by a factor 10 compared to spheres.

Sphero-cylinders consists of a combination of simple shapes: a cylinder for the particle body ended at its two extremities by two spherical caps [101], such as medicinal pills. The implementation details for sphero-cylinders applied to the DEM are given in Pournin et al. [161]. The influence of the elongation of the sphero-cylinders on the coordination number and the solid fraction of granular packs was addressed by Wouterse et al. [226] for a large range of particle aspect ratios. For very elongated aspect ratios, sphero-cylinders and ellipsoids have very similar geometrical characteristics.

Another example of the range of approach consists of associating discs or spheres connected by rigid or deformable links in order to obtain the desired particle shape [165, 142]. Practically, there are two ways of describing complex shapes with this method (Fig. 2.8): sphere/discs can either be glued without overlap or assembled with overlap. Favier et al. [51] implemented a method allowing the use of complex axisymmetrical particles build with arbitrary-sized spheres. The construction of perfectly arbitrary shapes with this method required more complex treatment with a volumetric approach of the problem. Difficulties arise from the large number of particles needed to discretise the particle surface, or from the unrealistic distribution of contact forces due to the discrete nature of the spheres/discs. Moreover, the irregularities of the surface of the sphere clusters hampers the tangential displacement of the particles and acts similarly to surface

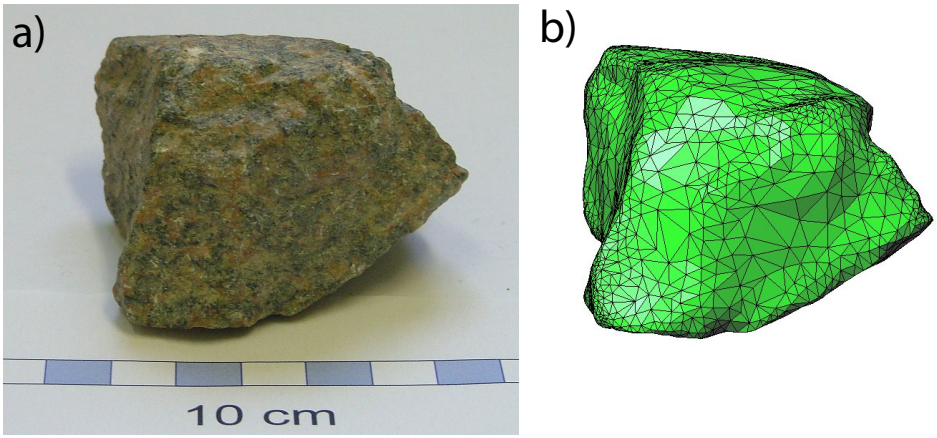


Figure 2.9: *Acquisition of a 3D particle shape. a) original rock sample. b) 3D mesh of the discretise particles*

friction. Optimised techniques have recently appeared consisting of using the surface mesh of real 3D particles (including re-entrant shapes) generated by a 3D scanner (Fig. 2.9) [163]. Interestingly, using the discs clumping method exposed by Poeschel et al. [165], where the angle of repose of heaps constructed with frictional spheres and clumped spheres is compared, reproduces static friction with more accuracy than conventional methods.

The outline of a wide range of particles can be generated mathematically by using superquadrics particles as seen in Fig. 2.7. Williams and Pentland [224] claimed that 80% of the particle shapes can be described using superquadrics. The shape of the particle is defined as follows [224, 33]:

$$f(\mathbf{x}) = \sum_{i=1}^{D} 1 - \left(\frac{x_i}{a_i}\right)^{\varepsilon_i} = 0, \tag{2.3}$$

where D is the number of dimension of the particle, a_i determines the size of the ellipsoid along each principle axis, and ε_i is a power that determines the curvature of the shape outline. Intersection between two superquadric particles is determined from the intersection of the two functions. In practice, the complexity of the analytical solution leads to prohibitive computational effort Hogue [81]. To enable the use of complex superquadric shapes [82] simplified the contact detection procedure by using discretised polar representation of the particle outline.

Polygons are one of the basic geometric entities employed in the DEM, as it provides a simple solution for the description of particles boundaries [159, 126]. The method consist of sampling the surface of the particle and linking the nodes by the means of linear segments. The discontinuities at the corner introduces complexity to determine normal and tangential directions for the contact forces and consequently most the contact models are of a heuristic nature [39]. As an alternative Feng et al. [52] proposed an energy based

polygon to polygon contact model which robustly identifies the normal contact forces although tangential frictional forces are not considered due to their history dependent nature.

As a consequence, there exist various types of alternative to use non-spherical particle within the DEM framework. The advantages of each method are usually counterbalanced by drawbacks such as heavy computational cost, complex implementation or unstable contact behaviours. Nonetheless, the DEM offers a useful range of tools to predict the behaviour of real granular materials composed of individual particles in physical interactions.

2.4.5 The Discontinuous Deformation Analysis (DDA)

The Discontinuous Deformation Analysis was initially developed by Shi [193, 192] at the end of the 80's in order to study the motion of joint-bounded pieces of rock moving independently and has since been applied to various geotechnical problems in which geological discontinuities dictate the temporal evolution of the system. The principle of DDA is to model discontinuous materials with a system of deformable blocks moving independently without penetration. Although both DEM and DDA aim to simulate the problem of discontinua, their theoretical formulation differs in the way energy is dissipated. Unlike DEM, the numerical integration of the block displacements is performed through a an implicit integration scheme. Conceptually, the DDA appears to be particularly adapted to the study of quasi-static systems with jointed rock masses such as the one encountered for geotechnical engineering problems such as slope stability. In contrast to the DEM, which is a force based method, the DDA is a displacement-based method [1].

2.5 Review of methods to produce granular packs

The numerical simulation of granular materials has drawn the attention of researchers wishing to explore the influence of various physical parameters independently. As a result, if carefully validated through benchmark problems, the numerical modelling of granular media can be used as a tool to access and investigate the properties of the granular media. Many granular phenomena that are notoriously difficult to handle experimentally can therefore be investigated through numerical models.

In order to examine the mechanical and structural properties of granular matter, the initial stage consists of the construction of a skeleton of particles. This preliminary step should be statistically representative of the desired initial configuration, which can include

[1] It means that the force is the controlling variable in DEM, while it is the displacement for the DDA.

the distribution of particle sizes, particle shapes, but also the initial solid fraction or the average particle coordination number. There are essentially two categories of algorithms to achieve it. The first category consists of using only geometrical criteria to position the particles (*geometric approaches*) while the second one takes into account the history of construction and complex mechanical interactions that take place during the physical construction of the system (*mechanical approaches*). In the following section a review of the main geometric algorithms is first presented and it is then followed by a description of the mechanical models of packing.

2.5.1 Geometric approaches

A micro-mechanical study of a problem involving granular materials requires the definition of the geometry of the sample with the simple purpose of defining the initial conditions prior to the analysis of the problem (compaction of grains, segregation). Since the preparation of these samples using micro-mechanical approaches is very time consuming, geometric methods were proposed in order to generate a random media with a structure as realistic as possible from real granular media with a requirement of minimum computational time. In particular, there is a necessity to reproduce systems with irregular dense arrangement because regular arrangements, e.g. crystalline packing with hexagonal structure, are generally unrepresentative of real granular systems [10].

Various packing algorithms are presented in the following section. For clarity two types of geometrical algorithms are distinguished: the sequential methods, if the particles are placed one at a time, and the collective ones, when all the particle positions are determine at the same time.

2.5.1.1 Sequential or Ballistic Methods

In the sequential algorithm, sometimes termed the ballistic algorithm, or ballistic deposition method the placement of the particle is made one at a time. When each particle is added to the preexisting substrate, the rest of the particles present in the domain to be filled are frozen so that the addition of a new particle does not influence the pre-existing media, i.e. no dynamic interactions occur.

To model the packing process, the ballistic deposition algorithm was first proposed by [215] and it has since been extensively used by several authors [92]. The model consists of depositing particles one at a time from a random position above a preexisting static substrate. The particle moves downwards towards other particles until it touches another particle. The grain is then translated around the surface defined by the substrate in a direction given by the steepest slope until it reaches a stable position. A minimum of

two contact points is required in 2D, and three in 3D. The extension of this algorithm to the deposition of irregular or arbitrary shape particles is non-trivial and interlocking phenomena may be difficult to reproduce.

2.5.1.2 Simple Sequential Inhibition (SSI)

The Simple Sequential Inhibition (SSI) models were originally defined for bounded domains [198]. The algorithm is built on a Monte-Carlo approach which consists of placing the particle randomly within a finite domain, insuring that the new particle is not overlapping with any existing particle. If the new particle overlaps with preexisting particles, the actual attempt is aborted and a new attempt is made to position the particle within the domain.

Among the SSI algorithm, the commercial software Macropac[2] is worth mentioning. In particular, it posseses the ability to produce random media composed of grain mixtures with arbitrary shapes and given size distributions. The grain shapes can be built individually as an assemblage of discs or spheres and various shapes such as cylinders, spheres and chunks can be mixed in the same system. However, the structural arrangement of the particles produced with Macropac differs significantly from the packing obtained by gravitational filling of identical mixtures. In particular, the Macropac method constantly over-predicts amount of void space and excessive segregation of particle mixtures is observed with this algorithm [66].

A 3D version of this algorithm was also proposed by [105] to analyse the packing of tetrahedra with a distribution of aspect ratio and size. In contrast to spheres which are smooth particles, tetrahedra are angular particles and in certain respects may be representative of many geomaterials (crushed grains of fragmented materials). The solid fraction, corrected from the wall effects, obtained with their algorithm is significantly higher with tetrahedra ($\phi = 0.416$) compared to random sphere packs ($\phi = 0.586$). This study tends to confirm the previous observations stating that the porosity of a granular medium increases with the particle angularity. Finally, it is observed that the random sphere packs generated from SSI models tend to produce structures with solid fraction significantly lower than the random close packing limit.

2.5.1.3 Constructive algorithms

Pack construction algorithms for two-dimensional systems composed of discs with a particle size distribution have been recently proposed as an efficient alternative for building geometrical packings (*Inwards Packing Method* [10] and *Advancing Front Method*

[2] http://www.intelligensys.co.uk/sim/macropac.htm

[52]). The method consists of filling up by addition of new particles in contact with the pre-existing substrate. The produced packs made of discs with a predefined size distribution have a relatively high coordination number (average number of contact between the particles) of 4 and a high packing density compared to other packing algorithms, and shows isotropic properties. Nevertheless, the packing properties of granular media generated with constructive algorithms appears to be very similar to gravitationally deposited media. A framework of this algorithm to produce packing made of particles with arbitrary shapes was suggested in Bagi's paper [10] but it has not yet been implemented. On the one hand, the main advantage of these techniques is their computational efficiency. The computational time required by constructive algorithms is typically three orders of magnitude faster than gravitational deposition using micro-mechanical approaches. On the other hand the distribution of particle sizes and shapes are out of control and the structural anisotropy observed with gravitationally sedimented grains is not reproducible [10].

2.5.1.4 Concurrent or Collective Methods

The essence of these methods is that instead of adding the particles sequentially, as seen in the previous section, the collective algorithms consist of starting with a domain randomly filled by a finite number of particles of zero size. A complete mathematical description of the the collective algorithms can be found in [198].

The generation of a random packing using the Stienen Model [198] consists of filling a domain with a finite number of grains, N, with no radius at random positions, c_i with $i = 1, 2, 3...N$. First the distance d_{ij} between a point, chosen randomly, and its nearest neighbour is calculated. Then, a disc (sphere) with a radius r equal to half of the distance with its nearest neighbour is allocated for every particle. The process is repeated until each of the c_i points are allocated finite size radius. At the final stage of construction, the system possesses a very low coordination number, as the number of contact per particle is either 0 or 1 (apart from some particular case when points are equidistant to several neighbour) and a low porosity. Additionally, the Stienen model produces a particle size distribution which can not be predefined.

The Lily-Pond model [72] of packing starts identically to the Stienen model with a finite number of grains with no radius randomly placed within a defined domain. After each iteration of the algorithm, the radius of each particle is increased at a constant grow rate until two neighboring particles are detected in contact. The procedure continues until all the particles present in the system touch another one so that they can no longer inflate. The final particle size distribution generated with this type of algorithm cannot be prescribed by the user, and it is related to the initial spatial distribution of the grains.

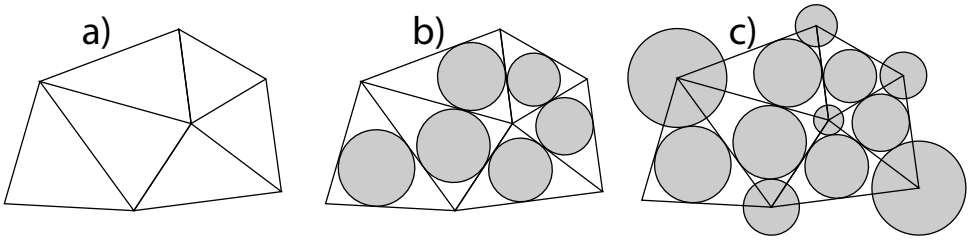


Figure 2.10: *Packing algorithm of Cui et al. [37]. a) Division of the computational domain in a triangular mesh b) insertion of the inscribed discs inside each triangular element. c) Optimisation of the solid area by addition of the maximum diameter discs at each vertex.*

A triangulation based approach has been proposed by Cui et al. [37]. The method, that can be applied either for two or three dimensional systems, consists of first decomposing a domain into triangular (2D) or tetrahedral (3D) elements using a Delaunay triangulation technique. Each element is then filled with its inscribed circle (sphere), which may represent grains. Following the first stage of filling, the system is then densified by adding a particle at vertex tangent with its nearest neighbour (Fig. 2.10). As a consequence of the construction method, the system will posses a particle size distribution sensitive to the mesh size and shape of the domain. The control of the mesh quality is thus the critical factor controlling the characteristic of the generated granular media. The simplicity of this method constitutes its main advantage as many meshing algorithms are available, while both packing density and coordination numbers produced by the method are under-predicted compared with real gravitationally sedimented media.

2.5.1.5 Membrane Methods

Other packing algorithms have been elaborated. Membrane algorithms consists either of particles surrounded by a contracting membrane or of particle shape inflated at a desired rate within a rigid membrane until the system reach constant characteristics. This method present strong similarities with the Lily-Pond model and was applied by Wouterse et al. [226] in order to study dense systems of sphero-cylinders. Like the previous packing method, the first step of the algorithm consists of placing particles randomly with no overlap within a space of finite volume. The volume V of the box is iteratively reduce by a fraction ΔV and the particle size is rescaled without changing its orientation. After a certain number of iteration, the particles start to overlap and this overlap is removed by readjusting the position of the particles. The compaction process ends when it is no longer possible to remove the overlap between the particles after a given number of attempts.

2.5.1.6 Digital packing approach

To avoid the difficulties encountered by conventional packing algorithms for non-spherical particles, [91, 62, 90] proposed an alternative digital packing algorithm, Digipack. The method consists of treating the particle shape as a collection of pixels (2D) or voxels (3D). The particle is allowed random displacements, one grid cell at a time, in any given directions (8 in 2D, 26 in 3D). No physical contact interactions are needed: the displacement of a particle is accepted only if no overlap between particles is created and is otherwise re-attempted in another direction. Digipack shows good qualitative and quantitative agreement with experimental packing structure in term of packing densities although other packing properties (coordination numbers) are not discussed.

2.5.1.7 Summary of the geometric packing algorithms

The geometric packing algorithms have benefit of many improvements and various techniques that permits almost every possible configuration of packing encountered to be created. However, when the geometric algorithms have been applied to non-spherical or arbitrary shaped particles, the results are very often biased by serious shortcomings and the structure produced are generally unrepresentative of what can be observed experimentally. For instance the interlocking between two concave particles is not reproduced with geometrical approaches. In this case mechanical approaches offer a physical alternative to geometric models. If random granular media can be reproduced using fast algorithms either sequentially or collectively, it must therefore be recognised that their microstructure is often a simplified view of what real systems exhibit. The extension of the proposed geometric algorithms to the case of non-spherical particles (2D or 3D) remains a complex task. Real grain packing are usually build under such conditions (a simple case being gravitational deposition) such that the apparent randomness of the whole system will show some correlations between particles (this is particularly true for elliptical particles) that cannot be reproduced efficiently by geometric algorithms. It is also worth mentioning that most of the algorithms presented in this section generate packs that are not mechanically stable, i.e. all the degrees of freedom of the particles are not frozen by particle contacts. As a result, additional densification of the geometrically constructed packing will occur if the structure is, for instance, imported to mechanical solver (DEM) in the presence of a gravitational field. A final remark is that packing algorithms produce stress-free assemblies while real granular systems concentrate significant amount of stress within particles, which is distributed heterogeneously within the whole system. This is why mechanical construction is often preferred to the geometrical ones.

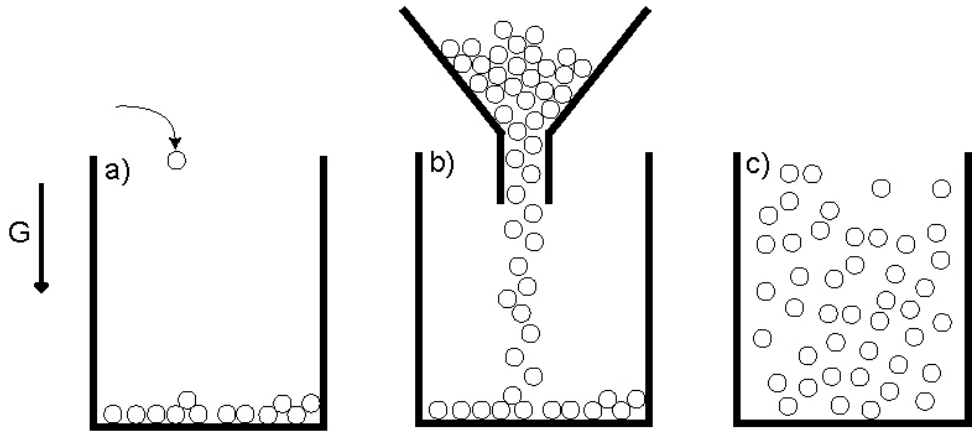


Figure 2.11: *Different method of packing construction using mechanical approaches. a) Individual deposition. b) Collective localised deposition. c) Collective deposition.*

2.5.2 The micro-mechanical approaches

In general, the properties of a granular systems cannot be known *a priori* but they are determined *a posteriori* as a function of the construction method applied to the packing by a set of properties known as emergent properties. The structural and mechanical properties of a packing are closely related to the construction method of the media. Geometric algorithms neglect the construction history of the system, and are therefore inadequate to reproduce the anisotropy observed in real media. Moreover, geometric algorithms are not appropriate to reproduce structures with realistic particle shapes. For instance, the gravitational deposition of discs generates some anisotropy related to the orientation of the external force field that can only be reproduced with micro-mechanical methods [10]. For this reasons, many research groups continue to use the computational algorithms introduce in section 2.4 to reproduce the experimental conditions that can be encountered by real granular systems.

Packing simulations using micro-mechanical approaches use computational algorithms and recreate a realistic environment in which a predefined set of particles, with given size and shape (when allowed by the computational method), are packed following a dynamic procedure. With micro-mechanical approaches, the particles composing the system are interacting dynamically with well defined mechanical rules given for instance within the framework of the DEM. Although micro-mechanical approaches come at a higher computational cost than the geometric ones, they provide physically controlled systems. These approaches also permit the control of a whole set of potential parameters that may or may not affect the packing such as the coefficients of sliding and rolling friction, the mechanical properties of the grains, the type of contact force model of the interactions or the construction mechanism.

Using this type of method, researchers have now reproduced complex systems formed

with irregular particles [106]. The differences between the micro-mechanical approaches concerns essentially the type of filling mechanism (Fig. 2.11). As mentioned previously the method of construction affects the properties of the granular packing in terms of packing densities and fabric tensors [100]. Among the different filling mechanisms, the pouring method, in which the particles are poured from a controlled position using for instance a funnel is worth mentioning and are efficient to reproduce heaps. In contrast to the pouring method, important for modeling mineral processing, the sedimentation or collective deposition algorithms, in which particles are collectively moving towards the direction imposed by the gravitational field, has been extensively used in particular to understand the principles of rock genesis.

To summarize, the micro-mechanical approaches can model the behaviour of granular media more realistically than the geometric methods. They also provide more flexibility as a variety of methods borrowed from computational mechanics, such as the DEM, can be employed and used to solve the dynamic interactions that occur during the formation of the granular system. To balance these advantages, it is worth mentioning that the micro-mechanical deposition approaches come with expensive CPU costs and that algorithms of great complexity have to be implemented to reproduce accurately the dynamics of particles with arbitrary shapes. As explained in Chapter 3, the approach adopted in this thesis is micro-mechanical, and it can cope with the deformation and interaction of particles with arbitrary shape.

2.6 Summary of the influence of shape on 2D packing densities

To finish this review a summary of the final packing density obtained for two-dimensional systems is presented. The different numerical method outlined in the previous section have been used to reproduce packs of particles. However, although a large quantity of studies have been devoted to the characterisation of discs packing, the understanding of the influence non-arbitrary shapes represents a major technological and economical challenge. First, a compilation of the packing density obtained for the random packing of discs is established. This is followed by a table summarising the main results of packing densities of non-circular particles.

2.6.1 Packing of discs

Among the quantity of packing values found in the literature, the work of Bideau et al. [18] provides the only experimental study of random packing. It is interesting to point out

Table 2.1: *Value of random close packing for monodisperse systems of discs.*

ϕ_{rcp}	Reference	Comments
0.82 ± 0.02	[16]	
0.81 ± 0.02	[196]	
0.821 ± 0.002	[93]	
0.82	[215]	
0.82-0.83	[201]	
0.830 ± 0.015	[167]	
0.81	[177]	
0.772 ± 0.002	[80]	Slightly polydisperse
0.835	[183]	Sequential addition
0.822	[183]	Collective rearrangement. crystalline region can be encountered
0.822	[108]	Experimental
0.84 ± 0.01	[18]	experimental work + slightly polydisperse
0.815	[10]	Polydisperse 1:2
0.8746	[91]	Geometrical, No friction, Presence of crystalline patterns

that their system are polydisperse in order to avoid hexagonal structures. However, the authors observe that the packing density of their system is independent of the degree of polydispersity of the particles. It was also speculated that experimental reproducibility is difficult to achieve for the reason that 2D packing are unstable in a random close packing configuration unlike 3D systems.

The low packing value obtained by Hinrichsen et al. [80] is inferred to be due to the construction process of the packing (Random Sequential addition which give an initial coverage $\phi = 0.5472 \pm 0.0002$ followed by a contraction of the surface to increase the density) and the author argue that, after several stage of compaction, their system reach a density of a random dense packing just above the random loose packing limit. However, it is still unclear whether 2D packing exhibits two critical extreme packing states (RCP and RLP) as do the 3D systems.

2.6.2 Packing of arbitrary shapes

The packing of 2D arbitrary shapes have also been investigated using several types of packing algorithms. Nevertheless, the strategies employed to produce the packs are far more complex than with discs, and the systems are mostly created by using geometric algorithms.

Table 2.2: *Value of random close packing for monosized arbitrary 2D shapes*

Shape	ϕ_{rcp}	Reference	Comments
equal ellipses, $\alpha = 1.6$	0.8753	[91]	
equal ellipses, $\alpha = 4.0$	0.76	[26]	
equal ellipse, $\alpha = 3.0$	0.8781	`http://pack-any-shape.com/`	No friction
equal squares, $\alpha = 1$	0.8753	[91]	
irregular pentagons, $\alpha = 1$	0.7500	[91]	
irregular pentagons, $\alpha = 1$	0.8078	[91]	No rotation
Short fiber, $\alpha = 4$	0.6035	[91]	
Short fiber, $\alpha = 4$	0.7363	[91]	No rotation
Snowflakes, $\alpha = 1.17$	0.7593	[91]	
Snowflakes, $\alpha = 1.17$	0.7021	[91]	No rotation
Polygons, $\alpha = 1.0$	0.78-0.82	[4]	Experimental

2.7 Conclusions

In this literature review, it was shown that the geometrical characterisation of the shape of a particle remains a challenging task. Shape descriptors can be divided into three categories with regard to the relative scale of the geometrical characteristics: the form, the roundness and the surface texture. Furthermore, experimental work on granular packing has underlined the importance played by the grading and the shape distribution on the final properties of the system such as coordination number and packing density.

The experimental difficulty to control the particle shape has leaded the community of researchers and engineers working with granular media to adopt numerical methods. The

technical specifications of these methods have been introduced and a particular emphasis was given to the different strategies proposed for the simulation of non-spherical particles.

An extensive number of packing algorithms has been presented and split into two main class of algorithms. Faster but less physically realistic, the first class of packing algorithms are based on purely geometric assumptions. They are however rather unsuited to provide structures composed of arbitrary shaped grains. In many cases, when particles shape or construction process plays a critical role, the mechanical construction methods, constituting the second class of algorithms, are generally preferred although they requires much larger computational requirements. Because of the simplicity of its implementation, the DEM appears to be the most suited method to reproduce physically realistic granular packings. In this thesis, the detailed characteristics of granular packing requires physical realism and a micro-mechanical model with collective deposition is therefore applied for the creation of the pack.

In the next chapter, the details of the numerical method proposed to simulate the granular systems presented in this thesis are described. The method combines the numerical concepts of the discrete element methods - to model the behaviour of particles in interactions, with the finite element method - to compute the mechanical deformations and the stress state within individual grains.

Chapter 3

Using the Combined Finite-Discrete Element method for the study of granular materials

3.1 Introduction and historical developments

There are in nature many phenomena that cannot be modelled by continuum-based approaches. In many of those case, the overall behaviour of the systems is governed by the interaction between distinct materials at a much smaller scale than the size of the system itself, a scale at which the discontinuities plays a critical role in the behaviour of the system. This category of material includes granular matter, where the interactions are relevant at several length scales. This category of problems called "problems of discontinua" needs specific approaches in order to be modelled with realism and to understand the complex nature of its behaviour. These problems of discontinua clearly need a higher level of understanding especially from a theoretical viewpoint. Introduced 30 years ago, the Discrete Element Method (DEM) was developed with the aim of modelling the behaviour of soils at the grain scale [40] in order to understand the behaviour of larger scale systems, but was then adapted in order to handle problems coming from a wide variety of disciplines [30, 33]. Originally DEM was considering rigid particles of simplistic shapes (cylindrical or spherical), interacting with each other with a contact law in order to calculate the contacts force.

The last three decades, this simple approach has been improved in many regards in order to face the needs of both engineers and researchers, as it has been proven to provide useful insights in many fields such as physics of condensed matter, astronomy, civil engineering, earth sciences, pharmacology or cellular biology. As explained in the

previous chapter, there have been a multitude of developments aimed at reproducing the particle behaviour in terms of contact interaction and particle shape. A natural evolution of the DEM is to replicate accurately the deformability of each discrete element, and to provide a robust model for the contact interaction unsensitive to the complexity of the considered particle shape. In order to incorporate these features encountered in the problem of discontinua, Munjiza proposed a method that merges the capabilities of the finite element method with the discrete element implementations. Technically, the first combined finite-discrete element method was developed between 1989 and 1991 during the PhD thesis of Prof A. Munjiza [134] in 1992. The original implementation, the *RG* code, was originally written in C++ and it incorporates finite strain elasticity-plasticity coupled with a smeared crack model for fracture and fragmentation. During the next 15 years, the method has gained from several algorithmic improvements such as fast contact detection algorithms, robust implementation of the contact interactions based on penalty function methods or the crack/fracture propagation within materials in order to tackle grand challenges problems that can involve millions of particles. An open source version of this code, called Y[1], with additional development by the author was used for the work performed throughout this PhD thesis. In this chapter, we describe the implementation of the different algorithmic stages encountered in the FEM-DEM.

In contrast to the classic implementation of the DEM with spheres or discs, the combined finite-discrete element method solves the continuum equation within a grain, assuming that the entire grain behaves either elastically, visco-elastically, visco-elasto-plastically, etc ... The grains deformation are solve computationally according to the rheological behaviour of the material (Finite Element Method). Moreover, if the considered material is subject to an excessive deformation, the material fracturing can be performed by using either single or smeared crack approaches [135, 131]. The major advantage of the formulation is its ability to handle the contact interaction of particles with arbitrary shapes independently of the contact configuration (edge to edge contact - node to node - node to edge).

The last 8-10 years have seen hybrid methods coupling both finite and discrete element methods becoming increasingly popular. As a result, the number of codes available to the scientific and engineering community has risen. Among them, two codes constitutes the starting point of most FEM-DEM simulations. The first is *ELFEN* owned by *Rockfield Software Ltd* and developed in collaboration with the University of Swansea, is also based on the pioneered work of Munjiza [134]. The *ELFEN* software, certainly the most advanced, includes advanced capabilities specific to both finite and discrete element method such as the possibility to simulate the behaviour of either rigid or deformable bodies interacting and impacting in two or three dimensions [74, 151, 157]. In particular

[1] http://webspace.qmul.ac.uk/amunjiza/

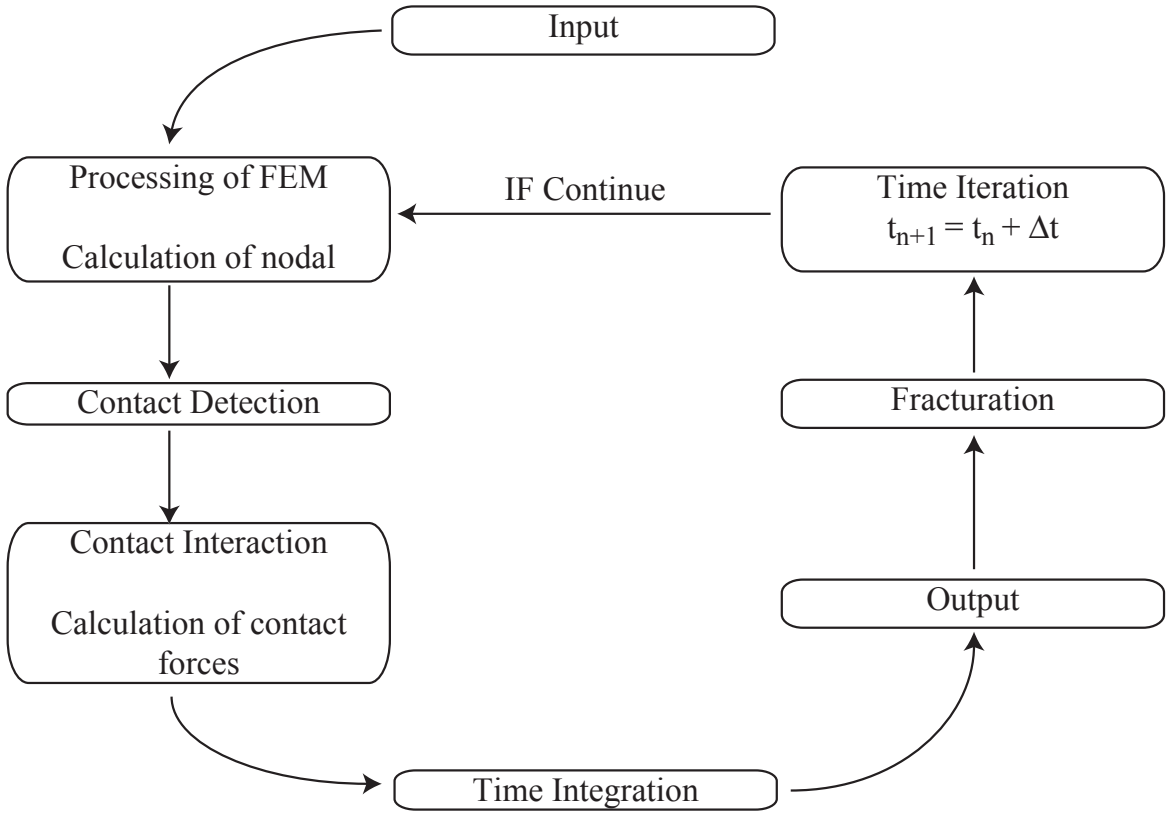


Figure 3.1: *Flow chart of the routines used in the combined finite-discrete element method.*

ELFEN provides the user a sophisticated platform that can simulate the particle fracture if the plasticity limit is reached. A concurrent development called LDEC (Livermore Distinct Element Code) has also been proposed at the Lawrence Livermore National Laboratory to simulate the reaction of underground structures subject to dynamic loading [130, 131]. The discrete element code LDEC determines the the motion of a block (of a given shape), firstly considered as rigid, by integrating the equations for the position of the mass center and a triad of vectors that characterises its spatial orientation. Then, LDEC is coupled with an explicit three dimensional finite element solver, DYNA3D, in order to model the continuum deformation at the block scale. This approach consists of computing the rock deformation using a Cosserat point method, valid for large deformations and large rotations, that may occur within a discrete particle [185]. In particular, it requires no internal discretisation of the blocks and is consequently efficient in terms of computational effort. The behaviour of many complex materials listed in a library of material properties, such as several types of geomaterials, have been validated with the DYNA3D software, which constitutes a strong basis for the discrete element simulations. Recently, several hybrid methods of finite and discrete element were proposed such as [95] and applied to diverse type of problems [66, 109]

The Combined Finite-Discrete Element Method (FEMDEM) applied to large scale

problems involving millions of finite and discrete elements is essentially confronted to two main algorithmic problems that concentrate most of the computational time. The first part consists of handling the contact interactions rigourously as it controls and influences greatly the overall behaviour of the granular system. The interaction between the particles is processed when 2 bodies are detected in contact. The contact detection is a classic problem in Discrete Element Method as it can require more than fifty percent of the total CPU time, especially for systems involving millions of elements. The improvement of the contact detection algorithm from a $T \propto N^2$ type, where T is the total CPU time and N the number of discrete elements, to a $T \propto N \log N$ type contributes widely to the popularity of the DEM addressed to very large systems. The latest generation of contact algorithms $T \propto N$ [136] reduces even more significantly the amount of CPU time spend at detecting contacts. In the case of very large systems, an efficient DEM code requires an efficient contact detection algorithm that is described in detail in the second section of this chapter. The last algorithmic aspect consists of computing the strain and the stress received by the particles. To solve this task, we are using a Finite Element formulation, which allows for a rigorous computation of particle deformation, given the material rheological law. A visual summary of the algorithm is displayed on Fig 3.1.

3.2 Contact Interaction

Among the different algorithmic sections included in the structure of the FEM-DEM code, the most important is certainly the contact interaction. Firstly it is crucial to provide a robust implementation of the contact interaction because the contact between the particles governs not only the dynamics of a granular system, but also the static phase for which the grains can from a "rigid" skeleton with structures and properties strongly related to the type of inter-grain interactions. The interaction with surrounding particles is usually the most efficient way to exchange or lose energy in a granular system. The dissipation rate of the total energy of the system is thus governed by those interactions. Secondly, the contact interaction usually has complex algorithmic formulations that include a consequent amount of operations and a significant CPU time (proportional to the number of contacts detected). A description of the method used to model the interaction is the purpose of this section.

The implementation of the contact force $\mathbf{f}_c$ in the Combined Finite-Discrete Element can be better understood by considering their normal and the tangential component separately, $\mathbf{f}_c = \mathbf{f}_n + \mathbf{f}_t$.

3.2.1 Normal Forces $\mathbf{f}_n$

3.2.1.1 Fundamentals

In the DEM, the normal contact force between identical spheres of radius r is commonly implemented using either linear (Hooke's law) or non-linear (Hertz law) model. In general way, the contact force can be expressed as a function of a parameter n which has to be adjusted with the contact model undertaken. Thus, the contact law can be written as follow:

$$f_n = h(Y, \nu, r)\delta^n, \tag{3.1}$$

where the function $h(Y, \nu, r)$ is a function of the Young modulus Y, the Poisson's ratio ν and the sphere radius r, and δ represents the amount of deformation of the sphere. As mentioned above, the parameter n characterises the nature of the contact interaction. For Hooke's linear spring contact model the exponent is equal to unity ($n = 1$), while $n = 3/2$ for Hertzian non-linear contacts [79]. The linear contact model is in fact not representative of real interactions, while the Hertz law, exact in the case of elastic homogeneous spheres contact, cannot be easily generalized to contacts of arbitrary shaped particles. Moreover, it appears that the Hertz law posses a range of validity only within the elastic domain of deformation, and is thus unsuitable for impact problems where plastic deformations are likely to occur.

The implementation of the contact force within the Combined Finite-Discrete Element method is performed through a completely different approach, which take into account both the amount of penetration between the bodies in interaction (estimated by the calculation of the contact area) and the shape of the contact area. In order to improve the realism of the contact behaviour, and to avoid the degenerated behaviours, the contact model implemented in the FEM-DEM adopts a contact distributed formulation instead of concentrating the contact force in a single region of the contact area. Most of the time, a contact generally involves a set of finite elements, and subsequently a finite number of nodes into which a component of contact force is systematically computed. The formulation of the normal contact force acting between two bodies in interactions will be described in the following part of this section. In addition, during the contact interaction, some energy is physically lost thorough viscous dissipation as a consequence of the conversion of mechanical energy into vibrations. Viscous dissipation is taken into account in our model, however, it is not implemented within the contact interaction routines but rather within the finite element calculation and is thus physically realistic. As a result, in the FEM-DEM, the coefficient of restitution is not define as a parameter (usually constant or velocity dependant) but it is the consequence of the material properties allocated to the bodies. The variation of the coefficient of restitution with the strength of the impact is

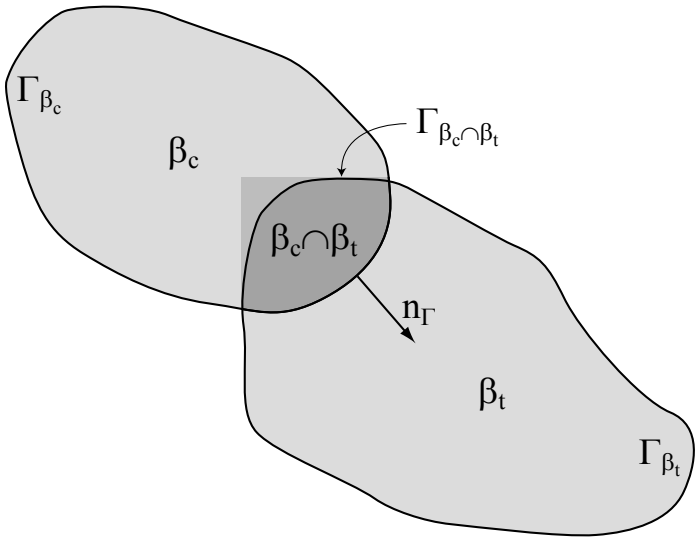


Figure 3.2: *Definition of the variables used for the contact forces.*

not know a priori, but can be assessed a posteriori as shown in the next chapter. As a consequence the contact law can be written as a function of the material parameters, the deformation, and the rate of deformation $\xi = \dfrac{dv}{dt}$:

$$f_n(Y, \nu, r, \chi, \xi, n, \gamma) = h(Y, \nu, r)\delta^n - \chi\xi^\gamma, \tag{3.2}$$

where v is the velocity of the body, χ is the coefficient of viscous dissipation, and γ is a coefficient that depends on the nature of the visco-elastic model. In the case of linear visco-elastic model, $\gamma = 1$. In this section, the notion of contact force has been introduced, while the precise implementation of the contact interaction is the aim of the next section.

3.2.1.2 General concepts: the penalty function method

Given a 2D problem, in FEM-DEM, the normal contact force is implemented to be a function of the overlapping area $S = \beta_c \cap \beta_t$, delimited by the boundary $\Gamma_{\beta_c \cap \beta_t}$, between the Discrete Element β_c, for the contactor, and β_t, for the target element (see Fig. 3.2). The overlapping area dS between the Discrete bodies produces an infinitesimal contact force $d\mathbf{f}$ given by:

$$d\mathbf{f}_n = [\nabla\varphi_c - \nabla\varphi_t]\, dA, \tag{3.3}$$

where φ_c is the a potential related to the amount of penetration of the contactor into the target and *vice versa* for φ_t. The calculation of this potential function is detailed in the next section.

The overlapping area between two Discrete Elements $V = \beta_c \cap \beta_t$ (*i.e.* the contact area) has a closed boundary $\Gamma_{\beta_t \cap \beta_c}$, with a normal direction given by the unit vector $\mathbf{n}_\Gamma$.

By integrating all the infinitesimal contact force over S, the total contact force between the contacting Discrete Element $\mathbf{f}_n$ can be written as follow:

$$\mathbf{f}_n = \int_{V=\beta_c \cap \beta_t} [\nabla\varphi_c - \nabla\varphi_t]\, dA. \tag{3.4}$$

The surface integral 3.4 over the closed area S can be rewritten as a circular integral over the close boundary $\Gamma_{\beta_t \cap \beta_c}$ delimiting the contact area S:

$$\mathbf{f}_n = \oint_{\Gamma_{\beta_c \cap \beta_t}} n_\Gamma(\varphi_c - \varphi_t) d\Gamma. \tag{3.5}$$

However, in contrast with the classic DEM [40, 33, 224], in the combined Finite-Discrete Element Methods the Discrete Elements are discretised into sets of Finite Elements. As a result, the contact area is delimited by a set of edges belonging to the Finite Elements of both the contactor and the target. Munjiza [137] shows that integration over finite elements was equivalent to integration over finite element boundaries and uses it for the determination of the contact force. The total contact force between the two discretised contacting Discrete Element can thus be expressed to be the sum of the contribution brought by each edge of the finite element identified to be a section of the boundary $\Gamma_{\beta_t \cap \beta_c}$:

$$\mathbf{f}_n = \sum_{i=1}^{n} \sum_{j=1}^{m} \int_{\Gamma_{\beta_{c_i} \cap \beta_{t_j}}} n_\Gamma(\varphi_{c_i} - \varphi_{t_j}) d\Gamma, \tag{3.6}$$

where n (respectively m) is the number of sections of the contactor (respectively the target) that forms the boundary of the total overlapping area V between the discrete elements.

3.2.1.3 The potential function

If a contact is detected between a pair of element, the nodes that penetrate the target elements are identified. Then, depending on the amount of penetration calculated, the impacting node is allocated a value that is used for determining the total contact force applied on the contacting element. This procedure is done by the use of a potential function which is defined as follows for a point R penetrating triangles (see Fig. 3.3):

$$\varphi(R) = \min(\frac{D_1}{D}; \frac{D_2}{D}; \frac{D_3}{D}), \tag{3.7}$$

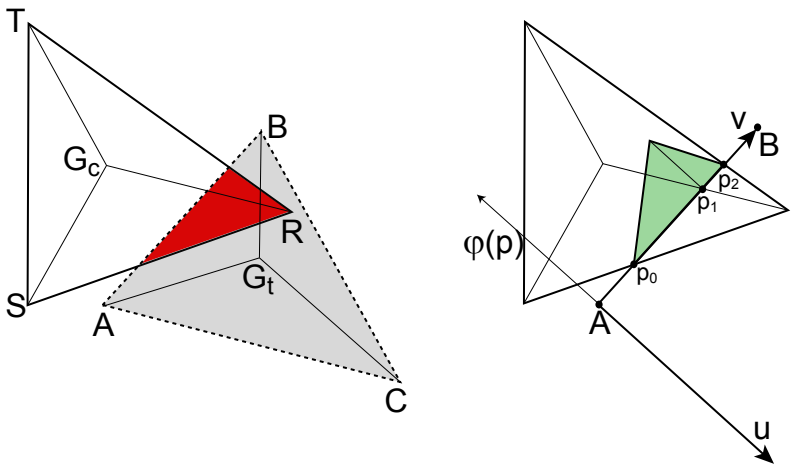


Figure 3.3: *Contact force interactions.*

where, D is the triangle area, and D_i are the areas of the sub-triangles of ABC sharing the summit R with the base that are respectively AB, BC and AC (see Fig. 3.3). The potential ϕ should be constant over the boundary of the finite element, and is equal to $\varphi(R) = 0$, if R is on the triangle edges, and $\varphi(R) = 1$, if R is positioned at the centre of the triangle.

3.2.1.4 Calculation of the normal contact force

In this subsection it is explained how the magnitude of the contact force is evaluated and is distributed among the nodes surrounding the contact area.

The nodal force is calculated by integration over the edges of each finite element and the total contact force is distributed among their nodes. The potential function defined in the previous section is used to determine the value of the force integral:

$$\mathbf{f}_{n,AB} = \frac{1}{\mathbf{u}^2}\mathbf{u}\int_0^L p\varphi(\nu)d\nu \tag{3.8}$$

where, $\mathbf{u}^2$ comes from the fact that $\mathbf{u}$ and $\mathbf{v}$ are not unit vectors. It is worth noticing that the orientation of the resulting contact force is pointing perpendicularly to the finite element edge AB, in the direction given by the vector $\mathbf{u}$.

An interaction force component with the same amplitude but in the opposite direction of $\mathbf{f}_{n,AB}$ is distributed among the nodes of the target element. In order to respect the action/reaction principle the equivalent contact force component, oriented is the opposite direction from the target forces, is given to the contactor nodes. This procedure is then repeated for every edges of both contactor and target elements in order to calculate the total contact force.

3.2.2 Tangential Forces $\mathbf{f}_t$

The computation of the tangential component of the contact force, i.e. the friction forces, is an essential feature of any discrete element code. The friction force is a dissipative force acting in the opposite direction of the relative velocity between the Discrete Elements in contact, and together with the viscous dissipations, it controls the energy losses during the deposition of a FEM-DEM simulation.

Contrary to the normal force, the tangential force is showing time dependance properties, which render more complex its implementation. This formulation of the tangential forces is either known as the "History-Dependant Method" or "increment method" in the DEM community.

3.2.2.1 Relative velocity between contacting FE

Prior to any contact, a variable recording the total displacement between two elements is created. Let us call this variable δ. At first, δ is initialized to 0 before any contact is detected. Once a contact is detected, the relative displacement between the overlapping bodies is evaluated and incrementally increased by the relative displacement that occurs between two successive time-steps as long as the contact is enduring. At the end of the contact, the relative displacement is re-initialized to 0.

The first step is to calculate the relative velocity $\mathbf{v}_{rel-ct}$ between the contactor and the target elements. In order to calculate $\mathbf{v}_{rel-ct}$, we assume that the relative velocity of the contactor and the target is the average velocity of the nodes describing those elements. The velocity can be expressed as:

$$\mathbf{v}_c = \frac{1}{n}\sum_{i=1}^{n}\mathbf{v}_{ci}, \tag{3.9}$$

for the contactor, and

$$\mathbf{v}_t = \frac{1}{n}\sum_{i=1}^{n}\mathbf{v}_{ti}, \tag{3.10}$$

for the target. In both cases, $i = 1, \ldots, n$ is the summation index over the nodes forming the element. The relative velocity can simply be written as:

$$\mathbf{v}_{rel-ct} = \begin{bmatrix} v_{x-rel} \\ v_{y-rel} \end{bmatrix} = \mathbf{v}_c - \mathbf{v}_t. \tag{3.11}$$

The relative velocity expressed in the global coordinate system $((\mathbf{i}, \mathbf{j}))$ can then be projected in a local frame of reference in order to extract the normal and the tangential

component of the relative velocity. The first axis of the local frame of reference is given by the direction of the normal component of the contact force (known at the time the tangential component is calculated), while the second axis is pointing in its perpendicular direction. Let us call this frame of reference $(\mathbf{n}, \mathbf{t})$. It is possible to express the relative velocity in the global frame of reference as a function of the relative velocity expressed in the local frame of reference:

$$\begin{bmatrix} v_{x-rel} \\ v_{y-rel} \end{bmatrix} = \begin{bmatrix} n_x & t_x \\ n_y & t_y \end{bmatrix} \begin{bmatrix} v_{n-rel} \\ v_{t-rel} \end{bmatrix}. \tag{3.12}$$

Vice versa, the relative velocity in the local frame of reference can thus be written as a function of the relative velocity expressed in the global frame of reference:

$$\begin{bmatrix} v_{n-rel} \\ v_{t-rel} \end{bmatrix} = \begin{bmatrix} n_x & t_x \\ n_y & t_y \end{bmatrix}^{-1} \begin{bmatrix} v_{x-rel} \\ v_{y-rel} \end{bmatrix}. \tag{3.13}$$

3.2.2.2 Relative displacement between contacting FE & tangential force

The tangential force interaction is adapted from the Hertz-Mindlin theory [128] and it has a dependence on the history of the contact. In other words, the tangential force is a function of the cumulative displacement that occurs between the particles during the whole duration of the contact. The tangential force is re-initialize to 0 as soon as the contact is finished. When the particles are in contact, the tangential displacement is gradually summed up as follow:

$$\delta_x = \int_0^T v_{t-rel} t(\tau) d\tau, \tag{3.14}$$

where τ varies between 0, when the contact is initiated, and T, when the contact stops. The cumulative relative displacement between the two bodies, in interaction after n time iterations, can now be expressed as:

$$\delta_x^n = \delta_x^{n-1} + v_{t-rel} \Delta t, \tag{3.15}$$

where δ_x^{n-1} is the cumulative displacement calculated at the previous time-step. If the contact is recognized as new, δ_x^{n-1} is set to 0. The tangential force is then evaluated to be the product of the relative displacement and the penalty parameter p, used for the calculation of the normal force.

$$\mathbf{f}_t^n = p \delta_x^n \mathbf{t} \tag{3.16}$$

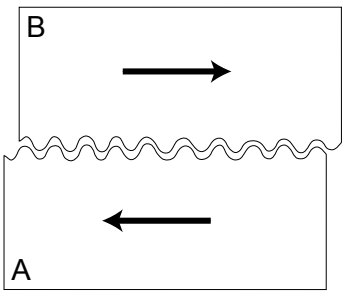


Figure 3.4: *Origin of friction between two surfaces. During the tangential motion between two surfaces, the asperities of the material deforms plastically which generates some resistance to the lateral motion and energy losses.*

3.2.2.3 The Coulomb friction

The surface of material is never perfectly smooth, and if two surfaces are moving laterally (see Fig. 3.4), a force parallel to the contact interface and opposite to the relative motion of the particles is created. A classic approximation to model the friction forces between two surfaces is given by the Coulomb friction formalism defined as follow:

$$\mathbf{f}_t^n \leq \mu \mathbf{f}_n^n \tag{3.17}$$

where, μ is the coefficient of friction, $\mathbf{f}_n^n$ and $\mathbf{f}_t^n$ are respectively the normal and the tangential force. The tangential force can thus take any value between 0 and $\mu\mathbf{f}_n^n$. Additionally, it is emphasized that we neglect the velocity dependence of the contact friction in the present implementation.

3.2.2.4 Nodal distribution of tangential force

Once the tangential force has been calculated, we distribute the force among the element nodes in the same fashion as for the normal forces.

$$\parallel \mathbf{f}_{ti}^n \parallel = \alpha_i \parallel \mathbf{f}_t^n \parallel \tag{3.18}$$

where α_i is a weighting coefficient for i^{th} the node of the element calculated *a posteriori* from the distribution of the normal forces. The coefficient α_i can take values ranging between 0 (if no contact force is distributed in a given node) and 1 (if the contact force of the element is concentrated in a single given node). As the normal force is calculated prior to the tangential one, α_i can be evaluated as follow,

$$\alpha_i = \frac{\parallel \mathbf{f}_{ni}^n \parallel}{\parallel \mathbf{f}_n^n \parallel} \tag{3.19}$$

where $\mathbf{f}_{ni}^{n}$ designates the normal force component applied to the i^{th} node and $\mathbf{f}_{n}^{n}$ is the total normal force received by the element after n time iterations.

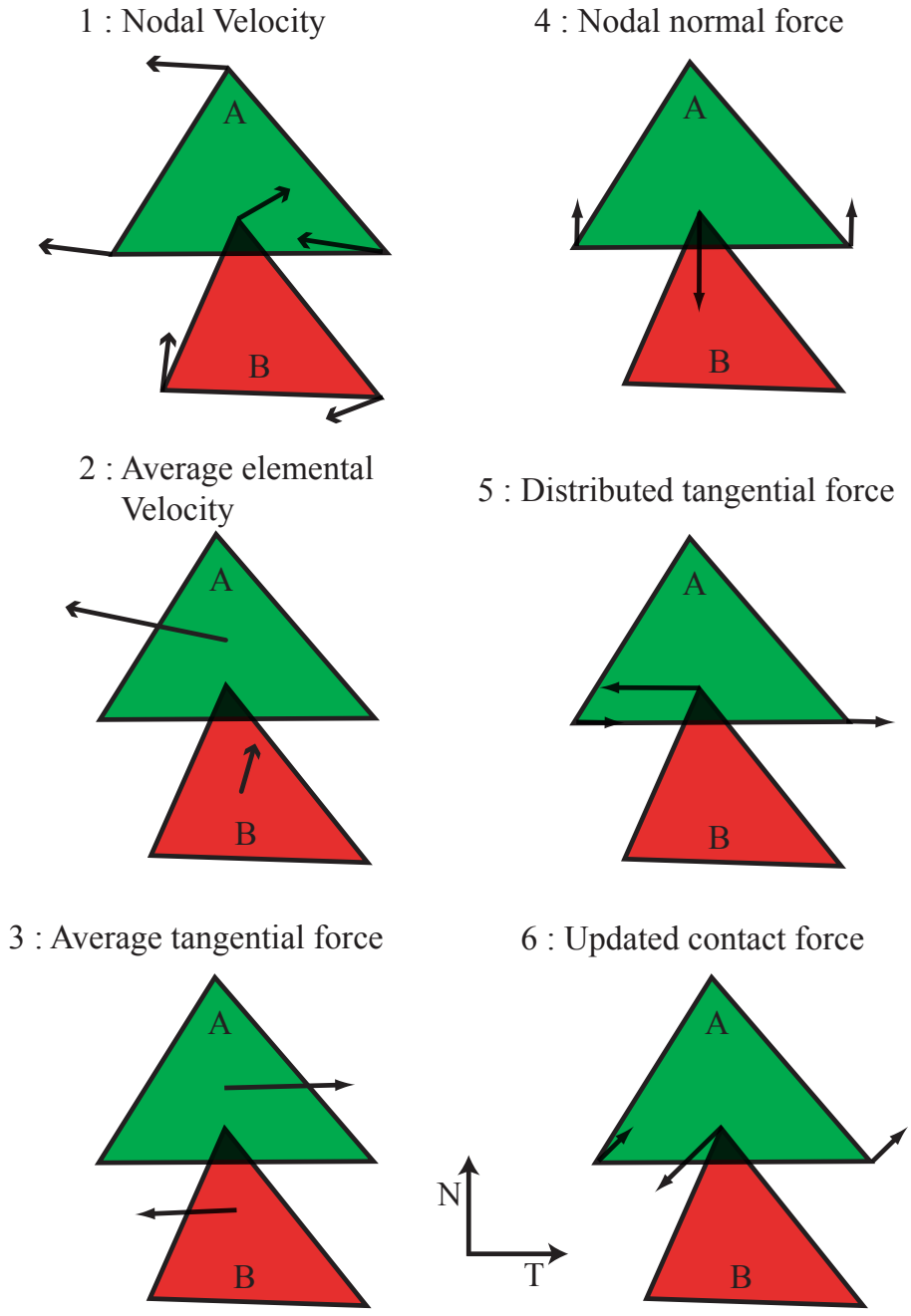


Figure 3.5: *Distribution of the tangential force among the finite element nodes.*

3.3 Contact Detection

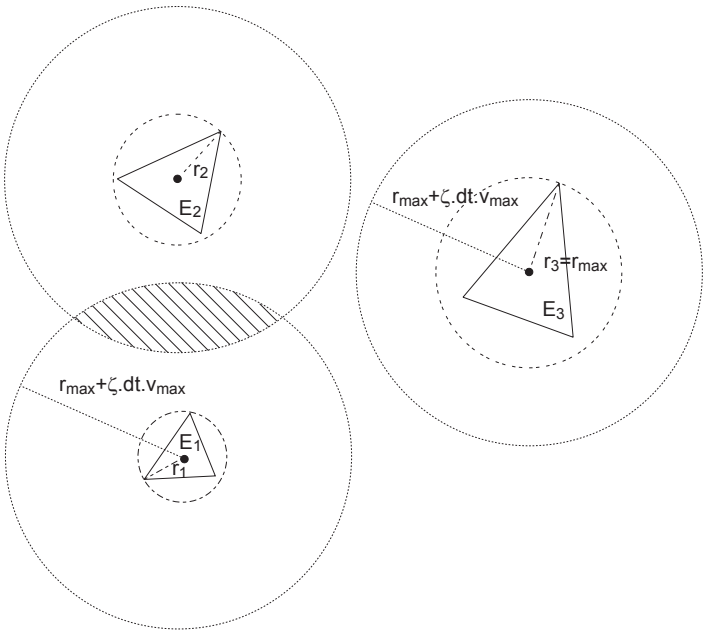


Figure 3.6: *Contact detections between 3 triangular particles E_1, E_2 and E_3.*

The contact detection is an algorithmic section of a discrete element method that consists of identifying the pair of discrete (or finite) elements that are either in contact or close to each other. In order to perform the simulation of systems composed of many particles, it is essential to optimize the computational effort for the detection of the collision. Technically, the contact detection has to be processed just before the computation of the contact interaction, once the particle positions have been updated.

The contact detection is a time consuming part of a discrete element code. The most straightforward implementation would consist of performing the contact detection at every time-step over all the possible contacts. This type of algorithm is extremely costly (in CPU time), and its use would waste a large amount of the CPU time detecting unlikely contacts. An optimized contact detection algorithm is then necessary to run simulations involving thousands or millions of finite elements. The contact detection algorithm used for our simulations is a non-binary search (NBS) type, so that the contact detection is performed among a pre-sorted list of particles which is updated after a finite number of time-steps [136]. In other families of contact detection algorithms, the mapping of the discrete elements cells requires the spatial decomposition of the domain into a large number of cells and requires important RAM space [8]. Considering that each cell should be occupied by no more than one particle, prohibitive amount of RAM are required when the particle number is high ($N > 10^6$) or that the density of grain is very small

($\phi < 10\%$). In NBS algorithm the RAM increases linearly with the number of cell used for the mapping, $RAM = n_y + 2n_x + 2N$ integer numbers (N is the number of DE, n_x and n_y are the number of cells in x and y direction respectively).

Contacts are detected at a given time-step, and the contact list is updated at a rate slightly smaller than the simulation time steps in order to warrant optimal computational time (if needed, the contact list can be updated at every time-step). This procedure is relatively secure under the assumption that the nodal velocity varies in a gentle manner, but it becomes very risky if the maximum nodal velocity jumps suddenly. It can be particularly dangerous for the case where the translational motion of a particle is, after bouncing, converted into rotation, which would imply sudden nodal acceleration. To establish the contact list, the maximum radius r_{max} surrounding completely a finite element has first to be assessed:

$$r_{max} = \max(r_1, r_2, \ldots, r_N), \tag{3.20}$$

where $i = 1, 2, \ldots, N$ denotes the finite element index. The maximum nodal velocity also needs to be assessed as follow:

$$v_{max} = \max(v_1, v_2, \ldots, v_M), \tag{3.21}$$

where $j = 1, 2, \ldots, M$ denotes the node index.

For the contact detection each element is replaced by a disc center of radius $r_{max} + \zeta \Delta t * v_{max}$ at the mass center of the triangular node. The coefficient ζ is adjusted depending on the number of time-steps between two updates of the contact list.

The CPU time spent to process the contact interaction in a system comprising N discrete (or finite) elements can be reduced from $t \propto N^2$, using systematic checking among all the contacts, to $t \propto N$, using the NBS contact algorithms. The consequence of the contact algorithm efficiency is that it extends the applicability of this method to very large scale simulations.

3.4 Deformability of DE (Finite Element Formulation)

3.4.1 Introduction to the different coordinate systems

In the Combined Finite-Discrete Element Method, the finite elements are used both for the computation of the contact interaction between the DE and the calculation of the

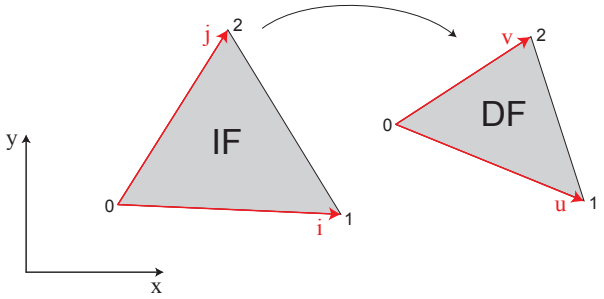


Figure 3.7: *Definition of the frame of reference for the computation of the material deformations.*

strain and the stress that occurs in each particle. In order to optimize the computation of the contact interaction and the deformability of the DE, the geometry of the FE needs to be simplified to the simplest possible shape, i.e. a triangle in 2D.

One of the key feature of the FEM-DEM is to compute realistically the mechanical behaviour of discrete grains. The FE are used to handle the computation of the strain and the stress in the DE at the FE scale. The purpose of this section is to describe the formalism used to calculate the deformation of the particle in the context of this thesis.

Let us first introduce two frames of reference, $(\hat{\mathbf{i}}, \hat{\mathbf{j}})$ and $(\breve{\mathbf{i}}, \breve{\mathbf{j}})$ respectively corresponding to the Initial Configuration (IC) and the Deformed Configuration (DC) of the Finite Element. The orientation and the magnitude of the base are defined by the edge of the finite element, and are thus neither orthogonal nor of unit length (see Fig. 3.7). Both of these frames can be expressed in the global coordinate system $(\mathbf{i}, \mathbf{j})$, which gives:

$$\hat{\mathbf{i}} = \hat{i}_x \mathbf{i} + \hat{i}_y \mathbf{j} \tag{3.22a}$$

$$\hat{\mathbf{j}} = \hat{j}_x \mathbf{i} + \hat{j}_y \mathbf{j} \tag{3.22b}$$

for the initial frame in the global coordinate system, and:

$$\breve{\mathbf{i}} = \breve{i}_x \mathbf{i} + \breve{i}_y \mathbf{j} \tag{3.23a}$$

$$\breve{\mathbf{j}} = \breve{j}_x \mathbf{i} + \breve{j}_y \mathbf{j} \tag{3.23b}$$

for the deformed frame in the Global Coordinate System (GBS). For convenience and clarity, the FEM will be formulated in the GBS using two transformation matrices named Initial Transformation Matrix (ITM) and Deformed Transformation Matrix (DTM) which are used to pass from one coordinate system to another one. The ITM is derived from (3.22) is expressed as:

$$\begin{bmatrix} \hat{i}_x & \hat{j}_x \\ \hat{i}_y & \hat{j}_x \end{bmatrix}. \tag{3.24}$$

Similarly, the DTM is derived from (3.23) and is expressed as:

$$\begin{bmatrix} \breve{i}_x & \breve{j}_x \\ \breve{i}_y & \breve{j}_x \end{bmatrix}. \tag{3.25}$$

3.4.2 Constitutive laws and calculation of the Cauchy stress and the strain in the FE

In this section, the computation of the stress tensor and the nodal force in order to calculate the strain occurring for each finite element is presented. The Hooke's Law which is valid for compression and stretching in the limit case of small deformations was applied to model the constitutive behaviour of the material. The Hooke's Law is adapted to model the elastic and reversible deformations of homogeneous and isotropic materials and is a reasonable approximation for individual grains. Considering the stiff material simulated in this thesis and the relatively small constraints applied to each grains, the hypothesis of small deformations is reasonable. A term viscous dissipations, function of the rate of deformation, is added in order to dissipate energy during grain collisions.

In order to calculate the Cauchy stress tensor $\mathbf{T}$ and the magnitude and orientation of the nodal forces $\mathbf{f}$ implied by the material deformations, the first step is to determine the components of the deformation gradient tensor, noted $\mathbf{F}$ and defined as:

$$\mathbf{F} = \begin{bmatrix} \frac{\partial x_c}{\partial x_i} & \frac{\partial x_c}{\partial y_i} \\ \frac{\partial y_c}{\partial x_i} & \frac{\partial y_c}{\partial y_i} \end{bmatrix} = \begin{bmatrix} \frac{\partial x_c}{\partial \hat{x}_i} & \frac{\partial x_c}{\partial \hat{y}_i} \\ \frac{\partial y_c}{\partial \hat{x}_i} & \frac{\partial y_c}{\partial \hat{y}_i} \end{bmatrix} \begin{bmatrix} \hat{i}_x & \hat{j}_x \\ \hat{i}_y & \hat{j}_x \end{bmatrix}^{-1} = \begin{bmatrix} x_{1c} - x_{0c} & x_{2c} - x_{0c} \\ y_{1c} - y_{0c} & y_{2c} - y_{0c} \end{bmatrix}. \tag{3.26}$$

It is worth noticing that the change of volume δV is obtained from the deformation tensor:

$$\delta V = |\det \mathbf{F}|. \tag{3.27}$$

Similarly, the velocity gradient tensor $\mathbf{L}$ is obtained as follow:

$$\mathbf{L} = \begin{bmatrix} \frac{\partial v_x}{\partial x_i} & \frac{\partial v_x}{\partial y_i} \\ \frac{\partial v_y}{\partial x_i} & \frac{\partial v_y}{\partial y_i} \end{bmatrix} = \begin{bmatrix} \frac{\partial v_x}{\partial \hat{x}_i} & \frac{\partial v_x}{\partial \hat{y}_i} \\ \frac{\partial v_y}{\partial \hat{x}_i} & \frac{\partial v_y}{\partial \hat{y}_i} \end{bmatrix} \begin{bmatrix} \hat{i}_x & \hat{j}_x \\ \hat{i}_y & \hat{j}_x \end{bmatrix}^{-1} = \begin{bmatrix} v_{1xc} - v_{0xc} & v_{2xc} - v_{0xc} \\ v_{1yc} - v_{0yc} & v_{2yc} - v_{0yc} \end{bmatrix}. \tag{3.28}$$

To compute the Green-St Venant strain tensor $\mathbf{E}$ we need to use two intermediate matrices, the left Cauchy Green strain tensor $\mathbf{B}$ accounting for the elastic part of the deformation, and the rate of deformation $\mathbf{D}$ used to calculate the viscous dissipations. As

a result $\mathbf{B}$ is a function of the deformation gradient as expressed see below (Eq. 3.29):

$$\mathbf{B} = \mathbf{F}\mathbf{F}^T = \begin{bmatrix} \frac{\partial x_c}{\partial x_i} & \frac{\partial x_c}{\partial y_i} \\ \frac{\partial y_c}{\partial x_i} & \frac{\partial y_c}{\partial y_i} \end{bmatrix} \begin{bmatrix} \frac{\partial x_c}{\partial x_i} & \frac{\partial y_c}{\partial x_i} \\ \frac{\partial x_c}{\partial y_i} & \frac{\partial y_c}{\partial y_i} \end{bmatrix}. \tag{3.29}$$

The rate of deformation is a function of the velocity gradient tensor, which is calculated as follow:

$$\mathbf{D} = \frac{1}{2}(\mathbf{L} + \mathbf{L}^T) = \frac{1}{2}\left(\begin{bmatrix} \frac{\partial v_x}{\partial x_i} & \frac{\partial v_x}{\partial y_i} \\ \frac{\partial v_y}{\partial x_i} & \frac{\partial v_y}{\partial y_i} \end{bmatrix} + \begin{bmatrix} \frac{\partial v_x}{\partial x_i} & \frac{\partial v_y}{\partial y_i} \\ \frac{\partial v_x}{\partial y_i} & \frac{\partial v_y}{\partial y_i} \end{bmatrix} \right). \tag{3.30}$$

Finally the Cauchy strain tensor is a single function of the left Cauchy stress tensor and it can be written as:

$$\mathbf{E} = \frac{1}{2}(\mathbf{B} - \mathbf{I}) = \frac{1}{2}\left(\begin{bmatrix} \frac{\partial x_c}{\partial x_i} & \frac{\partial x_c}{\partial y_i} \\ \frac{\partial y_c}{\partial x_i} & \frac{\partial y_c}{\partial y_i} \end{bmatrix} \begin{bmatrix} \frac{\partial x_c}{\partial x_i} & \frac{\partial y_c}{\partial x_i} \\ \frac{\partial x_c}{\partial y_i} & \frac{\partial y_c}{\partial y_i} \end{bmatrix} - \begin{bmatrix} 1 & 0 \\ 0 & 1 \end{bmatrix} \right), \tag{3.31}$$

where $\mathbf{I}$ is the identity matrix.

The final constitutive law for the Cauchy stress tensor $\mathbf{T}$, known as Hooke's Law, expressed as a function of the Green-St. Venant strain tensor $\mathbf{E}$, the velocity gradient $\mathbf{D}$, the Lamé parameters λ and μ, and the coefficient of viscous damping γ takes the form:

$$\mathbf{T} = 2\mu\mathbf{E} + \lambda trace(\mathbf{E}) + 2\gamma\mathbf{D}, \tag{3.32}$$

or in component form:

$$T_{ij} = 2\mu\varepsilon_{ij} + \lambda\varepsilon_k k\delta_{ij} + 2\gamma D_{ij}, \tag{3.33}$$

where δ_{ij} is the Kronecker delta ($\delta_{ij} = 1$ if $i = j$, and $\delta_{ij} = 0$ if $i \neq j$)

The Lamé parameters can be written as a function of Young's modulus Y and Poisson's ratio ν:

$$\begin{cases} \lambda = \dfrac{\nu Y}{(1+\nu)(1-2\nu)}, \\ \mu = \dfrac{Y}{2(1+\nu)}. \end{cases} \tag{3.34}$$

As a result, the compressive law can be rewritten as a function of Young's modulus and Poisson's ratio.

$$\mathbf{T} = \frac{2Y}{2(1+\nu)}\mathbf{E} + \frac{\nu Y}{(1+\nu)(1-2\nu)} trace(\mathbf{E}) + 2\gamma\mathbf{D}. \tag{3.35}$$

The third term of 3.35 is the viscous dissipation term. The viscous damping is introduced to damp the amplitude of the oscillation of the vibrational modes of the material. The viscous dissipation act as an inelastic process controlling the rebound energy of colliding grains. This is an important feature of discrete element simulation in order to lead the system to a state of rest. The velocity dependence of grain collision is discussed in the next chapter.

3.5 Temporal Discretisation

3.5.1 Choice of the integration scheme

In order to study the temporal evolution of a granular system, the Newton's equation of motion should be integrated in order to calculate the updated position of each discrete element. The time integration of these equations can be process through various integration schemes that present some specific characteristics in term of stability and accuracy. Also important, by allowing the use of larger time step, the time integration scheme can lead to important improvement of the CPU requirements.

The dynamic equilibrium of an undamped transient system consists of solving the second law of Newton for each discrete and finite element included in the computational domain. The system to solve can thus be expressed as follow:

$$\mathbf{M}\ddot{\mathbf{x}} + \mathbf{K}\mathbf{x} = \mathbf{p}, \tag{3.36}$$

where $\mathbf{M}$ is the mass matrix and $\mathbf{K}$ is the stiffness matrix and $\mathbf{p}$ are the external forces. The temporal evolution of a combined finite-discrete element method is given through the temporal integration of this equation of motion. An explicit integration scheme such as the central difference is usually employed in order to limit the manipulation and storage of large matrices as would normally be the case with implicit time integration schemes.

There are several options offered to integrate the Eq. 3.36 for each element. However, given the number of degrees of freedom imposed by a large scale system, the numerical integration of the equations has to remain efficient, robust and easy to implement in regards to the combined finite-discrete element method requirements. There are two families of integration schemes:

- Explicit integration schemes: for which the time step use for the integration of the equations remains constant during the simulation. The explicit integration schemes are conditionally stable, and consequently they impose a constraint on the minimal value to be employed in order to ensure the stability of the numerical

solution. The critical value of the time step used in the FEMDEM is given by considering the smallest finite element. The explicit integration schemes, such as the Central Difference scheme, are the most commonly employed among the DEM community. For a practical reason the integration of the equations of motion is performed through an explicit formulation in the combined finite discrete element method. Practically, in large scale DEM simulations, the time step has to be lower than the value imposed by the stability threshold, but as high as possible in order to reduce the computational time.

- Implicit integration schemes: While minimizing the errors for a given time-step and improving the stability of the integration scheme, in contrast to explicit formulations, the implicit schemes have a higher computational cost. In very large systems like those that can be encountered in the FEM-DEM, the price to pay by using these method is generally too high and as a result explicit methods are usually preferred. An implicit time integration scheme was applied by Shi [193] in the Discrete Deformation Analysis (DDA). However the DDA method is expensive computationally and is adapted for simulations over short time duration compared to the FEM-DEM method (DDA is typically 10 times slower than the FEM-DEM).

A complete discussion concerning the comparison between an extensive list of time integration scheme was presented and discussed in the papers of [182] and [58]. The study of [182] is restricted to explicit integration schemes as the implicit schemes are unsuited to large scale FEM-DEM. In this research it was concluded that among all the tested algorithms the low order schemes such as the Central Difference integration scheme, which reduce the number of operations between large matrices, appear to be more adapted for FEM-DEM simulations as it is can involved millions of calculation points and several hundreds of hours of CPU time. The simulation of dynamic of granular systems usually requires large amount of particles which can involved very large amount of CPU time. Although it requires smaller time steps, the use of the Central Difference scheme is totally justified in FEM-DEM simulations.

3.5.2 The Central Difference Time Integration Scheme (CD)

The forces, velocities and displacements of each nodes are updated at each time step using a CD time integration scheme. The accelerations, velocity and displacements are calculated in this order using the data from the previous time-step.

$$\begin{cases} \mathbf{v}_n(t+\Delta t) = \mathbf{v}_n(t) + (\mathbf{a}_n(t+\Delta t) + \dfrac{\mathbf{F}_n(t+\Delta t)}{m_n})\Delta t, \\ \mathbf{x}_n(t+\Delta t) = \mathbf{x}_n(t) + \mathbf{v}_n(t)\Delta t, \end{cases} \tag{3.37}$$

where $\mathbf{v}_n^t = (u_n^t, v_n^t)$ and $\mathbf{x}_n^t = (x_n^t, y_n^t)$ are the nodal velocity and displacement of the node n at the instant t computed from the previous time-step, $\mathbf{a}_n^t$ and $\mathbf{F}_n$ are the nodal acceleration and the nodal force calculated at the current time-step, and m_n is the updated mass of the node n.

3.5.3 Critical time step

As mentioned previously, the CD time integration scheme is conditionally stable, and it requires the time-step to be lower than a critical value Δt_{crit}, conventionally given by the highest frequency, ω_n, of the whole system. The value of the critical time step can be approximated by considering the analogy with a 1-dimensional undamped model which can be expressed as follow:

$$\mathbf{M}\ddot{\mathbf{x}} + \mathbf{K}\mathbf{x} = \mathbf{p}, \tag{3.38}$$

where $\mathbf{M}$ is the mass matrix and $\mathbf{K}$ is the stiffness matrix. Then the critical time step is simply given by:

$$\Delta t_{crit} = \frac{2}{\omega_n}. \tag{3.39}$$

Based on this undamped 1D system, the critical time step to be employed in the combined finite-discrete element method can be approximated by the following inequality:

$$\Delta t_{crit} \leq 2\sqrt{\frac{m}{Y}} \approx 2h_{min}\sqrt{\frac{\rho}{Y}}. \tag{3.40}$$

If the time step is set at a lower value than Δt_{crit}, then the integration scheme is always stable. However, it should be pointed out that the mono dimensional analysis of undamped system is only an approximation of the real critical time step that has to be used for general two or three dimensional damped systems. In order to secure the stability of the integration scheme, the critical time step Δt_{crit} is usually further divided by a factor comprised between 5 and 10. It is worth noticing that the numerical error introduced through the integration of the motion equations can also be reduce by lowering the value of the time step to lower values.

In conclusion, the calculation of the critical time step is a critical stage that should be performed before processing any simulations. This prior analysis to evaluate the critical value of the time step is necessary in order to 1) performed steady simulations and 2) save an important amount of CPU time. In any case the temporal evolution kinetic energy curve $E_K(t) = \sum_{i=1}^{N}(1/2)m_i\mathbf{v}_i^2$, where N is the total number of nodes, is systematically recorded during the numerical experiment in order to insure the stability of the integration scheme. If $E_K(t)$ shows some discontinuities or extremely high or low values, then the simulation is cancelled and restarted with a lower time increment value.

3.5.4 Dissipation of energy of the combined finite-discrete element simulation

In many cases, the finite-discrete problems involve transient motion that leads to a static state. The energy of the discrete and finite elements of the system is progressively dissipated through various mechanisms such as fracture, friction, permanent or viscous deformations until all discrete elements reach virtually a state of rest. In the combined finite-discrete element methods the energy dissipation mechanisms that occur during transient dynamics problems are such that a state of rest can be achieved. The method used to dissipate the energy is called the "dynamic relaxation". The dynamic relaxation is a technique use to solve the static problems through an explicit integration scheme. In the FEM-DEM the dissipation of energy is limited to viscous dissipations as stated in Eq. 3.35.

In dynamic relaxation, the static system is replaced by an equivalent transient one which can be expressed as follow:

$$\mathbf{M}\ddot{\mathbf{x}} + \mathbf{C}\dot{\mathbf{x}} + \mathbf{K}\mathbf{x} = \mathbf{p}, \tag{3.41}$$

where $\mathbf{M}$ is the mass matrix, $\mathbf{C}$ is the damping matrix and $\mathbf{K}$ is the stiffness matrix. Note that this equation is identical to 3.36, with an additional damping term that was neglected for the calculation of Δt_{crit}. Nevertheless we should keep in mind that the critical time step is also depending on the amount of damping present in the system. If the system is linear and dynamic, the CD integration scheme is stable if the time step respects the condition $\Delta t_{max} < \frac{k}{\omega_n}$, where ω_n is the highest frequency of vibration of the system and k is a constant which depends on the damping supplied.

3.6 Finite Element mesh creation

The combined finite discrete element method is aimed at modelling the behaviour of discrete materials that can either deform, fracture or fragment. In order to compute the stress and the strain within the discrete elements, the finite element method is applied at the discrete element level. The finite element mesh is produce by decomposing spatially the discrete element into a system of triangular domains connected along their edges. The set of edge-connected finite elements forms an approximation of the desired particle shape as shown in Table 3.1.

We did not attempt to write software to generate unstructured finite element meshes. It is relatively difficult to discretise a domain into unstructured finite elements and the

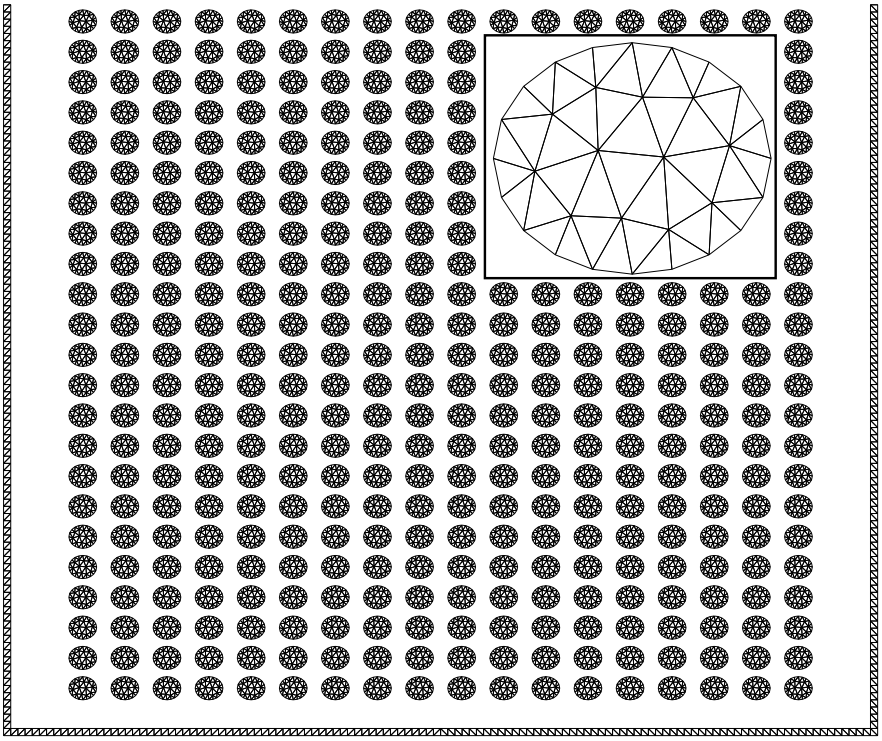
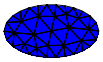
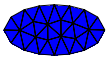
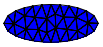
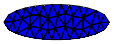
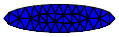


Figure 3.8: *Initial mesh of a combined finite-discrete system. Notice that the boundary possesses a structured mesh while each discrete elements contained within the domain are divided into an unstructured meshed that was created by using the meshing tool of the GID software. This structure is made of 30244 nodes and 39244 finite elements. The inset shows a magnified particle mesh (an ellipse of aspect ratio* $\alpha = 1.2$*).*

problems can increase significantly if the size and the shape of the finite element mesh is constrained by quality criteria. The finite element mesh can be created with various free softwares. In particular, one needs software that can mesh each particle and export the mesh characteristics (node position, properties and connectivity). The software used in this thesis is "GID version 7.2", which can act as a preprocessor and can be used free of charge for domains containing less than thousand nodes. To describe properly the particle outline, most of the particles require between 30 and 60 nodal points. The particle mesh is then exported in a calculation file containing the nodes and element properties. The GID software was used to create the set of particles summarised in Table 3.1. The ensemble of calculation files contains the discrete element information and constitutes a library from where the particles of interest are selected in order to build the initial configuration of the system.

Table 3.1: *Reference table of the number of mesh and nodes per particle. α is the aspect ratio of the particle.*

α	Nb Element	Nb Nodes	shape
1.0	32	25	
1.1	44	34	
1.2	42	32	
1.3	42	32	
1.4	44	34	
1.5	40	29	
1.6	52	39	
1.8	54	41	
2.0	34	26	
2.5	50	38	
3.0	60	44	
4.0	58	44	
5.0	62	48	

However the final mesh of a combined finite discrete element method can comprise a large number of discrete elements that are themselves contained within a close domain which constitutes the boundary of the system (Fig. 3.8). A preprocessing tool was additionally developed in order to prepare the input data requested by the combined finite discrete element software. The software consisted of creating the boundary of the domain with finite elements, filling the domain with the particles selected from the shape library scaled at the desired size (a variety of shapes with different sizes can be introduce within one domain), setting up the initial condition of the discrete elements (nodal force, nodal

velocity, nodal acceleration) and allocating the properties of the nodes and the elements of the system.

3.6.1 Mesh criteria and creation of particles with arbitrary shapes

As explained, the particle shape in the FEM-DEM consists of an assemblage of adjacent element (each triangular element shares between 1 and 3 edges with with its surrounding elements). The aspect ratio of the finite element can take any shape, however, in order to reduce the computational errors, the finite elements are given a reasonable shape, preferentially equilateral. Thus, if ψ_i, with $i = 1, 2, 3$, is the angle of each finite element corner, it was insured that the condition $\psi_i > 30°$ is respected for each particle mesh.

As mention previously, finite elements with excessively small size penalises strongly FEM-DEM simulations, principally for two reasons. Firstly, the total computational time is roughly proportional to the total number of finite elements involved in the problem and the subdivision of a discrete element into an excessive amount of finite element would eventually lead to life-time simulations. Secondly, the minimum time step required for obtaining stable behaviour is controlled by the size of the smallest finite element (Eq. 3.40). As a consequence, a finer discretisation of the particle shape is counterbalanced by a very large increase in computational time.

As a result each discrete element was decomposed into a reasonable amount of finite elements N_{el} (typically $N_{el} = 40$) that maintain the computational cost within reasonable limits but that also ensured a good approximation of the ideal particle shape by limiting the discretisation error. Nevertheless, in order to improve the quality of the discretisation of the outline of the most elongated particles, a larger number of elements is usually requested. A reference table showing both the particle shapes and their respective meshes of all the particle used in the thesis is provided in the table 3.1.

3.7 Computational cost

Due to the large amount of calculation points needed for the simulation of systems with reasonable size (few thousands of discrete elements), the combined Finite-Discrete Element simulations is computationally heavy both in term of CPU time and RAM requirements. For a packing simulation of 1000 particles of 10 cm of diameter divided into 50 elements (about 50,000 elements of a centimeter length scale) such as those presented in the next chapter, a FEM-DEM simulation requires 10 to 15 days of computational when running on a single processor. This cost is singularly heavier than an equivalent DEM simulation with 1000 discs of the same size, for which the computation typically last 2 hours to simulate

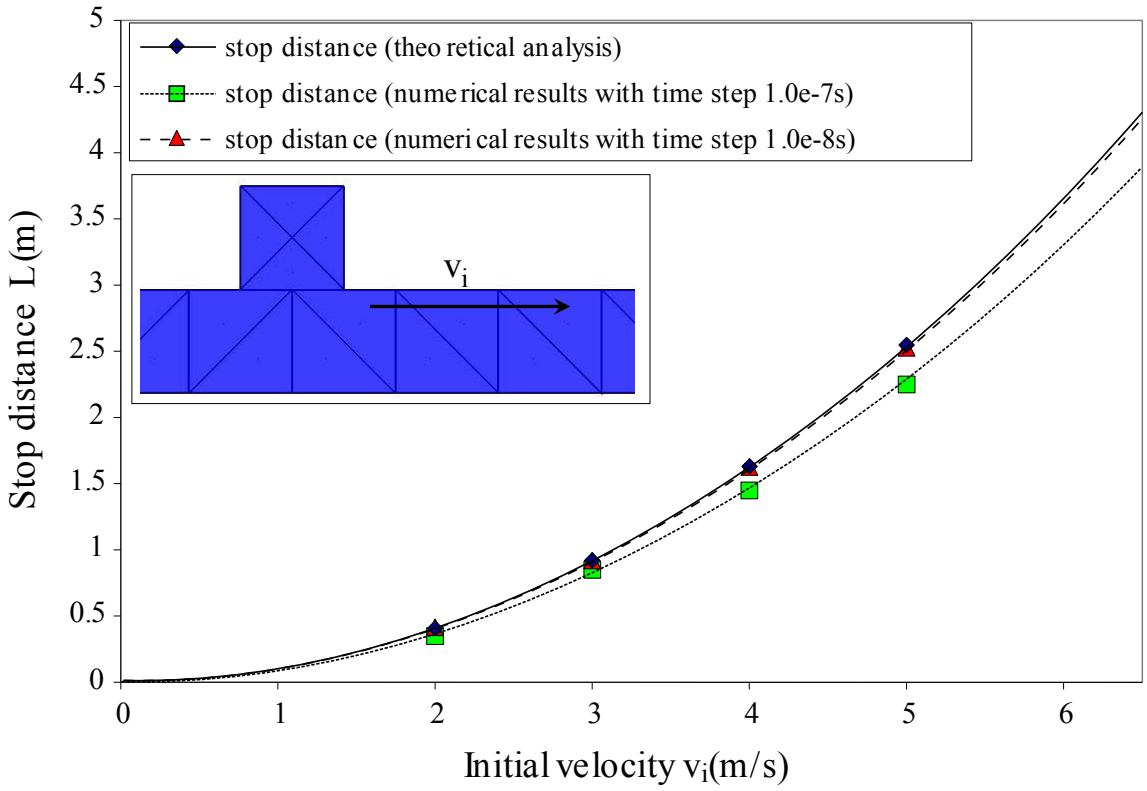


Figure 3.9: *Verification of the run out distance traveled by a sliding cube for varying time steps. The scale of the inset picture is 1:2.5.*

the same amount of time step. On the other hand, DEM simulation with elliptical grains are more requesting and 1 to 2 days of simulations are commonly needed.

To improve the computational efficiency, and reducing the CPU time [135] underlines the importance of providing some parallel implementations to the actual code Y2F. However, this enhancement falls outside the scope of this thesis as the time needed for the implementations of a parallel code would not have been compensated by the subsequent decrease in computational time. However, the importance of developing a parallel implementation in the future is clearly essential to improve the simulations efficiency and to open the doors for larger scale simulations, involving up to several billion of discrete elements.

3.8 Friction validation: The sliding block model

It is crucial to simulate the frictional motion of material with confidence. The case of a rectangle which is placed on a horizontal plane with initial horizontal velocities is carried out as a benchmark test for 2D FEM-DEM with sliding friction. The stop distance L can

be theoretically derived and is given by the following equation,

$$L_{th} = \frac{v_i^2}{2\mu g}, \tag{3.42}$$

where, L_{th} is the theoretical run-out length, v_i is the initial translational velocity, μ is the coefficient of sliding friction and g is the gravitational acceleration ($g = 9.81$ m.s^{-2}).

The FEM-DEM simulation of a sliding rectangle is performed for a square rectangle of edges $l = 0.05$ m, density $\rho = 2650$ kg.m^{-3}, frictional coefficient $\mu = 0.5$, and Young's modulus $Y = 1.0 \times 10^9$ Pa. The rectangle is given an initial velocity v_i tangent to the surface of the plane so that the square has a purely frictional displacement. The block then slows down due to the work of the frictional force at the interface between the cube and its support, and finally it stops at a distance L. Two sets of simulation tests were repeated with different initial velocities with two different time steps, $\Delta t = 1.0 \times 10^{-7}$ s and $\Delta t = 1.0 \times 10^{-8}$ s. Results are compared with the analytical solution (see Fig 3.9). They show that with a smaller time step, the numerical results are in excellent agreement with the theoretical values. It is worth noting that with the larger of the two time steps, when Δt is close to the stability limit of the time integration scheme, the errors become significant. However, using the larger time step, the calculation of FEM-DEM with zero friction is fairly stable. This conclusion suggests that in order to reduce the numerical error for calculation of tangential forces, a smaller time step is required. It also underlines the difficulty of obtaining a stable implementation for the friction with the FEM-DEM [54] due to its history-dependent nature. Consequently, the time step used for all the simulations performed in the thesis is chosen to be $\Delta t \leq \frac{1}{2}\Delta t_{crit}$ in order to reduce the numerical error caused by the friction.

3.9 Conclusion

In this chapter, the implementation of different algorithmic sections encountered in the combined finite-discrete element method have been covered in detail. This includes the implementation of the contact interaction, the contact detection, the material deformation and the time integration of the motion equations.

A history-dependent implementation for the Coulomb friction is proposed and validated with a simple test of pure frictional displacement. A good agreement between the theoretical expectations and the numerical results is found for the calculation of the run out length of a cubical sliding block.

The simulation time step has to be set at smaller value than Δt_{crit}, which is controlled by the size of the smallest finite element and the material properties, and an additional

security factor of 2 is applied for each simulation to ensure the numerical stability of the integration scheme. Finally, a framework to discretise and allocate properties to each discrete element, as needed by FEM-DEM simulations, was presented.

Chapter 4

Numerical deposition and geometrical characterization of the packing of elliptical particles

4.1 Introduction

A Random packing of grains possesses some structural properties 1) that are related to the nature of the material and to the history of creation of the system and 2) that governs their mechanical response [205, 63, 121, 46]. Monodisperse spherical grains are known to produce media that possess a packing density that is maximised if the grains are positioned along a hexagonal lattice($\phi < \phi_{hex}$). For uniform spherical particles, this gives a limit density of $\phi_{3D} \approx 0.74$ and $\phi_{2D} \approx 0.91$. It has been demonstrated numerically and experimentally that when poured randomly, circular particles reach a final state with a packing density typically lower than the hexagonal upper bound, with a value between the Random Loose Packing (RLP) and the Random Close Packing (RCP) limits [194, 100, 99]. Unlike monodisperse grains, bimodal (or above) distribution of grains are well known to pack more densely [38], a property that is for instance used for the improvement of concrete strength or to increase the conductivity of metallic granular systems. The remaining interstices between the largest particles are filled by addition of smaller particle components within an existing structure in such a way that the resulting density of the medium is optimised (see Chapter 2). In particular, a binary mixture of grains attains a maximum density when using a precise ratio of small particles.

In contrast to the monodisperse and polydisperse systems, the properties of which have been widely studied, granular systems composed of arbitrary shaped or sized particles are more difficult to characterise. Although the influence of the particle shape on the

properties of a granular system is widely recognised, quantitative description of systems with non-spherical particles remains a non-trivial task. Given that discs or spheres are known to be special case of shapes, we can expect the particle shape to influence both the system ordering and the solid fraction of the deposit generated. For instance, the recent experiments and simulations performed in the University of Princeton have shown that ellipsoids (like M&M's®) pack more efficiently than spheres [45, 122]. It is however unclear whether the two dimensional equivalent, i.e. ellipses, are affected similarly by slightly elongated particles. In comparison to a disc, which possess rotational symmetry, a slight angular rotation of an elliptical particle can help to improve the local density which could in principle lead to a higher packing fraction. However, simulations and experiments performed for very elongated particles ellipses ($\alpha \geq 10$) have shown that the solid fraction decreases with the particle elongation [140, 225]. However, no investigations comparable to the ellipsoids packings exits in 2D, and subsequently the influence of weakly elongated 2D particles on the final density of the granular media has not been clarified. Interestingly, in the experiment reported by Donev et al. [45], the maximum volume fraction obtained with ellipsoids was close to the HCP limit whereas no sign of orientational ordering between the ellipsoidal grains was detected. The case of completely arbitrary particles shapes, representative of real particles, is made complex by the emergence of interactions such as interlocking that limit the spatial position of the particles which provides lower final packing density and higher mechanical resistance to compaction. As a consequence, the problems associated with particle packing are numerous and complex. Although shapes and sizes are difficult to characterise precisely, they control most of the physical or mechanical properties of a granular assembly.

Moreover, the existence of the widely accepted concepts of Random Close Packing (RCP) and Random Loose Packing (RLP) has recently been questioned due to their ambiguous definition [209] and the possibility to generate random packing above the RCP threshold [160]. In particular, the notion of RLP and RCP are based on empirical observations of spheres and discs systems, which can hardly be extrapolated to more complex shapes (nor to ellipses or ellipsoids). Finally, there are other parameters linked to the material properties that are known to be of extreme importance. This is especially the case of the inter-particle friction which impacts on the interactions between the grains and subsequently the structure of the granular substrate. The influence of the construction method can also lead to very different type of properties [100, 23]. For example, using an initial condition with relatively dense non-touching particles promotes the obtention of lower density and lower contact numbers than when the initial configuration is made of distant grains [23].

In this chapter, the influence of the particle shape on the properties of a granular system is addressed and quantified. Naturally, the importance of the particle friction

and its crucial effect on the structure of the system is highlighted. At first the numerical experiment and its parameters are described. The effect of particle shape on the packing properties is studied by pouring irregular particles into a container with rigid walls. This collective deposition method, where all the particles interact dynamically, is a classic method to build granular systems and it permits the obtention of structural anisotropy as encountered in granular media under the influence of a gravitational field. To name but a few examples, the collective deposition is present in agricultural silo filling, rock avalanches or when pouring sand into a box. Following the description of the emergent properties of the deposited media, an analysis of the structure is performed through the use of correlation functions. A method to characterise the 2D pore size distributions is proposed and a comparison of the pore network is characterised for several particle shapes and friction.

4.2 Description of the numerical experiment

4.2.1 Numerical Experiment

The aim of the numerical experiment is to highlight the structural differences between packs of grains with various particle shapes having been deposited under similar conditions in a domain with finite boundaries. As explained in the review Chapter 2, the notion of particle shape is generally ambiguous and is hardly definable. The simplest grain shapes are perfect discs (in 2D) or spheres (in 3D), but their simplicities can lead to marginal behaviours and unrepresentative systems. Though it is largely convenient to approximate shapes by discs or spheres (the inter-particle force is well approximated by the Hertz law, simply dependent on the inter-particle penetration) [203, 110], systems of arbitrary shapes are more representative of real granular media and their understanding has to be addressed rigorously. In two dimensions the complexity inherent to the computation of the contact force is reduced and shape can be handled and characterised more easily. The present work aims to identify the influence of the simplest aspect of shape, the form, generally described as the particle elongation but numerically characterised by the ellipse aspect ratio defined below:

$$\alpha = \frac{\text{major axis}}{\text{minor axis}} = \frac{a}{b}. \tag{4.1}$$

Other studies [232] have preferred the use of particle sphericity (see chapter 2) because this parameter is more suitable to characterise natural rocks as it takes into account the amount of surface heterogeneities. On the other hand, the particle aspect ratio is the most simple shape descriptor and it neglects various geometrical factors that could also influence the particle behaviour such as the surface rugosity or the presence of concavity.

This section describes the set up of the numerical experiment of the packing of elliptical particles. Granular matter can exhibit some very complex behaviours that are related to the micro-mechanical interactions that occur at the particle scale. It is therefore important to recreate accurately both their mechanical and their geometrical characteristics. Using the numerical method described in Chapter 3, both the particle deformations and the particle shape are included. Those particle deformations and the energy dissipation of the system are controlled by realistic mechanical parameters; the Lamé parameters, λ and μ, and a viscous damping term, γ. In this respect the material behaviour is highly accurate when compared to the classic DEM approaches for which many assumptions are made to characterise the particle behaviour.

Prior to the deposition, 900 particles are placed inside a rigid container (walls can not deform) along a regular lattice. The presence of boundaries in the systems poses the problem of finite size effects when considering the properties of the system. This problem was overcome numerically by other researchers using periodic boundary conditions, in which case particles that leave the computational domain are automatically reintroduced from the opposite side of the boundary [43]. Nevertheless, there exists many experimental situations where small samples of particles are confined within domains delimited by rigid boundaries [66], which is the case treated in this chapter. A discussion of the finite-size effect is then given in the section 4.3.2. To ensure a constant mass of material in the domain, the length of the main axes of each ellipses, a and b, is adjusted and the area of each particle remains identical independently of their aspect ratio. In the initial configuration the particles are separated by a vertical and horizontal distance equal to a particle radius d_{gap} in the case of discs. In the case of ellipses, the separating distances become $d_{gap} = \sqrt{ab}$. During the processing of the simulation, the particles are positioned in the presence of an external force field $\mathbf{G}$ directed vertically and pointing downward.

At the initial time-step, a random velocity is given to every particle in order to randomize the media. As a consequence, the system is at a random state shortly after the initial impulsion. Under the influence of the gravity field the particles settle downwards, bounce, dissipate energy by the inelastic collisions and frictional displacement, and gradually reach a state of rest. In real materials, the energy is lost through wave propagation within the grains, plastic deformations of the grains, work of the frictional contact forces, etc. In the FEM-DEM, energy dissipation incorporates the viscous deformation and the work of the friction forces whereas plastic deformations are omitted. Because of the infinitesimal vibration of the material, the granular system never reaches a perfectly static state. Nevertheless, the structure is assumed static when the total kinetic energy of the system becomes so small that the particle dynamics are negligible (Fig. 4.3). At this stage the systems possesses some geometrical properties that remain constant over time. These properties, usually known as emergent properties, are characteristic of the

granular systems. As these properties (coordination number, packing density, particle orientation) can be sensitive to the condition of preparation of the system [38, 64], special care is taken to perform each packing simulation with the same initial conditions. Because the initial configuration of the particles affects the final properties of the systems, an initial random orientation was allocated to the particles before the sedimentation is started but no significant changes were observed. The packing simulations have been repeated for mono-disperse systems of particles of aspect ratio in the range $\alpha = 1 - 5$.

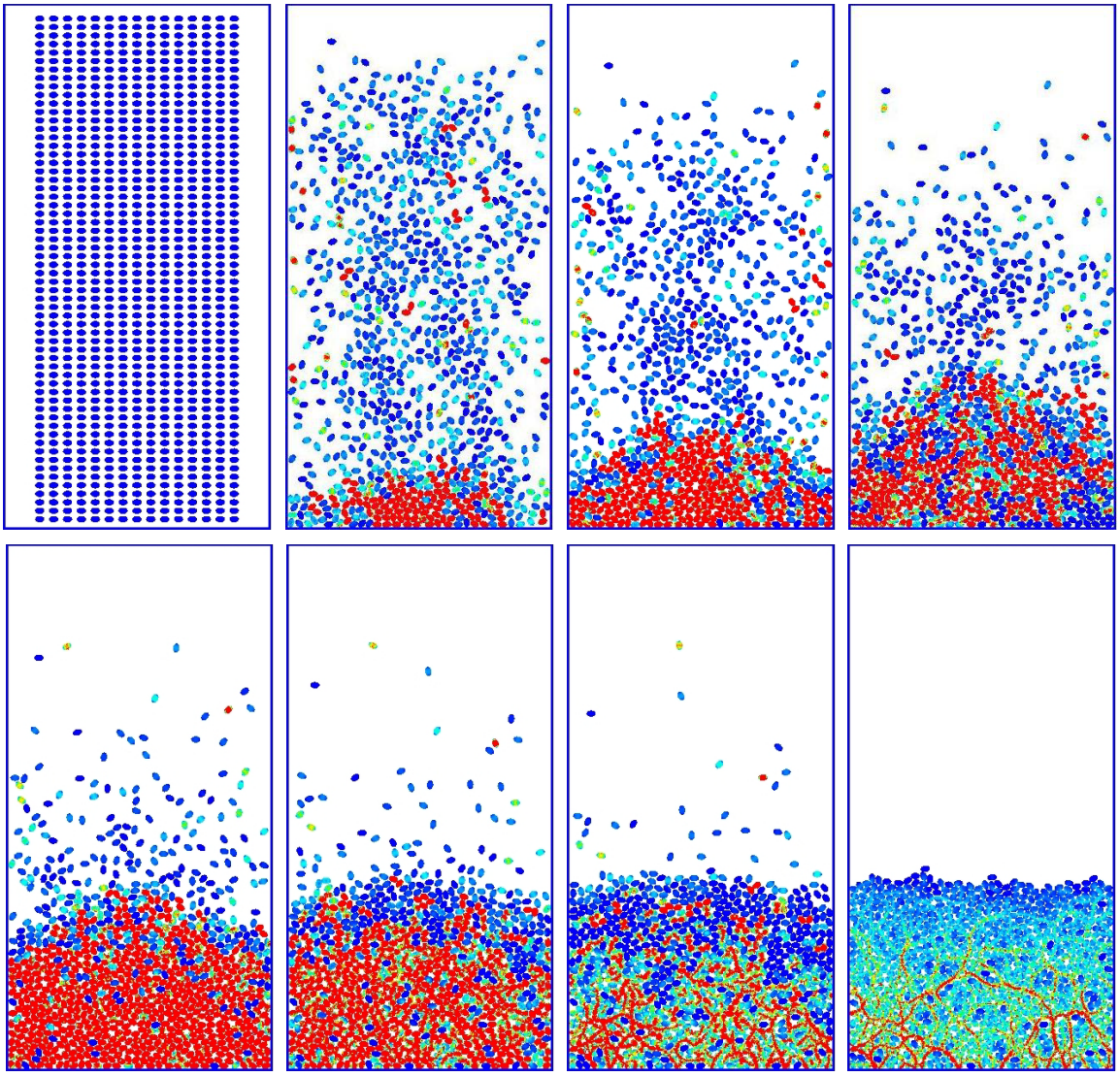


Figure 4.1: *Deposition sequence of granular particles, ellipses of aspect ratio* $\alpha = 1.5$ *with friction. The colour scheme indicates the magnitude of the differential stress calculated inside each element of each particle. The stress state of the final deposit is characterised by force chain patterns that are carrying high load through several grains. The frames are taken at* $t = 0; 0.5; 1; 1.5; 2; 2.5; 3; \infty s$.

4.2.2 Parameters of the numerical experiment

The parameters used for the simulation are summarised in the table 4.1

Table 4.1: *simulation parameters*

Parameter	Symbol	Value	Units
Aspect ratio	α	$1-5$	-
Particle size	r_g	~ 10	cm
Young modulus	Y	28	GPa
Poisson's ratio	ν	0.17	-
Viscous damping Coefficient	γ	510^{-5}	Pa.s
Mass Density	ρ_g	2.6510^3	kg/m^3
Friction coef.	$\mu_{pp} = \mu_{pw}$	$0-0.5$	-
Time step	Δt	$1.10^{-6} - 5.10^{-6}$	s
Number of particles	N	900	-
Number of elements/particles	M	$32-60$	-
Gravitational acceleration	**G**	9.81	$\mathrm{m.s}^{-2}$

4.2.2.1 Velocity dependence interaction of the binary collision between 2 discs

The collision between two grains is a dissipative process during where complex physical actions takes place simultaneously such as plastic deformation and inelastic wave propagation. It is far beyond the scope of this thesis to reproduce all the source of dispersions operating during the contact interaction. Nevertheless, a rough analysis of the binary impact problem of two frictional elastic discs ($d = 10$cm) with viscous dissipations was performed in order to estimate *a posteriori* the relationship between the coefficient of restitution and the impact velocity v_i. The coefficient of restitution $\varepsilon = \frac{v_f}{v_i}$ is the ratio of the particle velocity before, v_i, and v_f, after the impact.

As mentioned in chapter 3, the contact forces, as implemented in the FEM-DEM, depend not only upon the geometry of the contact and the amount of penetration between discrete elements, but also on the mechanical constants of the material. The material deformations are controlled by three mechanical parameters: λ, ν (Lamé parameters) and γ, related to the rate of deformation of the material. The consequence is that a particle in interaction behaves as an elastic material (similar to a spring) damped proportionally to the rate of deformation (similar to a dashpot). The coefficient of restitution of an impact

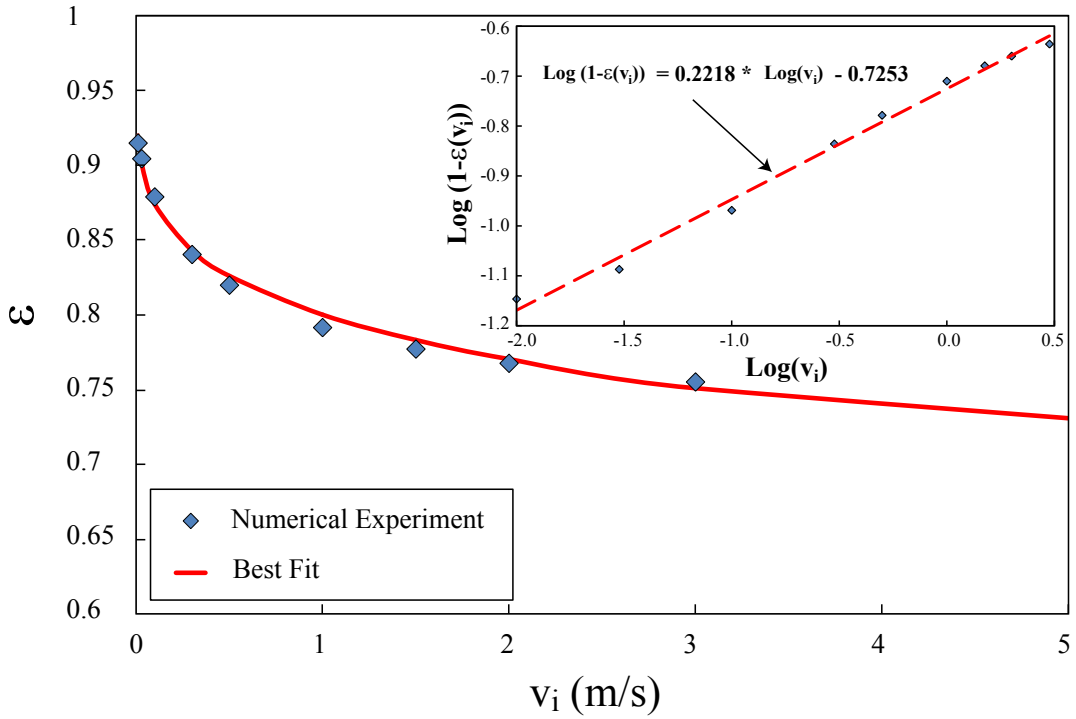


Figure 4.2: *Coefficient of restitution for an impact between two discs of 10 cm diameter. The curves in inset shows the exponential relationship between coefficient of restitution and impact velocity.*

between 2 viscoelastic discs is a non-linear function of the impact velocity and it decreases exponentially with the impact velocity (see Fig. 4.2). Its expression which was measured a posteriori takes the following form:

$$\varepsilon(v_i) = 1 - Bv_i^{\frac{1}{5}}, \tag{4.2}$$

where ε is the coefficient of restitution of the discs, v_i is the impacting velocity, and $B = 0.2$ is a fitting parameter. The relationship is that which is operating during the packing simulations conducted in this investigation and is especially sensitive to the value set for the damping coefficient γ. In the same way, the coefficient of restitution between ellipses can be evaluated. Nevertheless, the results are not presented here because the value of ε for the case of the impact between ellipses depends not only on the impact velocity between the particles but also on the relative angle of impact between the particles.

4.3 Structural dependence of the packing with the particle aspect ratio

The objective of this section consists of presenting a range of procedures to characterize the similarities and differences observed in the structure of grain packing created with

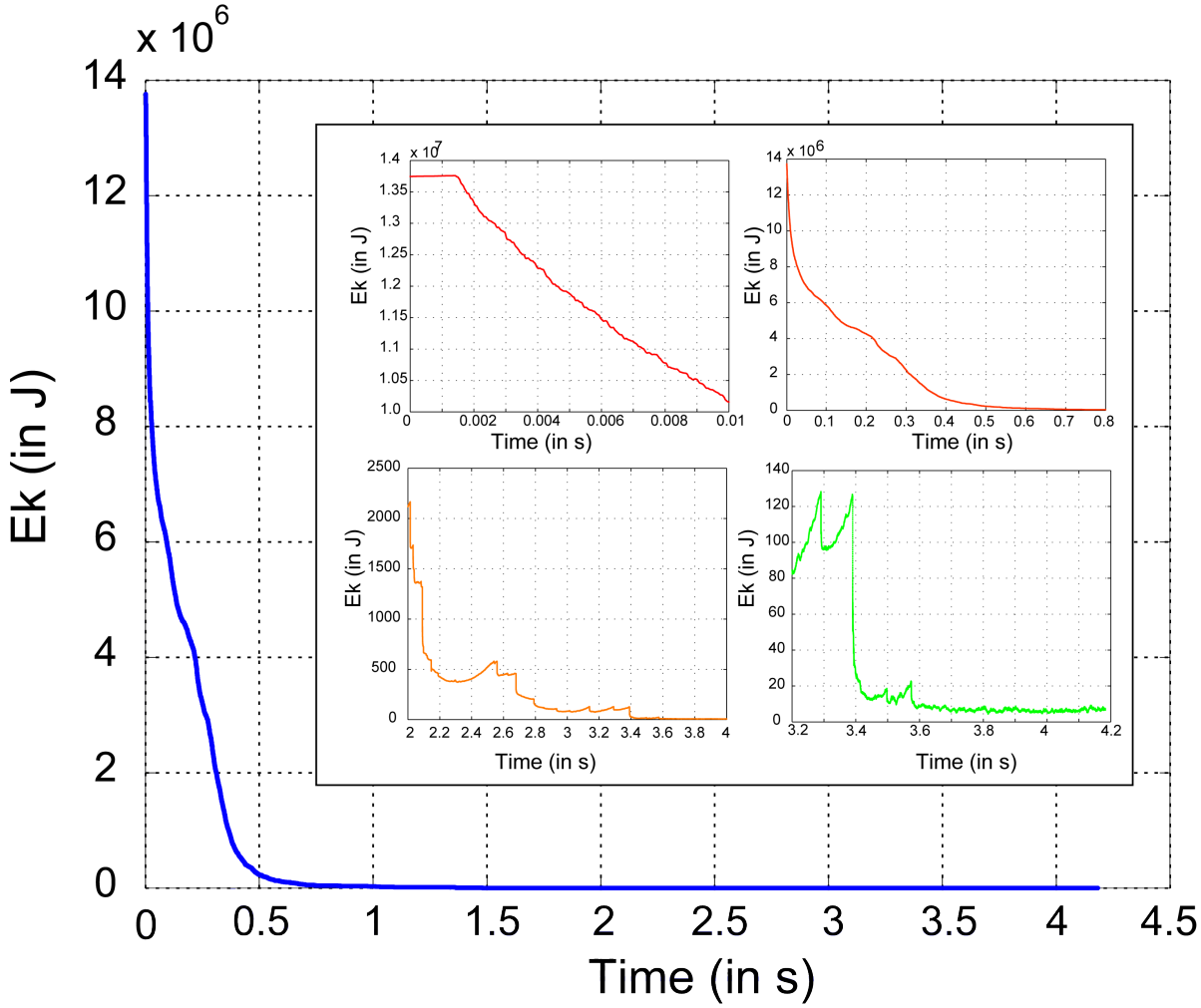


Figure 4.3: *Evolution of the kinetic energy curve during the dynamic deposition of the grains. The different zoom in illustrates the different stages of the deposition sequence, starting from the initial mixing and ending with the micro adjustment of the structure as a consequence of the material relaxation.*

particles of various elongations. The properties of the granular system are evaluated *a posteriori* by the measurement of characteristic quantities - the emergent properties - related to the microstructure of the media such as the coordination number of the system, its packing density or the distribution of voids in the system.

4.3.1 Evolution of the emergent properties during the deposition stage

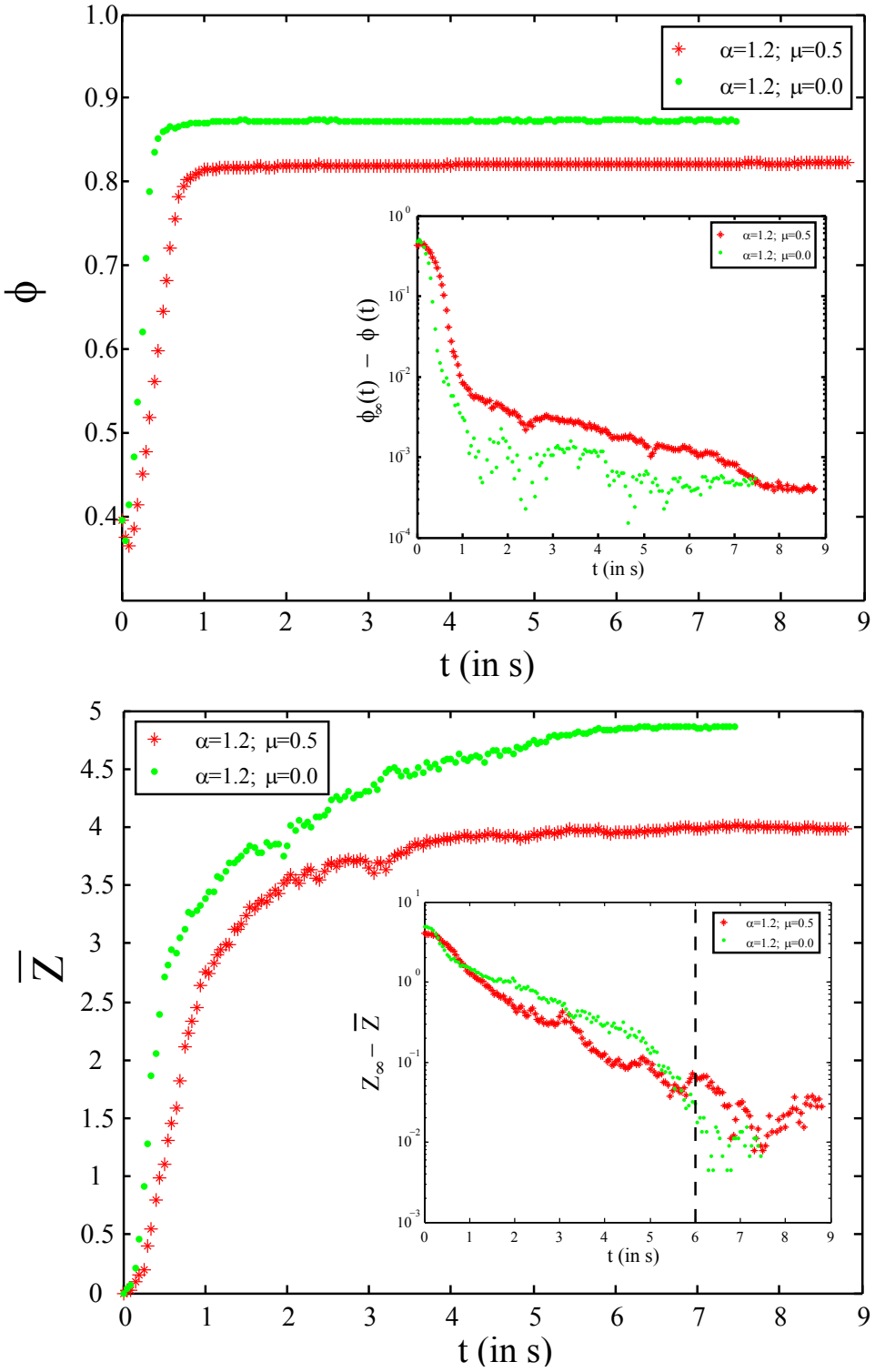


Figure 4.4: *Temporal evolution of the emergent properties for a packing simulation performed with particles of aspect ratio 1.2 interaction with friction (red diamonds) or without friction (green discs). The final values are taken once both porosity and coordination number reach a stable value over a long time.*

The depositional stage can be split into two distinct phases. Firstly, the grains are initially randomized by applying a random velocity field for each particle. During this phase, the particles interact energetically, dissipate their energy both viscously and by the work of friction forces, and are slowly deposited in the bottom of the container (see Fig. 4.1). This initial stage is followed by a phase of reorganization during which the particle displacement is small, and the energy dissipation is dominated by the work of the friction forces. During the second phase of deposition the kinetic energy of the system, E_k decreases, and the particles become pseudo-static (i.e. $E_k \approx 0$).

Phase A: the deposition: During this phase, the particles move and are subject to large displacement and rotations over short time scales. The particles interact through highly energetic impacts, and the mean free path of the particle, i.e. the distance traveled by a particle between two consecutive impacts, is typically larger than the particle size. During the packing process, the bulk density of the granular media increases smoothly, while the average distance between particles decreases. The media properties are thus highly dependent on the time, $\phi = \phi(t)$. In Fig. 4.1, phase A ends at about $t = 1s$.

Phase B: the rearrangement: Due to the many collisions that occur between particles during the previous phase, the remaining kinetic energy of the system is low and only a few modifications are encountered. However, coordination number and packing density continue to rise until the energy is too low to induce major particle displacements. At the end of this stage, the system is assumed to be pseudo-static and the emergent properties become time independent so that $\lim_{t\to\infty} \phi(t) = \text{cst}$, where cst is a constant.

The simulations are stopped once the particles are in pseudo-static equilibrium, which imply that the temporal evolution of both the emergent properties and the kinetic energy of the system should remain constant over a long period of time (see Fig. 4.4). For each simulation, it is ensured that this condition is satisfied before measuring the characteristics of the system, i.e. at $t > 6s$ for the frictionless system of Fig. 4.4.

The inset of the Fig. 4.4 suggests that the coordination number follows the relationship $\overline{z}(t) = z_\infty - e^{-\beta t}$, where the coefficient β can be determined directly from Fig. 4.4. The value of $1/\beta$ is proportional to the characteristic relaxation time of the coordination number. This coefficient is slightly lower for frictional systems than for frictional ones, passing from $1/\beta_{\mu=0} = 2.0$, to $1/\beta_{\mu=0.5} = 1.5$ with frictional ones. It confirms that the relaxation of frictional grains is faster than frictionless one. For $t > 6s$, the system is close to rest and the relationship is no longer appropriate.

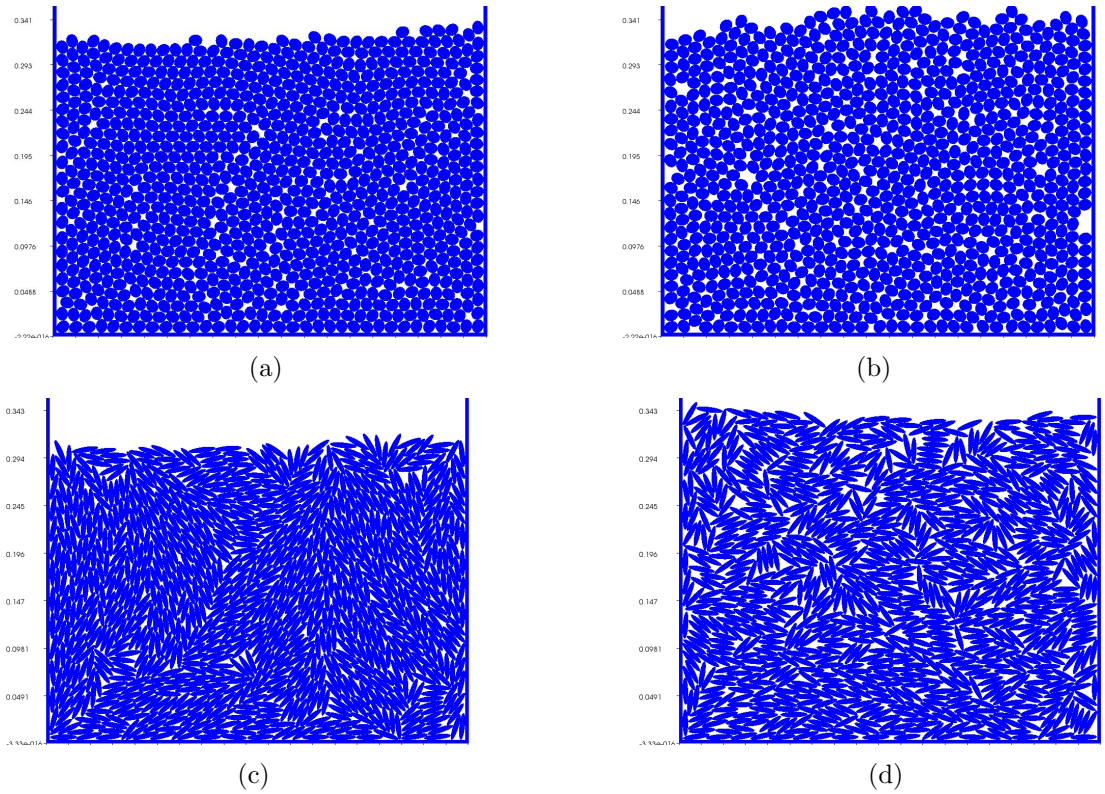


Figure 4.5: *Packing of two systems with N=900 particles, with a)* $\alpha = 1.2$ *and* $\mu = 0.0$*, b)*$\alpha = 1.2$ *and* $\mu = 0.5$*, c)* $\alpha = 5.0$ *and* $\mu = 0.0$*, d)* $\alpha = 5.0$ *and* $\mu = 0.5$*. The initial condition are identical for the frictional and the frictionless systems to allow comparison.*

4.3.2 Coordination number and packing density

4.3.2.1 Packing density

The packing density ϕ is the volume fraction of solid matter comprised in an elementary volume. The packing density is related to the porosity n, the volume fraction of void space in a granular mass, by the relation $\phi = 1 - n$. In our 2 dimensional systems we define ϕ as:

$$\phi = \frac{A_{grains}}{A_{RVE}} = 1 - n, \tag{4.3}$$

where A_{grains} is the area of grains and A_{RVE} is the area the Representative Volume Element comprising the volume of the grains plus the voids. The RVE is in fact a finite domain that is considered large enough to exhibit representative statistics. The RVE excluded from the calculation of the properties a layer of grains of 2 equivalent diameters, r_g because ϕ in the proximity of the walls is unrepresentative from the bulk part of the system. Large amount of particles is usually needed to minimise the wall effects [122] but it affects critically the computational efficiency. An alternative option would consist of using periodic boundary conditions, however, this type of approach is incompatible with

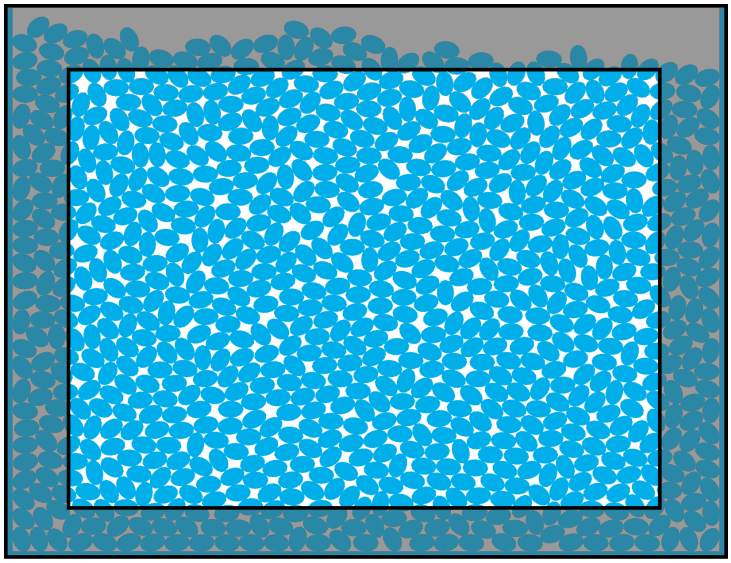


Figure 4.6: *Definition of a representative volume element (RVE) within which the packing density is measured. The RVE exclude from the calculation a layer of 2 equivalent diameters near the wall, in order to reduce the uncertainties generated by the walls.*

the numerical scheme employed.

In the container problem, it is recognised that the container walls induce a particle ordering in the vicinity of the walls while the particles more distant from the wall are randomly arranged. It is necessary to provide a measurement of the packing density either corrected or removed from the density fluctuation that are present near the walls. The effects of the container walls on packing density in a container has been extensively studied [190], and it was shown that for the case of discs or spheres, the perturbation caused by the walls are essentially concentrated in a relatively narrow layer with a thickness of 2-4 particle diameters [100]. Non-spherical particles generate more random packs and therefore the range of influence of the walls is lowered [38]. As such the packing density is calculated within a representative volume element excluding a narrow band of 2 particles diameters wide (see Fig. 4.6). This keeps enough particles within the domain to be statistically meaningful and discards from those statistics the particles that are influenced by the container wall. Additionally, the measurement errors of the packing density due to the container walls decrease with the size of the system. Based on Verman's experiments, [213] it was shown that the packing density was underestimated by the presence of the container walls. To assess this error, it was proposed that the density within the container follows the relationship

$$\phi = \phi_0[\frac{n_x}{(n_y - 1)}]^2$$

, where n_x and n_y are the number of particles in contact with the horizontal and vertical walls respectively and ϕ_0 is the final expected density. By extension, Eq. 4.3.2.1 provides

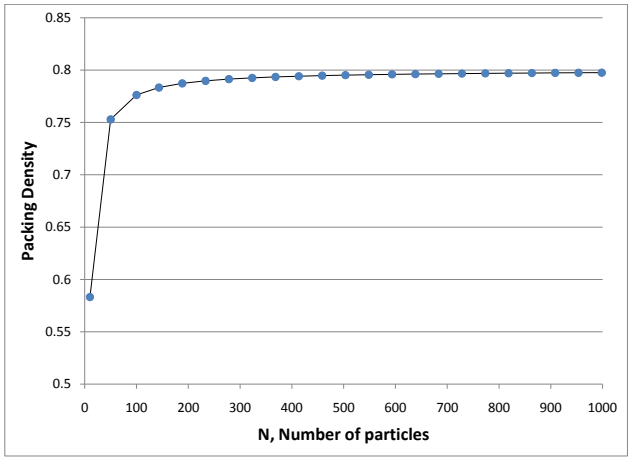


Figure 4.7: *Influence of the wall effect on the final packing fraction with the number of particles comprised inside the container. Above 1000 particles near the container walls, the finite size effects becomes negligible (error* $< 0.3\%$*).*

Table 4.2: *Reproducibility errors.* $< \phi >$ *is the average packing density calculated from n realisations of the experiment with particle of aspect ratio* α *and friction* μ*.* S_ϕ *is the standard deviation of the packing density.*

$\{\alpha; \mu\}$	$\{\phi_1; \phi_2; ...; \phi_n\}$	$< \phi >$	S_ϕ
$\{1.2; 0.0\}$	$\{87.31; 87.33; 87.43; 87.81; 87.70\}$	87.52	0.23
$\{1.2; 0.5\}$	$\{82.50; 82.56; 82.48; 82.11; 82.81\}$	82.49	0.26

an estimation of what should be the minimum number of particles in order to obtain a packing density not biased by the particle walls. Using this equation on a system of about 1000 particles ($\sim$ 100 particles touching the basal and the lateral walls), it is observes that the packing density is affected by the presence of the container walls by less than 2% (see Fig. 4.7). Keeping in mind that the computation time can become prohibitive for simulating very large systems, our granular system containing 900 particles provides a reasonable precision of the packing densities.

Although it is true that the packing density is influenced by the method of preparation of the system, in this study we chose not to consider this aspect. The influence of the influx density of grains on the final packing density is studied carefully in [23] or [100], where the reader is referred if needed.

The size of the error bars for the determination of packing density and coordination number of both frictional and frictionless systems were assessed by repeating each simulation five times. It is observed that the variation of packing fraction between each

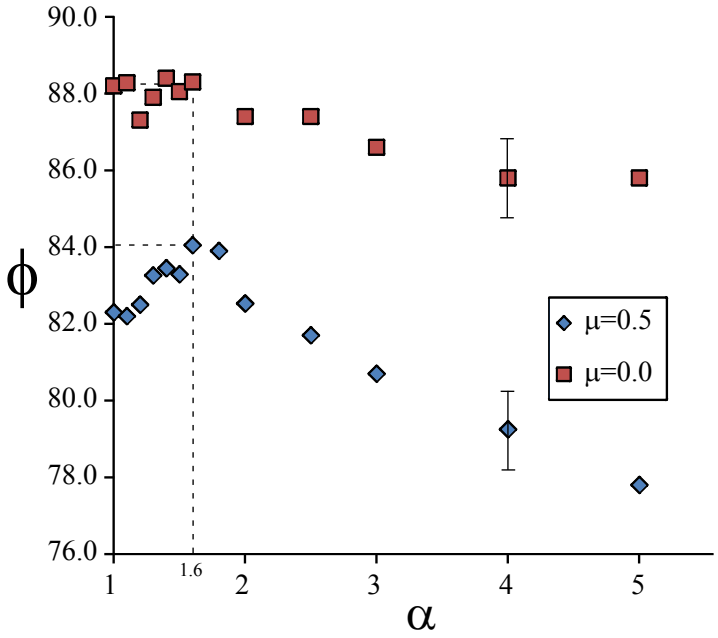


Figure 4.8: *Evolution of the packing density as a function of the particle aspect ratio. Note dotted lines intersecting the horizontal axis at $\alpha = 1.6$ highlight a maximum for the frictional case and a transition for the frictional case. Error bar $= \pm 1\%$*

.

realisation is of small magnitude compared to the density variation as being due to the particle shape effect. The reproducibility errors, i.e. the standard deviation of the set of realisations of an experiment, are estimated to be less than 0.3% for frictional and frictionless systems (see Table 4.2).

Influence of the particle friction Without any inter-particle friction the grains can arrange themselves into the most dense configuration. For the discs, a large majority of the grains have a crystalline structure which maximizes the packing density ($\phi_{max} = 0.9069$). In this case, the packing density is reduced by the presence of fault lines that propagate across the structure like dislocations in crystal lattices and ultimately break the symmetry of the system. The packing densities observed for elliptical particles are similarly high due to the high ordering of the structural arrangement. Despite the fact that the crystalline arrangement of the particles is enhanced by the frictionless interactions, the trend of the packing density to reduce with the particle aspect ratio (that was observed for frictional systems) is maintained. Structural defects with very elongated particles causes larger voids than rounded ones, hence the packing fraction decreases when α increases.

Influence of the particle shape at constant friction At constant friction, the solid fraction of the granular media varies as a function of the particle aspect ratio for α varying between 1 (disc) and 5 (rice grain shape). Interestingly, the packing densities obtained for

uniform discs ($\phi \approx 0.82 \pm 0.005$) can be improved by about 2% by using slightly elliptical particles. The maximum packing density is found to occur when ellipses of aspect ratios of about $\alpha = 1.6$ are used. For larger particle elongations, the volume fraction decreases approximatively linearly $\phi(\alpha) \propto 1/\alpha$. This is the same trend that was suggested to match experimental and numerical observations in 3D [156, 225]. It is important to note that for the larger aspect ratios, the coordination number has been found to keep a constant value while the packing density decreases without changing the value of the coefficient of friction. This observation is significant and suggests that very elongated particles are systematically harder to pack efficiently, unlike rounded particles that possess a better ability to cover a surface. Finally, considering that the number of contacts insuring the mechanical stability of the granular systems is constant at large aspect ratios (Fig. 4.11), we proposed that the diminution of the packing density when $\alpha > 2$ can be explained by the expansion of the excluded area per particle [225, 226].

Additional comments The comparison of the dependency of the packing density with the particle aspect ratio is comparable with those of [46] or [26] obtained from event driven molecular dynamic and Monte-Carlo simulations respectively. With molecular dynamic simulations, ellipses which are free to translate and rotate, reach an optimal packing density for $\alpha = 1.5$. A similar peak is noticed with Monte-Carlo simulations where the particle displacement is stochastically determined. However, the profile of the packing density curves differs significantly from purely geometric algorithms applied to packing of angular beams and beam with round corners of varying aspect ratios, particularly when the grains only possess a small elongation ($\alpha < 1.5$) [91]. This recent geometric packing algorithm does not produce an optimal packing density for slightly elongated systems.

Finally, the influence of polydispersity on the emergent properties of grains packing were not analysed in this work. Using a distribution of particle sizes influences greatly not only the structure of the packs and the packing density but also the coordination number of the particles. Larger particles will naturally tend to possess larger number of contacts than smaller ones. More generally, the influence of polydispersity is complex and for a complete discussion about polydispersity, the reader is referred to the books of German [64] and Cumberland [38].

4.3.2.2 Coordination number

In pseudo-static granular media, the weight and the pressure received by each grain is supported by their surrounding particles via contact points. In order to be mechanically stable, the particle needs to possess a minimum number of contacts related to their shape and their contact friction (see Table 4.4). The average number of contact points per

Table 4.3: *Reproducibility errors for the coordination numbers.* $< z >$ *is the average coordination number calculated from n realisations of the experiment with particle of aspect ratio* α *and friction* μ*.* S_z *is the standard deviation of the average coordination number.*

$\{\alpha; \mu\}$	$\{z_1; z_2; ...; z_n\}$	$< z >$	S_z
$\{1.2; 0.0\}$	$\{4.70; 4.75; 4.75; 4.70; 4.75\}$	4.73	0.03
$\{1.2; 0.5\}$	$\{3.52; 3.55; 3.54; 3.65; 3.50\}$	3.55	0.06

particle is referred to as the "coordination number". It is possible to distinguish the average coordination number, which is the total number of contacts counted in the system divided by the number of particles, from the distribution of coordination number, i.e the statistical distribution of the number of contacts per particle. The coordination number is evaluated by counting all the contacts particle/particle and particle/wall. As the deposits have a free top surface, the top layer of grains is lacking on average 1 contact as compared to a lower layer, which may causes underestimation of the overall value. We compensate this bias by adding 1 "virtual" contact to all the particles forming the upper free surface. In consequence the average coordination number can be expressed as:

$$\overline{z} = \frac{Z_{pp} * 2 + Z_{pw} + Z_{wv}}{N}, \tag{4.4}$$

where N is the total number of particles in the system, Z_{pp} is the number of particle/particle contacts, Z_{pw} is the number of particle/wall contacts, and finally Z_{wv} is the number of virtual contacts. The value of $\overline{z}$, corrected for the boundary effects, is thus theoretically equal to the coordination number calculated within the RVE.

It appears that at the final stage of the packing, at which the particles are assumed to be quasi-static, a proportion of neighbouring particles are in fact still vibrating which lead to a situation where some contacts are not constant over a period of time. "Near-contact" or "pseudo-contacts" occurs where the particles are very close but not in contact. It is likely that due to the small vibrations that occur within the grain during their dynamic relaxation, those pseudo-contacts become a "real" contact within a few time steps of computation. Over a long enough time frame, the particle in "near-contact" configuration can be assumed to be in fact a real contact. In order to evaluate the proportion of particles in this situation, the coordination number was recalculated after inflating artificially each particle by a factor $f = 1.002$ as done by [226]. Because there is only very little difference between the coordination number of the systems of non-inflated particles and inflated ones, it is possible to rely on the coordination number values obtained from the real contacts at a given time step as reported in Fig. 4.11.

The error bars have been estimated both for frictional and frictionless systems by

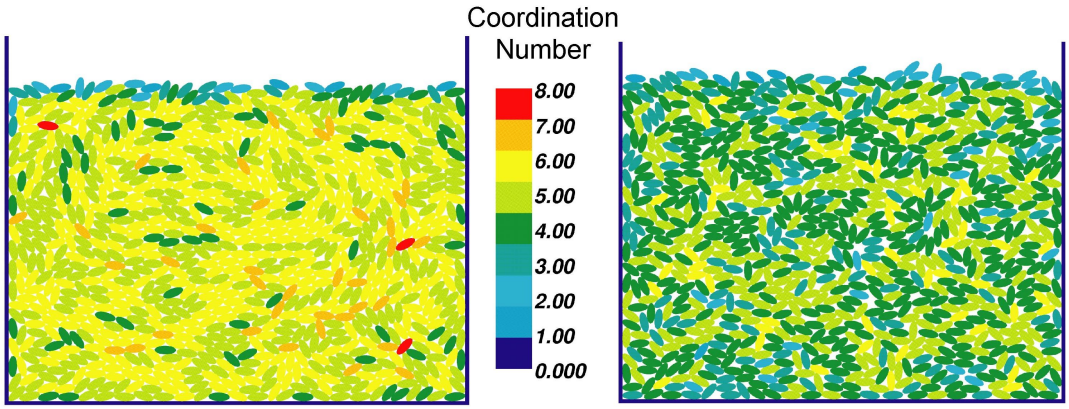


Figure 4.9: *Distribution of the number of contact per particles for a packing of ellipses of aspect ratio 2.5 for a)frictionless systems, and b) frictional ones.*

repeating each simulation five times. As mentioned above, the source of errors are essentially due to the fact that some contact are not perfectly stable over the time because of the small vibrations of the grains during their relaxation. As a result during a fragment of time the contact between two grains can be lost and recovered shortly after. This source of error is minimized by letting the system dissipate a maximum of energy. For each of the simulated systems, the average coordination numbers converges towards stable values over a long period of time (see Fig. 4.4). The standard deviation was found to be $S_z < 0.1$ for frictional particles and $S_z < 0.05$ for frictionless ones (see Table 4.3).

4.3.2.3 Distribution of the number of contacts per particle

It is interesting to consider that although the frictional systems present some kind of geometrical ordering between the particles, only a few of them possesses exactly six contacts. The situation for frictionless particles is that the majority of the particles pack into a hexagonal structure where each particle contacts with its six neighbours. The fault lines, observed for the frictionless packing propagate through ordered arrays of particles, reducing substantially but only locally the average coordination number from its theoretical value $z_{hex} = 6$ to values as low as 4 (Fig. 4.9). For elongated ellipses, it is observed that both the average coordination number and the maximum number of contact for a single ellipse is higher. Due to their geometry, ellipses can possess a maximum number of contacts that is higher than for discs, and this maximum increases with elongation. This is why in the frictionless system of Fig. 4.9 some particles attain a maximum of 8 contacts.

In the case of frictional materials, the movement of the particles becomes more limited so that less freedom is allowed for each particle to readjust its position. As a consequence, frictional particles pack systematically with a lower number of contacts

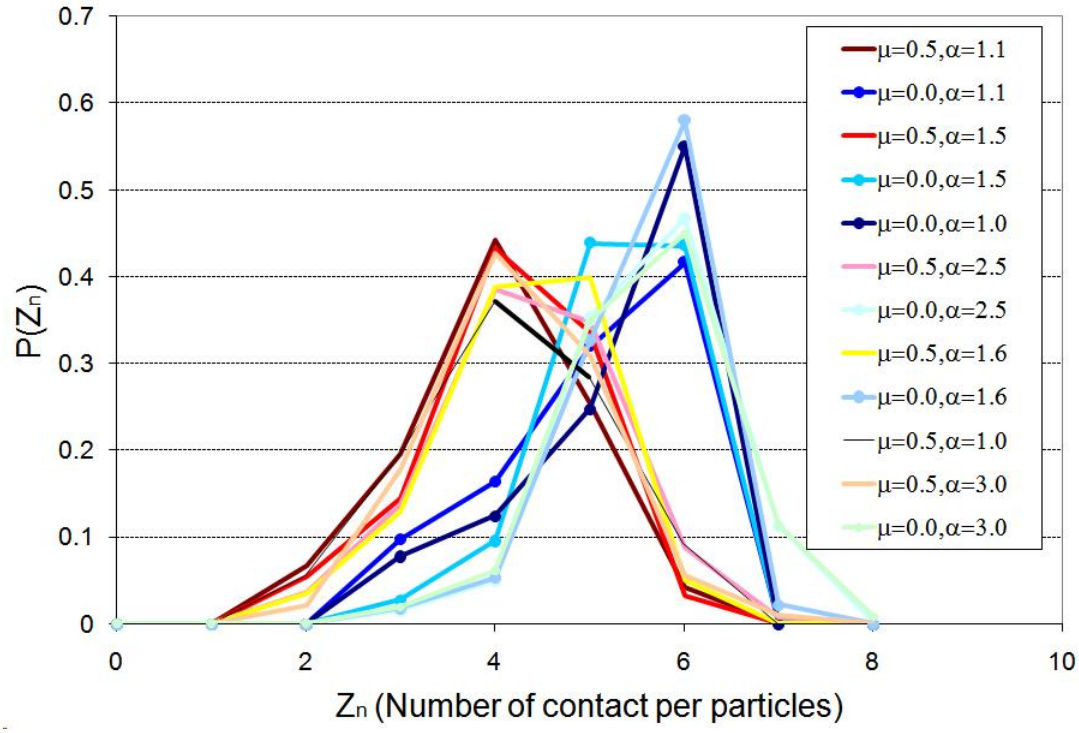


Figure 4.10: *Distribution of the number of contacts per particle, Z_n, for a packing of ellipses for frictionless systems (Cold colors) and frictional ones (Warm colors). The coordination number of ellipses of aspect ratio of $\alpha = 1.5$ has the same coordination number as frictionless disc. These two systems are compared in terms of stress distribution in the Chapter 5.*

than their frictionless equivalents. Additionally, the frictional system seems to be less ordered which results in a wider distribution range of coordination number. While the most probable number of contacts of the frictionless system is usually 6 (independently of the particle elongation), a frictional particle is likely to have either 3 or 4 contacts.

4.3.2.4 Average coordination number

Consider first the frictionless case (red squares in Fig. 4.8 and Fig. 4.11). The packs built with an aspect ratio lower than $\alpha = 1.6$ posses a reasonably constant packing density of $88.3 \pm 0.5\%$ while an increasing coordination number evolves in accordance with an increasing α until reaching a plateau for the largest aspect ratios ($\alpha > 1.8$). The packing fraction of the systems with low aspect ratios have values only 2% below the maximum packing density observed for hexagonal structures. This slight difference is caused by the propagation of defects, perturbing the geometry of the pile of grains, generated from the wall of the container and that propagate through the grain packs. It is worth pointing out the presence of clusters with crystalline arrangement where the system locally reaches maximum possible packing density (Fig. 4.5a). For large aspect ratios ($\alpha > 1.8$), the packing efficiency decreases and the coordination number of the system remains constant ($\overline{z} \approx 5.5$) with the volume fraction dropping to values of about $86\% \pm 0.5$ at $\alpha = 5.0$. Note

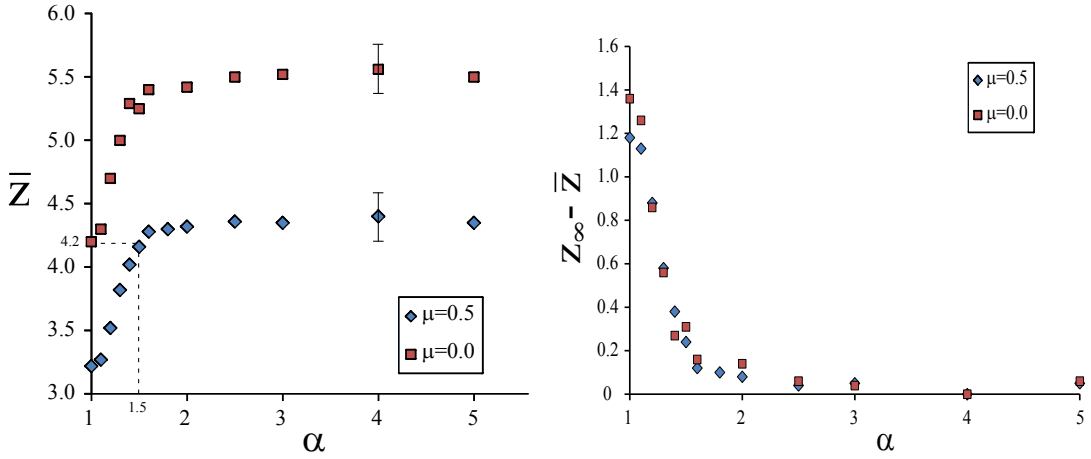


Figure 4.11: *Left) Evolution of the coordination number with the aspect ratio of the ellipses for both frictionless (red squares) and frictional systems (blue diamonds). Right) The evolution of the coordination number towards its limiting value is shown by plotting* $z_\infty - \overline{z}(t)$ *vs.* α.

also that the development of defects or fault lines for the systems comprising the most elongated particles is not observed in contrast to the disc case.

For the case with friction, as expected, the packs are less dense with a lower coordination number. At low aspect ratio the packing density increases and reaches a well defined peak (Fig. 4.8) representing the most efficient packing when $\alpha \approx 1.6$. Considering the uncertainties due to the reproducibility of the system, the maximum packing density lies probably within the range of aspect ratios $\alpha = 1.4 - 1.8$ although larger number of particles would be required for the precise determination of the aspect ratio that optimize the packing fraction. The increase in packing density is associated with a rise in coordination number. Above this threshold value, the packing density drops linearly with α to values lower than 78% while the coordination number stabilizes at around $\overline{z} = 4.3$. Such a dependence was observed in 3D systems with ellipsoids using various types of numerical approaches [45, 226], but this is the first statement of this type for monodisperse assemblies of ellipses. The rigorous method used here for 2D lends support to the fact that the interpretation of 2D results is qualitatively valid to explain the observed 3D phenomena.

4.3.2.5 Discussion

To reach mechanical equilibrium, a granular system requires a minimum number of contacts, related theoretically to the total number of degrees of freedom of the system that need to be satisfied. For frictionless systems, the isostatic conjecture [45, 184] states that the average coordination number per particle is given by $\overline{z} = 2d$ ($d = 2$ for discs, and $d = 3$ for ellipses). Similarly, $\overline{z} = d + 1$ when the friction plays an active role between the particles. The relationship that exists between coordination number, particle shape and

Table 4.4: *Summary of the theoretical [184, 45] and experimental results for $\overline{z}$ in 2D. Note that values are only reported for discs and ellipses with large aspect ratios.*

	frictionless ($\mu = 0.0$)		frictional ($\mu = 0.5$)	
shape	theory	results	theory	results
discs ($d = 2$)	$\overline{z} = 2d = 4$ ($\alpha = 1$)	4.2	$\overline{z} = d + 1 = 3$	3.2 ($\alpha = 1$)
ellipses ($d = 3$)	$\overline{z} = 2d = 6$ ($\alpha \to \infty$)	5.5	$\overline{z} = d + 1 = 4$	4.3 ($\alpha \to \infty$)

friction, evaluated from the simulations, is reported in Fig. 4.11. The simulation results are in agreement with the theoretical expectations, which suggests that the isostatic limit of the coordination number for frictional discs is close to $\overline{z} = 3$ and that one more contact is needed to balance the frictionless systems. However, the simulation results (see Fig. 4.11 and table 4.4) diverge significantly from the theoretical expectation in the limit case of very small aspect ratios $1 < \alpha \leq 2$. With slightly elongated shapes, the final coordination number expected theoretically is $\overline{z} = 4$ and $\overline{z} = 6$ for frictional and frictionless systems respectively. In the limit case of small aspect ratios, theoretical arguments over-predicts the coordination number of frictionless grains and isostaticity is unappropriated. This gap is fill up gradually as $\overline{z}$ increased when α departs from unity and reach a constant value $\overline{z} = 5.5$ for $\alpha > 2$. The results of the Fig. 4.11 shows that the average coordination number becomes constant when $\alpha \geq 2$ both for frictional and frictionless cases. Furthermore, the Fig. 4.11b shows that the limiting value of the coordination number is approached in a similar manner, suggesting that the shape affects the coordination number in a similar way, independently of the friction coefficient.

Additionally, it is relevant to mention that the difference of coordination number of a frictional and a frictionless system at a given aspect ratio is constant and equal to a value between 1 and 1.2 although the isostaticity rules requires 2 more contacts with frictionless ellipses compared to frictional ones. Although the isostatic conjecture provides a good estimate of the coordination number of frictional systems, it overestimates the coordination number of frictionless packs of monodisperse ellipses (Table 4.4). Indeed, six contacts per ellipse is an upper limit which corresponds to the particular case of crystalline packs when no defects propagate.

4.4 Structure characterisation with particle correlation functions

4.4.1 Radial distribution function

While the coordination number or the packing density are emergent properties that characterize the packing at large scale, the presence of translational order between the particles constituting the packing can also be analysed by using correlation functions [55, 133, 194]. The high packing density obtained suggests the possibility of spatial correlations between the grains. Clearly, we have demonstrated that the solid fraction of a static pile of grains is a function of the grain aspect ratio and that the presence of friction, by hampering the grain's motion, systematically produced lower packing density. The visual analysis of the final structure shown on Fig. 4.5a-d) of both frictionless and frictional systems suggest the presence of order between the particles. In the absence of friction, the motion between the grains is encouraged, producing systems close to the dense packed limit, with a high degree of ordering between the grains. On the contrary, frictional particles pack less efficiently and it is visually harder to detect the presence of spatial correlations between the grains.

To calculate the radial distribution function, the positions of a grain centres provide a primary data set that can be used to quantify the degree of correlation of each grain with its neighbours. The RDF is define as follows [133]:

$$g(r) = \frac{1}{N n_0 \pi r} \sum_{k=1}^{N} \sum_{l=k+1}^{N} \delta(r_{kl} - r), \tag{4.5}$$

where, N is the total number of particle, n_0 is the average density of points and r_{kl} is the distance between the center of the particles k and l. The particle positions are given by their centres of mass. The kroenecker symbol $\delta(r)$ is defined as follows:

$$\begin{cases} \delta(r) = 0 \text{ if } r \neq 0, \\ \delta(r) = 1 \text{ if } r = 0 \end{cases} \tag{4.6}$$

The RDF may be thought as the probability that a particle is surrounded by another one within a distance r and $r + dr$. This function is thus particularly adapted for highlighting periodicity of the structure. For a random packing, the position of a particle should theoretically be completely uncorrelated from the position of other particles in the pack that are separated by more than a few diameters. Over small distances (typically less than 5 diameters) the systems described in this research present some structural

Table 4.5: *Distance between first neighbour for ordered (hexagonal packing) for 2 monodisperse systems with varying aspect ratios. The indices $< ij >_\alpha$ designates the location of the i neighbour in direction j for a monodisperse system of ellipses with aspect ratio α. To keep simple notations, each distinct direction is given by an integer value. The distance are expressed as a function of b, the ellipses short axis*

$\alpha = 1.0$		$\alpha = 1.2$, CP1		$\alpha = 1.2$, CP2	
neighbour	Distance (in b)	neighbour	Distance (in b)	neighbour	Distance (in b)
$< 10 >_{1.0}$	1.00	$< 10 >_{CP1}$	1.00	$< 10 >_{CP2}$	1.05
$< 11 >_{1.0}$	1.73	$< 11 >_{CP1}$	1.15	$< 11 >_{CP2}$	1.20
$< 20 >_{1.0}$	2.00	$< 12 >_{CP1}$	1.83	$< 12 >_{CP2}$	1.74
$< 12 >_{1.0}$	2.65	$< 20 >_{CP1}$	2.00	$< 13 >_{CP2}$	1.98
$< 30 >_{1.0}$	3.00	$< 13 >_{CP1}$	2.08	$< 20 >_{CP2}$	2.10
$< 21 >_{1.0}$	3.46	$< 21 >_{CP1}$	2.30	$< 21 >_{CP2}$	2.40

correlations disappearing after a few particle lengths. The distance ξ_s, which gives the limiting range of the spatial correlation between the grains, denotes the typical correlation length of the system and is expressed in particle diameters. In this work the influence of two parameters has been addressed, firstly the effect of the coefficient of friction between the grains and secondly the aspect ratio of the particles.

4.4.1.1 Effect of the inter-particle friction and aspect ratio on the RDF

The presence of friction between the grains has a large influence on the structural [32, 121, 19] and mechanical [68, 97] properties of the granular media as it controls the nature of the contact interactions. Quantitatively, it has been explained in section 4.3.2 that the presence of friction reduces significantly not only the packing density but also the average coordination number of the systems at equilibrium. Furthermore, a system built with particles interacting with friction changes the spatial configuration of its grains, generating more pores and increasing the average distance between neighboring particles. Unlike frictional systems, frictionless packs tend to be naturally arranged into ordered states as suggested by their higher packing density values (Section 4.3.2). For instance, with frictionless discs, hexagonal-close packed (HCP) structures are clearly identified as predominant in the system, and are only disrupted by the presence of walls [66, 71].

The theoretical distance separating the center of neighbouring frictionless grains $< ij >$, where i designates the position of the i neighbour in the direction j, in hexagonal packing is summarised in Table 4.5 for values of α, $\alpha = 1.0$ and $\alpha = 1.2$. For the ellipses, two packing configurations $CP1$ and $CP2$, illustrated in Fig. 4.13, are given. The direction $j = 1$ is given by the direction in which the first neighbour is found, $j = 2$ indicates the direction in which the second nearest neighbour is pointing, and $j = n$ the directions of the n^{th} nearest neighbour. In the case of discs, the values reported in Table 4.5 match with

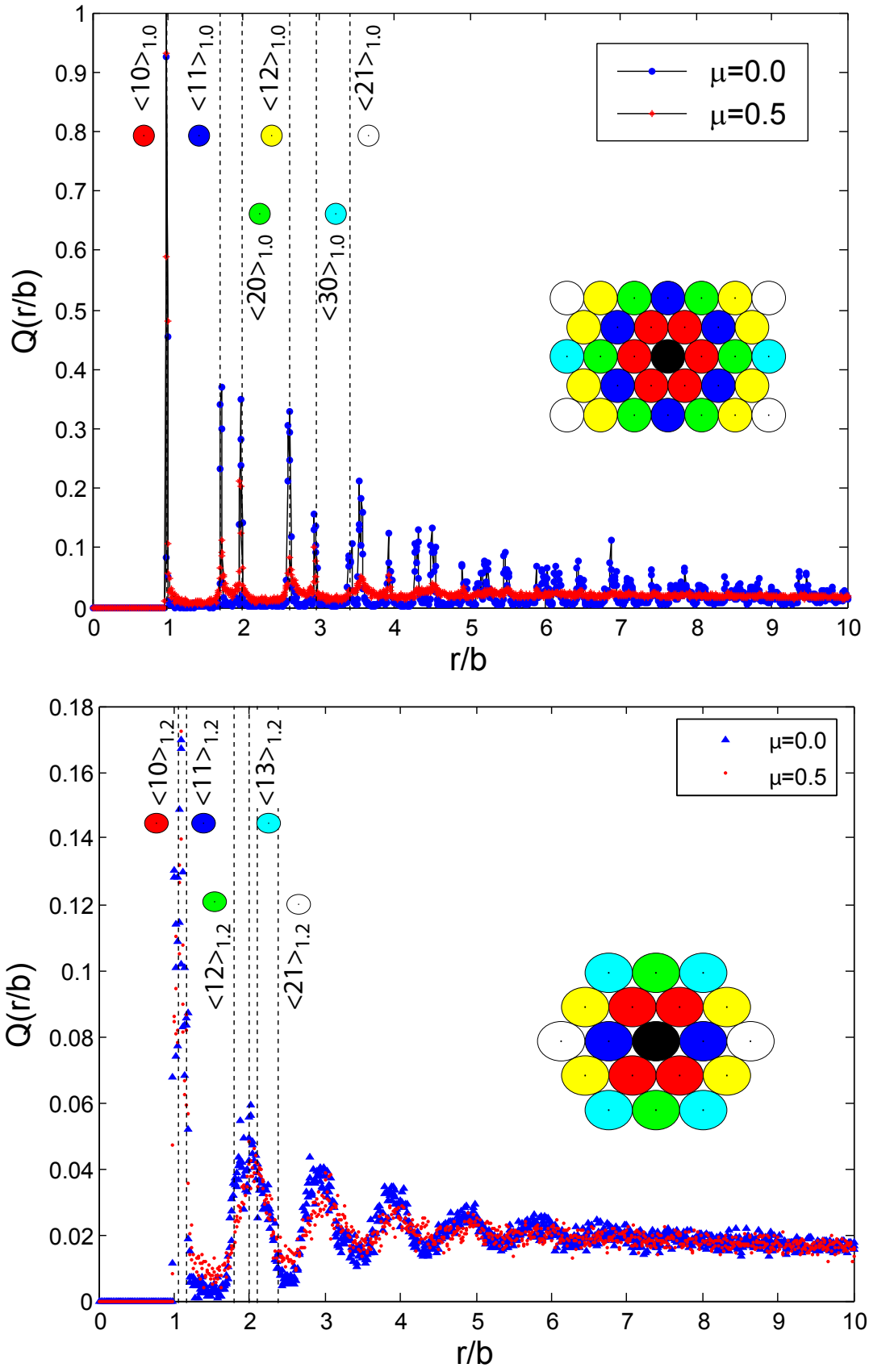


Figure 4.12: *Radial distribution function of a packing composed of rounded particles (aspect ratio of $\alpha = 1.0$ (Top) and $\alpha = 1.2$ (Bottom)). Blue colors (• and ▲) are indicating $g(r)$ for particles without friction and red colors ($*$ and .) correspond to particles interacting with a coefficient of friction $\mu = 0.5$. The inset plots show the geometry of idealised dense packed systems and the color key used to identify the peaks. Vertical lines indicate the distances between points separated in an hexagonal lattice.*

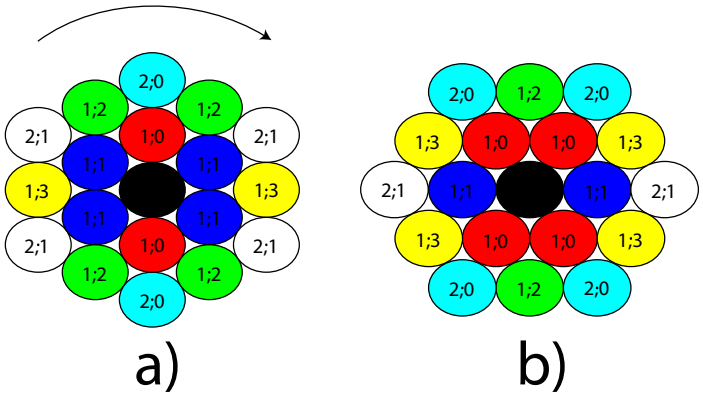


Figure 4.13: *Random close packing of ellipses. There exists several configurations of close packing for ellipses. The pack in a) is called CP1 and in b) CP2. Both packs are in a close configuration but as indicated by the colour scheme, the nearest neighbour configuration differs, which has consequences for the radial distribution function.*

the position of the correlation peaks observed (see Fig. 4.12a), which confirms that 2D systems of discs are unstable and that they naturally crystallise. However, it is possible to remove most of the crystallisation simply by using frictional particles. With friction the typical translational correlation length is observed to be about 6 times the short ellipse axis, $\xi \approx 6b$, which is significantly lower than when $\mu = 0.0$ ($\xi_s > 10b$). The translational correlations are reduced further when using elliptical particles. In particular, with ellipses of very small aspect ratios (see Fig. 4.12b), hexagonal packing is not observed and the correlation peaks becomes gradually diffused with elongated particles. With frictionless packing of ellipses the ideal HCP structure is not reached and the translational correlation completely disappears at $\xi_s \approx 8b$, which is significantly lower than for the case of discs.

Fig. 4.13 shows that with a simple uniform system of ellipses, the pack can reach a maximally dense configuration with two distinct neighbours positions. The distance of the first nearest neighbours for $\alpha = 1.2$ is reported in Table 4.5. The correlation function applied to a system of ellipses (Fig. 4.15 and Fig. 4.14) shows diffuse peaks around the expected values of near neighbours, unlike discs. This is due to the fact that in its dense configuration, the nearest neighbours of ellipses are likely to stand within a window of values rather than at an exact distance as for discs. For example, in the configuration CP1, $< 20 >_{CP1} = 2.00b$ while $< 20 >_{CP2} = 2.10b$ in the configuration CP2. In the elliptical packing we observe that with frictionless particles, an infinitesimal disorder of the ellipses (caused for instance by the walls), results in some small rotations of the ellipses and in a close packing state, CP, $< 20 >_{CP}$ can take any value between $2.00b$ while $2.10b$. For very elongated ellipses, the same phenomenon also occurs, but the correlation peaks become so diffuse that no peak can be observed (see Fig. 4.14 and Fig. 4.15).

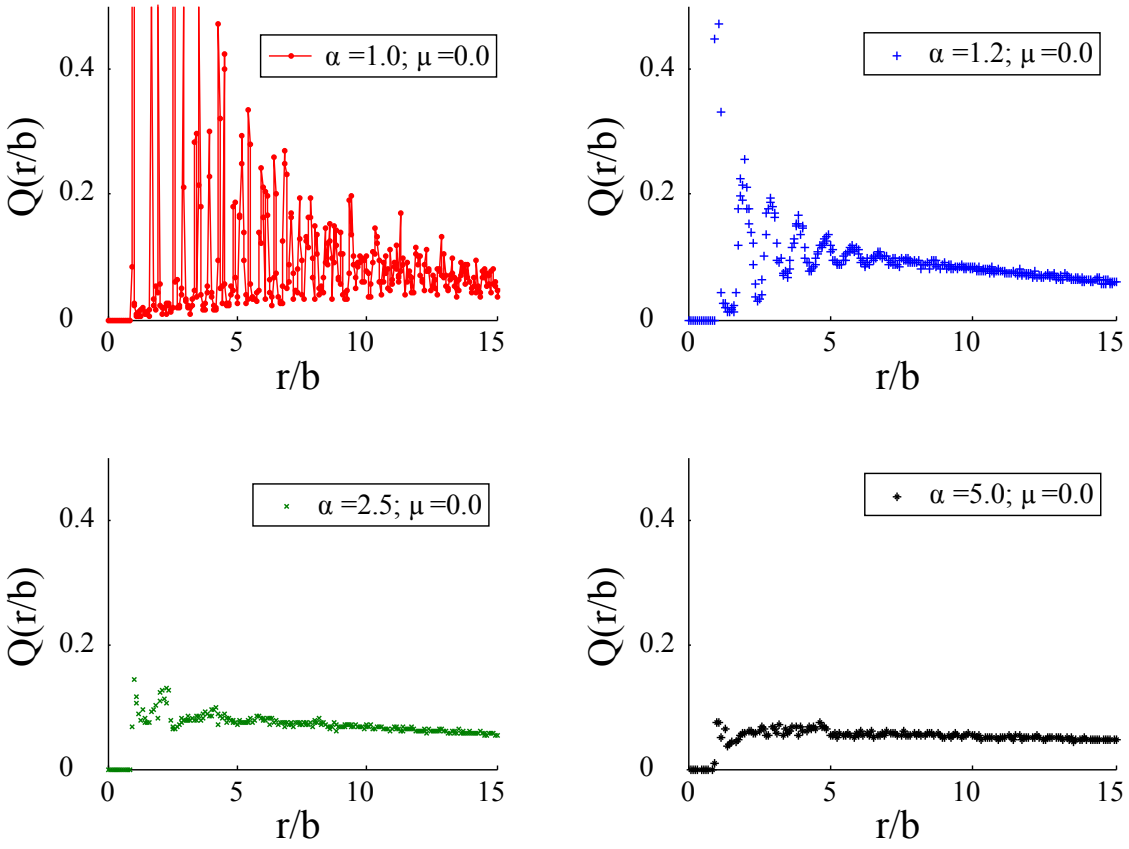


Figure 4.14: *Radial distribution function of frictionless system of particles with varying aspect ratios ($\alpha = 1.0$ (top left), $\alpha = 1.2$ (top right), $\alpha = 2.5$ (bottom left), $\alpha = 5.0$ (bottom right)). It is important to point out the dispersion of the correlation peaks with ellipses when $\alpha = 1.2$. For larger aspect ratios, the correlation peaks become attenuated and diffused that RDF is no longer useful to detect the presence of ordered structure.*

4.4.1.2 Discussion

Both the shape of the correlation function and the typical correlation lengths are functions of the presence of friction within the system. For each of the particle shapes reported in Fig.4.14 and Fig.4.15, the amplitude of the correlation peaks detected by the RDF is attenuated when friction is active. Consequently the distance ξ_s, expressed in short particle diameter, at which the correlation peaks disappear is systematically shorter for frictional particles than for frictionless ones. This confirms in particular that, in two dimensional systems, the particles ordering into honeycomb-like periodic structures is noticeably reduced. If discs only are considered, the correlation length drops from $\xi_s > 10r_g$ in the case of frictionless particles to $\xi \approx 6r_g$ for frictional particles. Similar conclusions can also be drawn for elongated particles.

At constant friction, the particle shape has a considerable effect on the RDF. The correlations peaks clearly observed for circular particles becomes gradually more diffused

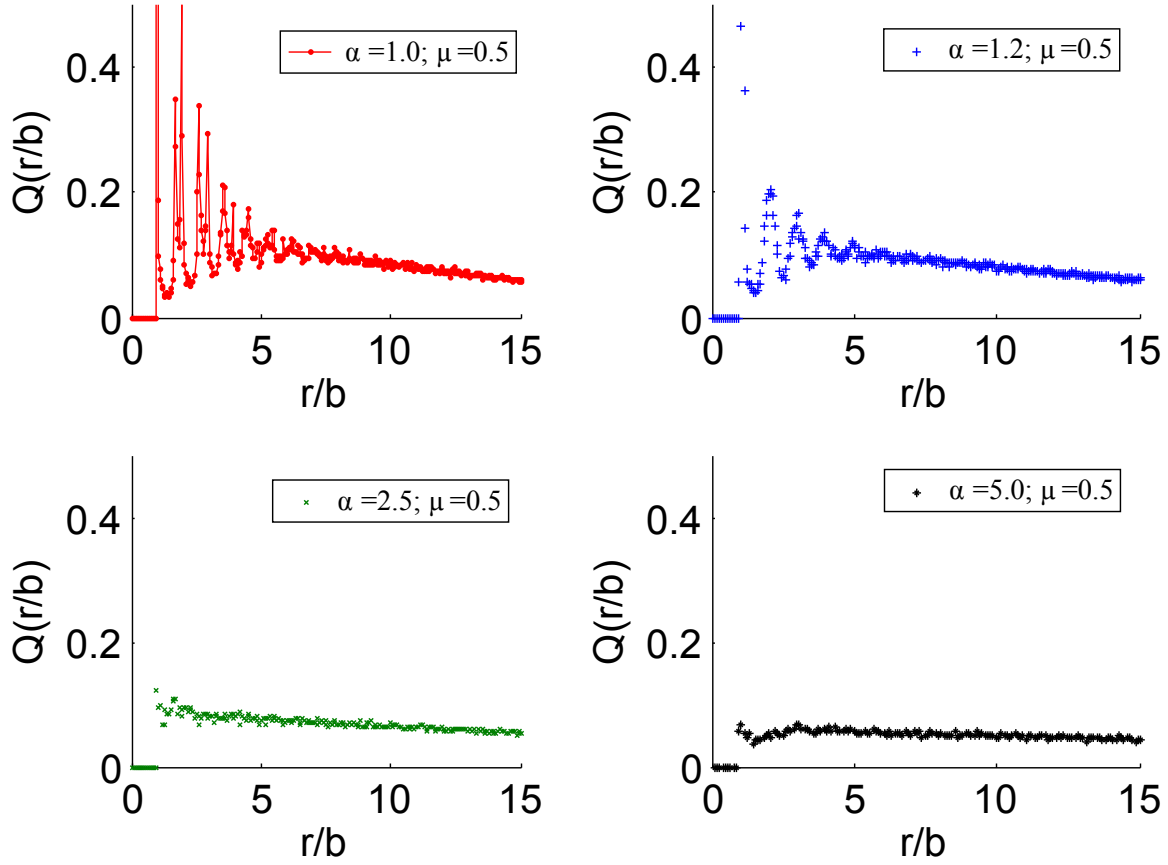


Figure 4.15: *Radial distribution function of frictional ($\mu = 0.5$) system of particles with varying aspect ratios ($\alpha = 1.0$ (top left), $\alpha = 1.2$ (top right), $\alpha = 2.5$ (bottom left), $\alpha = 5.0$ (bottom right)).*

with a smaller amplitude as the eccentricity of the ellipses is increased. The correlation peaks vanishes when α becomes large such that elongated grains appear to be radially uncorrelated. Omitting to take into consideration the rotational ordering would mean that ellipses, in contrast to discs, permits the creation of amorphous structures in the sense that very little crystallisation occurs. However, the RDF is relatively ineffective at characterising the structure of ellipse packs as it does not explicitly take into account their rotational degree of freedom. This consideration suggests that in the case of ellipses, a complete analysis of the ordering within the structure has to consider the orientational correlation between grains. The characterisation of the orientational ordering is treated in the following section.

4.4.2 Characterization of the particle orientation

Whereas the spatial correlation between discs and spheres can be analysed with the RDF, it has been seen that correlation lengths are hardly identifiable in packs of ellipses, particularly those with very elongated particles. However, there are alternative measures.

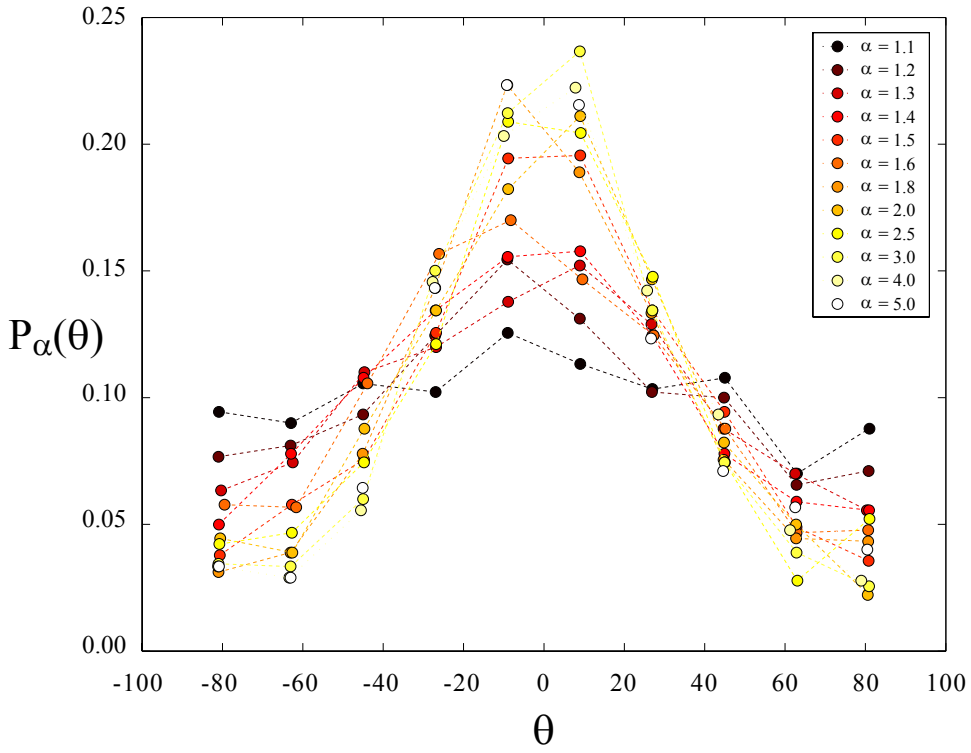


Figure 4.16: *Orientational distribution of particles within a packing made of ellipses with increasing aspect ratios* ($1 < \alpha < 5$).

It is for instance possible to use the additional degree of freedom of the ellipses to give a measure of the ordering of the system. Although elliptical particles are allowed to settle with a random orientation, the action of the external gravity field imposes preferential direction of settlement of the particles. This spatial ordering can be characterised by performing statistical analysis of the particle orientation.

The particles orientation can be evaluated in different ways. Firstly, the angular distribution of the ellipses provides a visual estimate of the preferential direction in which particles are pointing. In addition, the non-uniformity of the distribution angle can also be quantified using the orientational order parameter [197, 26], which can in fact be viewed as a scalar measure of the orientational ordering of the granular media. Finally in order to measure the level of correlation that persists between the particles, we define the orientational correlation function. This function, similar to the RDF, is more suitable to characterise the presence of structural correlations within elongated systems and it permits in particular the identification of clusters of particles with similar orientation.

4.4.2.1 Orientational distribution

As mentioned in Chapter 2, the arrangement of the particles in a container filled by a collective deposition technique is never completely random. For instance, a granular media

composed of discs possess a structural anisotropy that is related to the orientation of the gravitational field [10]. For elongated particles such an anisotropy is also observable and particles are oriented along preferential directions. Experimental studies and Monte-Carlo simulations of 2D packings of non-spherical particles show that the presence of orientational anisotropy of the grains also appears to be a characteristic feature [197, 26]. The global indication of the orientational ordering is given by the angular distribution of the ellipses.

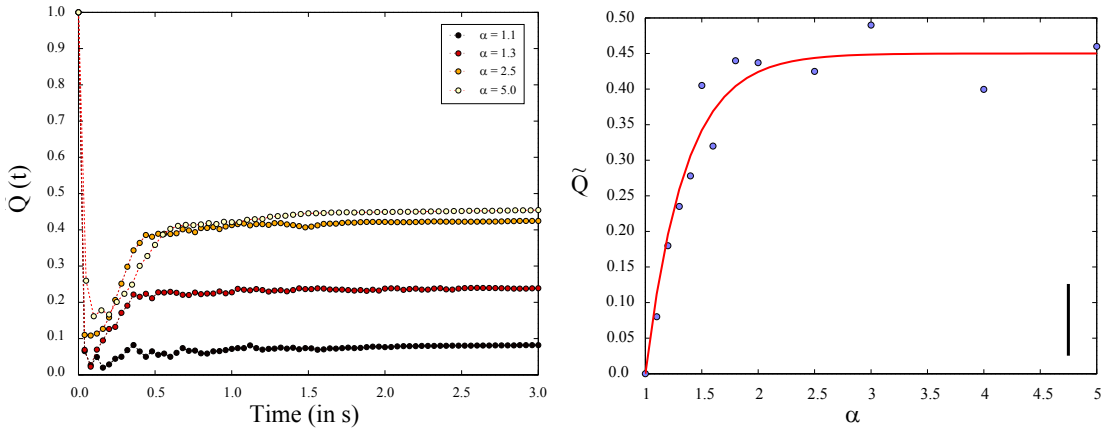
The angular distribution $P_\alpha(\theta)$ of the ellipses was measured for each simulated aspect ratio. The angle θ, is the angle between the ellipse long axis and the horizontal direction. θ varies between $-90°$ and $90°$. Fig.4.16 shows that the function $P_\alpha(\theta)$ confirms that elongated particles repose preferentially horizontally inside the container while the most rounded grains are typically more randomly oriented. For the most elongated shapes ($\alpha > 2.0$), the shape of the angular distribution curve is independent of the aspect ratios and the functions $P_\alpha(\theta)$ are superimposed for $\alpha > 2.0$. This suggests that the angular anisotropy created during the settlement of the particles is clearly a function of the particle shape when considering rounded particles. However, the orientational anisotropy saturates above a critical value of ellipse eccentricities, and this saturation threshold can be identified around $\alpha = 2.0$. To confirm this phenomena, a scalar quantity, the orientational order parameter, is introduced in the following section.

4.4.2.2 Orientational order parameter (OOP)

As shown in the previous section, it is clear that the particle orientations are a function of their aspect ratio. Interestingly, it appears that the particle orientation in a packing of elliptical particles present two types of correlation: 1) when considering the whole system of particles, the orientational anisotropy is caused by the collective deposition technique coupled with the presence of the gravity field so that on average each particle's orientation is correlated with the direction of this field; 2) presence of orientational correlations between neighboring particles confirmed by the visual representation of the system which suggests that elongated ellipses are more likely to form clusters of aligned particles than packs of rounded grains. To quantify the importance of the global orientational disorder in the whole medium, a scalar parameter, the OOP (sometimes known as nematic order), is introduced and defined as follows:

$$OOP = \widetilde{Q} = \frac{1}{N}\sum_{i=1}^{N}\cos(2\theta_i), \tag{4.7}$$

where N is the total number of particles and θ_i is the angle between the long axis of the i^{th} particle and the horizontal unit vector $\overrightarrow{n}$. The OOP can be taken as a complementary



(a) (b)

Figure 4.17: *a) Temporal evolution of the orientational order parameter during the deposition process for four different aspect ratios ($\alpha = 1.1, 1.3, 2.5, 5.0$). It is worth mentioning that in the early stage of the deposition, the OOP goes to 0, confirming the efficiency of the particle mixing phase. It then tends towards a steady value while the ellipses stabilize in their final position. We call Q_∞ the value of the OOP when the time tends to infinity. b) Evolution of the final orientational order parameter Q_∞ as a function of the particle aspect ratio. One can see rapid rise of $Q_\infty(\alpha)$ at low aspect ratios and the stagnation of Q_∞ when $\alpha > 2$ which suggest that above $\alpha = 2$, the system reach of maximal amount of orientational correlation. The vertical thick black line is the estimated error and the fitting red line is only a guide.*

measurement to the angular distribution of the particles. The scalar nature of the OOP provides subsequently a simple tool for comparison of the global amount of orientational disorder in each system. The OOP varies between -1 and 1, when the particles are perfectly ordered (all the particles possess the same orientation), and take a value near 0 when the particles are completely uncorrelated. Considering a perfectly randomly generated medium, where the distribution of orientation θ_i of the ellipses is symmetrical and uniform, $\cos(2\theta_i)$ can take any values between -1 and 1 and $\widetilde{Q}$ is theoretically centered around 0.

At the beginning of the deposition, the system is first randomised and $\widetilde{Q}(t)$ takes values close to 0 (Fig. 4.17a). During the packing process, some ordering between the elliptical grains is generated and after a finite amount of time, corresponding to the final spatial configuration of the packing, $\widetilde{Q}(t)$ stabilizes at a level that gives an estimate of the orientational disorder (see 4.17a). Fig.4.17b illustrates the growth of the orientational order parameter with increasing aspect ratio α, which emphasizes that, elongated particles, unlike the rounded ones, possesses a strong tendency to rest horizontally. However, above a critical aspect ratio $\alpha \approx 2$, the OOD saturates at $\widetilde{Q}(t) \approx 0.45$, in reasonable agreement with the limit values of 0.4 found by [26] and similar to [197] observed for very large aspect ratios. This latest observation further confirms the statement expounded in the previous section that elongated particles cannot exceed a maximum amount of ordering when deposited randomly.

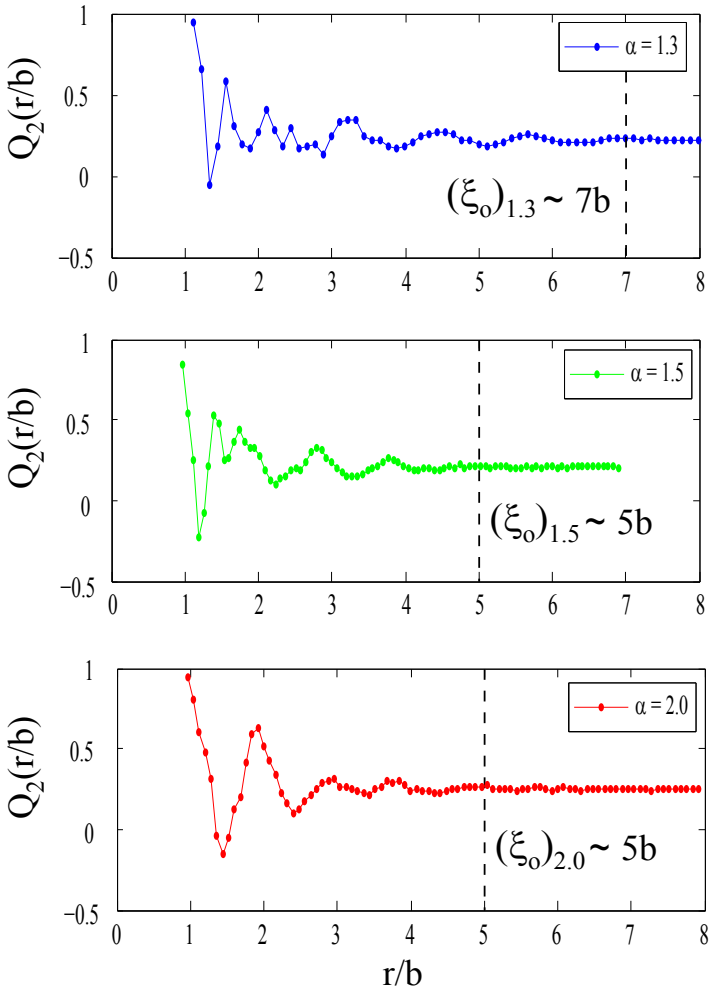


Figure 4.18: *Angular correlation between ellipses with different aspect ratios,* $\alpha = 1.3$, $\alpha = 1.5$ *and* $\alpha = 2.0$ *(*$\mu = 0.5$*).*

The quantification of the orientational ordering is shown to be strongly related to the particle shape. In the next section, the range of influence, in terms of ordering, specific to each particles aspect ratio is analysed by the mean of the radial orientational correlation function. This function permits the determination of correlation length, which characterises the size of clusters of ordered ellipses.

4.4.2.3 Radial orientational correlation function (OCF)

As demonstrated in the previous subsection elongated particles settled by gravitation into a container possess an orientation correlated with the direction of the gravity field. Elongated particles tend to stabilize preferentially with their long axis along horizontal. This phenomena becomes increasingly important with the particle elongation and saturates when $\alpha > 2$. Additionally, a visual analysis of the structure of the packing suggests that neighboring particles are likely to align with each other. This alignment can be quantified

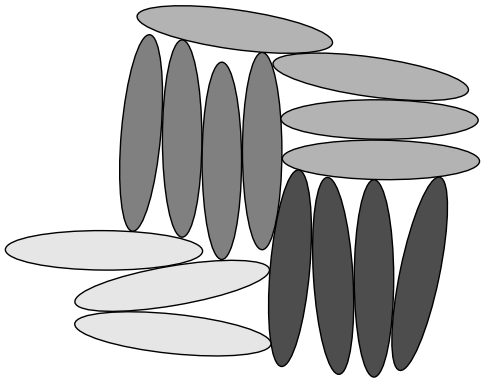


Figure 4.19: *Scheme of the typical clusters form with elongated particles of large aspect ratios.*

with an orientational correlation function defined as follows:

$$Q_l(r) = \frac{\sum_{k=1}^{N}\sum_{l=k+1}^{N}\delta(r_{kl}-r)\cos(l(\theta_i)-\theta_j)}{\sum_{k=1}^{N}\sum_{l=k+1}^{N}\delta(r_{kl}-r)}. \tag{4.8}$$

This function is a measure of the angular correlation between the particles as a function of the distance separating the particles. By extension, the OCF also permits an estimation of the typical orientational correlation length, ξ_o, the distance at which variations of $Q_l(r)$ no longer exist. Here we use the second order so that $l = 2$.

The orientational correlation function was applied to several systems of elliptical particles, elongated and rounded, interacting with or without friction. The distance at which the particle is no longer correlated ξ_o, expressed in terms of b the ellipse's short axis, is reported in Fig.4.18. This shows that although elongated particles have no radial correlations, the packing are in fact not amorphous because of the angular correlation between particles persisting over 5 to 7 particles. This also underlines that elongated particles are likely to form clusters typically comprising 5 particles aligned in the same direction and connected along their short axes (see Fig. 4.19). Although the orientational anisotropy of the rounded particles is hardly noticeable on the packing snapshots of Fig.4.5, the variation of the function $Q_2(r/b)$ demonstrates that angular correlation spans over long distances even with rounded particles. This analysis shows that elongated ellipses have shorter orientational order compared to the rounded ones, which seems in contradiction to the first impression in Fig.4.5. This is a the consequence of the fact that elongated particles can only be ordered along their short axis for mechanical stability, and the distance $\xi_o \approx 5$ observed for very elongated ellipses, at which short range correlation can no longer be distinguished from the long range ones, gives a measure of their cluster size. As suggested by the larger amplitude of the variations of the OCF for the elongated ellipses (see Fig. 4.18), ellipses with large aspect ratios are more ordered at short length scale than the rounded particles. Nevertheless the correlation disappears faster than for

rounded bodies and disappear after shorter distances (about 5 short axes of lengths). We proposed that the clusters consists of few elongated particles, typically 3 or 4 as indicated by the orientational distribution function. Together, they support more efficiently the loads imposed by the particles. In other words, systems of elongated particles can be viewed as a collection of clusters of a few ordered elongated particles, and each of these cluster are mechanically equivalent to a larger rounded particle. The orientation between neighbouring clusters is rather random because of their rounded nature (see Fig.4.19) and this resulting structure is more effective at sustaining the weight of the overlying grains than a completely random configuration.

4.4.2.4 Conclusion

The information provided by the angular orientation of the particles emphasises the fact that the ellipses are not packed completely randomly. The orientation of the particles appears to be controlled by the direction of the external force field in which the particles are deposited. Our results show that ellipses tend to lie preferentially naturally with their long axis in the horizontal direction, which is geometrically their most stable position. We also demonstrate that the self-orientation of the particles is highly sensitive to their aspect ratio. Very rounded particles exhibits a highly random particle orientation, which gradually disappears at large aspect ratio. It is shown that for $\alpha > 2$, the orientational order parameter remains constant.

However, the orientation of the ellipses is highly correlated to its neighboring particles as two neighboring particles are likely to have a very similar orientation. At a longer range, the particle correlation is lost as a consequence of the global geometrical disorder present in the particle assembly.

Finally, the collective sedimentation technique is therefore not adapted to generate packs of elongated particles exempt of any orientational or translational correlations, although rounded grains tend to show few signs of large scale ordering. To perform the mixing more efficiently, other strategies should be employed such as the specific packing algorithm of [45].

4.4.3 Statistical analysis of the pore space

The structure of a granular system can be analysed from the solid side, by analysing different types of spatial correlations between particles as explained in the previous part of this chapter. However, the characterisation of the interstitial space between the particles, the pore space, has a particular relevance as it represents a significant proportion of the total volume of the system. This empty space is complementary to the material space

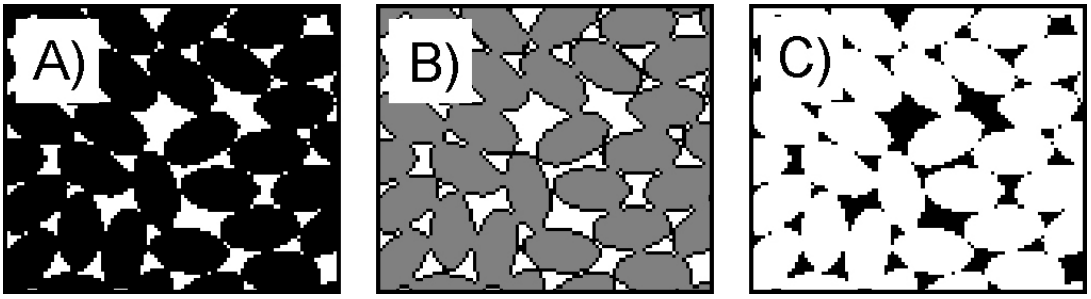


Figure 4.20: *Extraction of the particle outline using an image analysis software. a) Original binary picture of the particles and associated pores b) Extraction of the particle outlines. c) Determination of the pore characteristics by analysis of the size distribution of the black areas (pores).*

constituted by the particles. In particular, the pore size and subsequently the pore space is very sensitive to the global disorder within the granular media. A network of particles perfectly arranged along a regular lattice results in a unique pore size value while a very random packing produces pores of various sizes. In contrast to three-dimensional systems for which the pore structure has proven to be extremely complex to describe due to the lack of geometric delimitations, the statistical analysis of the pores in a two-dimensional system is easier to analyse. The aims of this section are 1) to identify if a particular pore size distribution can characterize a granular packing, and 2) to understand the influence of the elliptical particles on the pore distribution. The present work was motivated by the fact that the characterisation of the pore space of 3D media has crucial importance in many industrial context such as the oil industry, where the characterisation of the pore space and the pore connectivity has a strong economic importance. By comparison to 3D media, 2D granular systems produces pore structures that can be simply analysed. To some extent, the characterisation of these systems could improve our understanding of 3D media. However, a linkage between 2D and 3D pore characteristics is a very wide and open research topic that falls outside the scope of this thesis and it will not be treated here.

4.4.3.1 Method

An image analysis of the packed particle can be regarded as a technique of interest for extracting qualitative information characterising the pore space. We choose to use the free software "image J" for windows[1] that will allow a simple image treatment in order to recover the distribution of the pores sizes. The analysis is processed by firstly providing an image of the packing for which the solid particles are displayed in black color while the pore space is colored in white, producing a binary input. Among the image analysis tools

[1] http://rsb.info.nih.gov/ij

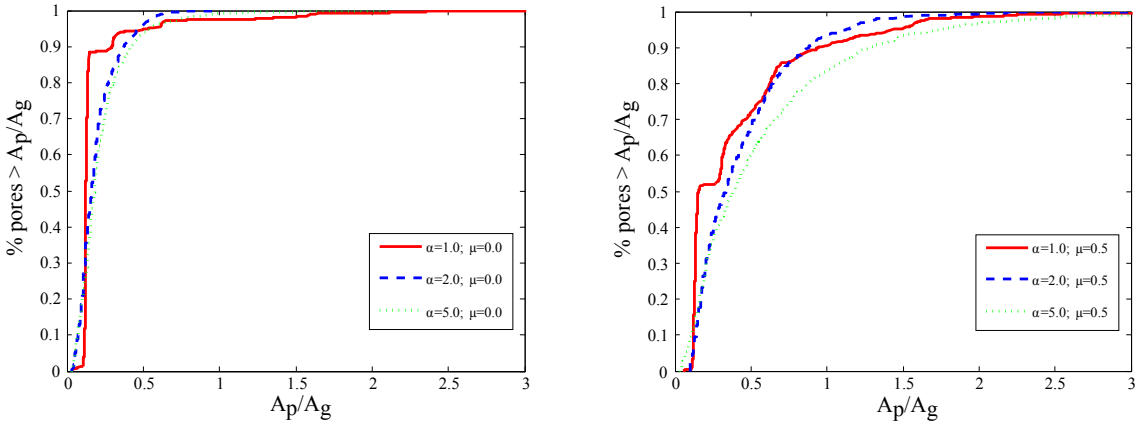


Figure 4.21: *Dependance of the pores size cumulative distribution function with the particle aspect ratio. a) for frictionless systems and b) for frictional ones ($\mu = 0.5$), as generated in the simulations described in this chapter.*

provided with the "ImageJ" software, the possibility to isolate the particle outlines from their background is offered. This treatment is used to detect the borders of the pores and thus to identify the pores and their respective sizes. The data are then exported and post-processed to see the influence of the particle shape on the pore size distribution of 2D granular systems made of dry, cohesionless granular particles.

4.4.3.2 Results and discussion

Distribution functions were used to demonstrate the large differences of the pores sizes encountered for the different systems. Fig.4.21 shows the cumulative distribution function of the pores area, A_p, normalised by grain area, $A_g = \pi r_g^2$, for particle with varying aspect ratios ($\alpha = 1.0, 2.0$ and 5.0) in both frictionless and frictional cases. The pores of frictionless systems are systematically very narrow and only a negligible proportion have a size exceeding the grain area (See Fig. 4.21b), while the lower packing densities obtained with frictional grains are characterised by larger pores sizes (See Fig.4.21b). When $\mu = 0$, we observe that the cumulative distribution of pore size is a function with several steps for the systems with the monosised discs, which results from the high degree of crystallisation of the particles. However, for higher aspect ratios, the pores possesses quasi similar distribution of sizes, without size of crystalline ordering. The symmetry identified in frictionless systems is reduced by the presence of friction although still widely spread within the system. On the other hand, friction increased the influence of the grains shape on the voids size as observed in Fig. 4.21b and the average amount of void per grains raises significantly with α.

Statistical mechanics considerations predict that the area of the voids/pores of a

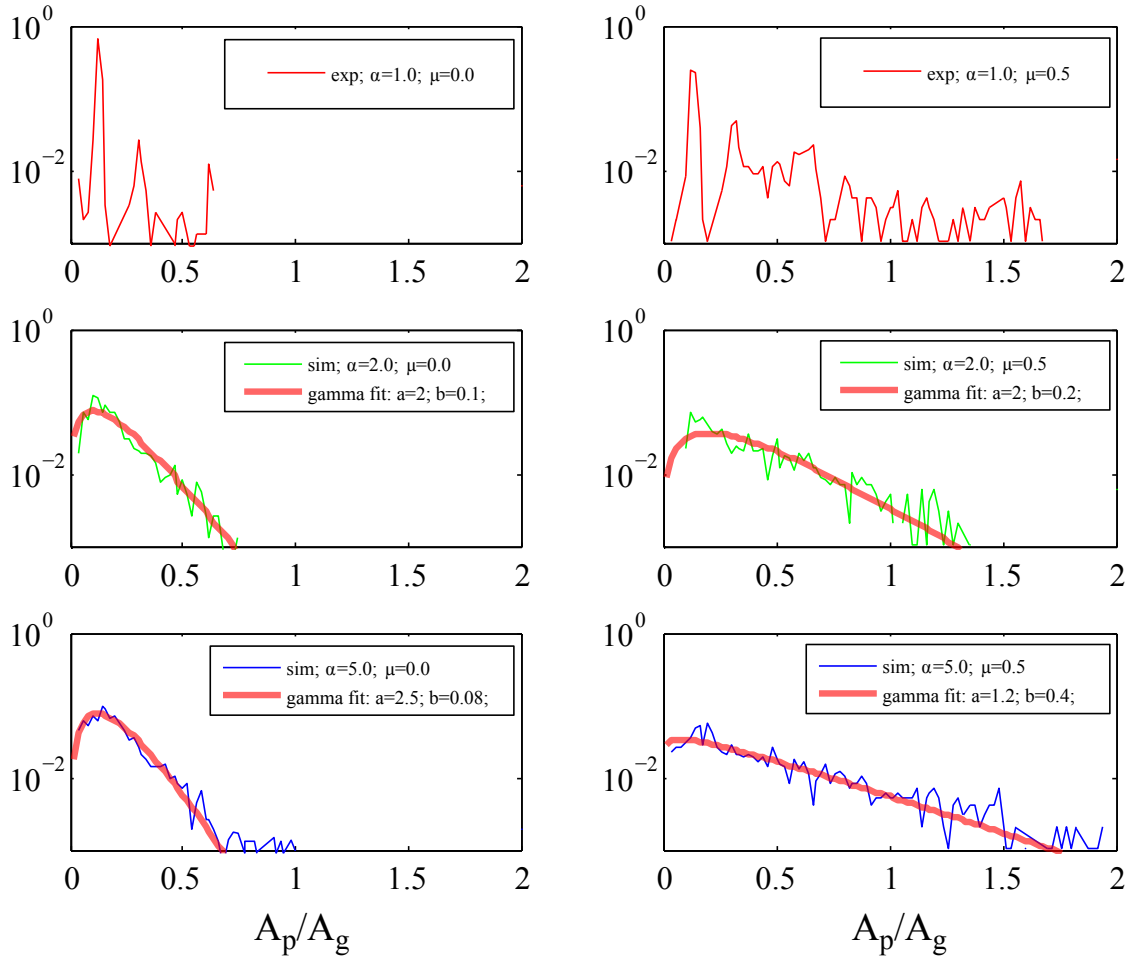


Figure 4.22: *Distribution of the pores sizes for the simulated frictional and frictionless systems. Best-fit gamma distribution have been superimposed.*

granular system in equilibrium follows a gamma distribution law [60] expressed as:

$$P(A_p/A_g) = \frac{b^a A_p^{a-1}}{\gamma(a) A_g} e^(- A_p/(bA_g)), \tag{4.9}$$

where A_p/A_g is the normalised pore size, and a, b are two parameters that condition the shape of the distribution. As seen in Fig. 4.22, the simulated void distributions can be described successfully with a gamma distribution for the elliptical particles. However, due to the high degree of order encountered in the system composed of discs, in particular frictionless ones, the pore sizes can not be reasonably predicted with gamma distributions. It is observed that the exponent b which controls the spread of the void size is a function of both the particle shape and the presence of friction. The larger value of b characteristic of frictional systems signifies a lower decay or lower inhibition of the larger voids and a tendency for the systems to create larger voids and exhibit a wide range of void sizes (see Fig. 4.22).

4.5 Conclusion

In this chapter the influence of the particle shape, as characterised by the ellipse aspect ratio, on the structure of granular media produced by the random sedimentation of mono-sized visco-elastic grains in a rigid container is investigated. The dynamic deposition sequence of visco-elastic elliptical grains was performed using the combined finite-discrete element methods described in detail in the previous chapter. It allowed the creation of dense packing close to the random close limit. As a consequence arbitrary shaped deformable particles have been considered. In this set of simulations, the large size of the particles considered means that the influence of cohesive forces between the grains can be neglected. The systems are representative of the deposition of a granular system dominated by gravitational and inertial forces, settling to a state of rest. A complete analysis, characterising the structures and the correlations present in the resulting pseudo-static media was performed, showing the influence of particle shape and the inter-grain friction on the final structure of the deposit.

The numerical simulations show the decisive role played by the coefficient of friction between the grains. The presence of friction has a crucial importance in granular matter and it was shown that it largely affects the structure of the packing, the number of contacts between the grains and also the packing density. Decreasing the presence of friction affects the grain interaction in a similar fashion to a lubricant and facilitates the sliding between neighboring grains. The consequence is that frictionless systems need more contacts to reach stable structural configurations. This tends to increase the packing density of the media and increase the amount of ordering between the grains. In particular, it was observed that frictionless particles generates system with local crystalline order.

The study shows that the final packing density of the granular system can be improved when particles with small ellipticity are packed, which tends to confirm the recent observation made by [45, 226] with ellipsoids. The analysis of the correlation curves suggest the presence of ordered clusters of particles, despite the presence of friction and despite the fact that the particles were randomly settled. However, for elliptical particles with an aspect ratio larger than $\alpha = 2$, the coordination number tends towards a constant value while the packing density falls which suggests that the exclusion volume per particle becomes higher. This also confirms that using elongated particles subsequently hampers the possibility of rearrangement within the grains by reducing the relative freedom of the particle motion. At large aspect ratios, the packing density drops roughly linearly with the particle aspect ratio.

We also demonstrate that the gravitational sedimentation of elliptical particles naturally produces short range and long range ordering between the grains which results in anisotropic properties of the systems. For discs the radial distribution function is an

efficient way to characterise the structure of the grains, but it is rather unsuitable for non-spherical particles. We thus use orientational descriptors that quantify accurately the amount of ordering within a system of elliptical grains. Ellipses have a statistically greater chance to settle with their longest axes pointing in the horizontal direction as it represents their most stable spatial configuration. In elliptical systems, the particles tend to be ordered with their neighbouring ones as indicated by the orientational correlation function. It is worth pointing out that the amount of long range orientational order, indicated by the function $Q_\infty(\alpha)$, increases significantly with the particle aspect ratio. Nevertheless, we demonstrate that the orientational disorder saturates with particles of aspect ratio larger that $\alpha = 1.5$. The presence of orientational order have been investigated in the past [197, 26] with Monte-Carlo simulations and it is important to point out that despite the fundamental difference of the simulation methods, the results are in quantitative agreement with previous research. However, the relationship between the orientational order shown by a sedimentation-created system and the particle aspect ratio has not been presented previously for small aspect ratios and was highlighted in this chapter.

The particle ordering is in fact the result of the gravitational field that acts on the particles during their settlement and it becomes increasingly important with elongated frictional particles. However, the amount of ordering generated in our systems saturates above a critical aspect ratio $\alpha \approx 2$, which interestingly correspond to 1) the limit at which the coordination number becomes constant and 2) the limit at which the packing density decreased with the particle aspect ratio. Above this critical aspect ratio, exclusion effects [156] are expected to increase the average amount of voids per particle.

Image analysis software, freely available and simple to use was able to provide quantitative information about the size of the pores generated by the granular system. It was shown that the voids distribution follows a gamma distribution for which the exponent value is influenced by the particle shape and the presence of friction.

Chapter 5

Analysis of the heterogeneities of stresses and forces of a granular packing

5.1 Introduction

It is has been shown that the stress response of a granular system to an external perturbation is complex [63], and is clearly different from elastic continuum media. The various experiments performed on small scale granular media have resulted in contradictory conclusions concerning which type of partial differential equations (PDE) govern the propagation of the stress. There has been experimental or analytical evidence that elliptic (elasticity equations), parabolic (diffusion equations) or hyperbolic (wave and plasticity equations) PDEs can characterise granular systems depending on the scale of the system and also to the type of grain interactions as well as to their shape (because it affects the structure of the contact network, cf. Chapter 4) [41, 63, 67, 21, 116, 68]. In particular very distinct stress patterns have been observed when the granular systems are submitted to an external local load, depending on the shape of the particles (Fig. 5.1). In cubic-shaped cohesionless grains [41] diffusive like stress propagation was observed with no evidence of force chains. To the contrary, by using extensive experimental work with spherical photo-elastics grains, [63, 175] came to the conclusion that an elastic-like stress transmission is statistically consistent in depicting their experimental systems in which force chains clearly propagate. The work of [63] also suggests that there exists a strong influence of the spatial ordering of the particle in the propagation of the stress.

The inability of describing the stress propagation of small systems of granular materials comes essentially from the fact that strong heterogeneities control the stress propagation

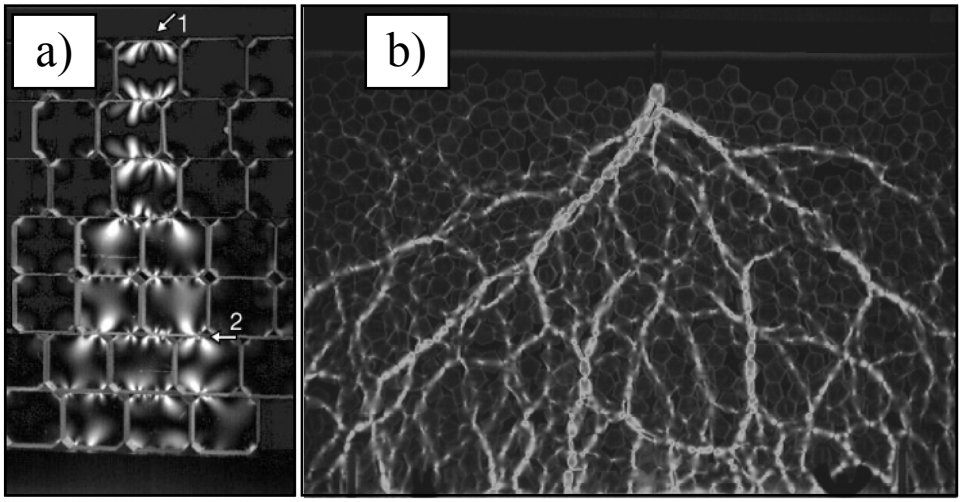


Figure 5.1: *Experimental comparison of the stress response of a granular media to an external punctual pressure point. Photo-elastic beads are used to visualize the stress path. The stress response is shown to depend on the particle shape. a) case of bricks packing (adapted from [41]). b) case of packing of pentagonal shaped particles (adapted from [63]).*

over length scales of a few particle diameters, whereas continuum descriptions are under certain conditions rather better adapted for very large systems of grains. However, many applications involve relatively small amounts of granular materials, and in this case the stress characterisation is largely influenced by the presence of structural heterogeneities. Moreover, it remains unknown how the stresses in those small scale systems are affected by the particle shape.

An essential question consists of establishing the relationship that link the microscopic structure of the contact network to the macroscopic stress in a granular material [115, 114, 117]. This homogenization procedure requires average material properties. Although mean properties can be predicted for periodic structures, disordered granular systems require alternative strategies. In such circumstances, discrete element methods are a useful tool as it permits the description of the micro variables (contact forces, particle positions) characterising the system. Thus, each component of the stress tensor is computed within a representative volume containing a representative number of particles [125] by using the Love formulae:

$$\sigma_{ij} = \frac{1}{S} \sum_{k} f_l^k l_j^k, \tag{5.1}$$

where S is the representative volume, f^k is the k^{th} contact force, l^k is the branch vector that joins the particle in contact, and the lower indices i and j refers to the vector component. The problem with homogenised descriptions is that the characterisation of the stress heterogeneities observed experimentally (such as force chains) can not be quantitatively addressed at the particle level. Consequently, evidence of a linkage between the shape of the particles constituting a granular media and the propagation of stress

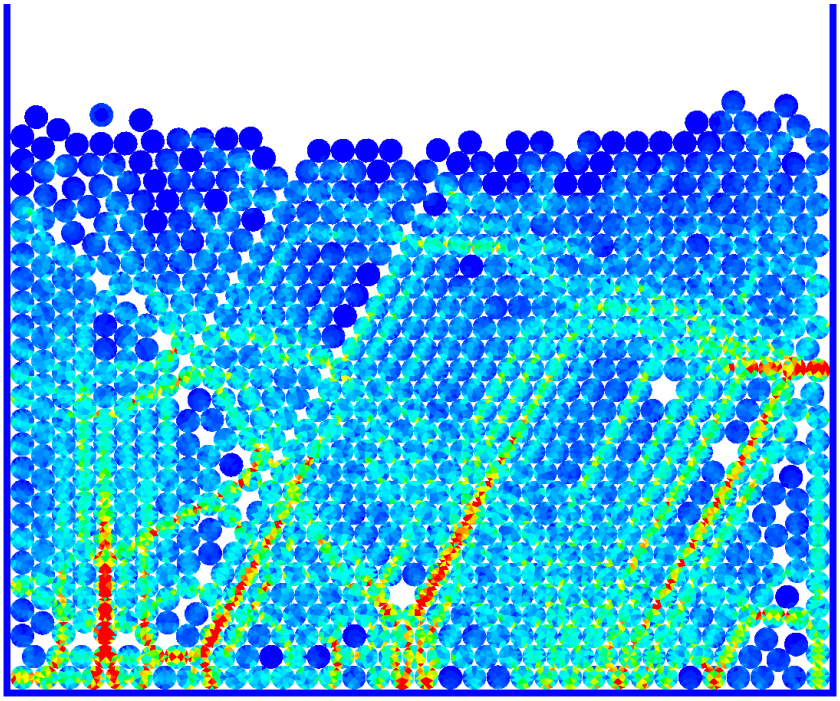
heterogeneities are challenging to highlight. Thus the combined finite-discrete element method, described in Chapter 3, appears to be the most appropriate strategy to overcome the problem of stress characterisation in a granular material.

In this Chapter, an analysis of the stresses and contact forces is performed in order to identify a possible influence of the particle shape on the transmission of the load between particles. Following a qualitative description of the stress patterns described by frictional and frictionless particles, quantitative analysis of the stresses and contact forces is performed using distribution functions. Afterwards, the characteristic length scale of each system is extracted using spatial correlation functions, which underlines the critical role played by the particle shape in the stress distribution within a granular media.

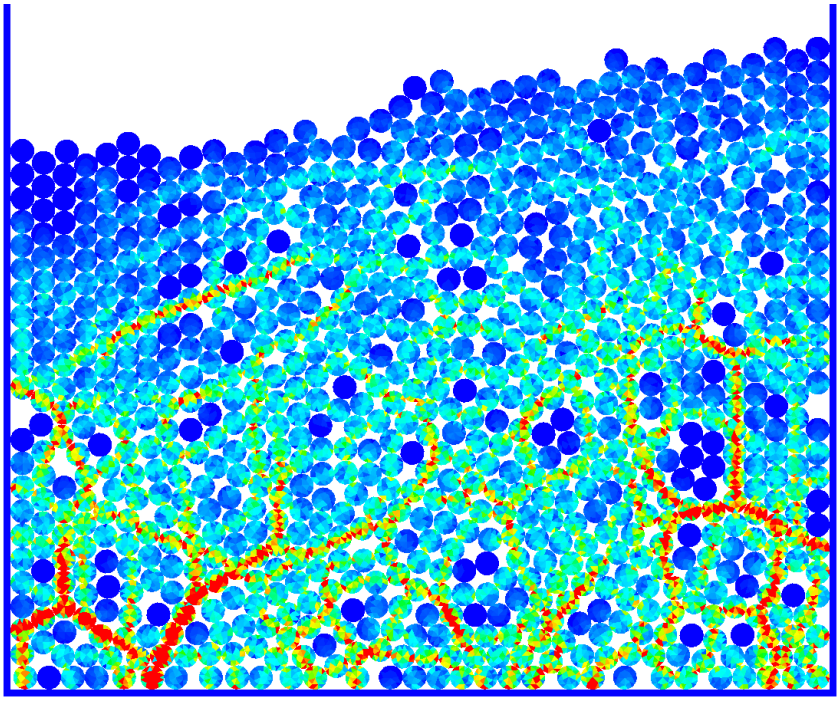
5.2 Effect of inter-particle friction and particle shapes on the stress distribution (Qualitative description)

Combined Finite-discrete Element simulations were performed to obtain packs constructed with elliptical particles of various elongations [135]. The numerical code was modified to accommodate the calculation of frictional forces and to output the position, the magnitude and the orientation of the contact forces. The particles considered were ellipses discretised into a set of joint triangular finite elements. Typically, 60 finite elements were required to obtain a reasonably smooth elliptical shape.

Extensive runs of particle deposition have been performed in order to form packing structures, following the procedure described in the previous chapter, with ellipses of various aspect ratios (varying between $\alpha = 1$ to $\alpha = 5$) both with and without friction. The structure of the packs was analysed in detail in Chapter 4 where the emergent properties were characterised. The main conclusions drawn concerning the inter-relation between particle shape and emergent properties was that a non-trivial relationship links the packing density of a system with the elongation of the ellipses deposited inside a container. Additionally, the dependence of the average coordination number of a granular media with the ellipses eccentricity shows that one more contact is usually necessary to insure the stability of elongated particles compared to circular ones. The results discussed in this chapter demonstrates that inter-particle friction is not only an essential parameter that controls the fabric of the particles but they also suggest important differences between the stress patterns generated with different particle shapes.

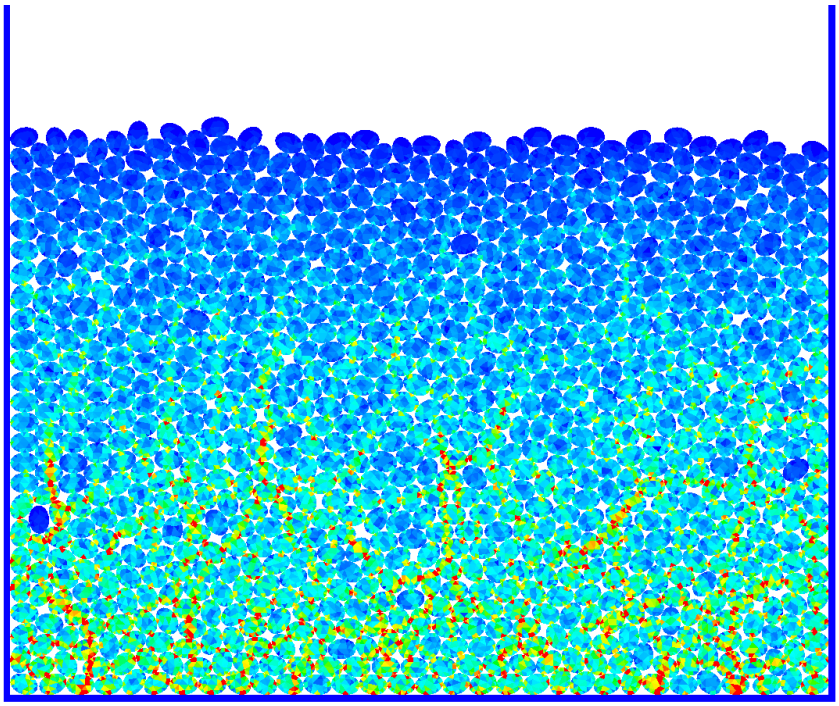


(a)

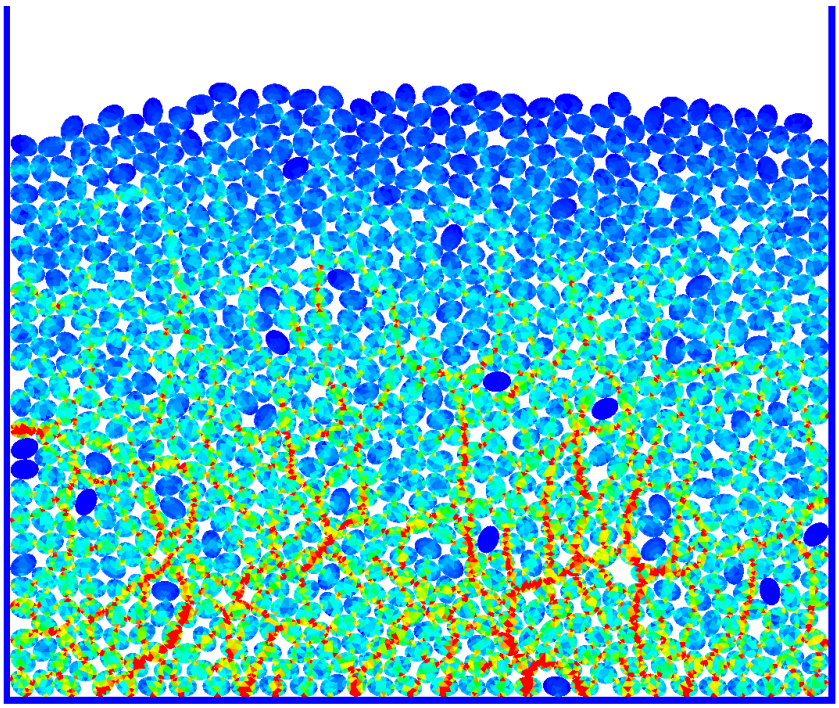


(b)

Figure 5.2: *Aspect ratio $\alpha = 1.0$. a) $\mu = 0$. b) $\mu = 0.5$. Colour ranges from blue (low stress) to red (high stress)*

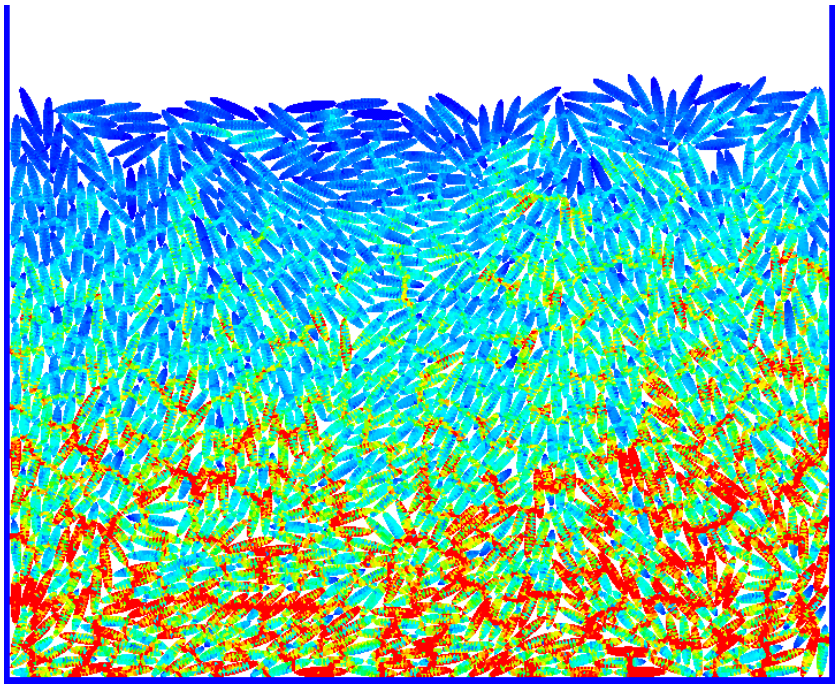


(a)

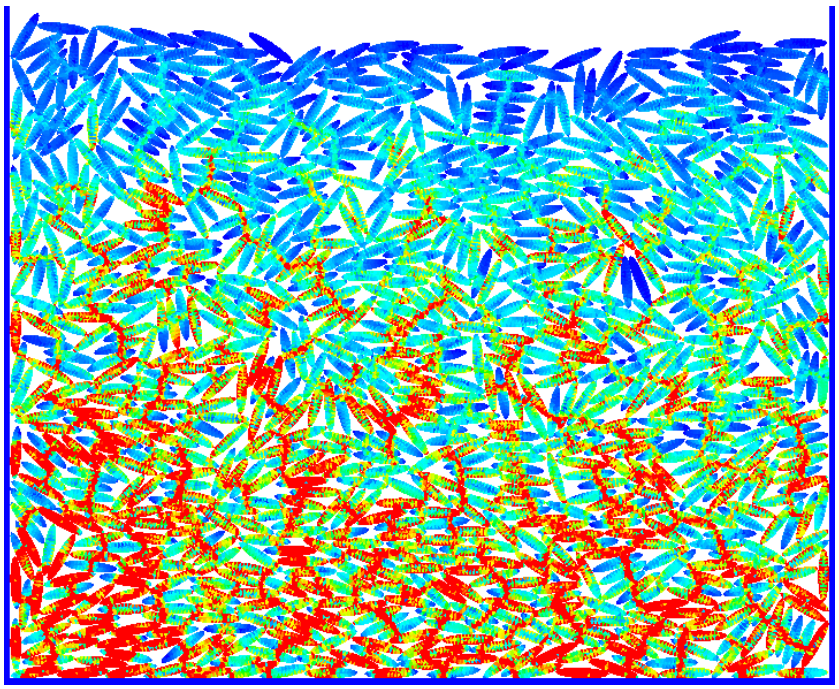


(b)

Figure 5.3: *Aspect ratio $\alpha = 1.4$. a) $\mu = 0$. b) $\mu = 0.5$. Colour ranges from blue (low stress) to red (high stress)*



(a)



(b)

Figure 5.4: *Aspect ratio $\alpha = 5.0$. a) $\mu = 0$. b) $\mu = 0.5$. Colour ranges from blue (low stress) to red (high stress)*

5.2.1 Frictionless case

The absence of friction forces the particles to be naturally arranged in a way that maximizes the packing density in a given space. The pack made of frictionless discs (Fig. 5.2a) shows large regions with a crystalline network of packing density $\phi = 0.9069$, known to be the densest possible configuration. Away from the influence of the walls, where the symmetry of the structure can be broken, the particles are geometrically organised. It is worth noticing the presence of "defects" where a particle is missing without creating any disorder. This affects the packing properties of the system by decreasing both the packing density and the coordination number. The case of elliptical bodies (Fig. 5.3a and 5.4a) is more complex to characterise as the particles are arranged along a more irregular network. However, at a local scale they tend to organise into almost crystalline structures. The colour scheme of the pictures, varying between the blue (low stress) and the red (high stress) suggests a linear increase of the static pressure, similar to the hydrostatic pressure observed in Newtonian fluids.

5.2.2 Frictional Case

In Fig. 5.2b, we can visualize the development of force chains across the granular system where the stress is clearly concentrated among a few particles. Typically, 40% of the particles are supporting more than 60% of the total load by transmitting the stress at the contact points when considering discs. Fig. 5.2b and 5.3b also suggests that a connected network of forces takes place throughout the pack along regular patterns, defining a "strong" network of contacting particles surrounding weakly constrained ones. We also observe that the particle shape influences the spatial correlations of the stress distribution significantly. The stress network observed for the case of elongated particles is more heterogeneous than for rounded ones; in particular the presence of force chains does not emerge clearly with elliptical particles as it does with rounded ones (Fig. 5.2b). In the following sections the work is aimed at characterising quantitatively the emergent properties of the granular packing. These results will be followed by a quantitative characterisation of the effect of the particle shape on the mechanical properties of the system (contact forces + stress tensor).

5.2.3 Distribution of the forces

In the FEM-DEM framework, the contact forces are distributed among all the nodes of the element involved in a binary contact. The total contact force, F^{ij} is thus calculated by summing all the residual contact forces of the the nodes involved in the contact between

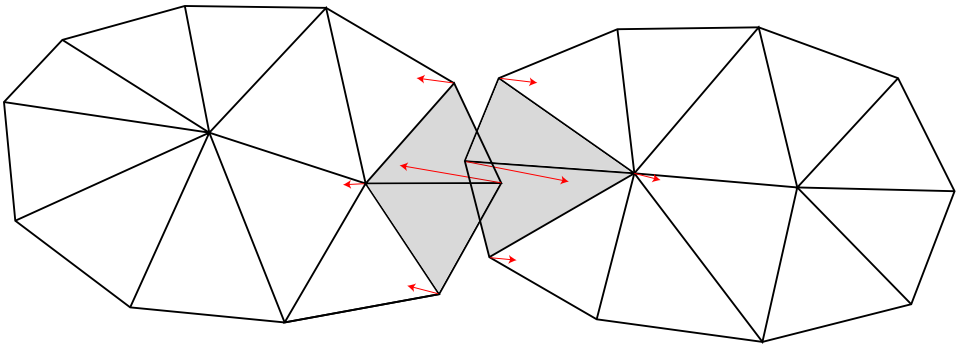


Figure 5.5: *Identification of the nodes contributing to the total contact force (local contact forces are represented by a red vector)*

the particles i and j:

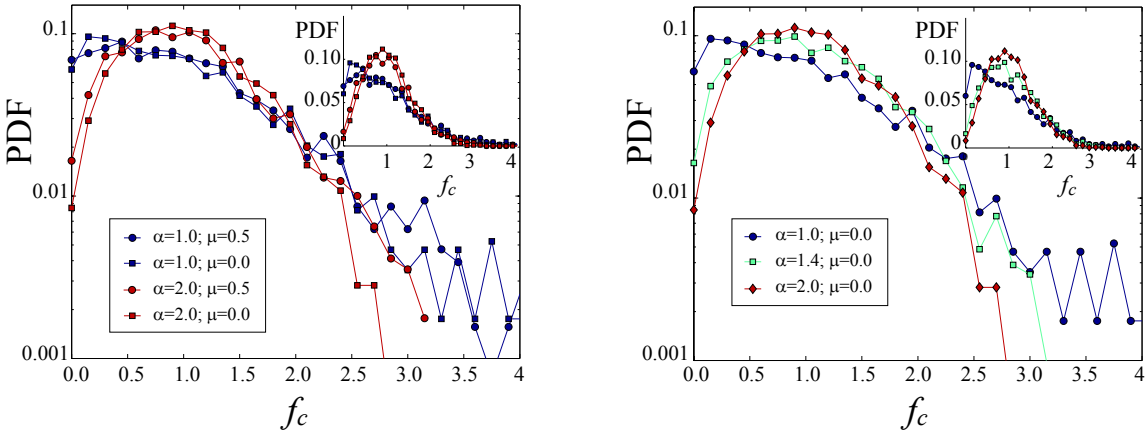
$$F^{ij} = \sum_{k=1}^{\Omega} (f^{ij})_k, \tag{5.2}$$

where $(f^{ij})_k$ is the contribution of the k_{th} node of the particle i that is added to the contact force with the particle j.

Former studies of granular packing have pointed out that the probability distribution of the contact forces exponentially decreases while the contact force magnitude increases. This observation, reinforced by theoretical models like the Coppersmith 'q' model and its improved versions [34] or statistical mechanics approaches [24, 49], is considered to be a strong characteristic of randomly deposited granular media. On the contrary from former implementations of DEM where the contact forces are localised at a single point (giving unstable behaviour for several types of contact configurations node/node, node/edge or edge/edge), in the current version of FEM-DEM the contact forces are distributed on all the nodes that surround the contact point. In that sense, the computation of the resultant contact force for a given contact is an integral of the force carried by all the nodes involved in this contact (Fig.5.5). An algorithm was developed to evaluate the total contact force, $\mathbf{f} = \mathbf{f}_n + \mathbf{f}_t$, for which the distributions are plotted in Fig. 5.6a and Fig. 5.6b for particles with varying friction and shape.

In Fig. 5.6a and Fig. 5.6b the contact forces data are corrected for the depth dependent force gradient and rescaled by the average contact force of the system $\bar{\mathbf{f}}$, assuming that the force increases linearly with the depth. The depth normalisation procedure is discussed in Chapter 6. The depth normalised contact forces are labeled f_c The normalization enables a comparison between simulation results that is independent of the total number of contact forces measured in the system.

The results shows the exponential decrease of forces larger than the average force. This is coherent with experimental results and with molecular dynamics simulations [169, 121, 118]. At low forces, $P(f^*)$ shows a dependence on the particle aspect ratio. The



(a) (b)

Figure 5.6: *a) Force distribution for packing with constant shape and varying friction. b) Force distribution for frictionless packing with varying aspect ratio*

stress distribution presented in the snapshot of Fig. 5.2 to Fig. 5.4 suggests that both the particle shape and the friction affect the stress distribution, and that the curves of Fig. 5.6a and Fig. 5.6b support this observation. For high contact forces the exponential tail of the contact force distribution, which appears to be a strong characteristic of granular systems composed of rounded particles [169, 204, 133, 118], is observed although the decay is steeper for elongated particles. For low forces however the shape of the distribution of the contact forces is affected by particle shape and the PDF diverges from a strictly exponential distribution when α is increased. Experimental measurements of the contact forces performed at the boundary of the system [133] and numerical simulations computing the contact forces of the particle in the bulk [194] proposed that the shape of the force distribution can be fitted by the following functional form:

$$P(f) = a(1 - be^{-f^2})e^{-\beta f_c}, \tag{5.3}$$

where a, b and β are three parameters adjusted in order to match with the force distribution. The values $a = 3.0$, $b = 0.75$ and $\beta = 1.5$ proposed by [133] are satisfying to describe the force distribution of discs. The nice feature of this functional is that it captures both the exponential tail observed for large forces and the plateau for the weakest ones. Because of the relatively small size of the systems, a potential effect of the inter-particle friction was not clearly identified whereas it was possible to notice an influence of the particle shape.

Larger scaled simulations performed in the Section 5.3.2 show clearer results, in particular that the equation 5.3 only applies for the discs. As explained later, the distribution of the contact forces with ellipses gradually evolves towards a gaussian-like distribution as the aspect ratio increases. Nevertheless, the PDF of the contact forces of frictionless systems seems to decrease slightly faster compared to the frictional ones,

which confirms the observation of [149]. In the next section, the PDF for the differential stresses is investigated in order to identify a signature for the particle shape.

5.3 Distribution of the differential stress

5.3.1 Elemental approach

In experiments, photo-elastic materials permit the visualisation of the stress within the particles. For birefringent materials, the principal planes of optical symmetry coincides with the eigenvalues of the stress tensor in each point of the material. As a consequence the amount of light that they emit is proportional to the differential stress received by the material [42, 210, 86, 76]. In our numerical simulations, each component of the stress tensor, determined numerically, can be used for the determination of scalar values, characterising the magnitude of differential stress. Experimentally, it is non trivial to establish the relationship between the average brightness of a grain and its applied load because of the periodic structure of birefringent materials. Numerically, this is bypassed and the total load supported by the particle can be characterised by using the average value of the differential stress over the area of the grain. As a consequence it is convenient to display the differential stress in each element of the material in order to compare the stress paths obtained numerically with experimental data sets.

Just as noted for the force distribution, the stress is highly heterogeneous and its magnitude varies over two orders of magnitude from particle to particle. In the combined finite-discrete element method, all the components of the Cauchy stress tensor $\mathbf{T}^{el}$ are calculated for every finite element. In order to compare the stress patterns to those observed in experiments [63, 118], it is convenient to display the differential stress T^{el}_{diff}, difference between the principal stresses T^{el}_1 and T^{el}_2 of the tensor $\mathbf{T}$:

$$\mathbf{T}^{el} = \begin{bmatrix} T^{el}_{ii} & T^{el}_{ij} \\ T^{el}_{ji} & T^{el}_{jj} \end{bmatrix} = \begin{bmatrix} T^{el}_1 & 0 \\ 0 & T^{el}_2 \end{bmatrix}. \tag{5.4}$$

In their final static configuration, the vertical load supported by the walls is negligible so that the pressure supported by the particles increases linearly with depth. To remove hydrostatic pressure gradient on the particles, the stress is normalised following the procedure described in Chapter 6.2.1.2. Depth-normalised quantities are tagged with a *.

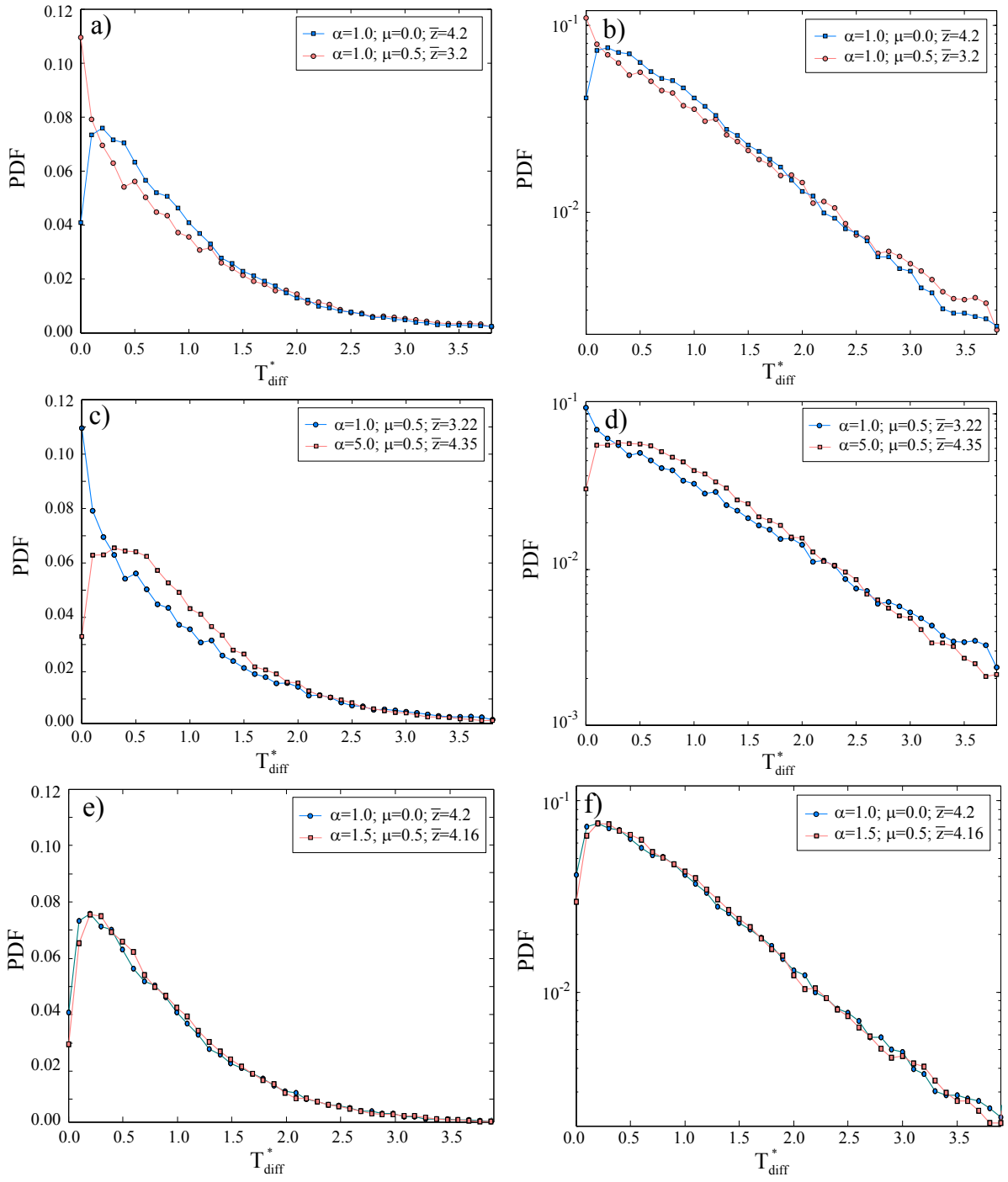


Figure 5.7: *Stress distribution of the differential stress of the granular packs plotted on linear and log scales. The stress is calculated inside each finite element of each particle. a) and b) influence of the particle friction, c) and d) influence of the particle shape, e) and f) Stress distribution of two systems with different particle shape and inter-particle friction at constant* $\overline{z}$.

5.3.1.1 Influence of friction on stress distribution

In granular systems, the stress is usually distributed heterogeneously and concentrated along force chains. The particles remaining around the regions with high stress concentrations are significantly less constrained. Each finite element provides data about the stress state of a particular zone within a particle and can be considered as a sampling point. Considering that a particle is divided into an average of 50 finite elements, a system containing 900 hundred discrete ellipses possesses typically more than 45,000 sampling points characterising the stress state at several position within the particle. As a results, the statistics performed on the stress are more reliable compared to the contact force for which "only" $\overline{z}N$ data points are available. In the previous section (Section 5.2.3) we made clear that the presence of friction leads to lower packing density and lower coordination numbers compared with frictionless systems. With the mass of material being kept constant, the reduction of the average coordination number implies that the load received by each particle will be distributed among fewer contacts. Fig.5.2 to 5.4 shows that the stress heterogeneities are more pronounced when friction acts between the grains and that the force chains propagate differently. For constant shape, Fig. 5.7a and Fig. 5.7b show that the differential stress is affected by the presence of friction. The probability of encountering low stressed elements is enhanced by the friction (Fig.5.7a). The exponential decays at large stresses is consistent for both frictional and frictionless systems although it is steeper for the frictionless interactions at a given aspect ratio (on the log-linear plot the slope of the exponential decay is 1.1 for $\mu = 0.5$ and 0.9 for $\mu = 0$) (Fig. 5.7b).

Similarly to the force distribution, the PDF of the differential stress decays exponentially for large stress magnitude (i.e. T^*_{diff}). However, at low stresses, it appears that the PDF is significantly affected by the presence of friction, and while a gap is observed for frictionless systems, it is found that frictional systems have a higher probability of exhibiting differential stresses near zero. Additionally at high stresses the characteristic slope of the PDF becomes steeper with frictionless interactions compared to the frictional ones. The change of slope indicates that the presence of friction modifies the degree of stress heterogeneities.

5.3.1.2 Influence of the particle aspect ratio on stress distribution

The influence of the particle shape is demonstrated by comparing the PDF of the differential stress of several packs constructed using particles interacting with friction ($\mu = 0.5$) and various aspect ratios. The results presented in Fig. 5.7c) and Fig. 5.7d) highlight the particle shape influence on the stress distribution. Increasing the ellipticity produces a

more pronounced gap at low stress and a steeper exponential decay of the most stressed elements. The elliptical particles ($\alpha = 5$) in Fig.5.4a) and 5.4b) need approximately 1 more contact than the disc pack with the same friction. It can be inferred that the differences of stress distribution are due to the fact that ellipses need a higher coordination number than the discs to be in mechanical equilibrium which affects both stress transmission and stress distribution by making it more homogeneous. We expect systems with low coordination number to exhibit a distribution curve that spreads over a larger range. Furthermore, those same systems are expected to propagate force chains more efficiently than systems requiring a large number of contacts per particle. For clarity, the results for the intermediate aspect ratios are not displayed.

5.3.1.3 Competition between the effect on the inter-particle friction and the particle shape

As explained above, both the particle shape and the presence of friction modify the distribution of the differential stress of a granular medium. In Chapter 4, it was shown that using less frictional or more elliptical particles results in a higher coordination number per particle. In term of stress, the increase in the number of contacts per particle changes the shape of the distribution by inhibiting the low stress regions and by enhancing the exponential decay tail at large stress. The stress distributions of two systems prepared with distinct shapes and friction, with the same average coordination number of 4.2 were compared (see Fig. 4.8 and Fig. 4.11). The first medium is composed of 900 discs interacting with a coefficient of friction $\mu = 0.0$, while the second one is composed of frictional ($\mu = 0.5$) ellipses of aspect ratio $\alpha = 1.5$. Fig. 5.7e and Fig. 5.7f show that both stress distributions superimpose perfectly for both small and high stress values. Although frictional and frictionless systems can respond similarly in terms of stress distribution if their average coordination number is equivalent, the final porosity of both systems differs significantly. For this particular example, the frictionless system fills 88.3% of the total volume while the frictional ones reaches a packing density of 83.3% (see chapter 4).

The most important criteria to account for the stress characterisation in a granular medium seems to be the mean coordination number. The stress distribution of the systems with high mean coordination numbers (frictionless systems, systems with ellipses of large aspect ratios) shows major differences compared to the granular media with lower coordination number as seen on Fig. 5.7a to Fig. 5.7d. For lower $\overline{z}$, the stress distribution to be nearly constant at low stress appears while it dips when $\overline{z}$ is larger.

The friction and the particle shape also affects the stress distribution at large stress as the slope of the exponential decay increases with α and decreases with μ. Therefore, it seems reasonable to suggest that every parameter that has an effect on the coordination

number, such as friction and shape, is expected to lead to a change of the stress distribution of the system as it changes the characteristics of the force propagation.

5.3.2 Particle averaging approach

5.3.2.1 The system

In addition to the element based approaches, stress data averaged over the particle area was also treated. As mentioned above, large systems are necessary to perform particle based statistical analysis. As a result, 4 additional simulations comprising 15000 particles were launched. Because of the computational cost of such large simulations, the results of the present section are restricted to the characterisation of frictional systems. However, as shown in section 5.2.3, contact forces are weakly dependent on the friction imposed between the grains. Due to the fact that the variations of the system properties occurs mostly at when α is small $\alpha < 2$, the range of study for the aspect ratios is restricted between $\alpha = 1.0$ and $\alpha = 2.0$.

The large size of the considered system (16 times larger than the typical system) imposes some assumptions concerning the size of the particles for the computational feasibility of the simulations. The particle size is artificially increased by a factor 10 in order to use larger time steps (cf. chapter 3, section 3.5.3 for the discussion about the critical time step), while all the mechanical parameters are allocated realistic values. This type of scaling is regularly used for discrete element simulations, and is similar to the mass scaling used by [205, 206, 164], but implies less restrictive assumptions. It is additionally ensured that the substantial increase of the particle mass does not induce an excessive deformation of the particles as a consequence of the larger overburden pressure received. In particular, using mass scaling with the value proposed in [206] (density multiplied by a factor 10^{12}) leads to particles that deform under their own weight. This is however successfully avoided using the size scaling technique. To restrict the influence of the Janssen effect, the width of the box is adjusted in order to obtain final a width/height ratio of static particles comparable to the tests presented in the previous section.

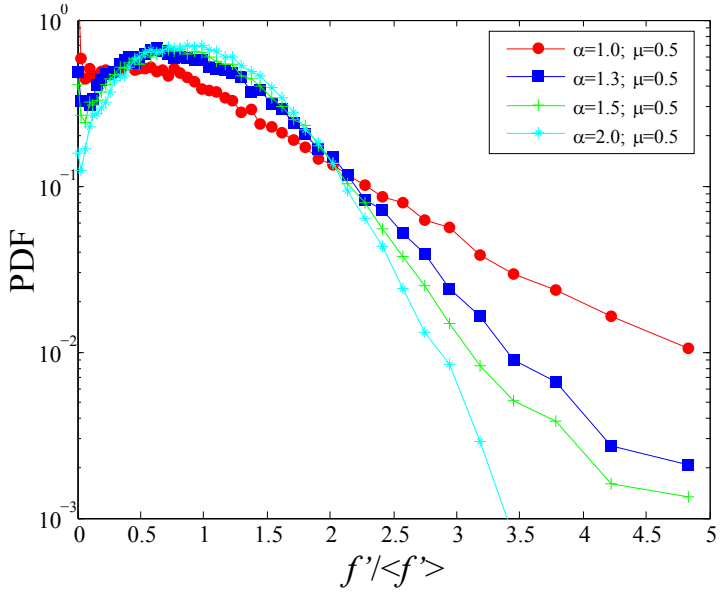


Figure 5.8: *a) Force distribution for the 4 large systems of ellipses.*

5.3.2.2 The particulate stress tensor $\mathbf{T}^p$

In a particle with M finite elements, each component of the stress tensor can be averaged independently:

$$\begin{cases} T^p_{xx} = \sum_{i=1}^{M} (T^{el}_{xx})_i, \\ T^p_{yy} = \sum_{i=1}^{M} (T^{el}_{yy})_i, \\ T^p_{xy} = \sum_{i=1}^{M} (T^{el}_{xy})_i, \end{cases} \tag{5.5}$$

where T^{el}_{ij} is the ij component of the elemental stress tensor, and T^p_{ij} is the ij component of the particulate stress tensor. Because the non-diagonal components of the stress tensor are symmetric, $T_{xy} = T_{yx}$, an average stress tensor is fully known for each particle. The average differential stress per particle is defined to be the difference of the principal stress component of the particulate stress tensor, which gives:

$$T^p_{diff} = T^p_1 - T^p_2, \tag{5.6}$$

where T^p_1 and T^p_2 are, respectively, the major and minor principal stresses of the tensor $\mathbf{T}^p$, with $T^p_1 > T^p_2$.

5.3.3 Results and discussion

As the considered systems are larger than the ones described in the first part of this chapter, to show that the method used is robust it is important to show that the packings are characterised by the same distribution of contact forces. Fig.5.8 shows that the contact forces follow the same distribution for the large systems as for the smaller ones. However, because a large amount of contact forces are generated in a large system, the influence of the particle shape becomes clearer. Packing of discs are well described by an exponential decay of the large forces, while the the smallest ones are nearly equiprobable although a small peak of higher probability appears when the contact forces approach 0. In particular, it is emphasized that the shape of the distribution curve of the contact force within a packing of discs is in good agreement with experimental [133], analytical [34, 49] and numerical [169, 121, 195] predictions. For the elongated particles, the distribution evolves towards a more homogeneous gaussian-like distribution. As the aspect ratio is increased, the contact forces takes values close to the average contact force of the systems, which is characterised by a more pronounced peak around $f^* = 1$, the disappearance of the exponential tail and the gradual rarefication of the smallest contact forces.

In Fig.5.9, the distribution of each component of the stress tensor is presented. The curves of the Fig. 5.9a, 5.9b and 5.9d are normalised by the average value in order to represent the distribution over a similar range of values. Because of its symmetrical nature, T^p_{xy} is normalised by $< |T^p_{xy}| >$, the average of its absolute value. The distribution of the diagonal components, T^p_{xx} and T^p_{yy}, is influenced in a similar way by the particle shape compared to the distribution of contact forces. As a consequence, for discs, the distribution is found to be exponential for the stress component larger than the mean while lower forces lower than average are uniformly distributed. By increasing the aspect ratio, the exponential decay is gradually attenuated and the particles with low stress becomes rarer, which results in a distribution with a peak of probability around the average value. Despite the great similarities between the distribution of Fig. 5.9a and 5.9b, it is observed that the component T^p_{yy} is more sensitive to the particle shape than T^p_{xx}, as each distribution curve of T^p_{yy} is more distinctively separated.

The non-diagonal terms however present specific distributions. Firstly, the trend of the curve presented in Fig. 5.9c) is symmetrical and centered around $T^p_{xy} / < |T^p_{xy}| >= 0$. The symmetry of the curve is caused by the symmetry of the systems in which the load supported by a particle from one direction is counterbalanced by the load applied from the opposite direction. Interestingly, the distribution is exponential over the whole range of experimental values obtained, with a positive exponent if $T^p_{xy} < 0$ and a negative one if $T^p_{xy} > 0$. It is observed that the distribution curves are independent of the aspect ratio of the particles as the PDF are superimposed. Additionally, it seems that the PDF of T^p_{xy}

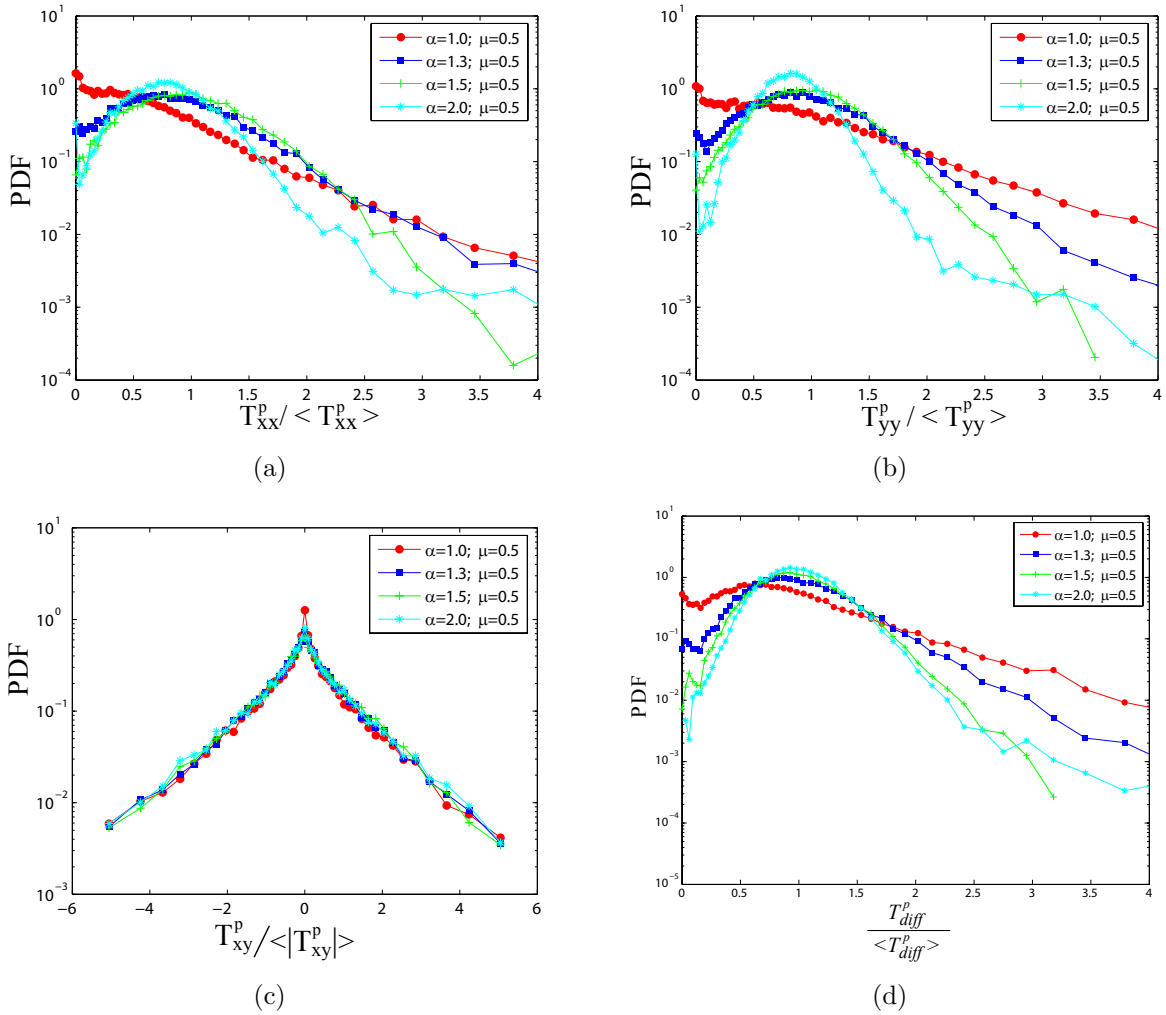


Figure 5.9: *Distribution of each of the component of the particulate stress tensor inside the large packing of ellipses a) Distribution curve of T^p_{xx}. b) Distribution curve of T^p_{yy}. c) Distribution of the non-diagonal component T^p_{xy} d) Distribution of the differential stress average over the particle area.*

diverge close to 0, as an excess of particles are found to possess quasi-null non-diagonal terms for the stress tensors, i.e. when the particle principal axis correspond closely to T^p_{xx} and T^p_{yy}. The consequence of this result is that the heterogeneities are propagated mainly through the diagonal terms, as the distribution of T^p_{xy} is independent of the particle shapes. The complex dependance of the particulate stress tensor components on the particle shape. In particular the fact that only the distribution T^p_{xy} is independent of the particle shape underlines the complexity of characterising the stress propagation in small assemblies of granular particles.

Finally, the analysis of the distribution of the particulate differential stress was carried out (see Fig. 5.9d). As seen in Fig. 5.2, Fig. 5.3 and Fig. 5.4, the differential stress PDF responds differently for each of the considered particle shapes. The analysis of the distribution of the stress tensor components confirmed the observation suggested at

the beginning of the chapter stating that discs seem to be more efficient in transmitting stresses over large length scales, and that systems with very elliptical particles generates more random stress propagation hence the difference shown in the force distribution. We notice that the differential stress as shown in the Fig. 5.9d responds similarly to the contact forces on the applied load , where the elongated shape systems are characterised by gaussian-like distribution unlike packing of discs.

5.4 Stress correlations in granular packs

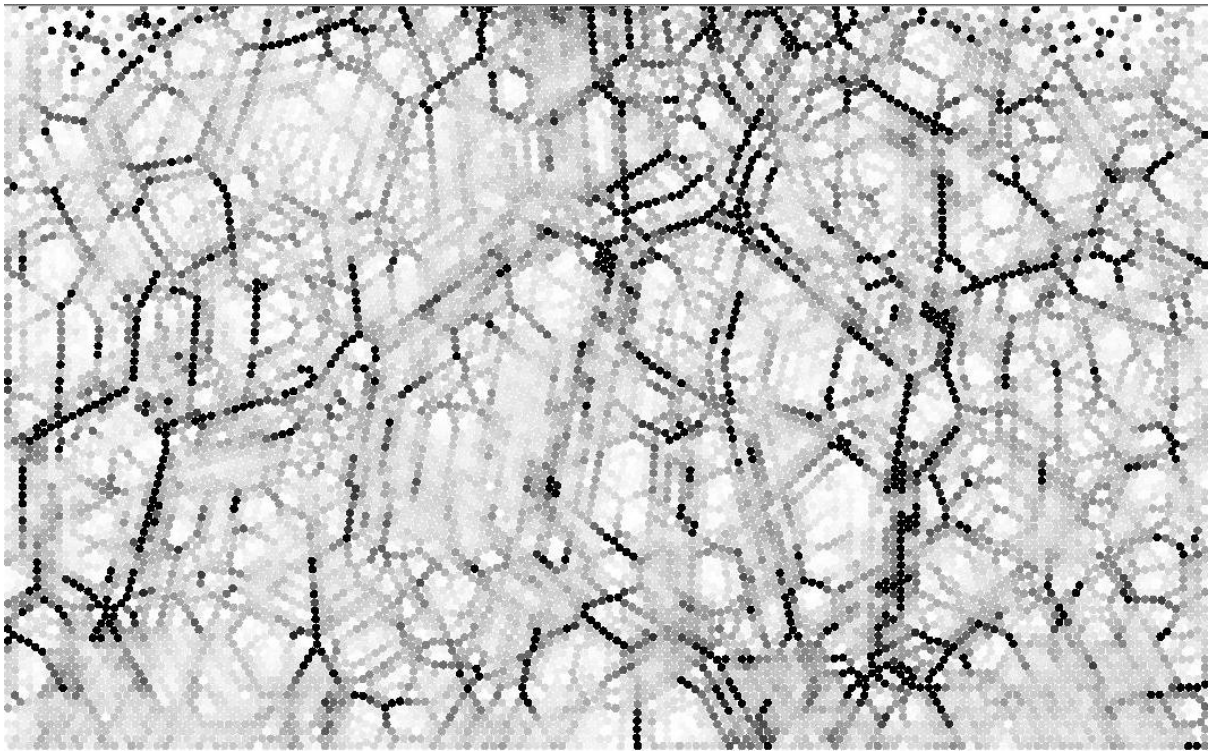
5.4.1 Motivations

The exponential distributions of the forces and stresses are a good indication that the mechanical response of a granular medium to the load imposed (here the weight of the particles) is not random. Theoretical considerations of force transmission have shown that simple and advanced models lead to an exponential distribution of contact forces both in 2D and 3D systems [113, 34, 24, 49] and that the shape of the force distribution curves is intimately related to the presence of spatial correlations between the contact forces [141]. In particular these theories predict that the specific shape of the distribution of the contact forces is related to the propagation of force chains within the system. Focusing on the differential stress as a stress measure, its spatial distribution is concentrated along preferential paths while other particles are exempt from any load, particularly for the most elongated particles (see Fig. 5.2 to Fig. 5.4). The idea in this section is to provide quantitative estimation of the correlation length of the differential stress for systems with different particle shapes.

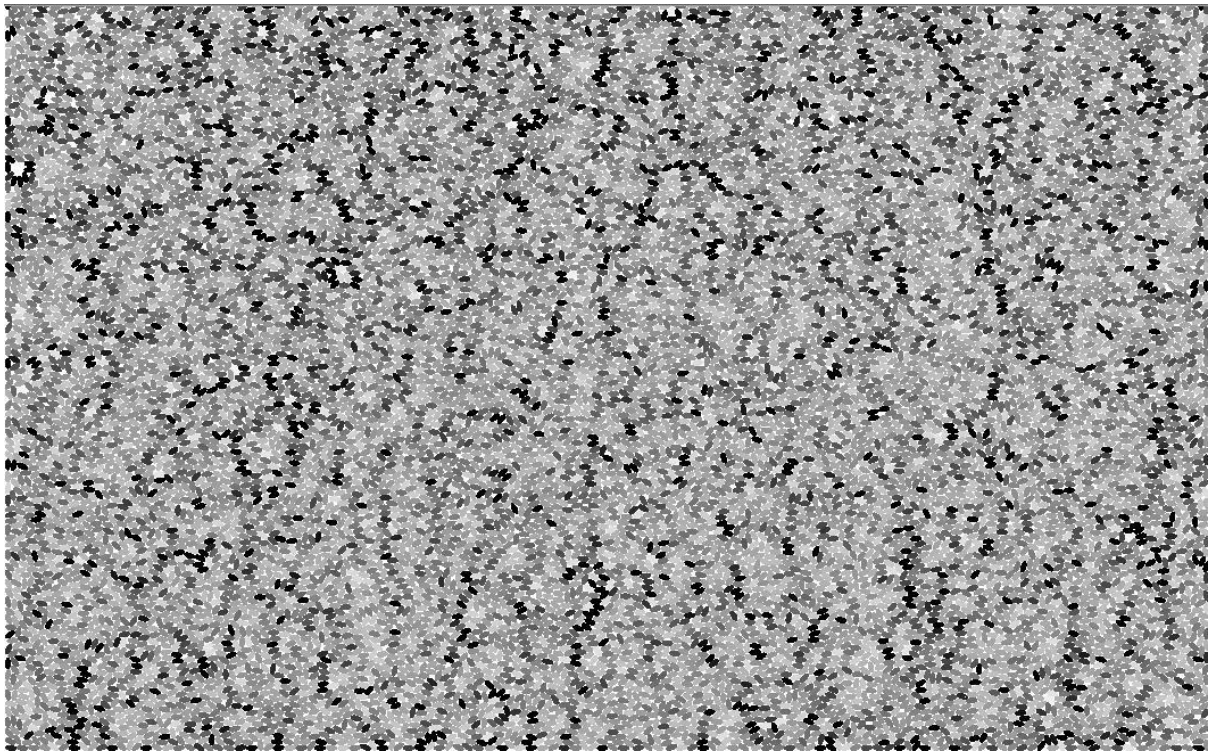
The spatial analysis of the differential stress distribution permits the determination of characteristic length scales of the stress patterns observed within a specific system. This is done as it allows the computation of correlation length in several independent directions, the method consists of analysing images in order to establish a correlation map.

5.4.2 Correlation map $C(x, y)$

The force chains are tracked visually by looking at the magnitude of the differential stress within their finite elements. As explained in the previous section, the stress tensor can be averaged over each particle area and each particle can be characterised by its average differential stress. As a result, a single scalar value can be associated to the area where a particle is located. As seen in Fig.5.10, the particulate differential stress map (PDSM) describes the same highly stressed patterns as the elemental ones, but it presents the



(a)



(b)

Figure 5.10: *PDSM image used for the computation of the correlations a) Stress map for* $\alpha = 1.0$. *b)* $\alpha = 2.0$. *The friction coefficient between the grains is set to* $\mu = 0.5$. *For the ease of comparison, the greyscale is identical in both packing. The particles stress is depth-normalised. We can see from this figures that the particulate differential stress possesses a spatial distribution which is a function of the shape of the particles employed.*

advantage of being depth-normalised so that the chains can e revealed independently of the depth. Additionally, averaging the stress data over the particle area reduces significantly the amount of noise in the image caused by the local fluctuations of the elemental stress.

The 2D stress correlation function can be calculated directly by image analysis of the PDSM. This function is in fact similar to an autocorrelation function and can be calculated in both real or Fourier space. For convenience, the computation of the autocorrelation function is performed in Fourier space. The procedure consists of first applying a Fourier transform of the PDSM, $I(f_x, f_y) = \mathcal{F}(PDSM)$, where $\mathcal{F}(\cdot)$ is the Fourier transform operator. Second, the resulting function is squared, and its inverse Fourier transform is taken which gives the correlation map, $C(x, y) = \mathcal{F}^{-1}(I^2(f_x, f_y))$. To obtain the final correlation map, the origin of $C(x, y)$ is shifted to the centre of the picture (see Fig. 5.11).

5.4.3 Results & discussions

The 2D correlation function is represented as a map, and the scale of the axis is expressed in equivalent particle diameters, r_g, which is the diameter of a disc with the same area as the ellipse. Fig.5.11 is a greyscale representation of the 2D stress correlation function. It is observed that the correlation maps differ significantly from one system to another. In particular the six branch star structure observed uniquely for the case of discs packing (Fig.5.11a) underlines the fact that differential stress is preferentially transmitted along directions given by the hexagonal structure of the packing for several particles and expands over several particle diameters in each of these directions. However, the star structure observed with discs is not present as soon as particles with very small aspect ratio are considered. Fig.5.11b, depicts the correlation of a pack consisting of particles with aspect ratio $\alpha = 1.1$, which indicates no such star structure patterns. Instead, it is observed that the horizontal correlations are attenuated very sharply, while the vertical ones extend over several particles. Moreover, the stress is transmitted not only vertically, but equivalently in a fan shape direction along the vertical axis with an aperture angle close to 60°. Similar patterns are distinguished for the packing of the elongated particles ($\alpha = 2$), but the orientation of the stress correlations are mainly vertical with a low aperture angle of less than 30°.

The analysis of the correlation maps suggests that each system is characterised by an anisotropic stress correlation map that is influenced by the particle shape. The correlation map permits the characterisation and the comparison of the mechanical anisotropy of each packing. In particular, Fig.5.11b indicates that in every case the maximal correlation length corresponds to the vertical direction and the minimal correlation length matches the horizontal. As a results, a section of the correlation map was extracted in both directions for each of the three cases, $\alpha = 1.0, 1.1$ and 2.0 (Fig.5.12). This function is

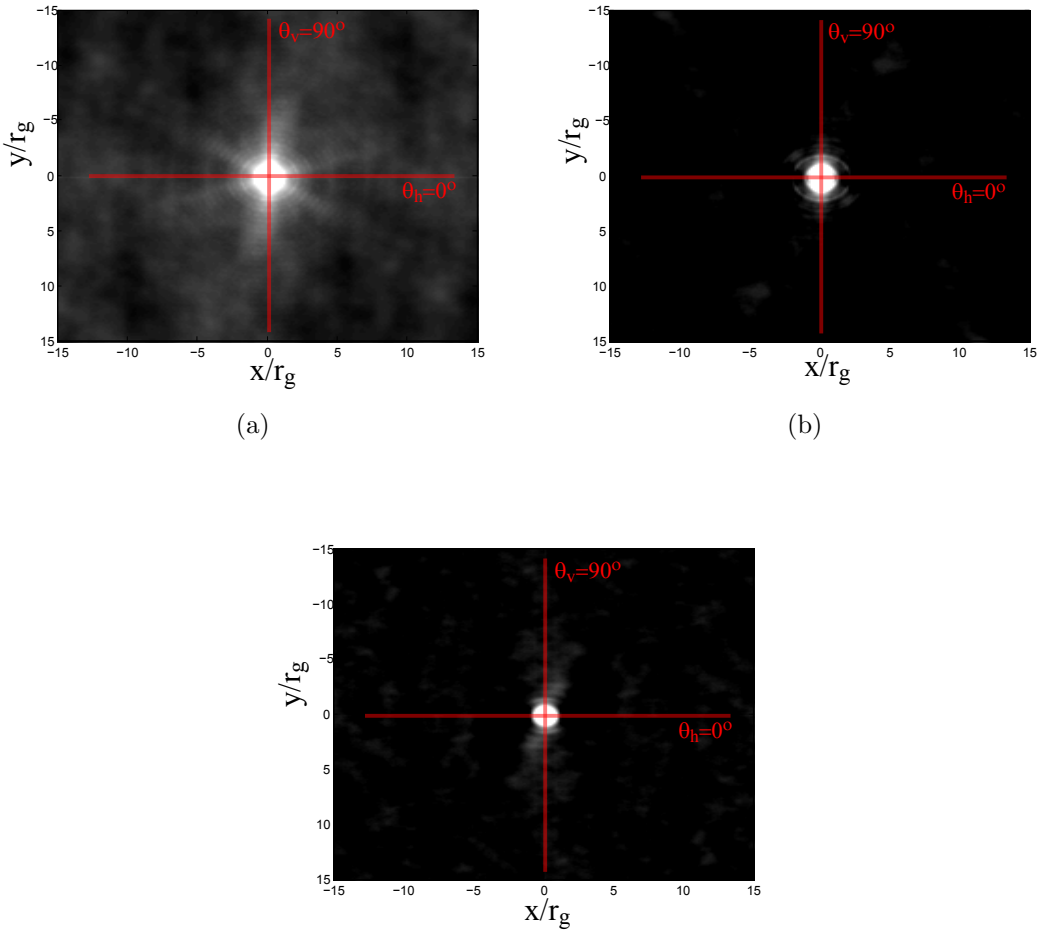
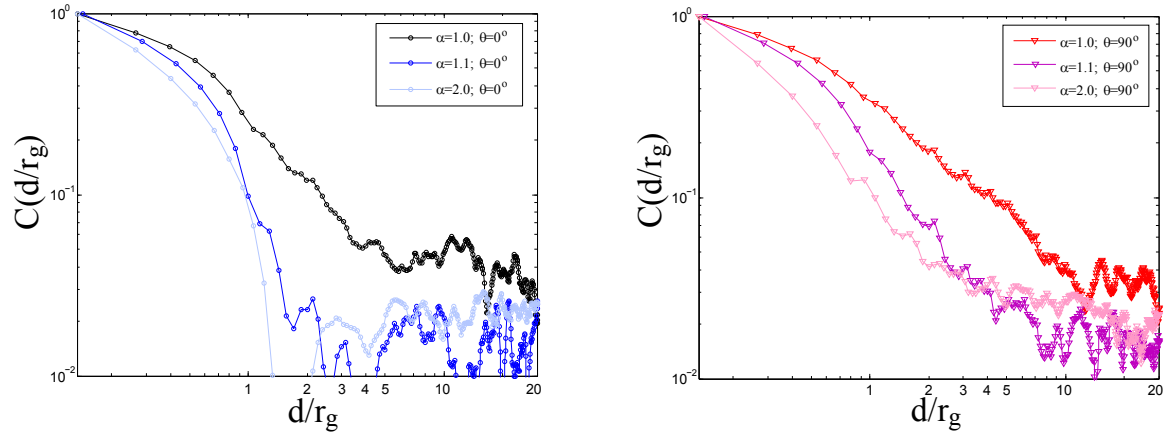


Figure 5.11: *Correlation map of the differential stress average over the particle area with a) $\alpha = 1.0$, b) $\alpha = 1.1$, c) $\alpha = 2.0$. The darker regions correspond to low correlation values, and brighter ones to high correlation values. The horizontal and vertical red lines indicates the direction of correlation represented in Fig.5.12*

calibrated so that is varies between 0, when the correlation is minimal, and 1, when the correlation is maximal. At long distances from the center, the correlation values fluctuate around small values close to 0 but are generally different from it, although the system shows no sign of correlations and may be treated as noise. The correlation function is usually expressed using an exponential form, $g(r) = Ae^{(\frac{r}{\xi})}$, where ξ gives the correlation length of the system. Small values of ξ indicates fast exponential decays of correlations, whereas large ξ indicates that the system is correlated over long distances. Physically, the correlation length gives a measure of the vertical and horizontal extension of the stress correlations, gives an idea of the typical distance separating two stress paths in a given direction.

The horizontal direction, perpendicular to the direction of the gravity which also



(a) (b)

Figure 5.12: *a) Correlation in the horizontal direction for pack with* $\alpha = 1.0; 1.1; 2.0$ *b)Correlation in the vertical direction for pack with* $\alpha = 1.0; 1.1; 2.0$*. The correlation along the vertical axis propagates over a larger range which confirm the influence of the particle shape on anisotropy of the stress distribution.*

gives the orientation of the main axis of compression, the stress correlations spread over short length scales. Nevertheless, in systems composed of discs the stress is correlated horizontally over larger distances than with elliptical grains. The correlation length increase from less than a particle diameter with ellipses to $\xi = 3$ for the discs.

Along the vertical direction, parallel to the natural axis of compression imposed by the gravity, larger correlation lengths are observed. For each of the three cases, the vertical direction corresponds to a direction in which the force chains are likely to be directed. Fig.5.12b confirms that the correlation of the differential stress span over larger lengths than along the horizontal direction, independently of the particle shape. Again, it is noted that the particle shape affects the transmission of the stress as increasing the particle aspect ratio results in less spatially correlated stresses. For a systems composed of discs at rest, the stress is correlated over more than 5 particle diameters. For ellipses the correlation distance decreases to about 2 particle diameters which is also significantly larger than the value obtained in the perpendicular direction.

Finally, the decay of the correlation function is better approximated by a power law in the case of discs, while an exponential law better characterises the case of the ellipses. In Fig.5.12b, the stress correlation function in the vertical direction decays more like a power-law for the discs. It indicates no evidence of a characteristic length, but rather suggests scale invariance of the stress in the vertical direction. This trend is supported by experimental measurements performed by Majmudar and Behringer [118], stating that the spatial force correlation function may be a power-law type in the direction of propagation of the force chains suggesting scale invariance of the stress propagation with isotropically constrained systems of discs.

The observed dependence of the mechanical property of a granular media with the particle shape has considerable consequences. The usual numerical analysis of granular materials are mostly limited to spherical particles, and in such peculiar conditions, the distribution of contact forces has been identified as a consistent way to characterise the force propagation in a granular media. By extension, some of the statements concluded for spherical particles are used for the description and the understanding of granular matter in general. Nevertheless in this work, we discovered that by simply using elliptical particles rather than spherical ones the distribution of both contact forces and stresses become significantly different. Considering that the granular system is build by using an ubiquitous collective deposition process realistic in many natural situations, it is suggested that the observations stated for a system of spheres are in fact exceptions more than rules, and that they are subsequently unsuitable for the understanding of most configurations encountered in granular media. The construction method of the media is important, notably because it affects the ordering between particles, which are also likely to happen in other type of media such as sedimentary rocks. Moreover, the interpretation of experimental evidences supporting the numerical observations remains restricted to the analysis of the contact forces measured on the boundary of the system and mostly to spherical particles. At this time, experimental work with non-spherical particles still requires extensive investigation. For instance Zuriguel et al. [234, 233] have recently shown experimentally by analysing the forces network of 2D heaps that elliptical particles transfers the stress differently than spheres. The present work confirmed that the stress propagation is strongly dependent on the particles elongation and subsequently support the idea that stress in granular media should not be characterised by only considering spherical particles.

5.5 Conclusions

The present numerical simulations and the subsequent analysis of the stress and contact forces possess the major advantage of removing the experimental limits encountered with granular material, in the sense that "ideal" systems can be fully described. In particular the method permits a complete calculation of each component of the stress tensor and the contact forces between interacting particles together with arbitrary shaped and deformable particles.

The stress distribution is seen to be related to the elongation, i.e. the ellipticity, of the particle and the commonly observed exponential decay of the large force, characteristic of granular systems with force chains, disappears when considering elongated particles. An analysis of the elemental stress distribution shows that the distribution of the stress is related to the average coordination number of the granular system. The analysis of the

individual components of the particulate stress tensor shows that the change of distribution of the differential stress with particle shape are uniquely supported by the diagonal terms of the particulate stress tensor. T^p_{xy} is found to be independent of the stress patterns shown in the systems, which interestingly shows that the information relative to the stress chains is mostly contained in the diagonal components of the particulate stress tensor.

The spatial distribution of the stress was analysed using 2D stress correlation functions in order to characterise the mechanical anisotropy of the packing. The direction and length of correlations shows a dependence on the particle shapes. Discs demonstrate singular stress transmission with a high degree of correlation directed in 6 preferential directions caused by the presence of hexagonal structures in some areas of the system. However, elliptical particles shows correlation directed mainly vertically that propagate over shorter lengthscales than discs. It is particularly noticeable that the correlation length decreases when the particle elongation increases, which suggests that force chains propagate more efficiently through rounded granular particles.

Following the results presented in this chapter, there is a need to quantify more precisely the stress heterogeneities of granular system. This can be done through a rigorous analysis of the force chain network. This is the aim of the next chapter, where an algorithm characterising the force chains will be introduced. The results will be used to differentiate more quantitatively the force chain network observed in granular systems built with variably elongated shapes.

Chapter 6

Force Chain detection: strategy, algorithm and calibration

6.1 Introduction and motivations

In contrast to heterogeneous solids or fluids, the stress in granular materials is distributed among discrete contacts between macroscopic particles. Experiments [113, 133, 85, 41, 50, 118, 233] and simulations [169, 171, 145, 194, 100], have shown that this distribution is often highly heterogeneous, with a small subset of contacts carrying relatively large forces while a significatively large fraction of contacts carry forces smaller than the mean. Moreover the large forces self organise along "force chains", giving rise to network structures [85, 118]. For decades, force chains have been consistently observed within granular materials both experimentally and numerically. It was proposed that the presence of these stress heterogeneities could have an impact on the fragility of the larger ensemble [31]. The subnetwork composed of the strongest inter-particulate forces has been tagged as the main structure responsible for supporting the external load, while the *weak* network of contacts carrying relatively small forces has been attributed to the properties of a supportive fluid-like phase [169]. Within this picture, the system as a whole has been conceived as a mixture of a fluid-like phase: the weak network, and a solid-like phase: the strong network.

However, the idea of a load-based criterion to differentiate the supposed fluid-like from the solid-like phases has been questioned in recent publications [195]. A recent experimental observation indicates the possibility for the force chains to follow distinct patterns of propagation in systems composed of (slightly polydisperse) discs compared to $\alpha = 2.0$ ellipses [234, 233]. Furthermore, a recent theoretical examination of the problem points out that the characteristics of force chains are related to the deviation of the system

connectivity from their isostatic state, predicting that force chains should scatter in the regions of high connectivity [21, 22]. Consequently, the test of such a theory, provided in [22] can be performed by analysing the evolution of the force chains in different systems close to the isostatic limit.

To advance the understanding of stress distribution in granular matter, we need to develop more realistic simulations that allow researchers to validate or to exclude theoretical assumptions in the description of the stress transmission within a granular material. The aim of this work is to demonstrate the effects of particle shape on the stress distribution in granular packs. Firstly, there is a need to quantify with precision the stress distribution as it guides the choice of partial differential equations to use for the description of the stress in granular media within the continuum theory framework. In particular an extension of the actual theories of stress transmission to the general case of arbitrary shaped particles is not straightforward. In this chapter, a modification of the force chain detection algorithm by Peters et al. [155] was used, based on the correlation between contact force rather than the average load carried by individual particles. Secondly, despite recent breakthroughs [133, 118, 234], the extraction of quantitative information from experimental setup remains complex and sometimes limited. As a result, an advanced numerical model, which possesses the ability to test various deformable particle shapes within which the stress tensor is determined, is necessary. The model can then be used to investigate and characterise the stress propagation in granular materials in a controlled way.

In this chapter, I introduce and illustrate an algorithm to detect the networks of force chains that develop in granular systems. A sensitivity analysis to the input parameters is performed in order to calibrate the constraining parameters. This stage is crucial in order to compare different systems and it can be viewed as a normalisation procedure. This algorithm is then used to perform a statistical analysis of the force chains in term of directionality, length and the fraction of particles carrying it.

6.2 Description of the FCD algorithm

6.2.1 Definition and principles of the algorithm

An algorithm based on a rigorous definition of a force chain [27, 29, 155] was applied in order to identify reproducibly all the force chains within a granular media. In particular, [155] proposed the use of three independent criteria to constrain the recognition of the force chains: the length, the strength (or intensity) and the linearity.

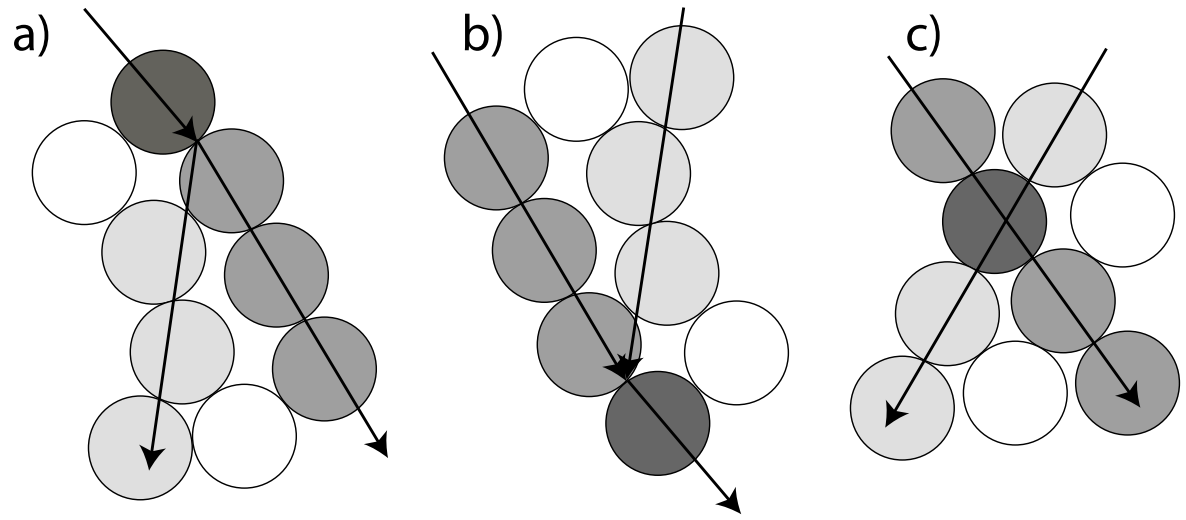


Figure 6.1: *Three types of force chain configurations handled by the FCD algorithm. a) Chain splitting, a old chain continue while a new connected chain is created. b) Chain joint, two chains joints in a single particle and the weakest stops automatically. c) chain crossing, two chains cross in a single particles, but both of the chains continue their way throughout the system with no (or negligible) attenuation of their strength.*

Length : A force chain transmits the stress across distinct particles. The stress is propagated through a finite number of particles before the chain eventually splits or vanishes. In this work, a minimum number of three consecutive particles [155, 27] is considered necessary in order to qualify the assembly as a potential force chain. The effect of the length constraint will eliminate isolated stressed contacts to be a potential force chain carrier.

Intensity : (high stress concentration) A force chain consist of a succession of particles linked to each other by strong contact forces. As a result, the weakest contact forces do not contribute to the transmission of large stress and need to be filtered. Because of the gravity, the load received by the particles increases with the depth. As a result, the contact forces are normalised with the depth to remove the effect of the overburden load (see Section 6.2.1.2). The average contact force, $\overline{f_c}$, is chosen as a cutoff value, $f_{cut} = \overline{f_c}$ to separate the small force from the large ones. This approach is different in essence from the criteria applied in [155], which consists of determining the orientation of the main axis of compression of each particle (by calculating the particle stress tensor and looking at the direction which gives the strongest eigenvalue, i.e. the maximum principal stress). In this work, the direction of the strongest contact forces are used for the determination of the force chain orientations rather than the direction given by the principal stresses.

Linearity : Experimental work, and previous numerical simulations have shown that the force chains have a quasi-linear direction of propagation over few particle diameters.

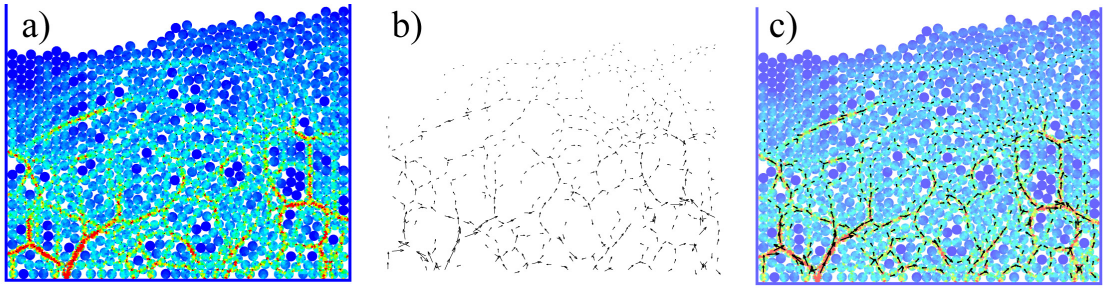


Figure 6.2: *a) Figure of a grain packing of discs. The color scheme represents the magnitude of the differential stress (blue is low differential stress and red is large differential stress). b) Network defined by the depth-normalised contact forces larger than a cutoff value ($f_{cut} > 1$). c) One can see that the force network superimposes upon the highly stressed paths hence justifying the use of the contact forces alone to identify the chains. Similar conclusions can be drawn for systems with non-spherical particles.*

This is due to the fact that a quasi-perfect alignment of contacts, for which the inter-particulate forces between the particles of a chain point in a similar direction, is a necessary condition to resist efficiently to the accumulation of load. A tolerance angle between the orientation of two consecutive links, θ, is used in order to prevent excessively curved chains that are not realistic.

The algorithm used to extract the force chains is inspired from the original algorithm proposed by Peters et al. [155] but it is modified in such a way that a force chain follows a continuous path connecting highly stressed contacts that support forces pointing in the same direction. With this approach only the contact force vectors are used to identify the force chains. The hypothesis that the stress chains can be analysed by considering the depth-normalised contact force vectors is justified by the illustration in Fig.6.2 where it is observed that the strongest force vectors follow the same patterns as the differential stress. This subtle difference makes the calculation algorithm and definition more suitable for non-circular particles as the stress paths do not necessarily pass through the particle centres. Additionally the identification of force chains crossing also becomes feasible as well as chains splitting or chains joining (see Fig. 6.1). Otherwise the present approach is similar to the proposal of Buchholtz [27] but including the constraint imposed by the logical definition of force chain given by Peters et al. [155]. In this Chapter, the implementation of the modified version of the algorithm is described and tested before being applied to systems comprising deformable particles of aspect ratios greater than one. Using the above definitions for the length, intensity and linearity, I describe the details of the implementation in the next stage.

Table 6.1: *simulation parameters*

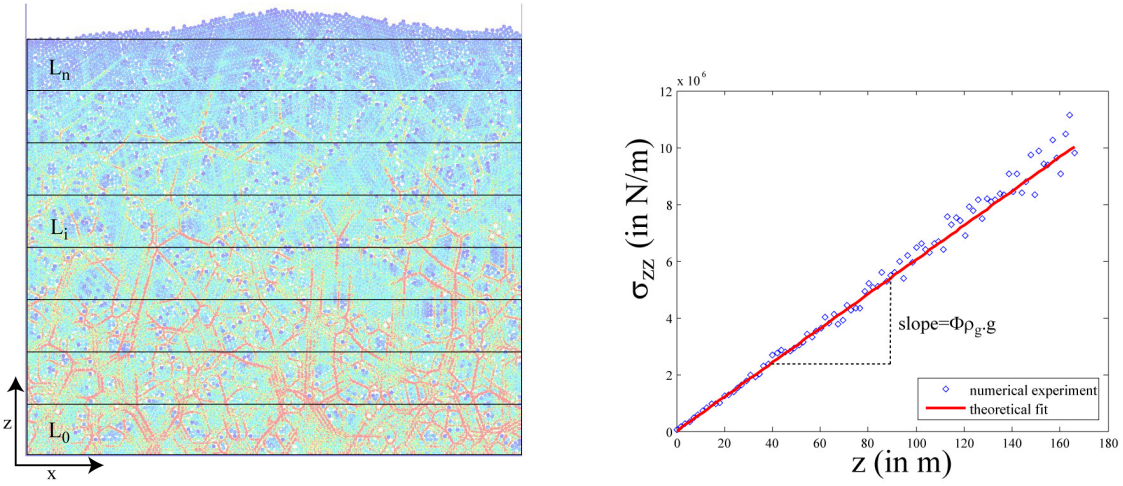
Parameter	Symbol
$\alpha = 1 - 5$	Aspect ratio
r_{eq}	Equivalent radius ellipses
ϕ	Packing density
σ_{yy}	Average vertical stress component of the grains
f^i	i_{th} non-normalised contact force in a given layer
$\overline{f_c}$	Average normalised contact force
f_{cut}	Force threshold
L	Minimum chain length
θ_1	Angle between consecutive contact forces
θ_2	Angle between branch vector and contact force
θ	Tolerance angle
C_i^j	Contact matrix, the superscript j indicate the contact number and the subscript i denotes all the contacts in the neighbourhood of j
f_k^j	Contact force in direction k at contact i. $f_1^j = f_2^j + 180°$
M^i	Total number of contact forces in the i^{th} layer
ℓ	Force chain length
ζ, γ	Fitting parameters of exponential distribution
z_{chain}	Coordination number of particles in force chains
z_{max}	Maximum coordination number of particles in force chains (obtained by varying f_{cut})
g	Gravity

6.2.1.1 Variables

6.2.1.2 Pre-step: depth-normalization of the force/stress

An array of data containing the list of contacts with their magnitudes, their positions and the particles involved in the considered contact is extracted from the packing data and read as input to the FCD algorithm.

Two types of physical entities $\mathcal{P}_i$ are extracted from the numerical simulations, the contact forces and the stress tensor, available in each subdivision of the particle. In order to reduce the influence of the lateral walls and of the Janssen effect, the final height of the granular system is smaller than the width of the container. As a result, both stress and force increase with depth and these entities have to be normalised with respect to their depth [100, 155]. To do so, the static system is decomposed into equal layers within which



(a) (b)

Figure 6.3: *a) Decomposition of the domain into iso-layers. b) σ_{zz} vs. depth z and the fit function $\sigma_{zz}(z) = \phi\rho_g g z$*

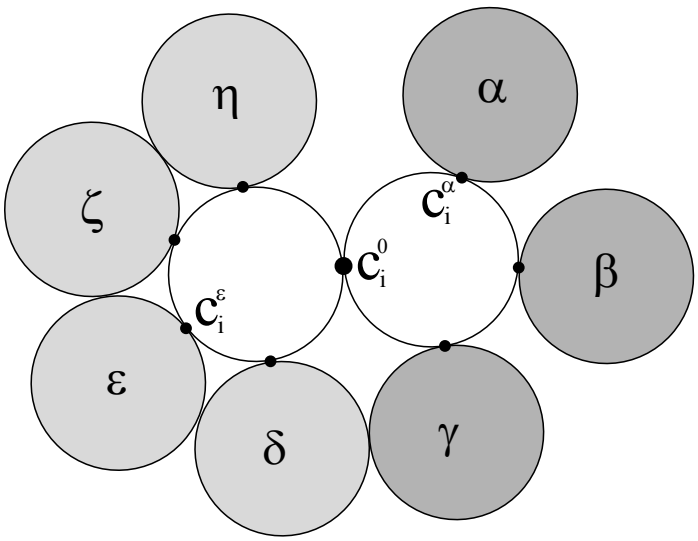
the M^j contact forces f^i located within the j^{th} layer are averaged $f_{av} = \dfrac{1}{M^j}\sum_{i=1}^{M^j} f^i$. At rest, we have to ensure that the granular system possesses a hydrostatic pressure profile [63] that has a slope $\phi\rho_g g$, where ϕ is the packing density of the considered medium, ρ_g the density of the grains and g the gravitational acceleration (see Fig. 6.3b). To perform the analysis of the data independently of their depth, each contact force is depth-normalised as follow : $\mathcal{P}_i^* = \frac{\mathcal{P}_i}{\phi\rho g}$.

6.2.1.3 Filter 1: Force magnitude

The first stage is to remove the contact points carrying forces smaller than a prescribed cutoff f_{cut}, leaving only contacts supporting relatively large forces in accordance with the idea that force chains involve contacts carrying stress higher than the average. Unless stated otherwise, f_{cut} is set in the following to be equal to the average force at active contacts of a packing configuration. Each of the remaining contacts C_i^j is labeled with an index $i = 0, 1, 2, \cdots$ relative to the contact number, and are grouped in a list of filtered "strong" contacts.

6.2.1.4 Filter 2: Force orientation

In the next stage, the first contact C_i^0 is arbitrarily selected in the list of filtered "strong" contacts in order to test if it belongs to a force chain. To do this, a sublist containing C_i^j neighbouring contacts is established, with $j = \alpha, \beta, \gamma \cdots$. The C_i^j list is formed from all



(a)

Figure 6.4: *Description of the neighbour list and sublist established in order to analyse the force chains.*

the contacts of the particle i and j surrounding the contact C_i^0 (see Fig.6.4a). Based on the idea that the contacts in a force chain must carry load in approximately the same direction [155, 24, 29], the neighbour list is filtered in order to leave only contacts carrying forces nearly aligned with the force at contact C_i^0. There are two possible directions associated with the force at contact C_i: the direction of the force that act on particle i and the opposite direction for the force acting on j ($j = \alpha, \beta \cdots$). Both these directions are considered in two separate steps, starting with the direction of the force $\mathbf{f}_k^i$ of the contact C_i, with $k = 0, 1$ indicating the search direction. Note that $\mathbf{f}_1^i = f_2^i + 180°$. The angle between the force $\mathbf{f}_k^i$ and the forces $\mathbf{f}_k^j$ in neighbouring contacts is calculated as in Eq. 6.1:

$$\pi - \theta_1 < acos \left[\frac{\mathbf{f}_k^i \cdot \mathbf{f}_k^j}{\|\mathbf{f}_k^i\| \|\mathbf{f}_k^j\|} \right] < \theta_1. \tag{6.1}$$

The contacts that satisfy the relation 6.1 are kept in the list while the rest are removed. The next contact is selected if $\theta_1 < \theta$ in Eq. 6.1, where θ acts as tolerance angle for the alignment of the local forces within a chain. The value of θ is set to $\pi/3$ based on the inter-grain friction between contacting particles. The contacts not respecting this criterion are deleted from the C_i^j neighbour sublist.

6.2.1.5 Filter 3: Branch vector - Force vector

The third stage is slightly more subtle: it consists of filtering the remaining contacts to ensure that the main orientation of a force chain coincides with the direction of the

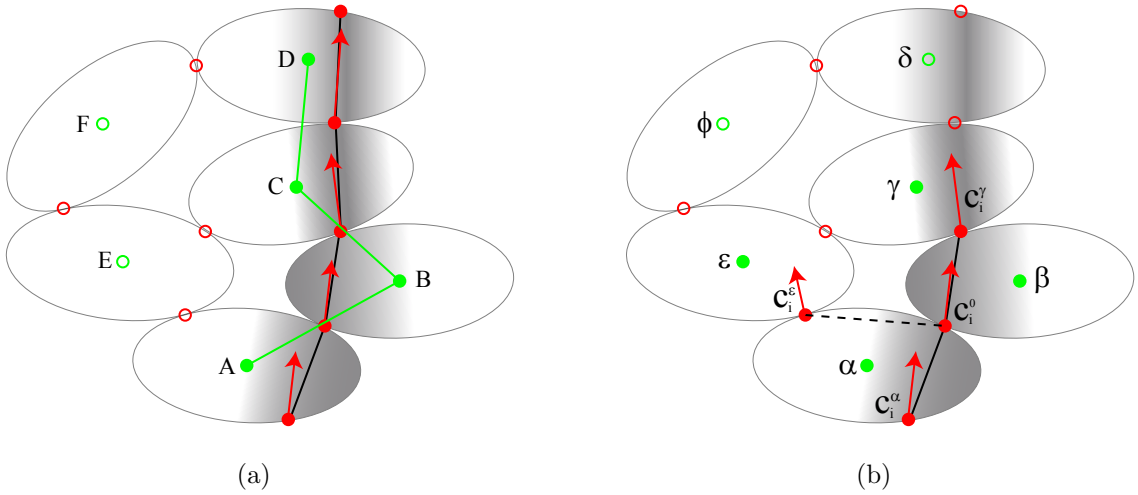


Figure 6.5: *a) Links between the contact forces and comparison with the path described by the connection between particle centres. This picture also illustrates that the angle between consecutive particle centres, i.e. the path ABCD, would be erroneous and non physical. b) Case where several contacts fulfill the condition imposed by the force orientation filter. An additional filter considering the angles between the branch vectors (black) and the force vectors (red) is applied in order to discard chains considered unrealistic for force chain propagation. The dashed line represents a potential chain direction that does not fulfill the requirement imposed by the second filter while the continuous lines do.*

load that they support. In other words, we apply an additional filter that calculates the angle between the branch vector of the chains $\mathbf{C}_i^j\mathbf{C}_i^0$ and the contact force $\mathbf{f}_k^j$ of the contact C_i^0. We check that this angle is not too large in order to avoid unrealistically twisted chains. To illustrate this, let us consider the situation illustrated in Fig. 6.5b) and assume that the contact C_i^0 is in the neighbourhood of C_i^α, C_i^γ and C_i^ε. The force vectors of the neighbouring contacts all fulfill the condition imposed on their direction as their contact forces have a similar direction to $\mathbf{f}_k^j$. However, the vector pointing from C_i^0 to C_i^ε forms a large angle with the direction given by $\mathbf{f}_k^j$. Therefore, the contact C_i^ε is not connected to C_i^0 and the force chain can not propagate in this direction. On the contrary the vectors $\mathbf{C}_i^0\mathbf{C}_i^\alpha$ and $\overrightarrow{C_i^0C_i^\gamma}$ respect the condition of alinement between the branch vector and the force vector and it can therefore be selected to form a new part of the force chain. With the third filter we reduce the sublist of contacts to all the contacts that respect the following condition:

$$\pi - \theta_2 < acos\left(\frac{\mathbf{C}_i^0\mathbf{C}_i^j \cdot \mathbf{f}_k^j}{\|\mathbf{C}_i^0\mathbf{C}_i^j\|\|\mathbf{f}_k^j\|}\right) < \theta_2, \tag{6.2}$$

where $\mathbf{C}_i^0\mathbf{C}_i^j$ is the branch vector, $\|\mathbf{f}_k^j\|$ is the norm of the force vector at the contact j and θ_2 is the second tolerance angle. In order to avoid overcomplicating the notation, both of the tolerance angles θ_1 and θ_2 are chosen such that $\theta_1 = \theta_2 = \theta$. In most of the case we use $\theta = 60°$ unless stated.

Once all the filters are applied, the neighbours sublist C_i^j is likely to be empty. In such

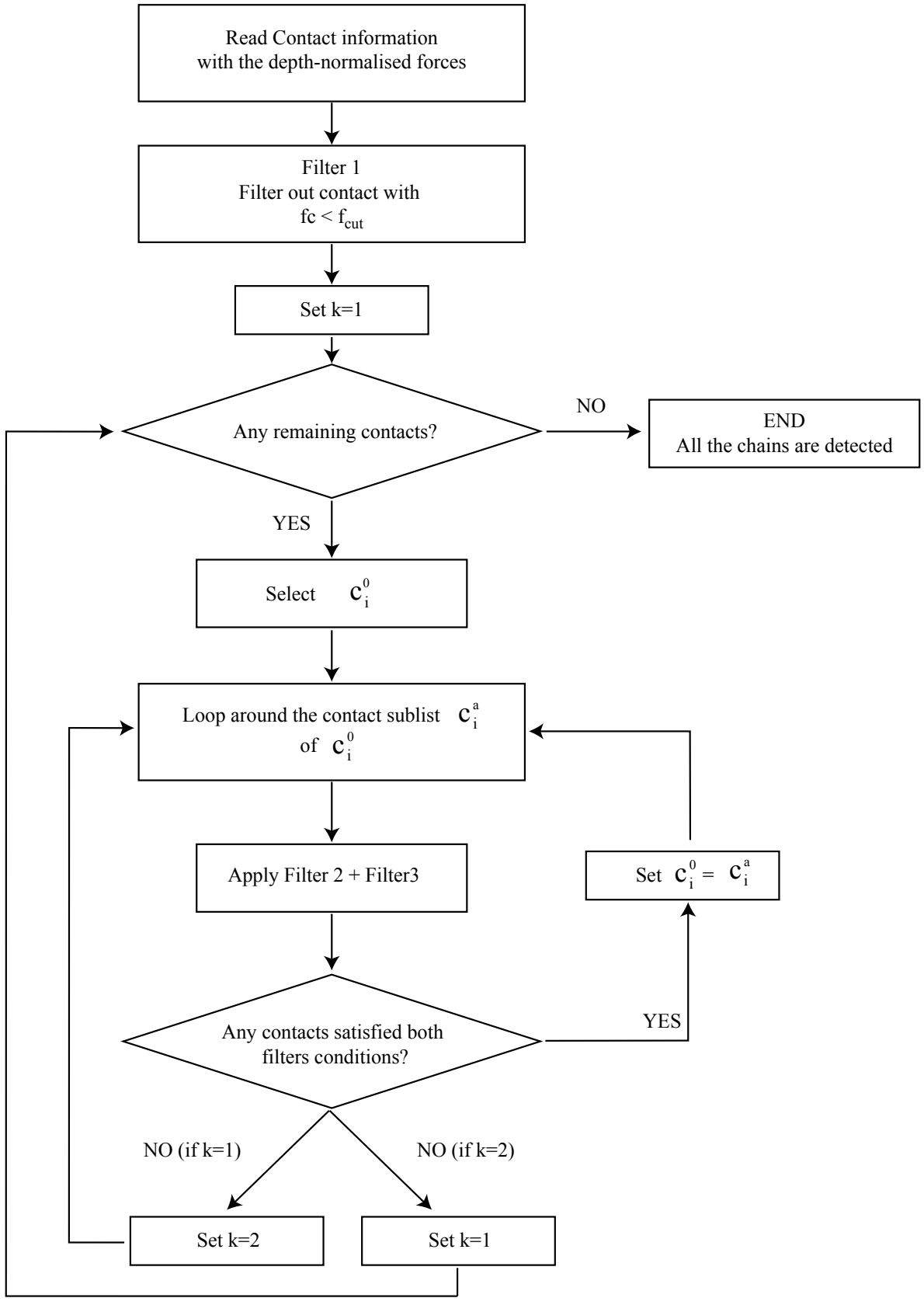


Figure 6.6: *Chart of the FCD algorithm*

case, the search for contacts in the chain along the direction chosen in step 2 (given by $k = 1$) ends and we start again from step 2, but choosing the opposite direction (given by $k = 2$). For instance, for the case (not illustrated) where the direction given by f_1^i is not correlated with the branch vector and the force vector of one of its neighboring contacts, the algorithm is re-applied from this contact but with the direction indicated by f_2^i. If this sublist is not empty, we select the next contact in the chain, for instance C_i^α, as to be the one carrying the greatest force among all the contacts contained in the C_i^j sublist. Then, the search for more contacts continues from C_i^α (which now becomes C_i^0) in the direction of the force supported in C_i^α. When no more contacts are found in both of the directions $k = 1, 2$, the set of contacts in the chain is complete.

Finally, the condition on the minimum force chain length, L, is imposed, stating that the minimal chain length must include at least three contacts. This criterion comes to eliminate highly stressed, but isolated, contacts.

6.2.1.6 Chart of the algorithm

The successive stage of the FCD algorithm are summarised in the Fig.6.6

6.2.2 Influence of the filter threshold criteria on force chain detection and calibration

The FCD algorithm, designed to detect the forces chains, produces results that are sensitive to the value allocated to each parameter, intensity, length and linearity. It is indeed important to quantify the effect of each of the criteria on the number of force chains identified in order to justify the values given as input for the algorithm.

6.2.2.1 Criterion 1 : force cutoff (parameter intensity)

The first parameter, the force cutoff, is expressed in terms of the average contact force of the system. As a results, if $f_{cut} = 0$, the algorithm will treat all the contact forces. In contrast, if $f_{cut} > 4$, most of the contact force will be filtered and automatically removed from the list of forces considered by the FCD algorithm. As seen on the Fig.6.7), between the two boundary values on f_{cut}, only a portion of the contacts are selected depending of f_{cut}. Firstly, it follows that the cutoff value influences greatly the number of contacts selected, and as a consequence the potential number of particles that will transmit the load. Secondly, at constant cutoff, the ratio of contact forces above the cutoff varies with the particle's shape, which shows that the contact forces are distributed differently from one shape to another for the case of the mono-shaped granular systems examined here.

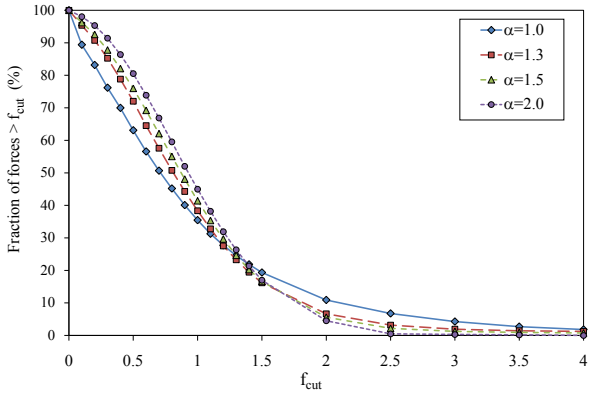


Figure 6.7: *Variation of the fraction of the total number of selected contact forces as a function of the cutoff value for different contact forces illustrated for ellipses with aspect ratios α from 1 to 2.*

When interpreting the f_{cut} plots of the Fig. 6.7, steep variations of the curves would suggests that a well defined cutoff exists and that stresses are clearly partitioned. Because the cutoff threshold is aimed at isolating the contacts that transmit the forces chains, only the large contact force have to be selected. This is done by setting the cutoff value at $f_{cut} = 1.5$ when interpreting quantitatively the characteristics of the force chain network.

6.2.2.2 Criterion 2 : force chain length L

The choice of a minimum length of a force chain is somewhat arbitrary. Three different length criteria, $L = 3$, $L = 5$ and $L = 7$ were considered, where L is the minimum number of contacts that a chain should exhibit in order to respect the selection criterion. Note that a force chains possessing L contacts comprise $L + 1$ grains. The influence of L on the percentage of particle forming force chains was tested for four different ellipse aspect ratios ($\alpha = 1.0, \alpha = 1.3, \alpha = 1.5, \alpha = 2.0$). As expected, increasing the value of L reduces the total number of particles within the chains because all the particles detected in chains shorter than $L = 7$ become excluded from the count. However, it is remarkable that the shape of the curve is conserved and that the only effect of increasing L is to shift the curves to the left. Importantly, the spreading of the transition zone for which the proportion of particle pass from, say 90% to 10% appears to be independent of L for each of the analysed systems.

6.2.2.3 Criterion 3 : angular sensitivity θ (parameter linearity)

Considering the FCD algorithm in detail, the linearity of the force chains is controlled by a set of 2 angles. To respect the fact that chains are transmitted through contact force pointing in similar directions, the angle between two consecutive contact forces θ_1

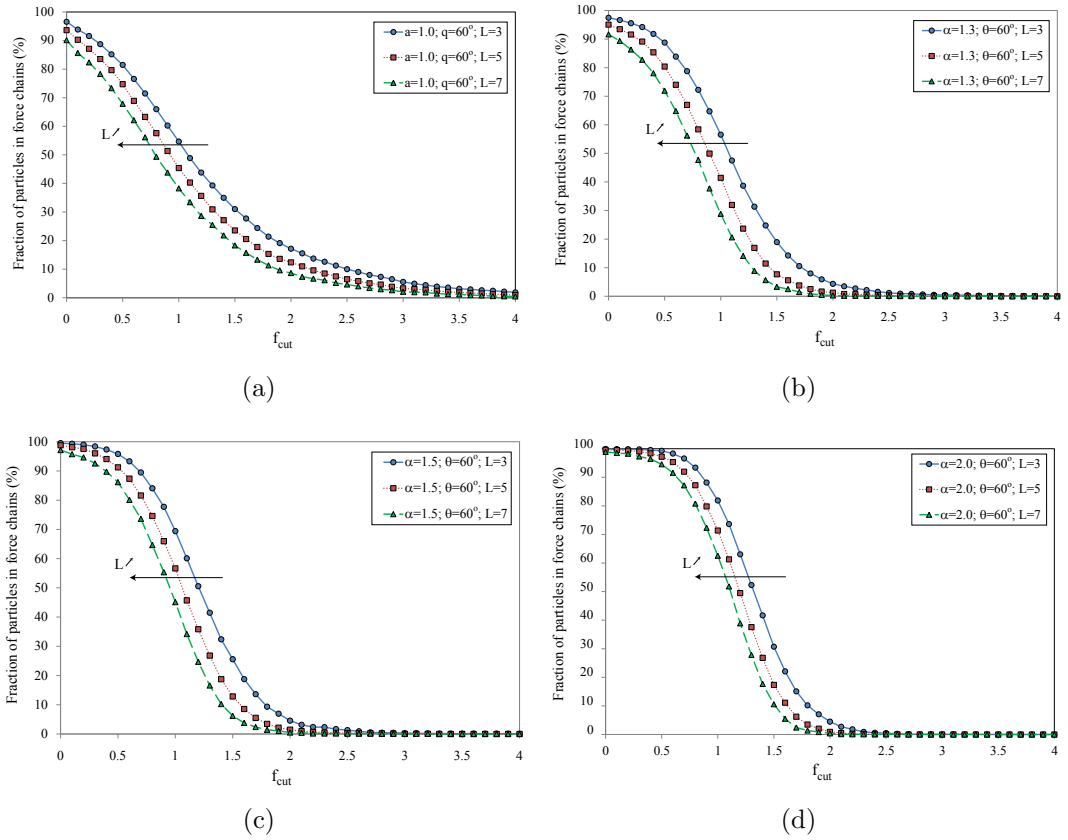


Figure 6.8: *Influence of the cutoff length on the proportion of particles composing the forces chains. a) $\alpha = 1.0$, b) $\alpha = 1.3$, c) $\alpha = 1.5$, d) $\alpha = 2.0$*

is used to constrain the directionality of the chain. In addition to θ_1, a second angle, θ_2 controlling the alignment between the contact force and the orientation of the vector that links a considered contact to the following one is used in order to avoid configurations where force chains cannot be propagated. For simplicity both of the tolerance angles are set to be equal so that $\theta_1 = \theta_2 = \theta$. In the following sections the angular sensitivity is simply referred to the angle θ, unless stated otherwise.

When θ is small, two successive links and two successive contact forces have to be aligned along very similar directions to fulfill the force chains requirements so that most of the paths identified after the application of the two previous criteria (intensity+length) are removed. In the limit case of $\theta = 0$, no chains can be identified. In order to take into account the fact that a force chain is not necessarily linear but rather sensitive to the spatial distribution of the contact, the critical angle of tolerance is increased to 60°. A value slightly larger than $\theta = 45°$ was proposed by [155, 139]. In [188] θ was reduced to a value below 30° to characterise the stress chains in dense gel. Note that the use of larger angles of θ is physically unrealistic as the stress cannot be transmitted efficiently through winding contact alignments.

For two packings with different particle shapes ($\alpha = 1.0$ and $\alpha = 2$), the length

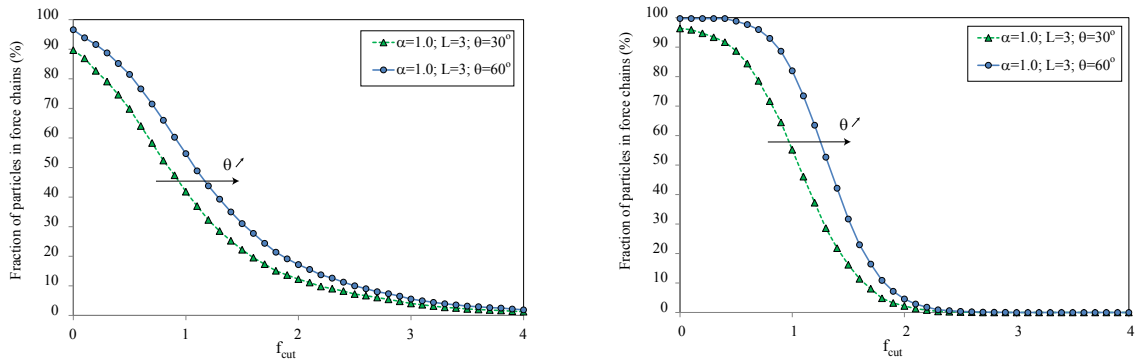


Figure 6.9: *Variation of the cutoff curve as a function of θ. a) $\alpha = 1.0$, b) $\alpha = 2.0$*

criterion was maintained constant and equal to $L = 3$ in order to see the dependence on θ expressed by the cutoff curve. For discs ($\alpha = 1.0$), the shape of the cutoff curve stays unchanged as θ varies. However, the reduction of θ from 60° to 30° reduces the number of particles carrying force chains and the cutoff curve is shifter to the left (Fig. 6.12a). The trend is different for the elongated particles $\alpha = 2$ (Fig. 6.12b). As for discs, the cutoff curve is translated to the left when lowering the angular tolerance.

The present analysis of the FCD algorithm shows that the profile of the cutoff curves are generally independent from the length parameter and the linearity parameter results (except for a slight angular sensitivity observed for elongated ellipses). As a result, the FCD algorithm is in practice weakly sensitive to the constraining parameters. This is true for reasonable values for θ and L (e.g. $30° < \theta < 60°$,$3 < L < 7$). Thus, it is plausible that the shape of the cutoff curves is uniquely a function of α. A small aspect ratio tend to spread the decays of the curves over larger values while the largest aspect ratios shows a narrow transition band between the domains in which force chains exist or do not. In other words, the force chains in systems of rounded particles, such as discs, are more persistent than for elongated particles, where the transition between a domain fully filled by force chains to a domain empty of force chains is confined to a narrow range of values of f_{cut}.

6.3 Comparison of the method and validation

6.3.1 Numerical experiment

To simulate the packing of the granular material, a combined finite-discrete element method is used [135]. In contrast with common DEM techniques, the method takes into consideration non-circular particle shapes. The particles, i.e. the discrete elements, are

divided into a subset of triangular finite elements within which stress and strain matrices are computed. Contrary to rigid irregular polygons employed in previous works[126, 2, 9], the finite elements composing our particles are allowed to deform according to a linear elastic stress-strain relationship, their mechanical constants under the influence of an external force field.

Following the method described in [71], the packs are created using a sedimentation type algorithm in which the particles settle on an initially flat surface under the action of gravity. To randomize the system, an initial random velocity is given to each particle originally positioned along a regular lattice. Due to an initial random impulsion, the particles start interacting with other particles and the container walls. The contact interactions cause the particles to translate and to rotate until they eventually settle in their final configuration (see Fig.6.10). Once the particles settle, sufficient time is given to reach a negligible level of kinetic energy and the pack reaches a mechanically stable configuration. At any stage of the deposition sequence the stress tensor of the entire particle system is readily accessible from our simulations as seen in Fig. 6.10.

Following this procedure packs of 15000 mono-disperse ellipses of different aspect ratios were created within a rectangular container of 120×140 units of length (given by the equivalent radius of ellipses $r_{eq} = \frac{\pi l}{\sqrt{\alpha}}$, where l is the long axis length, and α is the particle aspect ratio). The mechanical parameters used in all simulations were chosen to match stiff geomaterials such as concrete with a Young's modulus $Y = 25.8$GPa, Poisson's Ratio $\nu = 0.17$ and a density of $\rho_s = 2650$ kg.m^{-3} to which a viscous dissipative term is added in order to take into account the energy dissipated during the particle interactions. The inter-particle friction μ_{pp} is chosen to be equal to the friction between particles and container walls μ_{pw}, i.e. $\mu_{pp} = \mu_{pw} = 0.5$.

6.3.2 Algorithm validation

The force chain algorithm was validated by comparing the easily visualised differential stress intensity paths computed numerically with the combined finite-discrete simulations and the path identified by the FCD algorithm. It can be seen in Fig.6.10 the good agreement between the real network of force chains present in the granular systems and the chains identified with the FCD algorithm. The FCD algorithm is suitable for the force chain recognition and it is applied in the next section to several pseudo static packings produced with different particle shapes, for which a statistical analysis of the force chain properties is performed.

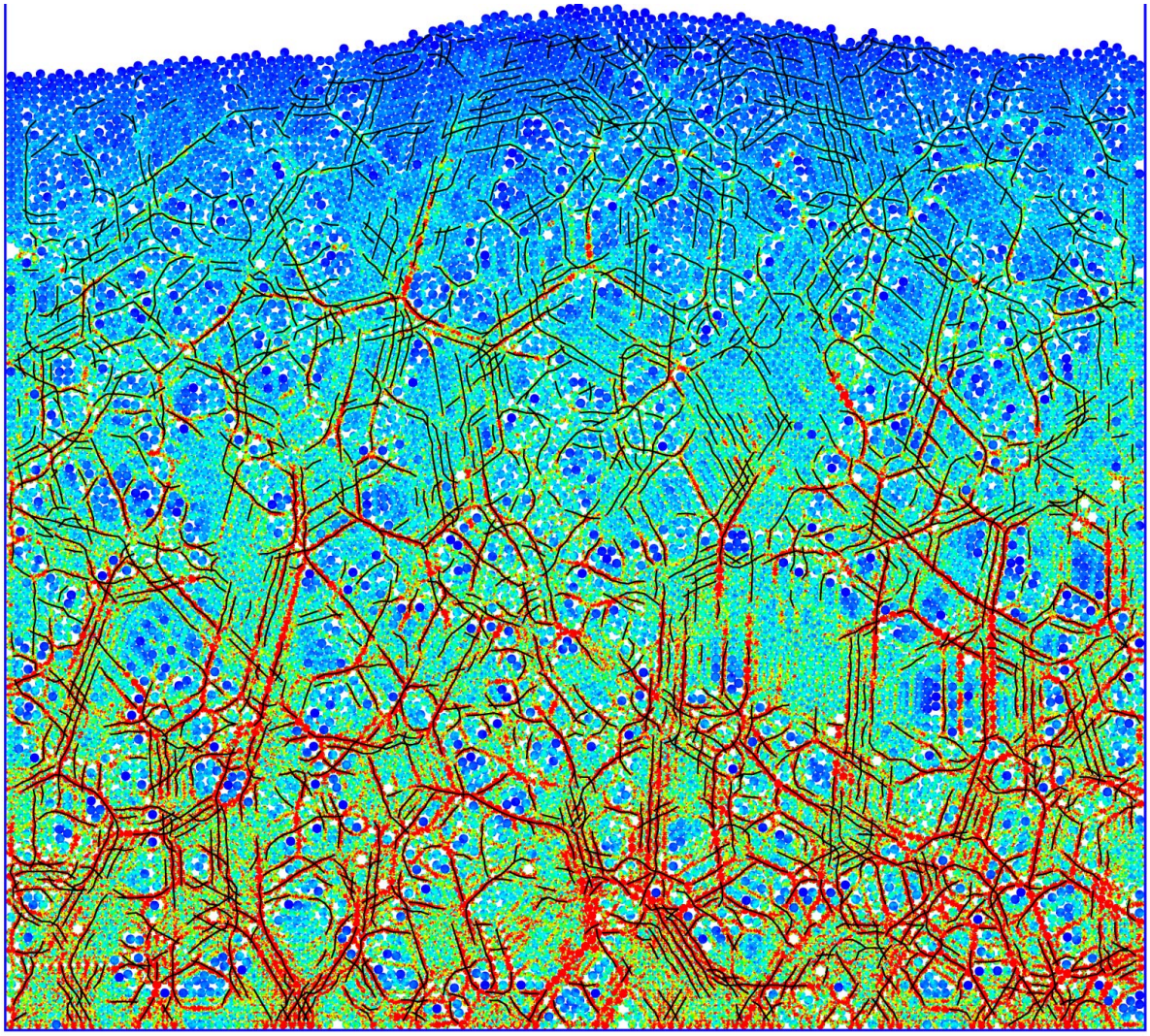


Figure 6.10: *Chain path recognition verification. In this figure, the differential stress received by the particles is used to evaluate the magnitude of the stress supported. The blue color correspond to the less stressed area while the red color represents the most constrained domains. A good agreement between the red patterns (i.e. the force chains) and the superimposed black lines which are the paths identified by the FCD algorithm is observed.*

6.3.3 Results and discussion

6.3.3.1 Fraction of particle carrying force chains

As explained previously, the fraction of particles that survives the successive filters is a function of the parameters used to constrain the FCD algorithm. Nevertheless, we have demonstrated that a change in the thresholds, i.e. L and θ shifts the cutoff curve laterally without modifying its profile. The fraction of particles that supports the load, as a function of the cutoff force, is shown in Fig.6.12 for 3 different particle shapes. The threshold values used for Fig.6.12 are $L = 3$ and $\theta = 60°$. For each particle shape, the fraction of remaining particles is lowered by increasing the magnitude of the cutoff

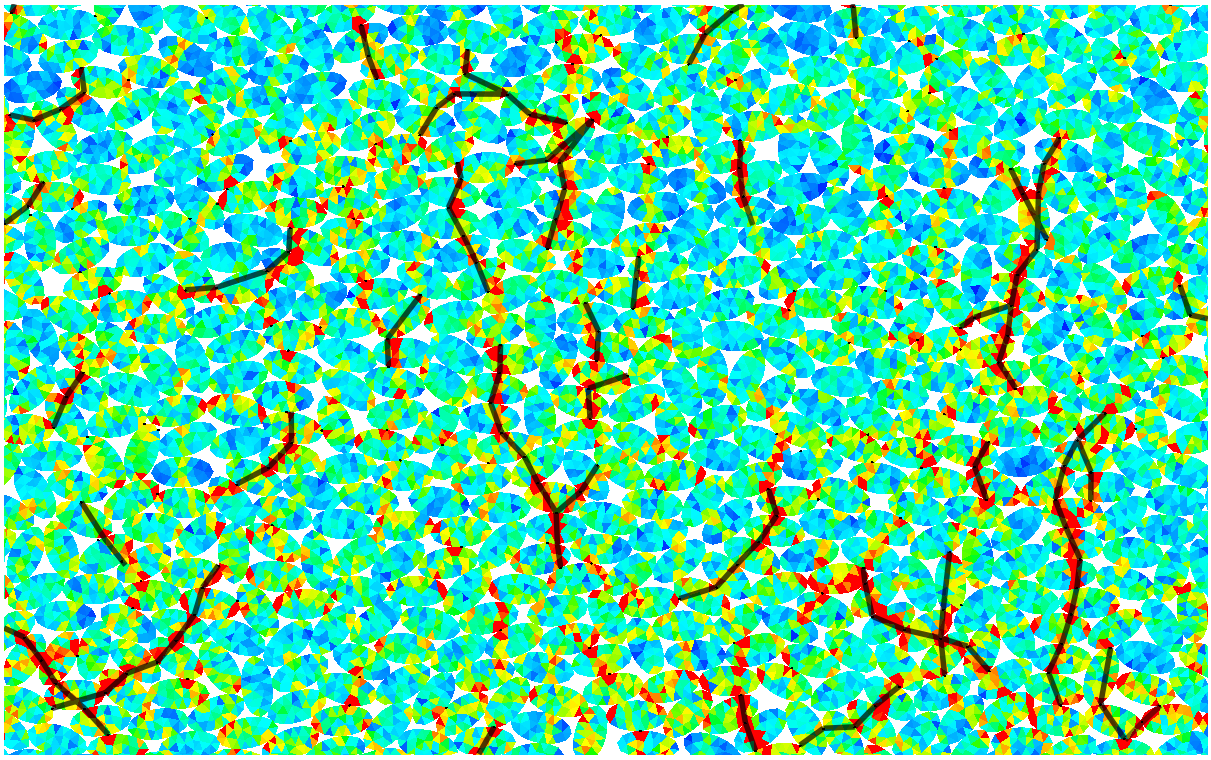


Figure 6.11: *Chain path recognition verification. The caption the Fig. 6.10 is identical with* $\alpha = 2.0$. *The figure in zoom in a small area of the system in order to insure the applicability of the algorithm to non-spherical particles.*

threshold. However, the slope of the f_{cut} plot decreases for low aspect ratios (rounded particles) and becomes steeper when considering systems of elongated particles. The stress response of the variation of f_{cut} is correlated with the particle elongation. This confirms that elongated particles transmit stress differently than discs. Packs of discs could in fact be viewed as a special case in this respect, not necessarily representative of the whole range of particle shapes that can be encountered. The force chains are connected by contacts carrying large magnitude of force, typically larger than $f_{cut} = 1$. To process the quantitative characterisation of the force chains, we set $f_{cut} = 1.5$ in order to filter the most dominant chains.

For well chosen values of f_{cut}, the total fraction of particles participating in the stress transmission through the force chains can be equal, and comparisons between the properties of the force chains identified in each systems can be made. As shown in the next sections, it is indeed important to consider that the characterisation of the stress consists not only to determine the total fraction of grains carrying the force chains, but also to characterise the orientation, the length or the connectivity of their particles.

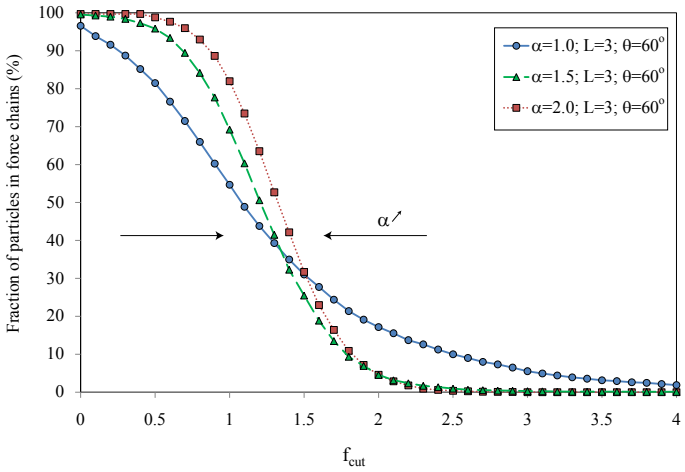


Figure 6.12: *Influence of the particle aspect ration on the shape of the curve.*

6.3.3.2 Force chains orientation

The directionality of the force chains was evaluated by considering the direction of the subsegments (or links) of a detected force chain in order to improve the quality of the statistical analysis. For a system of 15000 particles, an average number of 15000 links were used for the statistics. In Fig.6.13, where three peaks are well developed for discs, it is observed that the force chains are preferentially oriented along the directions $30° - 90° - 150°$, which is a consequence of the local ordering of the particles. In contrast, systems with elliptical particles do not transmit force chains along such linear "fault" lines but rather vertically. This does not indicate the presence of any type of structural ordering between the particles that would infer directionality for the chains. It is also worth pointing out that the elliptical systems respond to the same distribution laws, at the difference of the discs which has preferential direction of propagation. Although force chains can in principle be oriented horizontally, the direction of the external field imposes a constraint and it is supported by chains mainly pointing vertically.

6.3.3.3 Length distributions

As described above, the particle shape influences the directionality of the chains. The difference of patterns of stress transmission observed for different particle shapes can be inferred to the difference of the contact networks. Consequently, the length of the force chains, whose orientational distribution by the particle shape (see Fig.6.13), is also related to the geometry of the contact force network. The distributions of the chain lengths shown in Fig.6.14 for three different particles elongation ($\alpha = 1.0$, $\alpha = 1.5$ and $\alpha = 2.0$). Each distribution, is well fitted by an exponential function $P(\ell) = \gamma e^{-\frac{\ell}{\zeta}}$, where γ and ζ are fitting parameters. Note equally that ζ is also the mean value of the force

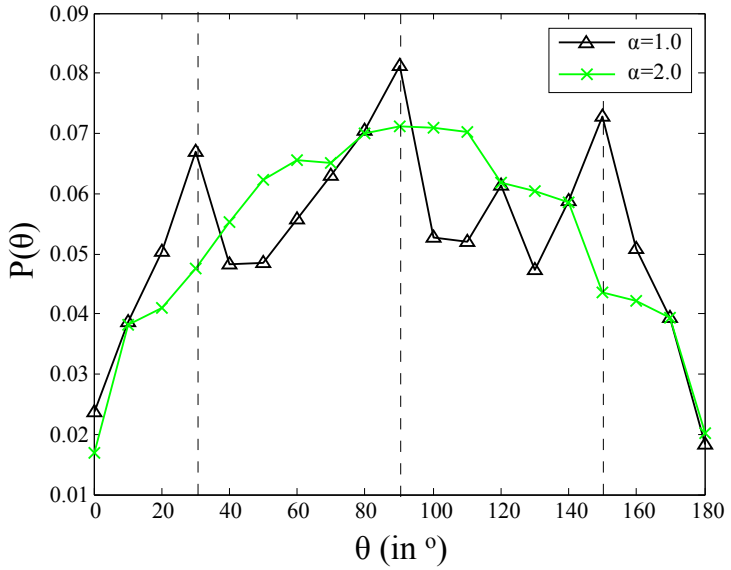


Figure 6.13: *Orientation of the chain links for a systems of discs and a system of ellipses both interacting with friction for $f_{cut} = 1.5\overline{f}$. A pronounced directionality of the chain in the case of discs with an orientation more likely in the direction $30° - 90° - 150°$ given by the direction of hexagonal packing. In contrast, the ellipses show a preferred $90°$ alignement with a broad dispersion of angles.*

chain length. For each of the three particle shape, the exponential decay is characterised by the slope ζ which is also a measure of the typical number of contact of an average chain. It appears that the distribution of the force chain length in the system differs with the ellipse aspect ratio. The average chain length reduced with the elongation of the particles. Put differently, the discs are more efficient in transmitting stresses and the typical chain length as given by ζ is almost twice as long as for ellipses with $\alpha = 2$. The analysis for the force chain lengths was performed by using the number of contact as a unit of length although similar conclusion can be drawn by considering absolute lengths. Such a difference between the three systems constructed with the same sedimentation technique and identical initial conditions is rather surprising but it confirms the recent experimental suggestion of [233] that force chains of elliptical particles have shorter typical length. Additionally, the decrease in force chain length observed for more eccentric shapes is consistent with the increase with the augmentation of the coordination number of the more eccentric particles. This observation is supported by the idea developed in [22], which suggests that a system closer to the isostatic state (discuss in Chapter 4) possess longer force chains. If the coordination number of the grains is larger than the isostatic limit, or significantly different, fewer force chains are expected to carry the load.

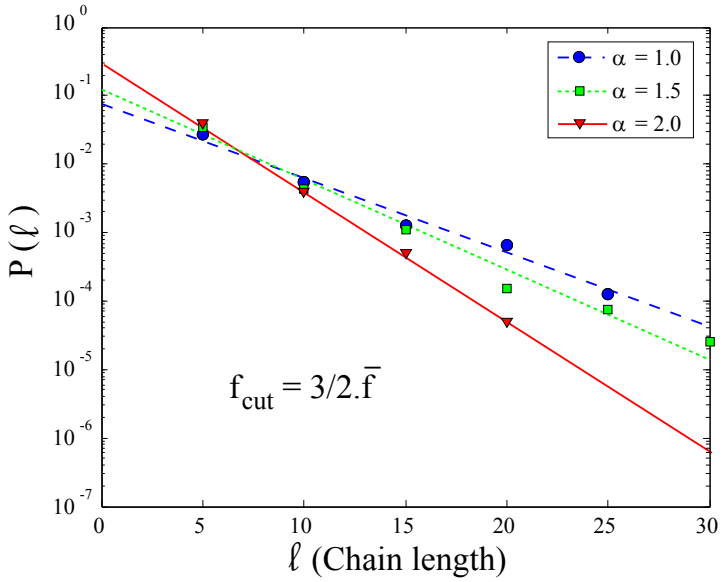


Figure 6.14: *Distribution of the force chain length (in terms of number of contacts) for a system of discs (blues circles) with $z = 4.37$ (z is the coordination number) and 2 systems of ellipses (green squares for $\alpha = 1.5$ and red triangles for $\alpha = 2.0$). All three curves exhibit a negative exponential distribution, $P(\ell) = \gamma e^{-\frac{\ell}{\zeta}}$, the shorter chains being the most frequent. The dashed blue line is the best fit distribution for the system of discs ($\gamma = 0.08$ and $\zeta = 4.0$), green is for ellipses of $\alpha = 1.5$ ($\gamma = 0.12$ and $\zeta = 3.3$) and red is for ellipses of $\alpha = 2$ ($\gamma = 0.3$ and $\zeta = 2.3$). All lengths are based on a f_{cut} threshold of $f_{cut} = 1.5\overline{f}$. Note that exponential distributions have the special properties that ζ is also the mean chain length.*

Table 6.2: *Average chain length versus aspect ratio for $f_{cut=1.5}$.*

α	Average Length	Average Force
1.0	5.78	3.06
1.5	5.04	2.30
2.0	4.54	2.07

The most important summary results are presented in Table 6.2. Here, the average length is expressed in absolute length unit normalised by the particles equivalent diameter, hence the average length value are different from ξ expressed in contact number. They show that the force chains that characterise systems of round particles are not only longer on average, but they also support larger loads than elliptical particles. This appears to be a systematic trend.

6.3.3.4 Force chains connectivity

To investigate whether the particles constituting a force chain posses different properties as previously suggested by some authors, the variation of the coordination of the particles that are part of a force chain as a function of the cutoff value chosen for the FCD algorithm

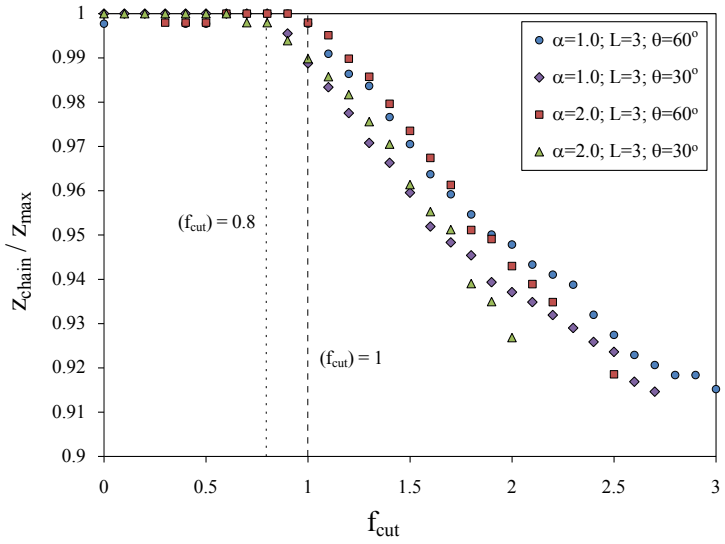


Figure 6.15: *Variation of the coordination number of the particles detected in the force chains, z_{chain} normalised by z_{max}, the average coordination number of the whole system. A clear transition is observed, which suggests that the particles constituting the force chains possess less contacts than the remaining ones. The value of f_{cut} at this transition can be used as cutoff value for the given set of L and θ.*

is calculated. If the threshold value is lower or equal than the average contact force, the coordination number of the force chains is equal to the average coordination number of the system. If the cutoff value is set to value larger to the average force $f_{cut} = 1$, the coordination number of the particles in the force chains, normalised by the coordination number of the whole system, decreases linearly with the cutoff value. The reason behind this result is that the particles interacting with strong contact forces are less connected that others grains [195]. From the Fig. 6.15, it is observed that by changing the value of θ from 60° to 30° translates the transition point to a lower cutoff value of 0.8. This is due to the fact that by restricting the tolerance angle, more contacts are filtered by the FCD algorithm and a similar number of particles are part of the force chains if $\theta = 60°$ and $f_{cut} = 1.0$ as if $\theta = 30°$ and $f_{cut} = 0.8$.

The presence of a supposedly strong and weak network of contact forces as proposed in [169, 171, 170] possessing distinct properties can explain the lower connectivity of the particles participating largely to the stress propagation. However, apart a lower connectivity, no additional specific properties could be attributed to the particles constituting the forces chains. Finally, an analogy to the theory of [22] can be established. To be in mechanical equilibrium, the particles (convex in this case) forming a granular medium need to possess a minimum number of contact. The system at which the mechanical equilibrium is critically stable balance exactly the number of degree of freedom of the system, this is the isostatic state. For instance, the average coordination for frictional discs ($d = 2$ degree of freedom/particle) should be $\overline{z} = d + 1$ (See Table 4.4 in Chapter 4). Note that locally, only particles with larger coordination numbers can exist. In the theoretical

framework proposed by Blumenfeld [22], it is suggested that force chains propagates through particles that are close to this isostatic state and scatters in many directions in the regions where particle coordination number is above the isostatic limit. In accord with this theory that predicts the apparition of force chains in granular materials, the present results suggest the possibility that force chains are indeed composed of less connected particles close to $z = 3$, the isostatic state, whereas the remaining particles possess larger values of z. (The reader is referred to the Chapter 4 for a description of the coordination of each of the systems as a function of the ellipse aspect ratio.)

6.3.4 Additional comments - drawback of the algorithm

The FCD algorithm is an efficient way to discriminate the particles that can be part of the force chains and to provide quantitative measurements about those particles. However, the results can suffer from the fact that the numerical simulations that generate the packing and calculate the magnitude of the contact forces requires an excessive amount of CPU time in order to reach a pseudo-static configuration where the force network remains unchanged. At the time simulations are stopped, the system is never perfectly static, some particles are subject to infinitesimal displacement during the relaxation of their material which can disconnect the contact between two grains for a fraction of second. Nevertheless, to overcome this issue ample relaxation time were allowed, and once the pseudo-static state is achieved, the nodal velocity of all the particles was automatically set to zero. Otherwise the FCD algorithm is computationally very efficient and it takes only a few second (typically less than 5s) to identify the network of force chains.

6.4 Conclusion

We have implemented an algorithm that identifies the particles constituting the force chains of a granular system. The algorithm connects the contact points based on three criteria: the length, the linearity and the strength of the chain in order to respect the constraints imposed by the proposed definition of a "force chain". The sensitivity of the tolerance criteria used for the recognition of the chains was compared and discussed. The plots showing the cutoff sensitivity were used to discriminate the influence of each individual criterion. It is observed that for a given particle shape, the variation of the chain detection criteria shifts the cutoff curve laterally while its slope remains practically unchanged.

Application of the FCD algorithm has facilitated a quantitative study of the differences of micro-scale stress propagation within static unloaded granular packs. This work focused

particularly on quantitative characterisation of the role played, if any, by particle shape. It is noticed that a packing of discs at rest possesses significantly different patterns than systems with ellipses. In particular the statistical analysis of the force chains shows that discs possess some ordering which results in preferential direction of propagation for the force chains. Our results shows that by increasing the particles aspect ratio, the typical length of a force chain is divided by a factor of almost 2. An analysis of the coordination number of the particles composing the chains shows that the most strongly connected particles possess a coordination number lower than the average. This particular point support the theoretical prediction expressed in the recent work of [22], suggesting that force chains propagates over longer length scale for minimally connected particles (thus at their isostatic limit). This is essentially due to the fact that no sharp transition of the force chains properties could be identified. To understand the fundamental influence of the particle shape on stress transmission and on the force chain characteristic, it would be of interest to compare the present results, for which the systems possesses some orientational correlation, with system exempt of any angular correlation. To address this task, different packing strategy are however requested.

Finally, even though a robust definition is used to highlight the concept of force chain, several problems remain mainly due to the difficulty to generate perfectly static systems numerically. Another source of error appears when chains are converging or diverging towards a single grain, i.e. branching, where the path is arbitrarily selected, but these cases are marginal. Additionally, the algorithm refinement could consider the angular detection window, controlled by θ, to be a function of the magnitude of the contact force rather than treating all the filtered contact forces with equal weight. Such an approach would take into consideration the fact that a very strong force has a much stronger influence than a weak contact. There are plenty of opportunities for future investigation and chain extraction algorithm improvements.

Chapter 7

Some applications related to FEM-DEM

7.1 Introduction

The combined finite-discrete element method can be applied to industrial problems involving minerals, powders and grains. The applications can simulate different scenarios with a range of physical characteristics in order to improve our understanding of the influence of variables such as the particle shape on the system behaviour. As a simple way of providing an example, the packs of particles analysed in Chapter 4 have been used as initial condition of problems often encountered in industrial applications: the compaction of granular material and the flux through a silo aperture. The aim of this chapter is to demonstrate that the FEM-DEM can be applied to various sets of systems and that it can help to understand the physical processes occurring in each of these cases. The two case studies presented in this chapter are also intended to act as validation examples of the 2D FEM-DEM method.

7.1.1 Compaction of granular materials

The stress-strain response of a granular media subject to an external load is investigated in this chapter. The discrete element method has become an important tool in investigating the micro-mechanical behaviour during the compaction of granular material [40, 205, 153]. The mechanical response is obtained by considering the dynamic interactions at the discrete level of the system. Discrete modelling generally considers a system composed of circular or spherical particles since these shapes are easily modelled. Often the complexity arising from the non-circularity of the particles forming real systems is neglected despite

experimental evidence. However, 2D numerical simulations conducted with angular particles showed that the mechanical behaviour and the strength of the assembly are affected by the grain angularity [129] or the particle eccentricity [180, 150] at both macro and microscopic level. Interestingly experiments and simulations carried out with elliptical particles show better agreement with the behaviour of real sands encountered in soils [143]. Other recent discrete element simulations suggest that the angularity of the polygonal particles affects the force propagation and subsequently the macro-mechanical behaviour [2]. Uniaxial test simulations with rounded and elongated grains performed with contact dynamics algorithms show that elongated particles respond distinctively from the rounded ones [143]. Also discovered in recent compression experiments on granular materials, the force required to push a vertical column of grains increases with the displacement velocity of the upper piston, which suggests a rate-dependent behaviour of cohesionless sand grains [6].

Bulk compression tests are commonly used in industrial applications, such as the pharmaceutical industry, 1) for the characterisation of macroscopic properties, and 2) for the characterisation of the mechanical properties of individual grains. Early experimental work on compression of grains performed by Walker [219] lead to a logarithmic relationship between the volume of the sample V and the applied pressure P, $V = a_1 - K_1 \ln P$, where a_1 and K_1 are constants related to the material type. Later, Heckel [78] remarked that the slope of the relationship, given by the coefficient K in his equation was inversely proportional to the stiffness of the metal powders. The Heckel relationship is usually written as $\ln\left[\dfrac{1}{1-D}\right] = A + KP$, where A and K are constants related to the material, D is the relative density and $1/K$ is the Heckel parameter which is believed to be related to the particle hardness. A study discussing the real significance of the Heckel analysis using the Discrete Element Method is proposed by Hassanpour et al. [77].

To investigate the fast compaction of real shape ductile and brittle powders, Ransing et al. [174, 66] coupled the discrete element method with a finite element solver (ELFEN). This work demonstrates the strong dependence of the system response to incremental loading with the materials properties of ordered arrays of circular particles. This hybrid approach increased the computational capabilities encountered by classic discrete element analysis. In this chapter the compaction of granular material is performed using a similar combined approach, with the addition of frictional interactions between distinct particles forming a random packing [71].

7.1.2 Silo discharge

The modelling methods of silos are classically based on continuum methods such as the finite element method [181, 83, 125]. Although these methods are generally sufficient to predict the wall and the bottom pressures, they rely on arbitrary assumptions concerning the calibration of the governing parameters (friction angle, dilatancy angle, cohesion, etc.). The discrete approaches such as discrete element methods permit an appropriate description regarding to the discontinuous nature of the system which has now been widely employed. Although most of the current DEM models are considering spherical particles [103, 104, 102, 125, 84, 228], the use of this method has permitted to address the issues of particles discharge with an emphasis on the influence of the particle shape on the system behaviour. The recent improvements of computer power coupled with suitable algorithms have improved the understanding of the role played by the particle shape during the process of emptying a silo, using superquadric [33], sphere intersections [101] or cubic particles [59]. Paradoxically, the mass flow of non-spherical particles respond very differently to the presence of inter-grain friction. With frictional aspherical particles, elongated shapes lead to lower discharge rates are obtained with than with rounded ones [33]. On the contrary, frictionless interactions tend to produce larger discharge rates with elongated articles [101].

The silo application presented in this chapter is aimed at investigating the role played by both the surface friction and the particle elongation during the discharge of a rectangular silo. A discussion on arching, stress distribution and velocity field is also proposed in this investigation.

7.2 Powder compaction

7.2.1 Objectives

The compaction of granular particles is a complex problem to model realistically because the overall behaviour of the systems depends on the properties of the grains themselves, the fabric network described by their contact, the presence of interstitial fluid, ... which can be difficult to model together. Nevertheless, recent numerical modelling methods permit the inclusion of realistic particle deformation and interaction, which is crucial to developing reliable simulation tools. Discrete methods, such as DEM, can be coupled with continuum approaches to model the local deformations at grains scale [65, 174, 164]. This recent approach was mostly used to investigate the impact of material properties for the compaction of discs, however, the micro-behaviour of non-spherical particles remains poorly documented.

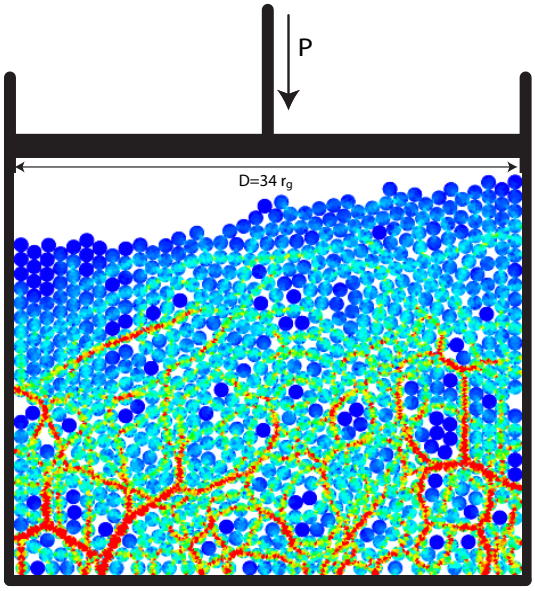


Figure 7.1: *Geometry of the system simulated for the powder compaction experiment.*

The aim of this case study is to investigate the applicability of the combined finite-discrete element method for analysing the compaction of arbitrary shaped (elliptical particles) and deformable particles. Additionally, the evolution of the internal properties of the system are evaluated at several indentation values of the piston.

7.2.2 Numerical set up

The system consists of a rectangular container of width $W \approx 34$ r$_g$, where r_g is the grains equivalent disc diameter of 177 mm, filled by 900 visco-elastic ellipses (see Fig. 7.1. The bottom and lateral walls of the container are assumed to be completely rigid. The microstructures of the initial ellipse packs that characterise the pre-compaction stage are identical to those described in Chapter 4. The area of the particle is constant and equal to 9.82e10$^{-2}m^2$. Each container possesses an identical mass of material. The material properties are set to match a concrete materials with: $\rho = 2650kg/m^3$ for the material density, $Y = 28$ GPa for the Young's modulus and $\nu = 0.17$ for the Poisson's ratio. A piston is positioned on top of the particles tangent to the upper part of the highest ellipse. When the compaction starts, a constant velocity v_p directed downwards is given to the piston so that the granular system is gradually compressed. Ideally, v_p needs to be very small in order to ensure quasi-static deformations. However, using discrete element techniques would require extremely long simulation time due to the large number of time-steps imposed by the small particle sizes and long duration of the compaction process. To overcome this, Thornton & Anthony [205] argued that it was reasonable to apply a density scaling to the system so that larger time steps can be employed. Unfortunately

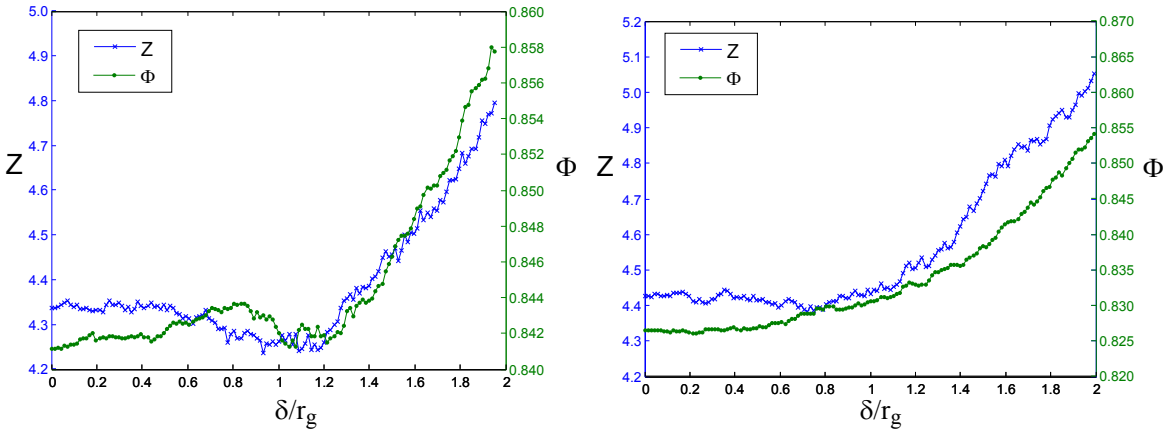


Figure 7.2: *Evolution of the packing density, Φ, and the average coordination number, Z, of the system with the indentation of the piston. a) $\alpha = 1.5$ b) $\alpha = 2.0$.*

this strategy can not be adopted in our case because particles will deform under their own weight. Instead, an approach similar to Ransing at al. [174, 66] was adopted where $v_p = 50\text{mm.s}^{-1}$ is chosen such that the deformations are slow considering the size of the container. In contrast to the compaction test performed in [65, 174], the initial stage of compaction in this work considers disordered particles interacting with frictional contacts ($\mu = 0.5$). Although it would influence the compaction process in many real systems, the presence of interstitial fluid was neglected in this work.

In this uniaxial compression test, the lateral and bottom walls are fixed during the compression, such that the horizontal strain of the sample is $\varepsilon_h = 0\%$. Assuming that the container is filled up by frictional particles and possess an average packing density close to 80%, it is straightforward to estimate the average height of packed particles, which is $34r_g$. Consequently the equivalent vertical strain, ε_v, for a piston indentation of $2r_g$ is $\varepsilon_v = 6\%$. The net vertical force, f_v, applied to the piston is recorded during the indentation of the piston. The relationship between the pressure and the force applied on the upper piston is given by $\sigma_v = f_v/W$, where W is the width of the container.

7.2.3 Results and discussion

7.2.3.1 Packing density & coordination number

The pressure imposed by the displacement of the upper piston leads to rearrangements between the particles, which increases both packing density and coordination number. Fig. 7.2 demonstrates that for each particle shape, the porosity of the system remains globally stable during the early stage of the compression. At this stage, the force applied by the piston is localised to the highest particles of the upper free surface. As a consequence,

internal shear observed within the grains causes particle rearrangements which promote dilatancy and minor packing density decrease. After large displacement of the piston, the pressure is uniformly distributed among the upper layer of grains and is transmitted homogeneously to the system (see Fig.7.6). At this stage, both packing density and coordination number increase rapidly and constantly with the piston indentation (Fig.7.2). This reflects a densification phase. The Young modulus of the particles is set to large values $Y = 28$ GPa and, as a consequence, the deformations of individual grains are relatively limited at low confining pressure and the grain rotations and translations dominate. The rearrangement stage stopped completely once the maximum contact number $z_{max} = 6$, valid for elliptical particle shapes, is reached. For larger strain, the confining pressure becomes very large and the high magnitude of the contact forces lead to important grain deformations. When the individual grain deformations are large, the coordination number of the systems stabilises while the average contact area between interacting grains starts to increase. Thus the compaction process involves a stage of rearrangement, where particles endure large displacements, followed by a stage where the density increases due to the particle deformations. It would be interesting in the future work to compare the evolution of the curves in the Fig.7.2 with softer particles (small Young modulus) where particle deformations become predominant due to low confining pressure. The comparison is not carried out in this case study due to timing restrictions of the project.

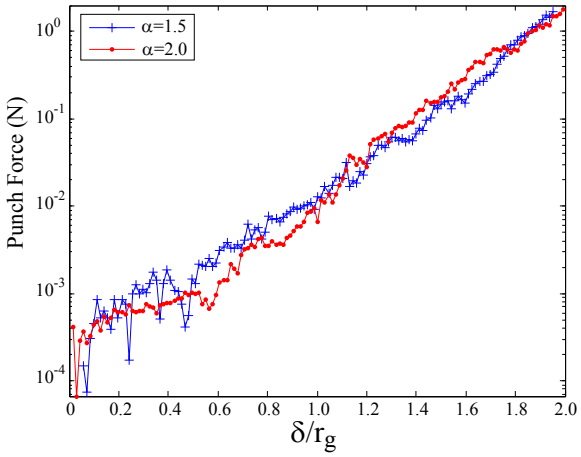
For the case of disc compaction, it is observed that the coordination number increases to a value close to 6 indicating an hexagonal structure in which the stress becomes more homogeneously distributed. At high level of compaction ($\delta/r_g > 3$), the force chains become unidirectional and the overall system supports the load more like conventional a solid.

7.2.3.2 Force displacement relationship

The incremental displacement of the piston generates an increasing pressure on the grains, which leads to the reduction of the porosity in the compacted medium. To keep the piston motion at a constant rate, the force applied on the piston has to be gradually increased as the resistance of the grains becomes larger. Fig. 7.3 shows that the piston force necessary for constant displacement rate increases exponentially with piston displacement:

$$f_{piston} \propto e^{\frac{\delta_{piston}}{r_g \gamma}}. \tag{7.1}$$

This relationship is in agreement with the early experimental results presented by Walker [219] characterising the compaction process, and it is valid for a wide range of materials. Fig. 7.3 also demonstrate the independence of the relationship with the particle



(a)

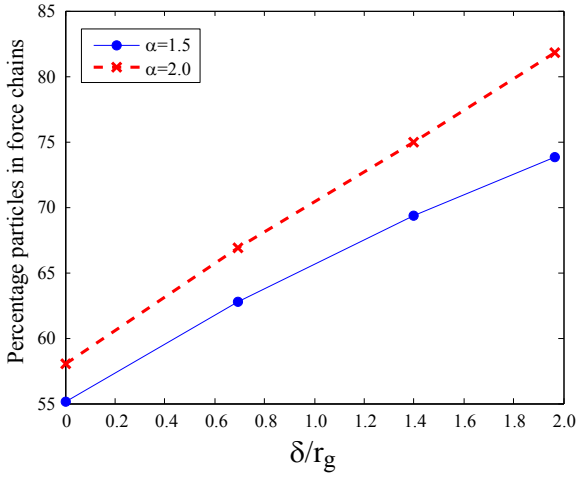
Figure 7.3: *Variation of the vertical force applied by the piston as a function of its vertical displacement for packs consisting of two different ellipse shapes ($\alpha = 1.5$; $\alpha = 2.0$).*

shape. Because the uncompressed systems possess a microstructure that depends on the shape of the packed particles, this suggests that the force displacement relationship is independent of the internal structure of the grains. The variations of the curves shown in Fig. 7.3, characterised by the coefficient γ, give an indication of the mechanical strength of individual particles. The trend can be modified using stiffer or softer particle materials. Eq. 7.1 is also controlled by other parameters such as the compression rate of the piston. Nevertheless, it is emphasized that the material considered in this exercise deforms purely visco-elastically, i.e. with an infinite yield stress. The estimation of the mechanical properties of powders and other granular systems, such as the yield stress of individual particles, is commonly performed through Heckel analysis [77]. However, the relationship existing between the properties of individual grains and the mechanical response of the whole system requires further investigation.

7.2.3.3 Evolution of the force chain network during the compression stage

Quantitative characterisation of the force chains is performed using the FCD algorithm described in the previous chapter. The compacted packs are analysed at four different piston indentations, $\delta_0 = 0r_g$, $\delta_1 = 0.7r_g$, $\delta_2 = 1.4r_g$ and $\delta_3 = 1.97r_g$ for elliptical particles. δ_0 corresponds to the initial indentation and δ_4 to the lowest position of the piston. Fig.7.6 shows that the compression increases the magnitude of the differential stress within the bulk. At high confining pressure, the contact forces network remains heterogeneous although the force chain network is subject to important readjustments.

The comparison of the force chain networks described by the samples composed of different particle shapes evolves with increasing strain. Substantial differences between



(a)

Figure 7.4: *Percentage of particles detected in the force chains for $f_{cut} = 1$, $\theta = 60°$ and $L = 3$ by the FCD algorithm developed in Chapter 6. Because the load supported by each particle becomes more similar with the increasing compaction, the percentage of particles carrying load in the force chains increases with the punch displacement.*

systems of discs and ellipses are perceptible. At high compression level, discs exhibit a clear hexagonal structure and the stress chains are almost unidirectional. For ellipses with $\alpha = 1.5$ and $\alpha = 2.0$, force chains are also observed but their spatial distribution does not suggest geometrical ordering of the contact force network and the stress appears randomly distributed within the grain assembly. The FCD algorithm, described in Chapter 6, was applied to each system in order to identify precisely the network defined by the force chains. The fraction of particles participating in the transmission of force chains increases linearly with the strain applied to the system (Fig. 7.4). The fact that most of the particles contribute to the stress transmission when increasing the compression suggests that the dual nature of the force transmission network disappears progressively.

Finally, Fig.7.5 shows that the distribution of contact forces evolves during compaction, passing from an exponential decay of large forces to a gaussian distribution for high amount of compression. This is in agreement with the compaction experiments of spheres published by Makse et al. [121]. This trend is not only valid for circular grains but also with eccentric ones. This transition from an exponential to a gaussian type of distribution is consistent with the fact that the granular material behaves more homogeneously when the confining pressure of the grains becomes large. Interestingly, the homogenisation of the stress distribution within the system responds to a similar trend regardless of the particle shape. Nevertheless, as explained in Chapter 5, the contact forces tend to be more narrowly distributed in systems with elliptical particles, indicating that elliptical particles are naturally at a constraint state in terms of force distribution. This difference inherent to the particle shape explains the narrower force distribution observed using the

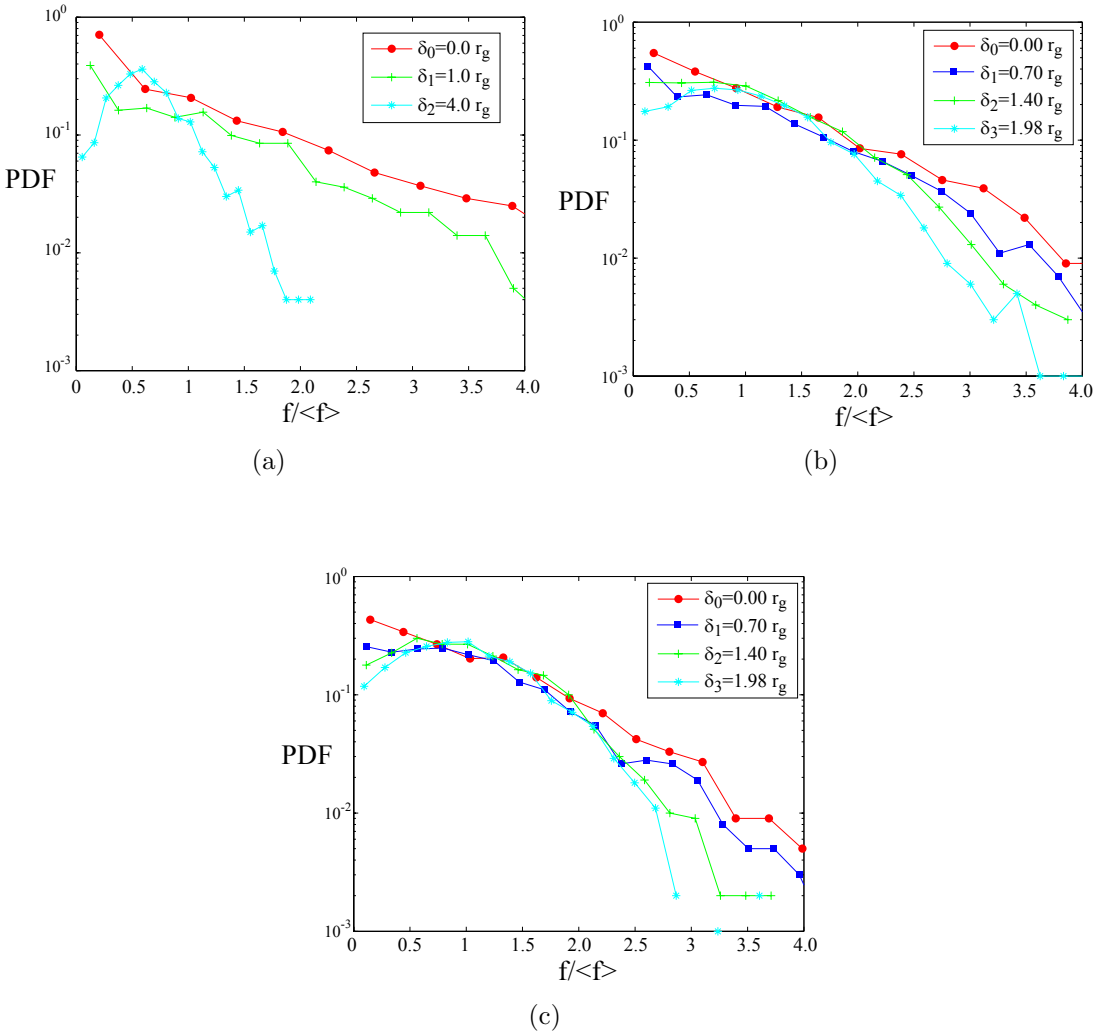


Figure 7.5: *Evolution of the contact force distribution with the punch indentation. a)* $\alpha = 1.0$*, b)* $\alpha = 1.5$*, c)* $\alpha = 2.0$

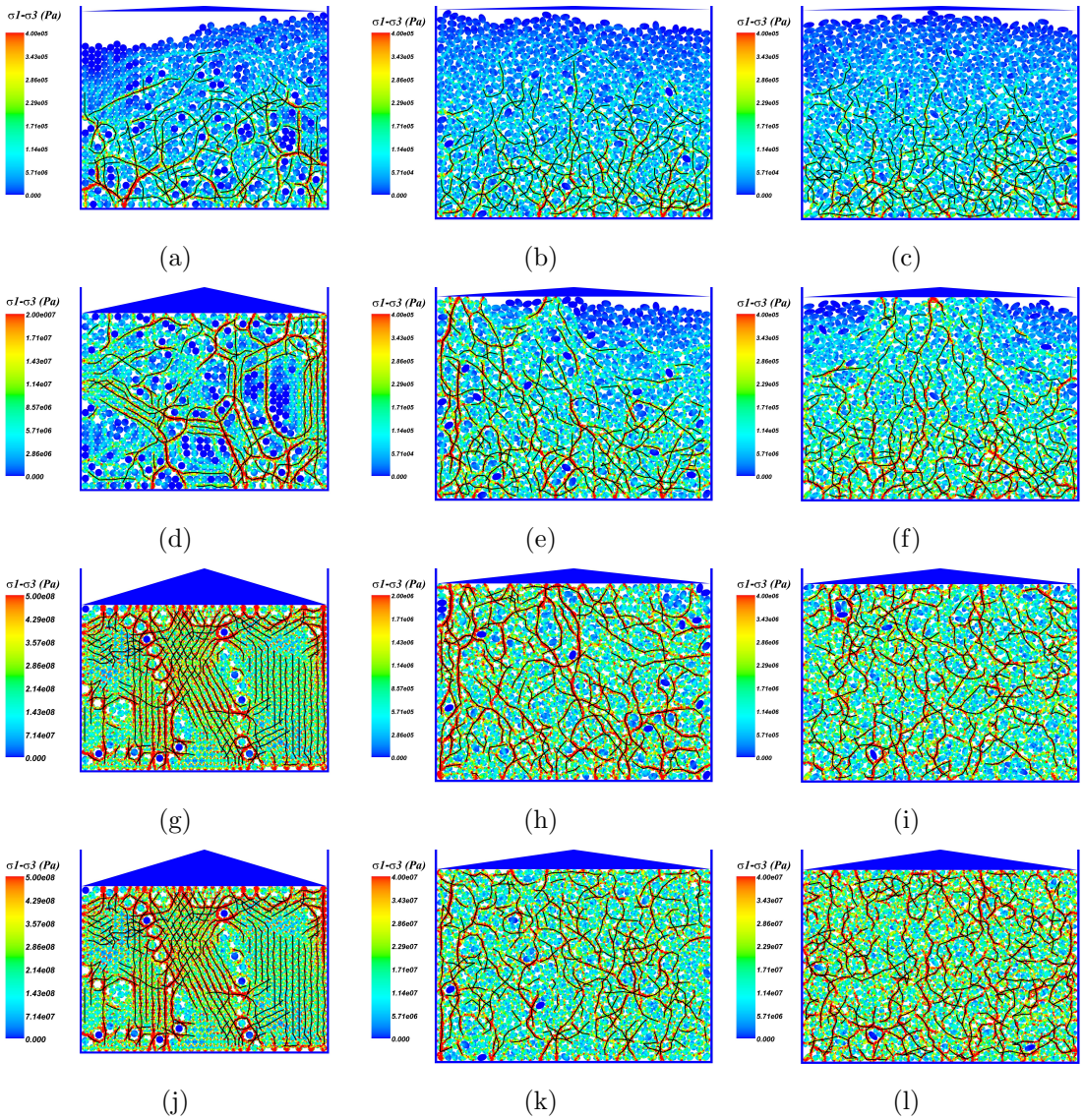


Figure 7.6: *Evolution of the stress patterns during the compaction of frictional particles ($\mu = 0.5$). a) $\alpha = 1.0, \delta = 0.00r_g$, b) $\alpha = 1.5, \delta = 0.00r_g$, c) $\alpha = 2.0, \delta = 0.00r_g$, d) $\alpha = 1.0, \delta = 4.00r_g$, e) $\alpha = 1.5, \delta = 0.70r_g$, f) $\alpha = 2.0, \delta = 0.70r_g$, g) $\alpha = 1.0, \delta = 6.00r_g$, h) $\alpha = 1.5, \delta = 1.40r_g$, i) $\alpha = 2.0, \delta = 1.40r_g$, j) $\alpha = 1.0, \delta = 6.00r_g$, k) $\alpha = 1.5, \delta = 1.98r_g$, l) $\alpha = 2.0, \delta = 1.98r_g$. The force chains identified by the FCD algorithm (cf. Chapter 6) are superimposed by black segments. The color scheme represent the differential stress calculated inside each particle.*

most elongated particles at a given strain (Fig. 7.5a and Fig. 7.5b).

7.2.4 Summary

In summary, compression tests have been performed on different granular systems. The compaction of the grains implicates grain rearrangements, larger coordination numbers and smaller porosity. Both the initial amount of void space within the samples and the contact network geometry are function of the particle shape, and distinct responses to compaction are expected when grain elongation is varied. However, at constant strain rates, the mechanical response of the granular material shows an exponential relationship between the applied compressive force and the piston's displacement which is independent of particle shape.

The analysis of the contact force network during the compaction process shows that the system is gradually homogenised when the compression increases. The force distribution evolves from a spread exponential distribution towards a narrower exponential one. When highly compacted, the amount of void decreases, the grains endure important ductile deformations and the contact areas between grains become larger. At this stage, it is suggested that the compacted granular materials behave similarly to conventional solids when grains are subject to high confining pressures.

A granular medium composed of elastic particles naturally produce plastic, i.e irreversible, deformations within the whole system and the particles endure irreversible displacement during the compaction process. Plastic deformations within grains were however not included in these simulations. Under large confining pressure ($\sigma_1 - \sigma_3 > 500$ MPa), brittle failures of the particles are also likely to happen although it was not modelled in the study. For this reason, the material response is more adapted to ductile grain behaviours. An investigation of the response of elasto-plastic grains is suggested in future studies for the interests of understanding their mechanical behaviours under high magnitude of compression.

7.3 Silo discharge

7.3.1 Aim

The second application study is aimed at describing the flux of granular material though an aperture in a silo configuration and to analyse the influence of the particle shape on the discharge flow.

Previous studies have attempted to quantify the relationship between particle and the discharge rate of a silo for 2D configurations [33, 101]. However, in both of these studies, the configuration of the systems allowed a continuous flow of particles and no jamming phenomena was observed because of the absence of friction [101] or the large diameter of silo aperture [33]. By reducing the silo aperture to a width typically smaller than 10 grain diameters, the system is known to behave unsteadily, and undesirable behaviour can be observed.

To model realistically the flow of material in a hopper, it is necessary to take into account the influence of several key factors that are representative of the mechanical and geometrical properties of the grains. This includes the representation of complex particles shapes and their deformations under the constraint imposed by the interaction with surrounding grains. The type of interaction law acting between the grains is also of key significance as it is known to affect the distribution of pressures on the container walls and on the flow properties [104]. Because the influence of the particle shape on the discharge flow is often neglected, we perform different simulations of frictional ellipses with varying elongations. Furthermore, considering that the implementation of the contact interaction using the FEM-DEM is fundamentally different compared to the usual DEM, the comparison between the behaviours produced in silo experiments with FEM/DEM and those produced by other alternative DEM approaches, such as proposed in [33, 101] can be used to validate the 2D experimental configurations.

7.3.2 Experimental set up

In this application, we consider a flat bottomed rectangular 2D silo of width $W \approx 34$ $\mathrm{r_g}$ and aperture $D = 5.656$ $\mathrm{r_g}$ at the middle part of the base (r_g is the equivalent diameter of the particles) as seen on Fig. 7.7. The width of the aperture is such that jamming is likely to occur. The container is filled up with densely packed particles with the method described in Chapter 4. The particle properties are summarised in Table 4.1. The discharge simulations were performed with three different ellipses aspect ratios, $\alpha = 1.0$, $\alpha = 1.2$ and $\alpha = 2.5$. The numerical method allows us to compute the velocity field and the internal stress of the particles as well as the contact forces, the coordination number and the packing density in any part of the system. At the beginning of the flow, the spatial configuration of the grains for a given shape is similar to those described in Chapter 4. When the silo is fully filled, the level of grains is slightly lower than the container width so that Janssen effect can be neglected. Furthermore, the particles that escape from the silo are not reintroduced at the surface of the packing which implies that the pressure, driving the flux of the grains, is not constant. The outlet flux is measured between two jamming events, when the flux of materials is nearly constant.

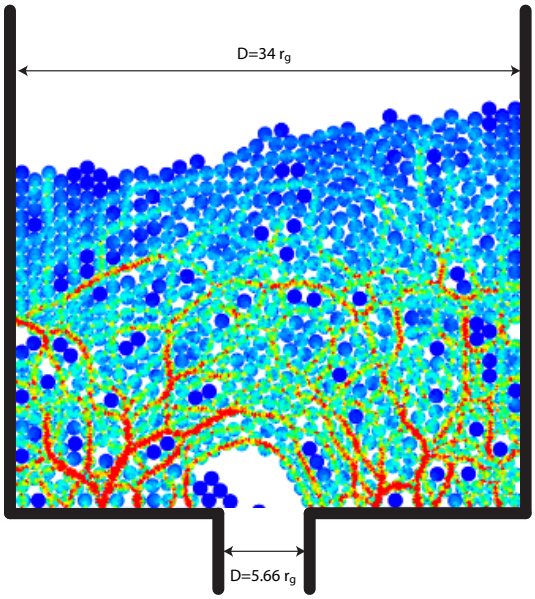


Figure 7.7: *Geometry of the system simulated for the silo discharge.*

7.3.3 Results and discussions

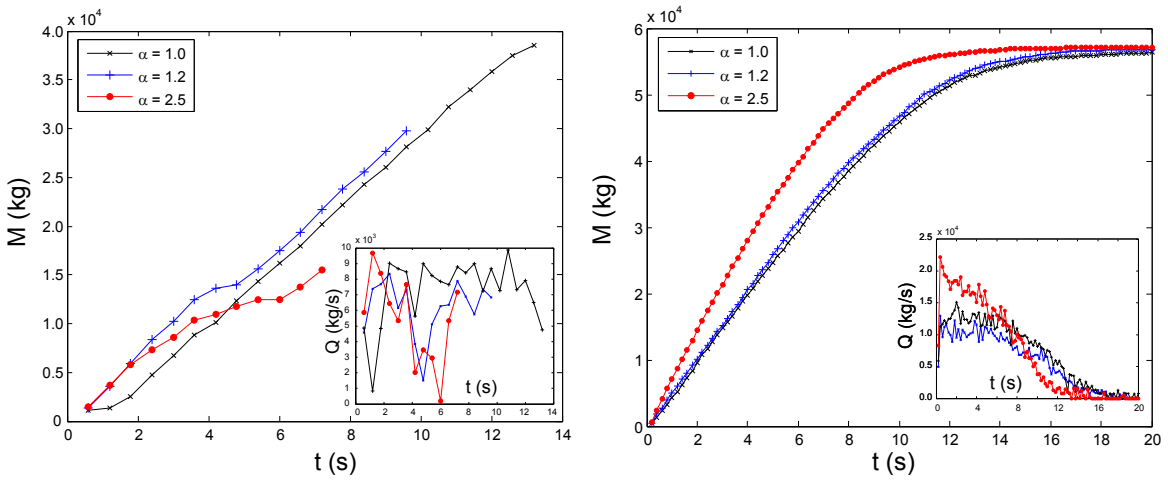
7.3.3.1 Discharge rate dependence on particle elongation

Numerically, the mass flux Q is easily determined by measuring the mass of grains ΔM discharged from the silo during a time interval Δt:

$$Q(t) = \frac{\Delta M}{\Delta t} \tag{7.2}$$

The calculation of the discharge flow $Q(t)$ was performed during the silo emptying process at several time intervals. Fig.7.8 shows that the discharge is clearly perturbed by bridging events that last over short time scales. The periods during which particle jamming occurs are in fact not representative from the real value of the discharge rate calculation as it causes an underestimation of $Q(t)$. In spite of the discharge rate fluctuations caused by bridging, the particles produce constant flow for large enough periods to be measured accurately. However, for the case of frictional ellipses with $\alpha = 2.5$, it is subject to higher uncertainties.

The particle shape appears to have little influence on the flow rate of frictional particles (for the periods of flow not perturbed by jamming) despite the different microstructure of the initial packing consideration. This contradicts the results of Cleary's work [33]. However, in the case of Cleary [33], the systems treated were of a larger scale, and the silo configuration was different with an inclined outlet. The case of frictionless particles is also instructive as it shows that the elongated particles discharge faster than the rounded ones.



(a) (b)

Figure 7.8: *a) Total mass discharged from the silo aperture for frictional particles. b) frictionless particles. In the inset of each figure is plotted the value of the discharge rate.*

Counterintuitively, the mass flux can be increased by up to 30 % when using particles with $\alpha = 2.5$ compared to the case of discs. Detailed investigation shows that the frictionless particles reorient with their long axis aligned vertically before leaving the silo. Because of this, the frictionless elongated particles pass the outlet with their long axis almost vertical. Therefore, the effective aperture appears larger for elongated particles, which results in a more efficient discharge.

The flux of grains through a silo orifice is known to respond to the Beverloo's law, given by $Q(D) = C\rho_b\sqrt{g}(D - kr_g)^{\frac{3}{2}}$ in 2D, where C and k are dimensionless constants depending on the grain properties and the dimension of the system, g is the acceleration of the gravity and $\rho_b = \phi.\rho \approx 2120$ kg/m^{-3} is the bulk density in the vicinity of the orifice. This relationship, valid for a large range of orifice apertures and material types, was tested uniquely for a constant orifice size D. The validity of the Beverloo's law in both 3D and 2D silos is discussed in [124]. The mass flux measured for the case of frictional particles, $Q = 8e10^3$ kg/s, is in good agreement with the empirical discharge rates predicted by the Beverloo's equation with constant values C and k equal to 35 and 2.9 respectively as suggested by Beverloo [17]. This results provides a partial validation of the FEM-DEM method. However, the shape dependence of the flow rate with frictionless systems suggests that the Beverloo's law is certainly oversimplified as it does not include shape related parameters.

7.3.3.2 Particle velocity

Fig.7.9 shows snapshots of the velocity field that characterises the flow of grains with variable ellipticity. The shape of the velocity field during the discharge provides information

concerning the internal resistance of the grain due to shearing. Both systems of rounded frictional particles ($\alpha = 1.0$ and $\alpha = 1.2$) show that when the system is not jammed, the velocity profiles have a distinct V-shape where the particles positioned near the apertures move with the highest magnitude. In this case, the particles close to the wall remain weakly displaced. Unlike rounded grains, the elongated frictional grains ($\alpha = 2.5$) are subject to larger resistance to shear induced by the flow. Therefore, the internal microstructure of the grains becomes important and the flow becomes concentrated within a narrow column at the centre of the system. This behaviour, called "rat-holing", was captured with DEM methods using superquadrics shapes [33]. Importantly, it is critical that a FEM-DEM simulation predicts this behaviour despite that the contact interactions and material deformations are handled in a completely different manner. For each of the systems, it was also possible to observe bridging phenomena, where the arches formed by the stress chains block the discharge of the silo.

The frictionless systems (not pictured) permit continuous discharge rates. In this case, "rat-holing" phenomena was not observed, however similarly to what can be observed with frictional interactions, the particles in the bottom corners are trapped during the emptying process.

7.3.3.3 Stress fluctuations

Differential stress is used to quantify the evolution of load supported by individual particles. For each of the particles, jamming is observed near the aperture and the grain load is clearly supported by concentric $\bigcap$-shaped arches (see Fig. 7.10). The vibrations caused by the motion and interactions of the bulk particles are accurately captured with FEM-DEM. These vibrations provokes the breakage of the supporting chains and subsequently reactivates the granular flow. Because of the shear caused by the discharge, the particle stress is constantly rearranged. For each system, the majority of stress is concentrated among the static particles situated in the vicinity of the walls. On the contrary, the particles located in regions of high velocities possess few contacts and are preserved from high stress magnitudes. The particles, initially constrained, are gradually freed when underlying bodies start their downwards motion towards the outlet permitting the grains to flow.

Although more computationally expensive than DEM, FEM-DEM simulations provide a more complete insight of the mechanisms involved during the discharge process. The arching, disrupting the continuity of the flow, are particularly important when the orifice aperture is narrow. Nevertheless the force chains sustaining the weight of other particles are successively broken and reactivated during the particles discharge. For the case of smooth grain surfaces, such processes are likely to occur and the particle discharge can be

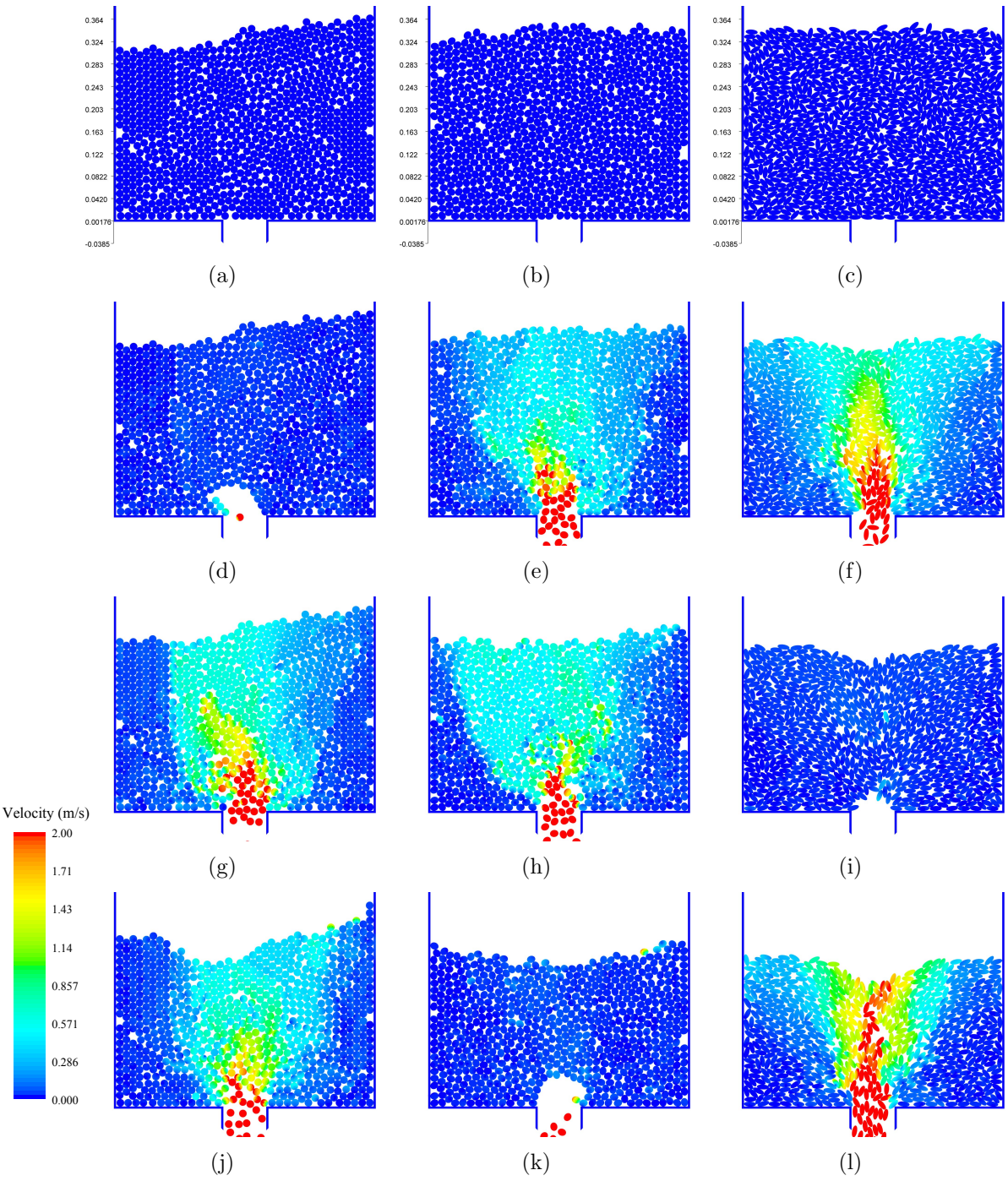


Figure 7.9: *Snapshots of the velocity field during the flux of grains through the aperture of the silo at different time for 3 types of frictional ($\mu = 0.5$) particles. The silo width is $D = 5.656r_g$. a) $\alpha = 1.0, t = 0s$, b) $\alpha = 1.2, t = 0s$, c) $\alpha = 2.5, t = 0s$, d) $\alpha = 1.0, t = 1s$, e) $\alpha = 1.2, t = 1s$, f) $\alpha = 2.5, t = 1s$, g) $\alpha = 1.0, t = 2s$, h) $\alpha = 1.2, t = 2s$, i) $\alpha = 2.5, t = 2s$, j) $\alpha = 1.0, t = 4s$, k) $\alpha = 1.2, t = 4s$, l) $\alpha = 2.5, t = 4s$*

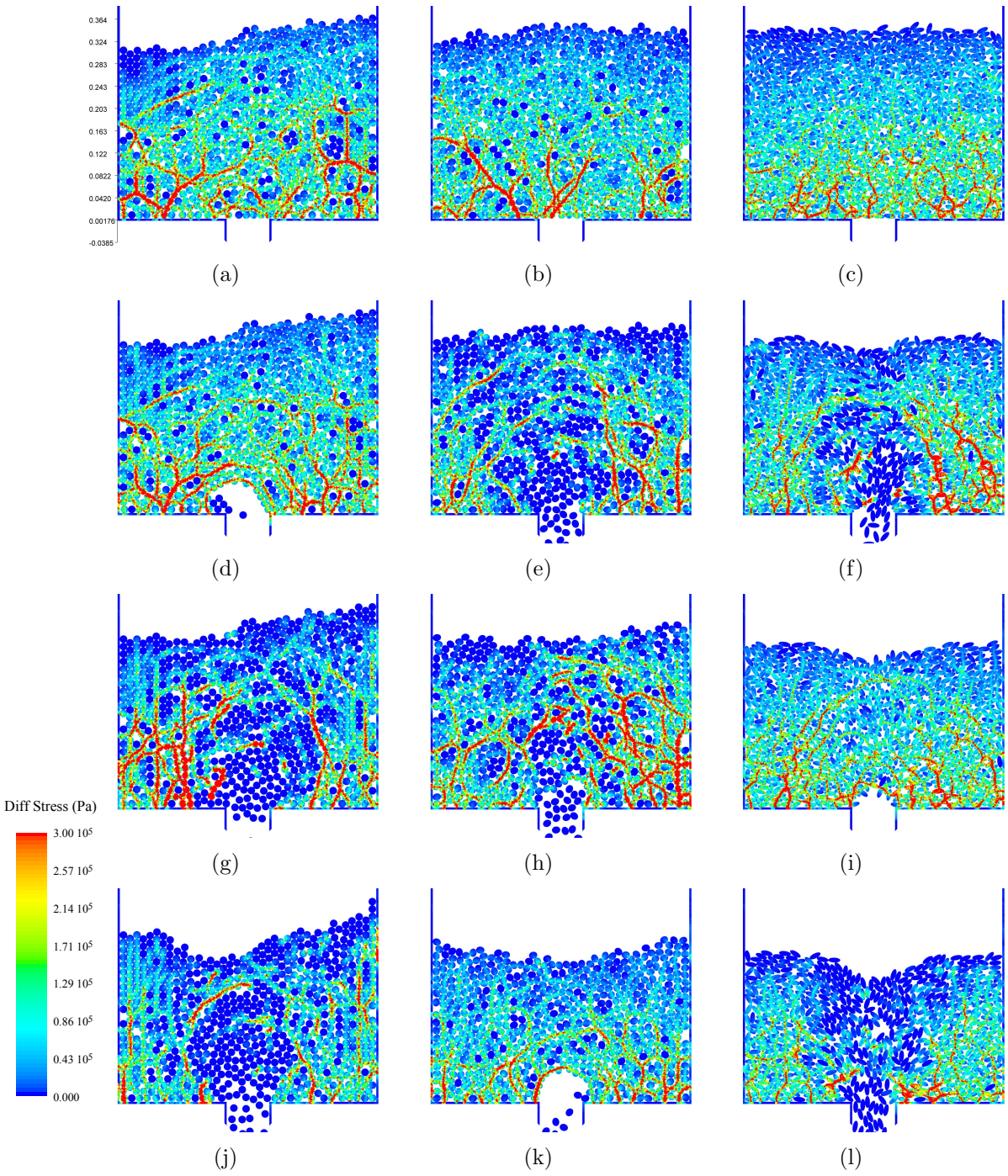


Figure 7.10: *Snapshots of the stress field during the flux of grains. It is observed that each system influence jams which consequently reduces the flux of grains. a)* $\alpha = 1.0, t = 0s$*, b)* $\alpha = 1.2, t = 0s$*, c)* $\alpha = 2.5, t = 0s$*, d)* $\alpha = 1.0, t = 1s$*, e)* $\alpha = 1.2, t = 1s$*, f)* $\alpha = 2.5, t = 1s$*, g)* $\alpha = 1.0, t = 2s$*, h)* $\alpha = 1.2, t = 2s$*, i)* $\alpha = 2.5, t = 2s$*, j)* $\alpha = 1.0, t = 4s$*, k)* $\alpha = 1.2, t = 4s$*, l)* $\alpha = 2.5, t = 4s$

re-initiated whereas very rough and irregular grains surfaces limits this effect because of the particle interlocking that hampers the particle motion geometrically.

7.3.3.4 Summary

Static packs with 900 hundred particles were used to identify the influence of the particle shape on the discharge rate of grains through a silo aperture. In addition to the importance of friction on discharge, it is observed that the flux of material through the outlet is greatly influenced by particle shape. The most clear feature of those flows is the presence of stagnant particles ("dead zones") near the wall of the container, and more notably next to the bottom corners of the silo. The shape of the base of the silos could be optimised to minimise this.

It is suggested that particle shape is an important factor that needs to be well understood for the improvement of silo design. However, the FEM-DEM simulations performed with different ellipse aspect ratios demonstrate that the flow rate with frictional grains is not necessarily influenced by the particle shape which contradicts [33]. Specific flow behaviours, such as "rat-holing", can be observed when using elongated grains which underlines the importance of considering non-spherical particles in the study. The simulations show that although flow patterns are essentially identical for each of the frictional ellipse, elongated grains generate variable mass flow rates. With frictionless contact interactions, the particle flow is no longer hampered by the stress chains and the discharge rate is constant over large time scales. Interestingly, it was noticed through the simulations that larger flow rates are produced with frictionless elongated grain shapes. This might be caused caused by the realignment of the particles parallel to the outlet when they flow through the orifice of the silo.

When relatively small orifice apertures were used ($D = 5.656r_g$), unsteady flow were observed, during which the action of the force chains is critical. Jamming events, during which the particle load is supported by arches of forces, are found to occur for each of the tested particle shapes. However, the force chains do not last over large time scale as they are broken by internal vibrations during the relaxation period of individual grains. To evaluate the importance of material relaxation time, elasto-plastic material can be considered to be tested in future studies.

7.4 Conclusion

Using the packs built by collective sedimentation, as depicted in Chapter 4, two applications of the FEM-DEM that are commonly encountered in industrial contexts have been

addressed. The method proves its potential applicability for a wide range of applications in the industry.

Unlike other DEM approaches, the most significant advantage of the FEM-DEM is perhaps the information that can be derived at the sub-particle level. There is no need for restrictive assumptions for determining the contact interaction model, which is considered to be critical as it governs the particle deformations and displacements. As a result, the method is particularly adapted to the analysis of systems where particle shapes and particle deformations are playing influential roles.

Chapter 8

Conclusions and future work

8.1 Conclusions

We still have much to learn about the influence of the particle shape on the structural and mechanical properties of granular media. In this thesis, a numerical method inspired by the Discrete Element Method was proposed in order to study particle packing from a geometrical and micro-mechanical point of view. The hybrid finite-discrete element method, originally developed by Munjiza [138, 135], has been improved upon in order to explore the micro-mechanical variables of packed particulate systems. In particular, a stable implementation of the history-dependent frictional contact forces was proposed and validated. Compared to more conventional approaches such as DEM, the use of the Combined Finite-Discrete Element method presents several advantages:

- The particle shape is intrinsically included into the computational framework. A discrete element, i.e. a particle, consists of an assemblage of triangular shaped sub-domains called the finite elements. Because of the rigorous contact interaction algorithm, the interaction between any 2D particle shapes, convex or concave, can be reliably performed.

- The particle deformation is handled through realistic rheological laws. The finite element method is used to compute the internal deformations within each grain while each component of the stress tensor is determined within each of the finite elements of all the grains in the system.

- The CPU requirements for a FEM-DEM simulation are usually heavy. Nevertheless, the optimisation of key algorithm sections permits the user to decrease substantially the computational time.

Consequently, the FEM-DEM is an appropriate method to understand the linkages that exist between the geometrical and the mechanical properties of a granular medium. In particular, the real wealth of this method derives from the accuracy at which the geometrical and mechanical parameters can be achieved.

The work presented in the thesis consisted of describing the structural properties of particles confined in a rigid container. The conclusions derived from the FEM-DEM simulations and related to the influence of the particle shape on the structure of a granular system are listed below:

- The structure of a pack of particles is strongly affected by the shape of the grains. By extension, the circular nature of the particles used regularly in classical discrete element simulation lead to a exceptional behaviour rather than a general case. Considering that most of the particles encountered in nature are non-spherical, the relationship between particle shape and the properties of a granular medium remains an important topic.

- The solid fraction of a packed granular medium of mono-sized particles can be improved by using elliptical particles instead of circular ones. An optimal packing density is found for ellipse-shaped particles of aspect ratio close to $\alpha = 1.6$ when particles interact with friction. For more elongated particles, the packing density decreases linearly with the aspect ratio, for the range of particle shapes simulated.

- The required average number of contacts per particle to be in mechanical equilibrium is larger for ellipses than for discs. Typically, elongated particles require one additional contact compared to circular grains. This observation is moreover in agreement with the simple argument that a static system is obtained when all the degrees of freedom present in the system are balanced.

- The presence of the friction between the grains affects greatly the structure of the granular media. Without friction, 2D systems tend to crystallise naturally, minimizing the porosity of the medium and maximizing the total number of contacts. In contrast frictional systems limit the tendency of the particles to crystallise.

- The packing method employed consists of a collective deposition technique. Under this type of construction process, elliptical particles are subject to orientational alignement and perfectly disordered systems, exempt of any orientational ordering cannot be obtained. The global degree of ordering between elliptical particles was quantified by using a scalar parameter, the orientational order parameter. It shows that the global disorder saturates when the ellipse aspect ratio is larger than $\alpha = 1.5$. The measure of the orientational correlations shows that elongated particles

are arranged preferentially into blocks or clusters of particles pointing in similar directions.

Using combined finite-discrete element simulations permits not only the characterisation of the granular structure but also the analysis of the stress propagation. The major contributions and results addressing the important problem of stress propagation in granular media are outlined below:

- On the basis that a force chain can be rigorously defined, an algorithm (FCD: Force Chain Detection) was developed to understand the characteristics of the force chain propagation. The influence of each constraining parameter on the total number detected in the force chains was discussed in detail and used to calibrate the FCD algorithm. The FCD algorithm permits the recognition of the main stress paths for spherical or non-spherical particles to be clearly distinguish. Consequently the force chain network can be described quantitatively.

- The influence of the particle shape is shown to have a major effect on the stress propagation. Rather than being a general mode of stress transmission, force chains are significantly longer and more directional in systems of disc shaped particles. For elongated particles, the stress chains disappear gradually and the stress distribution within the granular medium becomes more homogeneous.

- A comparison of the quantitative results obtained with the FCD algorithm with an analysis of the spatial correlation of the average stress carried per particle lead to the same conclusion: The stress propagation is naturally dependent on the particle geometry. The analysis of the alignment between neighboring particles suggests that for elongated grains, the load could spread out through clusters of aligned particles.

- The exponential tail of the contact force distribution, a feature of the distribution which has been consistently reported in numerous studies of granular media composed of discs and spheres, is also observed for systems of discs but disappears as it evolves towards a gaussian-like distribution for elongated particles.

To conclude, the particle shape is a crucial parameter that influences strongly the behaviour of a granular system. In a static configuration, both the geometrical structure and the mechanical characteristics of the stress transmission are shown to be affected. This suggests that the actual theoretical models of stress transmission, adapted to predict the force distribution in granular media composed of circular or spherical particles, will need to be extended in order to take into account the geometrical nature of the grains.

Furthermore, two examples of applications of the FEM-DEM model using random packs of elliptical particles were proposed in order to demonstrate the versatility of the

computational approach. In the first application, compaction of visco-elastic powders were carried out. During the phase of contraction of the particles, one observes that rearrangements of the contact network are coupled to an increase of the average coordination number of the grains. The pressure applied by the piston to deform the granular medium increases exponentially with the piston's displacement, independently of the particle shape constituting the system. The probability distribution of the contact forces shifts towards narrow distributions, suggesting an homogenization of the stress propagation.

The second application consists of a 2D analysis of the flux of particles through the aperture of a silo. In agreement with other simulation work of granular materials, the flux of material measured at the output is shown to be strongly related to the shape of the flowing material. The irregularity of the flux demonstrates that frictional grains are likely to jam at small apertures ($D \approx 6r_g$). During the jamming events, the structure is supported by arches of stress. With frictionless particles, the discharge is constant for a given particle shape. As already stated by Langston & al. [101] the most elongated particles lead to faster discharge rates than circular ones.

8.2 Recommendations for future work

Throughout the thesis, possibilities for future avenues of exploration have been highlighted. Fruitful areas for future research have been identified:

- From a computational point of view, the expansion of the combined finite-discrete element method to three dimensions is essential in order to perform real life case studies. This important development is, however, very complex and it needs to incorporate the wide range of possible interactions. The contact interaction method employed is valid for any geometry at contact and applicable intrinsically to any kind of 2D interactions. However, 3D extension of the contact interaction is a non-trivial task that requires extensive effort.

- Many phenomena implicating interaction between solid particle and interstitial fluid phase (liquid or gaseous) are commonly encountered in earth sciences. Economical interests to investigate the fluid flow through a realistic granular medium are critical with, for instance, important applications in the oil industry where sedimentary rocks are typical oil reservoirs. In consequence, advanced coupled methods are greatly needed.

- Interactions at the molecular level are of a different nature than for larger particles. In particular repulsive electrostatic forces can become so strong that particles barely touch as it is the case in systems of very fine particles. All types of repulsive contact

forces are neglected in the present work. However, to understand with realism some aspects of the rock genesis, the inclusion of these small scale interactions can become fundamental.

- Additional developments can be directed towards parallelisation strategies in order to address problems of large scale involving millions of calculation points.
- Creation of a library of material behaviours in order to extend the applicability of the FEM-DEM for a large set of material rheology. For instance the implementation of plastic deformations is essential to reproduce quantitatively the compaction of powders.

Another area for improving our understanding of granular media would consist of extending the investigation to more general cases of poly-disperse set of grains with arbitrary shapes. It would also be of interests to compare the structures and the force chains networks obtained with different construction mechanisms.

Finally, the establishment of a continuum theory to predict the stress transmission in granular materials remains a challenging research interests for the future. The accurate computation of the stress tensor with the FEM-DEM could be useful to validate this theory. For the validation, one can imagine comparing the theoretical mechanical response of a static granular assembly to a local stress perturbation - i.e the Green's function - with large scale FEM-DEM simulations.

Appendix A

Shape descriptors

A.1 Form factors

Table A.1: *Commonly used circularity (taken from [20])*

Index name	Formula	Range	Reference
Wentworth flatness index	$\frac{L+I}{2S}$	0 to ∞	[221]
Krumbein intercept sphericity, Ψ	$\sqrt[3]{\frac{IS}{L^2}}$	0 to 1	[96, 166]
Corey shape factor	$\frac{S^2}{\sqrt{LI}}$	0 to 1	[35]
Maximum projection sphericity, Ψ_p	$\sqrt[3]{\frac{S^2}{LI}}$	0 to 1	[56]
Aschenbrenner shape factor, F	$\frac{LS}{I^2}$	0 to ∞	[7]
Williams shape factor, W	$1-\frac{LS}{I^2}$(when $I^2 > LS$); $\frac{I^2}{LS}-1$ (when $I^2 \leq LS$)	-1 to 1	[223]
Janke Form factor, E	$\frac{S}{\sqrt{\frac{L^2+I^2+S^2}{3}}}$	0 to ∞	[88]
Oblate-Prolate index	$\frac{10(\frac{L-I}{L-S}-0.5)}{\frac{S}{L}}$	-∞ to ∞	[44]

Notations:
L is the longest particle axis (perpendicular to I and S)
I is the intermediate axis
S is the shortest axis

A.2 Sphericity

Table A.2: *Commonly used circularity (taken from [20])*

Formula	Range	Reference	Notes
$\frac{4A}{\pi L^2}$	0 to 1	[154]	Ratio of the area of the grain to the area of a circle with diameter equal to the longest diameter of the grain. Pentland called this "roundness"
$\frac{4\pi A}{p^2}$	0 to 1	[36]	Ratio of the area of the grain to the area of a circle with the same perimeter. Cox called this "roundness"
$\frac{4A}{\pi(D_c)^2}$	0 to 1	[207]	Ratio of the area of the grain to the area of the smallest circumscribing circle. Tickell called this "roundness"
$\frac{c}{C} = \sqrt{\frac{4\pi A}{p^2}}$	0 to 1	[217]	Ratio of the perimeter of a circle with the same area as the grain to the actual perimeter of the grain. Square root of Coxs formula
$\frac{d_c}{D_c} = \sqrt{\frac{4A}{\pi(D_c)^2}}$	0 to 1	[218]	Ratio of the diameter of a circle with the same area as the grain to the diameter of the smallest circumscribing circle. Formula also given in Wadell (1933) but in a different form
$\sqrt{\frac{D_i}{D_c}}$	0 to 1	[176]	Square root of the ratio of the diameter of the largest inscribed circle to the diameter of the smallest circumscribing circle. Riley called this the inscribed circle "sphericity"
$\frac{p^2}{A}$	4π to ∞	[89]	General ratio of perimeter to area

Notations:
P is the perimeter of the particle
A is the area of the particle
D_i is the diameter of the largest inscribed circle
Dc is the diameter of the smallest circumscribing circle

A.3 Roundness

Table A.3: *Commonly used roundness indices (taken from [20])*

Formula	Range	Reference	Notes
$\frac{D_k}{L_w}$	0 to 1	[220]	Ratio of the diameter of curvature of the sharpest corner to the long axis of the grain
$\frac{D_k}{(L+I)/2}$	0 to 1	[221]	Ratio of the diameter of curvature of the sharpest corner to mean pebble diameter
$\frac{\sum \frac{D_i}{D_r}}{n} = \frac{(\frac{\sum D_r}{n})}{D_i}$	0 to 1	[216] (First Formula)	Average ratio of the diameter of curvature of all corners to the diameter of the largest inscribed circle
$\frac{n}{\sum \frac{D_i}{D_r}}$	0 to 1	[216] (Second Formula)	Reciprocal of the average ratio of the diameter of the largest inscribed circle to the diameter of curvature of all corners
$\frac{D_k}{I}$	0 to 1	[98]	Ratio of the diameter of curvature of the sharpest corner to the intermediate axis of the grain
$\frac{D_k}{D_i}$	0 to 1	[44]	Ratio of the diameter of curvature of the sharpest corner to the diameter of the largest inscribed circle

Notations:
D_r is the diameter of curvature of any corners.
D_k is the diameter of curvature of the sharpest corner.
D_i is the diameter of the largest inscribed circle.
n is the number of corners, including those whose diameters are zero.
L_W is the longest diameter measured through the sharpest corner.
L is the length of the grain, in the projected plane.
I is the width of the pebble, in the projected plane.

Appendix B

Implementation details of the Discrete Element Method

The calculation of the trajectories and contact interaction in a system composed of large assemblies of identical spheres is easily handled by using discrete element method (DEM). The major advantage of the DEM is the simplicity of its numerical scheme and of its implementation, in particular for the case of spherical particles. The numerical scheme is classically divided into three main algorithmic sections: 1) the contact detection, 2) the contact interaction and 3) the time integration scheme. This appendix gives the successive details needed for the implementation of the DEM for the case spheres of identical sizes.

In the DEM, the translational and rotational motion of individual particles are given by the resultants of force and moment apply on a particles:

$$m_i \ddot{\mathbf{x}}_i = m_i \mathbf{g} + \sum_{j=1}^{N} \mathbf{f}_{ij}^n, \tag{B.1}$$

and,

$$I_i \dot{\theta}_i = \sum_{j=1}^{N} \mathbf{r}_i j \mathbf{f}_{ij}^s, \tag{B.2}$$

where N is the total number of particles, $\mathbf{g}$ is the gravitational acceleration vector, m_i is the mass of the i-th particle, I_i is the moment of inertia, $\mathbf{x}_i$ is the displacement vector, $\dot{\theta}_i$ is the angular velocity vector, $\mathbf{r}_i j$ is the vector linking the center of mass of the particle and the contact point with the j-th particle, $\mathbf{f}_{ij}^n$ and $\mathbf{f}_{ij}^s$ are the normal and tangential components of the contact force respectively ($\mathbf{f}_{ij} = \mathbf{f}_{ij}^n + \mathbf{f}_{ij}^s \neq 0$ only if the particle i and j are not in contact (for the case of macro-particles it is always true as the Van Der Walls force can generally be neglected)).

In a general manner, in the DEM the relationship between the force and the penetration

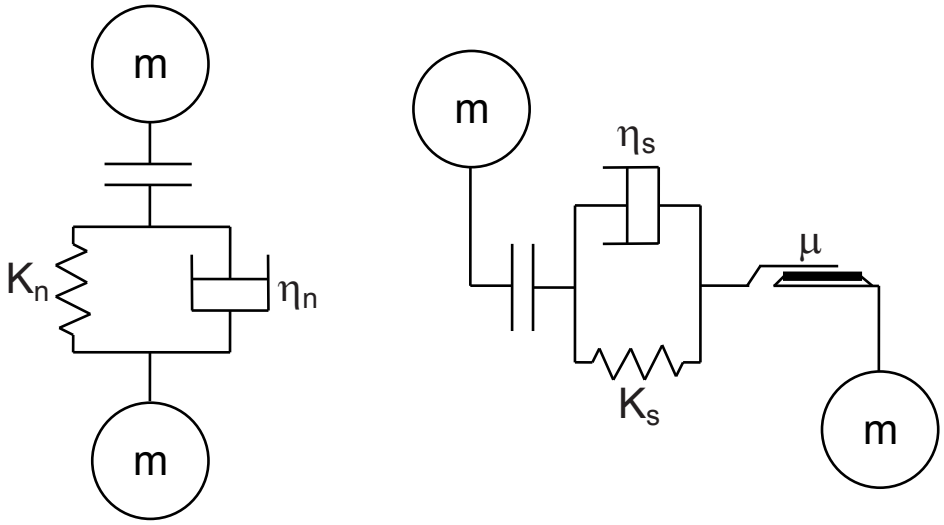


Figure B.1: *Model of force-displacement relationship that can be implemented with the DEM*

between the particle can be described by the spring-dashpot model shown in the Fig. **B.1**. The normal and the tangential component of the contact force are calculated separately. For the tangential force calculation, a slider block is incorporate in order to take into account the presence of friction. The most commonly used friction law, is the Coulomb law, as it appears to be the easiest form of friction to implement.

The normal component of the contact force can be seen as the sum of an elastic and an inelastic term:

$$\mathbf{f}_{ij}^{n} = -k_n \delta_n^{\alpha} - \eta_n \mathbf{v}_n, \tag{B.3}$$

where k is the spring constant, η the damping coefficient, δ_n the normal penetration of the particle and $\mathbf{v}_n$ the normal relative velocity between the particles in contact. In the case of spheres of identical radius r, the normal component of the contact force is given by the Hertz theory [79], so that $\alpha = 1.5$ and $k_n = \dfrac{Y\sqrt{2R}}{3(1-\nu)}$.

Similarly the tangential contact force can be expressed as:

$$\mathbf{f}_{ij}^{t} = -k_t \delta_t - \eta_n \mathbf{v}_t. \tag{B.4}$$

However if the sliding friction condition satisfies, i.e. $|\mathbf{f}_{ij}^{t}| > \mu |\mathbf{f}_{ij}^{n}|$, the contact between the particles i and j or the particle and the wall is sliding. As it was proved to be successful in many engineering and natural systems, the classic Coulomb friction law is commonly implemented, and the equation B.4 is substituted by:

$$\mathbf{f}_{ij}^{t} = -\mu |\mathbf{f}_{ij}^{n}| \frac{\mathbf{v}_t}{|\mathbf{v}_t|}, \tag{B.5}$$

where μ is the coefficient of static friction.

Often, the tangential contact stiffness k_t can be expressed as a function of the normal contact stiffness k_n. Similarly, the tangential damping coefficient η_t and the normal damping coefficient η_n can be related [202] as seen in the equation B.7:

$$\begin{cases} k_t = s * k_n, \\ \eta_t = \sqrt{s} * \eta_n. \end{cases} \tag{B.6}$$

It is worth noticing that the case described in this section can easily be modified in order to treat the case of polydisperse formations, or particles with different mechanical properties, by slightly adapting the contact law for the interaction of sphere with different sizes. There are two major advantages in using spheres in DEM simulations: the first one is the simplicity of the law employed to model the contact interactions, the second one is that the contact detection between the particles is simply performed by calculating the distance between sphere centres, which is an advantage both in term of implementation and algorithmic efficiency. The efficiency of the contact detection can be improved by using algorithms such as Non-Binary search algorithms, C-grid contact or Screening contact detection. For a detailed description the reader is referred to Munjiza's book [135].

Following the processing of (1) the contact detection and (2) the determination of the contact force, displacement and velocity (angular and translational) are updated by integrating explicitly the equation of motion/rotation with an *explicit* time integration scheme. There is a wide variety of explicit time integration schemes such as the central difference (CD), the Gear's predictor-corrector (of various order), the CHIN integration scheme, the Forest & Ruth integration schemes ... all aimed at improving the precision of the solution and the stability of the scheme. Using a CD integration scheme, the displacement and velocities are given by:

$$\begin{cases} \dot{\mathbf{x}}^{n+1} = \dot{\mathbf{x}}^n + \ddot{\mathbf{x}}\Delta t, \\ \mathbf{x}^{n+1} = \mathbf{x}^n + \dot{\mathbf{x}}\Delta t, \\ \dot{\theta}^{n+1} = \dot{\theta}^n + \ddot{\theta}\Delta t, \\ \theta^{n+1} = \theta^n + \dot{\theta}\Delta t, \end{cases} \tag{B.7}$$

where the exponent n denotes the previous time step, $n+1$ the current one, and Δt is the time step. As the explicit time integration scheme is *conditionally* stable, the simulation time-step has to be lower than a threshold value approximated by $\Delta t < \sqrt{\frac{m}{k}}$. It is also worth noticing that in order to produce a realistic contact model, a minimum of 20 time-steps is usually needed to compute the interaction of a binary contact so that Δt need to be accurately allocated.

References

[1] M. P. Allen, D. Frenkel, and J. Talbot. Molecular-dynamics simulation using hard particles. *Computer Physics Reports*, 9(6):301–353, 1989.

[2] F. Alonso-Marroquin, S. Luding, H. J. Herrmann, and I. Vardoulakis. Role of anisotropy in the elastoplastic response of a polygonal packing. *Physical Review E*, 71(5):051304–18, 2005.

[3] K. A. Alshibli and M. I. Alsaleh. Characterizing surface roughness and shape of sands using digital microscopy. *Journal of Computing in Civil Engineering*, 18(1):36–45, 2004.

[4] M. Ammi, D. Bideau, and J. P. Troadec. Geometrical structure of disordered packings of regular polygons; comparison with disc packings structures. *Journal of Physics D: Applied Physics*, 20(4):424, 1987.

[5] S. J. Antony and M. R. Kuhn. Influence of particle shape on granular contact signatures and shear strength: new insights from simulations. *International Journal of Solids and Structures*, 41(21):5863–5870, 2004.

[6] D. Arroyo-Cetto, G. Pulos, R. Zenit, M. A. Jimnez-Zapata, and C. R. Wassgren. Compaction force in a confined granular column. *Physical Review E*, 68(5):051301, 2003.

[7] B.C. Aschenbrenner. A new method of expressing particle sphericity. *J. Sed. Petrol.*, 26:15–31, 1956.

[8] B. N. Asmar, P. A. Langston, A. J. Matchett, and J. K. Walters. Validation tests on a distinct element model of vibrating cohesive particle systems. *Computers and Chemical Engineering*, 26(6):785–802, 2002.

[9] E. Azema, F. Radjai, R. Peyroux, and G. Saussine. Force transmission in a packing of pentagonal particles. *Physical Review E*, 76(1):011301, 2007.

[10] K. Bagi. An algorithm to generate random dense arrangements for discrete element simulations of granular assemblies. *Granular Matter*, 7(1):31–43, 2005. 10.1007/s10035-004-0187-5.

[11] S. G. Bardenhagen, J. U. Brackbill, and D. Sulsky. The material-point method for granular materials. *Computer Methods in Applied Mechanics and Engineering*, 187(3-4):529–541, 2000.

[12] S. G. Bardenhagen, J. U. Brackbill, and D. Sulsky. Numerical study of stress distribution in sheared granular material in two dimensions. *Physical Review E*, 62(3):3882, 2000.

[13] P. J. Barrett. The shape of rock particles, a critical review. *Sedimentology*, 27(3):291–303, 1980.

[14] J. D. Bernal. The bakerian lecture, 1962. the structure of liquids. *Proc. Roy. Soc., A*, 280(1382):299–322, 1964.

[15] J. D. Bernal and J. Mason. Packing of spheres: Co-ordination of randomly packed spheres. *Nature*, 188(4754):910–911, 1960. 10.1038/188910a0 10.1038/188910a0.

[16] J. G. Berryman. Random close packing of hard spheres and disks. *Physical Review A*, 27(2):1053, 1983.

[17] W. A. Beverloo, H. A. Leniger, and J. van de Velde. The flow of granular solids through orifices. *Chemical Engineering Science*, 15(3-4):260–269, 1961.

[18] D. Bideau and J.-P. Troadec. Compacity and mean coordination number of dense packings of hard discs. *J. Phys. C: Solid State Phys.*, 17:731–735, 1984.

[19] D.l L. Blair, N. W. Mueggenburg, A. H. Marshall, H.h M. Jaeger, and S. R. Nagel. Force distributions in three-dimensional granular assemblies: Effects of packing order and interparticle friction. *Physical Review E*, 63(4):041304, 2001.

[20] S. J. Blott and K. Pye. Particle shape: a review and new methods of characterization and classification. *Sedimentology*, 55(1):31–63, 2008.

[21] R. Blumenfeld. Stresses in isostatic granular systems and emergence of force chains. 93(10):108301, 2004.

[22] R. Blumenfeld. Stresses in two-dimensional isostatic granular systems: exact solutions. *New Journal of Physics*, 9, 2007.

[23] R. Blumenfeld, S.F. Edwards, and R.C. Ball. Granular matter and the marginal rigidity state. *Journal of Physics: Condensed Matter*, 17:2481–2487, 2005.

[24] J. P. Bouchaud, P. Claudin, D. Levine, and M. Otto. Force chain splitting in granular materials: A mechanism for large-scale pseudo-elastic behaviour. *The European Physical Journal E - Soft Matter*, 4(4):451–457, 2001. 10.1007/s101890170100.

[25] A. P. J. Breu, H. M. Ensner, C. A. Kruelle, and I. Rehberg. Reversing the brazil-nut effect: Competition between percolation and condensation. *Physical Review Letters*, 90(1):014302, 2003.

[26] B. J. Buchalter and R. Mark Bradley. Orientational order in random packings of ellipses. *Physical Review A*, 46(6):3046, 1992.

[27] V. Buchholtz, J. A. Freund, and T. Pschel. Molecular dynamics of comminution in ball mills. *The European Physical Journal B - Condensed Matter and Complex Systems*, 16(1):169–182, 2000.

[28] C. S. Campbell. Rapid granular flows. 22(1):57–90, 1990.

[29] C. S. Campbell. A problem related to the stability of force chains. *Granular Matter*, 5(3):129–134, 2003. 10.1007/s10035-003-0138-6.

[30] C.S. Campbell, P.W. Cleary, and M. Hopkins. Large-scale landslide simulations: Global deformation, velocities and basal friction. *JOURNAL OF GEOPHYSICAL RESEARCH*, 100(B5):82678283, 1995.

[31] M. E. Cates, J. P. Wittmer, J. P. Bouchaud, and P. Claudin. Jamming, force chains, and fragile matter. *Physical Review Letters*, 81(9):1841, 1998. Assumption for fragility states that the strong force network are minimally coordinated.

[32] Y. F. Cheng, S. J. Guo, and H. Y. Lai. Dynamic simulation of random packing of spherical particles. *Powder Technology*, 107(1-2):123–130, 2000.

[33] Paul W. Cleary and Mark L. Sawley. Dem modelling of industrial granular flows: 3d case studies and the effect of particle shape on hopper discharge. *Applied Mathematical Modelling*, 26(2):89–111, 2002.

[34] S. N. Coppersmith, C. h Liu, S. Majumdar, O. Narayan, and T. A. Witten. Model for force fluctuations in bead packs. *Physical Review E*, 53(5):4673, 1996.

[35] A.T. Corey. Influence of shape on fall velocity of sand grains., 1949.

[36] E. A. Cox. A method for assigning numerical and percentage values to the degree of roundness of sand grains. *J. Paleontol.*, 1(179-183), 1927.

[37] L. Cui and C. OSullivan. Analysis of a triangulation based approach for specimen generation for discrete element simulations. *Granular Matter*, 5(3):135–145, 2003. 10.1007/s10035-003-0145-7.

[38] D. J. Cumberland and R. J. Crawford. *The packing of particles*. Elsevier Science Pub. Co. Inc.,New York, NY, 1987.

[39] P. A. Cundall. Formulation of a 3-dimensional distinct element model .1. a scheme to detect and represent contacts in a system composed of many polyhedral blocks. *International Journal of Rock Mechanics and Mining Sciences and Geomechanics Abstracts*, 25(3):107–116, 1988. Times Cited: 104.

[40] P.A. Cundall and O.D.L. Strack. A discrete element model for granular assemblies. *geotechnique*, 1979.

[41] M. Da Silva and J. Rajchenbach. Stress transmission through a model system of cohesionless elastic grains. *Nature*, 406(6797):708–710, 2000. 0028-0836 10.1038/35021023 10.1038/35021023.

[42] P. Dantu. Contribution ltude mcanique et gomtrique des milieux pulvrulents. In *Proceedings of the 4th International Conference on Soil Mechanics and Foundations Engineering*, volume 1, pages 144–148. Butterworths Scientific Publications, London, 1957.

[43] A. Diugys and B. Peters. An approach to simulate the motion of spherical and non-spherical fuel particles in combustion chambers. *Granular Matter*, 3(4):231–266, 2001. 10.1007/PL00010918.

[44] J. E. Dobkins and R. L. Folk. Shape development on tahiti-nui. *Journal of Sedimentary Petrology*, 40(4):1167, 1970.

[45] A. Donev, I. Cisse, D. Sachs, E. A. Variano, F. H. Stillinger, R. Connelly, S. Torquato, and P. M. Chaikin. Improving the density of jammed disordered packings using ellipsoids. *Science*, 303(5660):990–993, 2004.

[46] A. Donev, R. Connelly, F. H. Stillinger, and S. Torquato. Underconstrained jammed packings of nonspherical hard particles: Ellipses and ellipsoids. *Physical Review E*, 75(5):051304, 2007.

[47] A. Donev, S. Torquato, and F. H. Stillinger. Neighbor list collision-driven molecular dynamics simulation for nonspherical hard particles. i. algorithmic details. *Journal of Computational Physics*, 202(2):737–764, 2005.

[48] D. J. Durian, H. Bideaud, P. Duringer, A. Schroder, F. Thalmann, and C. M. Marques. What is in a pebble shape? *Physical Review Letters*, 97(2):028001, 2006.

[49] S. F. Edwards and D. V. Grinev. Statistical mechanics of granular materials: stress propagation and distribution of contact forces. *Granular Matter*, 4(4):147–153, 2003. 10.1007/s10035-002-0117-3.

[50] J. M. Erikson, N. W. Mueggenburg, H. M. Jaeger, and S. R. Nagel. Force distributions in three-dimensional compressible granular packs. *Physical Review E*, 66(4):040301, 2002.

[51] J. F. Favier, M. H. Abbaspour-Fard, M. Kremmer, and A. O. Raji. Shape representation of axisymmetrical, non-spherical particles in discrete element simulation using multi-element model particles. *Engineering Computations*, 16(4):467–480, 1999. Times Cited: 14.

[52] Y. T. Feng, K. Han, and D. R. J. Owen. Filling domains with disks: an advancing front approach. *International Journal for Numerical Methods in Engineering*, 56(5):699–713, 2003.

[53] Y. T. Feng and D. R. J. Owen. A 2d polygon/polygon contact model: algorithmic aspects. *Engineering Computations*, 21(2-4):265–277, 2004.

[54] Y.T Feng, K. Han, and D. R. J. Owen. Some computational issues on numerical simulation of particulate systems, 2002.

[55] J. L. Finney. Random packings and the structure of simple liquids. i. the geometry of random close packing. *Nature*, 319(1539):479–493, 1970.

[56] R.L. Folk. Student operator error in determination of roundness, sphericity and grain size. *J. Sed. Petrol.*, 25, 1955.

[57] Y. Forterre and O. Pouliquen. Flows of dense granular media. 40(1):1–24, 2008.

[58] F. Y. Fraige and P. A. Langston. Integration schemes and damping algorithms in distinct element models. *Advanced Powder Technology*, 15(2):227–245, 2004.

[59] F. Y. Fraige, P. A. Langston, and G. Z. Chen. Distinct element modelling of cubic particle packing and flow. *Powder Technology*, In Press, Corrected Proof, 2008.

[60] G. Frenkel, R. Blumenfeld, Z. Grof, and P. R. King. Structural characterization and statistical properties of two-dimensional granular systems. *Physical Review E (Statistical, Nonlinear, and Soft Matter Physics)*, 77(4):041304–10, 2008.

[61] G. Frenning and G. Alderborn. Evolution of distributions and spatial correlations of single-particle forces and stresses during compression of ductile granular materials. *Physical Review E*, 71(1):011305–9, 2005.

[62] M. Gan, N. Gopinathan, X. Jia, and R. A. Williams. Predicting packing characteristics of particles of arbitrary shapes. *Kona*, 22:82–92, 2004.

[63] J. Geng, D. Howell, E. Longhi, R. P. Behringer, G. Reydellet, L. Vanel, E. Clment, and S. Luding. Footprints in sand: The response of a granular material to local perturbations. *Physical Review Letters*, 87(3):035506, 2001.

[64] R.M. German. *Particle Packing Characteristics*. Metal Powder Industries Federation, 1989.

[65] D. T. Gethin, R. S. Ransing, R. W. Lewis, M. Dutko, and A. J. L. Crook. Numerical comparison of a deformable discrete element model and an equivalent continuum analysis for the compaction of ductile porous material. *Computers and Structures*, 79(13):1287–1294, 2001.

[66] D. T. Gethin, X. S. Yang, and R. W. Lewis. A two dimensional combined discrete and finite element scheme for simulating the flow and compaction of systems comprising irregular particulates. *Computer Methods in Applied Mechanics and Engineering*, 195(41-43):5552–5565, 2006.

[67] C. Goldenberg and I. Goldhirsch. Force chains, microelasticity, and macroelasticity. *Physical Review Letters*, 89(8):084302, 2002.

[68] C. Goldenberg and I. Goldhirsch. Friction enhances elasticity in granular solids. *Nature*, 435(7039):188–191, 2005. 0028-0836 10.1038/nature03497 10.1038/nature03497.

[69] I. Goldhirsch. Rapid granular flows. 35(1):267–293, 2003.

[70] J. E. Guilkey and J. A. Weiss. Implicit time integration for the material point method: Quantitative and algorithmic comparisons with the finite element method. 57(9):1323–1338, 2003.

[71] R. Guises, J. Xiang, J.-P. Latham, and A. Munjiza. Granular packing: numerical simulation and the characterisation of the effect of particle shape. *Submitted to granular matter*, 2008.

[72] O. Haggstrom and R. Meester. Nearest neighbor and hard sphere models in continuum percolation. *Random Structures and Algorithms*, 9(3):295–315, 1996.

[73] T.C. Hales. A proof of the kepler conjecture. *Annales of Mathematics*, 162:121pp, 2005.

[74] K. Han, D. Peric, A.J.L. Crook, and D. R. J. Owen. A combined finite/discrete element simulation of shot peening processes part i: studies on 2d interaction laws. *Engineering Computations*, 17(5):593–620, 2000.

[75] R. Hart, P. A. Cundall, and J. Lemos. Formulation of a 3-dimensional distinct element model .2. mechanical calculations for motion and interaction of a system composed of many polyhedral blocks. *International Journal of Rock Mechanics and Mining Sciences and Geomechanics Abstracts*, 25(3):117–125, 1988. Times Cited: 71.

[76] R.R. Hartley. *Evolving Force Networks in Deforming Granular Materials*. PhD thesis, Duke university, 2003.

[77] A. Hassanpour and M. Ghadiri. Distinct element analysis and experimental evaluation of the heckel analysis of bulk powder compression. *Powder Technology*, 141(3):251–261, 2004.

[78] R.W. Heckel. Densitypressure relationships in powders compaction. *Trans. Metal. Soc. AIME*, 221:671–675, 1961.

[79] H. Hertz. On the contact of elastic solids. *Journal fr die reine und angewandte Mathematik*, 92, 1881.

[80] E. L. Hinrichsen, J. Feder, and T. Jssang. Random packing of disks in two dimensions. *Physical Review A*, 41(8):4199, 1990.

[81] C. Hogue. Shape representation and contact detection for discrete element simulations of arbitrary geometries. *Engineering Computations*, 15(2-3):374–+, 1998.

[82] C. Hogue and D. Newland. Efficient computer-simulation of moving granular particles. *Powder Technology*, 78(1):51–66, 1994.

[83] J. M. F. G. Holst, J. Y. Ooi, J. M. Rotter, and G. H. Rong. Numerical modeling of silo filling. i: Continuum analyses. *Journal of Engineering Mechanics*, 125(1):94–103, 1999.

[84] J. M. F. G. Holst, J. M. Rotter, Jin Y. Ooi, and G. H. Rong. Numerical modeling of silo filling. ii: Discrete element analyses. *Journal of Engineering Mechanics*, 125(1):104–110, 1999.

[85] D. Howell, R. P. Behringer, and C. T. Veje. Fluctuations in granular media. *Chaos*, 9(3):559–572, 1999.

[86] D. Howell, R. P. Behringer, and C. T. Veje. Stress fluctuations in a 2d granular couette experiment: A continuous transition. *Physical Review Letters*, 82(26):5241, 1999.

[87] J. P. Hyslip and L. E. Vallejo. Fractal analysis of the roughness and size distribution of granular materials. *Engineering Geology*, 48(3-4):231–244, 1997.

[88] N.C. Janke. Effect of shape upon the settling velocity of regular convex geometric particles. *J. Sed. Petrol.*, 36:370–376, 1966.

[89] V.C. Janoo. Quantification of shape, angularity and surface texture of base course materials. *US Army Corps of Engineers Cold Regions Research and Engineering Laboratory*, Special report 98-1:22, 1998.

[90] X. Jia, M. Gan, R. A. Williams, and D. Rhodes. Validation of a digital packing algorithm in predicting powder packing densities. *Powder Technology*, 174(1-2):10–13, 2007.

[91] X. Jia and R. A. Williams. A packing algorithm for particles of arbitrary shapes. *Powder Technology*, 120(3):175–186, 2001.

[92] R. Jullien, A. Pavlovitch, and P. Meakin. Random packings of spheres built with sequential models. *Journal of Physics A: Mathematical and General*, 25(15):4103–4113, 1992. 0305-4470.

[93] H. H. Kausch, D. G. Fesko, and N. W. Tschoegl. The random packing of circles in a plane. *Journal of Colloid and Interface Science*, 37(3):603–611, 1971.

[94] J. B. Knight, C. G. Fandrich, C.-N. Lau, H. M. Jaeger, and S. R. Nagel. Density relaxation in a vibrated granular material. *Physical Review E*, 51(5):3957, 1995. Copyright (C) 2008 The American Physical Society Please report any problems to prola@aps.org PRE.

[95] P. Komodromos. A simplified updated lagrangian approach for combining discrete and finite element methods. *Computational Mechanics*, 35(4):305–313, 2005. 10.1007/s00466-004-0609-6.

[96] W. C. Krumbein. Measurement and geological significance of shape and roundness of sedimentary particles. 11(2):64–72, 1941.

[97] N. P. Kruyt. Contact forces in anisotropic frictional granular materials. *International Journal of Solids and Structures*, 40(13-14):3537–3556, 2003.

[98] P. H. Kuenen. Experimental abrasion of pebbles. 2. rolling by currents. *J. Geol.*, 64:336–368, 1956.

[99] J. W. Landry and G. S. Grest. Granular packings with moving side walls. *Physical Review E*, 69(3):031303, 2004.

[100] J. W. Landry, G. S. Grest, L. E. Silbert, and S. J. Plimpton. Confined granular packings: Structure, stress, and forces. *Physical Review E*, 67(4):041303, 2003.

[101] P. A. Langston, M. A. Al-Awamleh, F. Y. Fraige, and B. N. Asmar. Distinct element modelling of non-spherical frictionless particle flow. *Chemical Engineering Science*, 59(2):425–435, 2004.

[102] P. A. Langston, M. S. Nikitidis, U. Tzn, D. M. Heyes, and N. M. Spyrou. Microstructural simulation and imaging of granular flows in two- and three-dimensional hoppers. *Powder Technology*, 94(1):59–72, 1997.

[103] P. A. Langston, U. Tzn, and D. M. Heyes. Continuous potential discrete particle simulations of stress and velocity fields in hoppers: transition from fluid to granular flow. *Chemical Engineering Science*, 49(8):1259–1275, 1994.

[104] P. A. Langston, U. Tzn, and D. M. Heyes. Discrete element simulation of granular flow in 2d and 3d hoppers: Dependence of discharge rate and wall stress on particle interactions. *Chemical Engineering Science*, 50(6):967–987, 1995.

[105] J. P. Latham, Y. Lu, and A. Munjiza. A random method for simulating loose packs of angular particles using tetrahedra. *Geotechnique*, 51(10):871–879, 2001. Times Cited: 6.

[106] J. P. Latham and A. Munjiza. The modelling of particle systems with real shapes. *Philosophical Transactions of the Royal Society A: Mathematical, Physical and Engineering Sciences*, 362(1822):1953–1972, 2004. 10.1098/rsta.2004.1425.

[107] G. Lees. The measurement of particle shape and its influence in engineering materials. *Journal of the British Granite and Whinestone Federation*, pages 1–22, 1964.

[108] J. Lemaitre, J.-P. Troadec, A. Gervois, and D. Bideau. Experimental study of densification of disc assemblies. *Europhys. Lett.*, 14:77–83, 1991.

[109] R. W. Lewis, D. T. Gethin, X. S. Yang, and R. C. Rowe. A combined finite-discrete element method for simulating pharmaceutical powder tableting, 2005.

[110] Y. Li, Y. Xu, and C. Thornton. A comparison of discrete element simulations and experiments for 'sandpiles' composed of spherical particles. *Powder Technology*, 160(3):219–228, 2005.

[111] X. Lin and T. T. Ng. A three-dimensional discrete element model using arrays of ellipsoids. *Geotechnique*, 47(2):319–329, 1997.

[112] X. S. Lin and T. T. Ng. Contact detection algorithms for 3-dimensional ellipsoids in discrete element modeling. *International Journal for Numerical and Analytical Methods in Geomechanics*, 19(9):653–659, 1995.

[113] C. h Liu, S. R. Nagel, D. A. Schecter, S. N. Coppersmith, S. Majumdar, O. Narayan, and T. A. Witten. Force fluctuations in bead packs. *Nature*, 269(5223):513–515, 1995.

[114] M. Ltzel, S. Luding, and H. Herrmann. From discontinuous models towards a continuum description. In *Continuous and Discontinuous Modelling of Cohesive-Frictional Materials*, pages 215–230. 2001.

[115] S. Luding. Stress distribution in static two-dimensional granular model media in the absence of friction. *Physical Review E*, 55(4):4720, 1997.

[116] S. Luding. Granular media information propagation. *Nature*, 435(7039):159–160, 2005. 0028-0836 10.1038/435159a 10.1038/435159a.

[117] M. Madadi, O. Tsoungui, M. Latzel, and S. Luding. On the fabric tensor of polydisperse granular materials in 2d. *International Journal of Solids and Structures*, 41(9-10):2563–2580, 2004.

[118] T. S. Majmudar and R. P. Behringer. Contact force measurements and stress-induced anisotropy in granular materials. *Nature*, 435(1079):1079–1082, 2005. 0028-0836 10.1038/nature03805 10.1038/nature03805.

[119] T. S. Majmudar, M. Sperl, S. Luding, and R. P. Behringer. Jamming transition in granular systems. 98(5):058001, 2007.

[120] H. A. Makse, S. Havlin, P. R. King, and H. E. Stanley. Spontaneous stratification in granular mixtures. *Nature*, 386(6623):379–382, 1998. 10.1038/386379a0 10.1038/386379a0.

[121] H. A. Makse, D. L. Johnson, and L. M. Schwartz. Packing of compressible granular materials. *Physical Review Letters*, 84(18):4160, 2000.

[122] W. Man, A. Donev, F. H. Stillinger, M. T. Sullivan, W. B. Russel, D. Heeger, S. Inati, S. Torquato, and P. M. Chaikin. Experiments on random packings of ellipsoids. *Physical Review Letters*, 94(19):198001–4, 2005.

[123] A. Mangeney-Castelnau, F. Bouchut, J. P. Vilotte, E. Lajeunesse, A. Aubertin, and M. Pirulli. On the use of saint venant equations to simulate the spreading of a granular mass. *Journal of Geophysical Research*, 110(B9), 2005.

[124] C. Mankoc, A. Janda, R. Arvalo, J. Pastor, I. Zuriguel, A. Garcimartn, and D. Maza. The flow rate of granular materials through an orifice. *Granular Matter*, 9(6):407–414, 2007. 10.1007/s10035-007-0062-2.

[125] S. Masson and J. Martinez. Effect of particle mechanical properties on silo flow and stresses from distinct element simulations. *Powder Technology*, 109(1-3):164–178, 2000.

[126] H. G. Matuttis, S. Luding, and H. J. Herrmann. Discrete element simulations of dense packings and heaps made of spherical and non-spherical particles. *Powder Technology*, 109(1-3):278–292, 2000.

[127] A. Mehta. *Granular Physics*. Cambridge University Press, 2007.

[128] R.D. Mindlin and H. Deresiwicz. Elastic spheres in contact under varying oblique forces. *Journal of Applied Mechanics*, pages 327–344, 1953.

[129] A. A. Mirghasemi, L. Rothenburg, and E. L. Matyas. Influence of particle shape on engineering properties of assemblies of two-dimensional polygon-shaped particles. *Geotechnique*, 52(3):209–217, 2002.

[130] J.P. Morris, L.A. Glenn, and S.C. Blair. The distinct element method - application to structures in jointed rocks. *Lecture Notes in Computational Science and Engineering*, 26:291–306, 2002.

[131] J.P. Morris, M.B. Rubin, S.C. Blair, L.A. Glenn, and F.E. Heuze. Simulations of underground structures subjected to dynamic loading using the distinct element method. *Engineering Computations*, 21(2/3/4):384–408, 2004.

[132] N. W. Mueggenburg, H. M. Jaeger, and S. R. Nagel. Stress transmission through three-dimensional ordered granular arrays. *Physical Review E*, 66(3):031304, 2002.

[133] D M. Mueth, H M. Jaeger, and S R. Nagel. Force distribution in a granular medium. *Physical Review E*, 57(3):3164, 1998.

[134] A. Munjiza. *Discrete elements in transient dynamics of fractured media*. PhD thesis, University of Wales, UK, 1992.

[135] A. Munjiza. *The Combined Finite-Discrete Element Method*. John Wiley and Sons, 2004.

[136] A. Munjiza and K. R. F. Andrews. Nbs contact detection algorithm for bodies of similar size. 43(1):131–149, 1998.

[137] A. Munjiza and K. R. F. Andrews. Penalty function method for combined finite-discrete element systems comprising large number of separate bodies. *International Journal for Numerical Methods in Engineering*, 49(11):1377–1396, 2000.

[138] A. Munjiza, D. R. J. Owen, and N. Bicanic. A combined finite-discrete element method in transient dynamics of fracturing solids. *Engineering Computations*, 12(2):145–174, 1995.

[139] M. Muthuswamy and A. Tordesillas. How do interparticle contact friction, packing density and degree of polydispersity affect force propagation in particulate assemblies? *Journal of Statistical Mechanics: Theory and Experiments*, 2006.

[140] M. Nardin, E. Papirer, and J. Schultz. Contribution a l'etude des empilements au hasard de fibres et/ou de particules spheriques. *Powder Technology*, 44(2):131–140, 1985.

[141] M. Nicodemi. Force correlations and arch formation in granular assemblies. *Physical Review Letters*, 80(6):1340, 1998.

[142] G. T. Nolan and P. E. Kavanagh. Random packing of nonspherical particles. *Powder Technology*, 84(3):199–205, 1995.

[143] C. Nouguier-Lehon, B. Cambou, and E. Vincens. Influence of particle shape and angularity on the behaviour of granular materials: a numerical analysis. *International Journal for Numerical and Analytical Methods in Geomechanics*, 27(14):1207–1226, 2003.

[144] E. R. Nowak, J. B. Knight, E. Ben-Naim, H. M. Jaeger, and S. R. Nagel. Density fluctuations in vibrated granular materials. *Physical Review E*, 57(2):1971, 1998.

[145] C. S. O'Hern, S. A. Langer, A. J. Liu, and S. R. Nagel. Random packings of frictionless particles. *Physical Review Letters*, 88(7):075507, 2002.

[146] C. S. O'Hern, S. A. Langer, A. J. Liu, and S.R. Nagel. Force distributions near jamming and glass transitions. *Physical Review Letters*, 86(1):111, 2001.

[147] George Y. Onoda and Eric G. Liniger. Experimental determination of the random-parking limit in two dimensions. *Physical Review A*, 33(1):715, 1986.

[148] George Y. Onoda and Eric G. Liniger. Random loose packings of uniform spheres and the dilatancy onset. *Physical Review Letters*, 64(22):2727, 1990. Copyright (C) 2008 The American Physical Society Please report any problems to prola@aps.org PRL.

[149] S. Ostojic, E. Somfai, and B. Nienhuis. Scale invariance and universality of force networks in static granular matter. *Nature*, 439(7078):828–830, 2006. .

[150] H. Ouadfel and L. Rothenburg. Stress-force-fabric' relationship for assemblies of ellipsoids. *Mechanics of Materials*, 33(4):201–221, 2001.

[151] D. R. J. Owen, Y.T. Feng, E. A. de Souza Neto, F. Wang, M. G. Cottrell, F. A. Pires, and J. Yu. The modelling of multi-fracturing solids and particulate media. *Int. J. Numer. Methods Engng*, 60(1):317–340, 2004.

[152] C. C. Pain, M. D. Piggott, A. J. H. Goddard, F. Fang, G. J. Gorman, D. P. Marshall, M. D. Eaton, P. W. Power, and C. R. E. de Oliveira. Three-dimensional unstructured mesh ocean modelling. *Ocean Modelling*, 10(1-2):5–33, 2005.

[153] A. A. Pea, A. Lizcano, F. Alonso-Marroquin, and H. J. Herrmann. Biaxial test simulations using a packing of polygonal particles. *International Journal for Numerical and Analytical Methods in Geomechanics*, 32(2):143–160, 2008.

[154] A. Pentland. A method of measuring the angularity of sands. *Roy. Soc. Canada Proc. Trans. (Ser. 3)*, 21, 1927.

[155] J. F. Peters, M. Muthuswamy, J. Wibowo, and A. Tordesillas. Characterization of force chains in granular material. *Physical Review E*, 72(4):041307, 2005.

[156] A. P. Philipse. The random contact equation and its implications for (colloidal) rods in packings, suspensions, and anisotropic powders. 12(5):1127–1133, 1996.

[157] R. J. Pine, D. R. J. Owen, J. S. Coggan, and J. M. Rance. A new discrete fracture modelling approach for rock masses. *geotechnique*, 57(9):757–766, 2007.

[158] T. Poeschel. *Computational Granular Dynamics: Models and Algorithms*. Springer-Verlag Berlin and Heidelberg GmbH & Co. K, 2005.

[159] A. V. Potapov, M. A. Hopkins, and C. S. Campbell. A 2-dimensional dynamic simulation of solid fracture .1. description of the model. *International Journal of Modern Physics C-Physics and Computers*, 6(3):371–398, 1995.

[160] O. Pouliquen, M. Nicolas, and P. D. Weidman. Crystallization of non-brownian spheres under horizontal shaking. *Physical Review Letters*, 79(19):3640, 1997. Copyright (C) 2008 The American Physical Society Please report any problems to prola@aps.org PRL.

[161] L. Pournin, M. Weber, M. Tsukahara, J. A. Ferrez, M. Ramaioli, and Th M. Liebling. Three-dimensional distinct element simulation of spherocylinder crystallization. *Granular Matter*, 7(2):119–126, 2005. 10.1007/s10035-004-0188-4.

[162] M. C. Powers. A new roundness scale for sedimentary particles. 23(2):117–119, 1953.

[163] M. Price, V. Murariu, and G Morrison. Sphere clump generation and trajectory comparison for real particles. In *Fifth International Conference on Discrete Element Methods*, Brisbane, Australia, 2007.

[164] Adam T. Procopio and Antonios Zavaliangos. Simulation of multi-axial compaction of granular media from loose to high relative densities. *Journal of the Mechanics and Physics of Solids*, 53(7):1523–1551, 2005.

[165] Thorsten Pschel and Volkhard Buchholtz. Static friction phenomena in granular materials: Coulomb law versus particle geometry. *Physical Review Letters*, 71(24):3963, 1993.

[166] W. Pye and M. Pye. Sphericity determination of pebbles and sand grains. *J. Sed. Petrol.*, 13:2834, 1943.

[167] Terence Ivan Quickenden and Gek Kim Tan. Random packing in two dimensions and the structure of monolayers. *Journal of Colloid and Interface Science*, 48(3):382–393, 1974.

[168] Y. I. Rabinovich, M. S. Esayanur, and B. M. Moudgil. Capillary forces between two spheres with a fixed volume liquid bridge: Theory and experiment, 2005.

[169] F. Radjai, M. Jean, J.-J. Moreau, and S. Roux. Force distributions in dense two-dimensional granular systems. *Physical Review Letters*, 77(2):274, 1996.

[170] F. Radjai, S. Roux, and J.-J. Moreau. Contact forces in a granular packing. *Chaos*, 9(3):544–550, 1999.

[171] F. Radjai, D. E. Wolf, M. Jean, and J.-J. Moreau. Bimodal character of stress transmission in granular packings. *Physical Review Letters*, 80(1):61, 1998.

[172] Ouamar Rahli, Louns Tadrist, and Robert Blanc. Experimental analysis of the porosity of randomly packed rigid fibers. *Comptes Rendus de l'Acadmie des Sciences - Series IIB - Mechanics-Physics-Astronomy*, 327(8):725–729, 1999.

[173] I. C. Rankenburg and R. J. Zieve. Influence of shape on ordering of granular systems in two dimensions. *Physical Review E*, 63(6):061303, 2001.

[174] R. S. Ransing, R. W. Lewis, and D. T. Gethin. Using a deformable discrete-element technique to model the compaction behaviour of mixed ductile and brittle particulate systems. *Philosophical Transactions of the Royal Society A: Mathematical, Physical and Engineering Sciences*, 362(1822):1867–1884, 2004. 10.1098/rsta.2004.1421.

[175] G. Reydellet and E. Clment. Green's function probe of a static granular piling. *Physical Review Letters*, 86(15):3308, 2001.

[176] N. A. Riley. Projection sphericity. *J. Sed. Petrol.*, 11:94–97, 1941.

[177] Anthony Rosato, Katherine J. Strandburg, Friedrich Prinz, and Robert H. Swendsen. Why the brazil nuts are on top: Size segregation of particulate matter by shaking. *Physical Review Letters*, 58(10):1038, 1987. Copyright (C) 2008 The American Physical Society Please report any problems to prola@aps.org PRL.

[178] L. Rothenburg and R. J. Bathurst. Numerical simulation of idealized granular assemblies with plane elliptical particles. *Computers and Geotechnics*, 11(4):315–329, 1991.

[179] L. Rothenburg and R. J. Bathurst. Micromechanical features of granular assemblies with planar elliptic particles. *Geotechnique*, 42(1):79–95, 1992.

[180] L. Rothenburg and R. J. Bathurst. Influence of particle eccentricity on micromechanical behavior of granular materials. *Mechanics of Materials*, 16(1-2):141–152, 1993.

[181] J. M. Rotter, J. M. F. G. Holst, J. Y. Ooi, and A. M. Sanad. Silo pressure predictions using discrete-element and finite-element analyses. *Philosophical Transactions of the Royal Society of London Series a-Mathematical Physical and Engineering Sciences*, 356(1747):2685–2712, 1998.

[182] E. Rougier, A. Munjiza, and N. W. M. John. Numerical comparison of some explicit time integration schemes used in dem, fem/dem and molecular dynamics. *International Journal for Numerical Methods in Engineering*, 61(6):856–879, 2004.

[183] L. Rouille, J.-M. Missiaen, and G. Thomas. Collective random packing of disks in a plane under the influence of a weak central force. *J. Phys.: Condens. Matter*, 2:3041–3051, 1990.

[184] J.-N. Roux. Geometric origin of mechanical properties of granular materials. *Physical Review E*, 61(6):6802, 2000.

[185] M.B. Rubin. On the theory of a cosserat point and its application to the numerical solution of continuum problems. *ASME J. Appli. Mech.*, 52:368–372, 1985.

[186] S. Sacanna, L. Rossi, A. Wouterse, and A. P. Philipse. Observation of a shape-dependent density maximum in random packings and glasses of colloidal silica ellipsoids. *Journal of Physics: Condensed Matter*, 19(37):376108, 2007. 0953-8984.

[187] S.B. Savage and K. Hutter. The motion of a finite mass of granular material down a rough incline. *Journal of Fluid Dynamic*, 199:177–215, 1989.

[188] I. Schenker, F. T. Filser, T. Aste, and L. J. Gauckler. Microstructures and mechanical properties of dense particle gels: Microstructural characterisation. *Journal of the European Ceramic Society*, 28(7):1443–1449, 2008.

[189] T. Schilling, S. Pronk, B. Mulder, and D. Frenkel. Monte carlo study of hard pentagons. *Physical Review E (Statistical, Nonlinear, and Soft Matter Physics)*, 71(3):036138–6, 2005.

[190] G. D Scott. Packing of spheres: Packing of equal spheres. *Nature*, 188(4754):908–909, 1960. 10.1038/188908a0 10.1038/188908a0.

[191] G. D. Scott and D. M. Kilgour. The density of random close packing of spheres. *Journal of Physics D: Applied Physics*, 2(6):863–866, 1969. 0022-3727.

[192] G.H. Shi. *Discontinuous Deformation Analysis: A New Numerical Model for the Statics and Dynamics of Block Systems*. PhD thesis, University of California, Berkeley, 1988.

[193] G.H. Shi and R. E. Goodman. Two dimensional discontinuous deformation analysis. *International Journal for Numerical and Analytical Methods in Geomechanics*, 9(6):541–556, 1985.

[194] L. E. Silbert, D. Erta, G. S. Grest, T. C. Halsey, and D. Levine. Geometry of frictionless and frictional sphere packings. *Physical Review E*, 65(3):031304, 2002.

[195] L. E. Silbert, G. S. Grest, and J. W. Landry. Statistics of the contact network in frictional and frictionless granular packings. *Physical Review E*, 66(6):061303, 2002.

[196] F. H. Stillinger, E. A. DiMarzio, and R. L. Kornegay. Systematic approach to explanation of the rigid disk phase transition. *The Journal of Chemical Physics*, 40(6):1564–1576, 1964.

[197] K. Stokely, A. Diacou, and Scott V. Franklin. Two-dimensional packing in prolate granular materials. *Physical Review E*, 67(5):051302, 2003.

[198] D. Stoyan. Random sets: Models and statistics. 66(1):1–27, 1998.

[199] D. Sulsky, Z. Chen, and H. L. Schreyer. A particle method for history-dependent materials. *Computer Methods in Applied Mechanics and Engineering*, 118(1-2):179–196, 1994.

[200] D. Sulsky, S.-J. Zhou, and H. L. Schreyer. Application of a particle-in-cell method to solid mechanics. *Computer Physics Communications*, 87(1-2):236–252, 1995.

[201] D. N. Sutherland. Random packing of circles in a plane. *Journal of Colloid and Interface Science*, 60(1):96–102, 1977.

[202] K. Tanaka, M. Nishida, T. Kuminochi, and T. Takagi. Discrete element simulation and experiment for dynamic response of two-dimensional granular matter to the impact of a spherical projectile. *Powder Technology*, 124:160–173, 2002.

[203] C. Thornton. Applications of dem to process engineering problems. *Engineering Computations*, 9(2):289–297, 1992.

[204] C. Thornton. Force transmission in granular media. *Kona powder and particle*, 15:81–90, 1997.

[205] C. Thornton and S. J. Antony. Quasi-static deformation of particulate media. *Philosophical Transactions of the Royal Society A: Mathematical, Physical and Engineering Sciences*, 356(1747):2763–2782, 1998. 10.1098/rsta.1998.0296.

[206] C. Thornton and S. J. Antony. Quasi-static shear deformation of a soft particle system. *Powder Technology*, 109(1-3):179–191, 2000.

[207] F.G. Tickell. *The Examination of Fragmental Rocks*. 1931.

[208] J. M. Ting. A robust algorithm for ellipse-based discrete element modelling of granular materials. *Computers and Geotechnics*, 13(3):175–186, 1992.

[209] S. Torquato, T. M. Truskett, and P. G. Debenedetti. Is random close packing of spheres well defined? *Physical Review Letters*, 84(10):2064, 2000.

[210] T. Travers, M. Ammi, D. Bideau, A. Gervois, J.-C. Messager, and J.-P. Troadec. Mechanical size effects in 2d granular media. *Journal de physique*, 49(6):939–948, 1988.

[211] L. E. Vallejo. Fractal analysis of granular materials. *Geotechnique*, 45(1):159–163, 1995.

[212] A. van Blaaderen and P. Wiltzius. Real-space structure of colloidal hard-sphere glasses. 270(5239):1177–1179, 1995.

[213] L.C. Verman and S. Banerjee. Effect of container walls on packing density of particles. *Nature*, 157:584, 1946.

[214] F. X. Villarruel, B. E. Lauderdale, D. M. Mueth, and H. M. Jaeger. Compaction of rods: Relaxation and ordering in vibrated, anisotropic granular material. *Physical Review E*, 61(6):6914, 2000.

[215] W.M. Visscher and M. Bolsterli. Random packing of equal and unequal spheres in two and three dimensions. *Nature*, 239(5374):504–507, 1972. 10.1038/239504a0 10.1038/239504a0.

[216] H. Wadell. Volume, shape, and roundness of rock particles. *J. Geol.*, 40:443–451, 1932.

[217] H. Wadell. Sphericity and roundness of rock particles. *J. Geol.*, 41:310–331, 1933.

[218] H. Wadell. Volume, shape, and roundness of quartz particles. *J. Geol.*, 43:250–280, 1935.

[219] E. E. Walker. The properties of powders. part vi. the compressibility of powders. *Trans. Faraday Soc.*, 19:73–82, 1923.

[220] C.K. Wentworth. A laboratory and field study of cobble abrasion. *J. Geol.*, 27:507–521, 1919.

[221] C.K. Wentworth. A method of measuring and plotting the shapes of pebbles. *US Geol. Surv. Bull.*, 730(C):91–102, 1922.

[222] H.E. White and S.F. Walton. Particle packing and particle shape. *J. Am. Ceram. Soc.*, 20, 1937.

[223] E.M. Williams. A method of indicating pebble shape with one parameter. *J. Sed. Petrol.*, 35:993–996, 1965.

[224] J.R. Williams and A. Portland. Super-quadrics and modal dynamics for discrete elements in interactive design. *Engineering Computations: International Journal for Computer Aided Engineering*, 9:115–127, 1992.

[225] S. R. Williams and A. P. Philipse. Random packings of spheres and spherocylinders simulated by mechanical contraction. *Physical Review E*, 67(5):051301, 2003.

[226] A. Wouterse, S. R. Williams, and A. P. Philipse. Effect of particle shape on the density and microstructure of random packings. *Journal of Physics: Condensed Matter*, 19(40):406215, 2007. 0953-8984.

[227] J. Xiang and D. McGlinchey. Numerical simulation of particle motion in dense phase pneumatic conveying. *Granular Matter*, 6(2):167–172, 2004. 10.1007/s10035-004-0161-2.

[228] Y. Xu, K. D. Kafui, C. Thornton, and G. Lian. Effects of material properties on granular flow in a silo using dem simulation, 2002.

[229] R. Y. Yang, R. P. Zou, and A. B. Yu. Computer simulation of the packing of fine particles. *Physical Review E*, 62(3):3900, 2000.

[230] R. Y. Yang, R. P. Zou, and A. B. Yu. Effect of material properties on the packing of fine particles. *Journal of Applied Physics*, 94(5):3025–3034, 2003.

[231] A. B. Yu and N. Standish. Characterisation of non-spherical particles from their packing behaviour. *Powder Technology*, 74(3):205–213, 1993.

[232] R. P. Zou and A. B. Yu. Evaluation of the packing characteristics of mono-sized non-spherical particles. *Powder Technology*, 88(1):71–79, 1996.

[233] I. Zuriguel and T. Mullin. The role of particle shape on the stress distribution in a sandpile. *Proceedings of the Royal Society A: Mathematical, Physical and Engineering Sciences*, 464(2089):99–116, 2008. 10.1098/rspa.2007.1899.

[234] I. Zuriguel, T. Mullin, and J. M. Rotter. Effect of particle shape on the stress dip under a sandpile. *Physical Review Letters*, 98(2):028001–4, 2007.